Problems in stellar and planetary dynamics

a thesis submitted for the degree of

Doctor of Philosophy

by

Gareth Francis Kennedy
B.Sc. (Hons)

November, 2008

Summary

This thesis is concerned with a range of problems in stellar and planetary dynamics, specifically the destruction of globular clusters as they orbit the galaxy; the disruption of stellar binaries by the massive black hole in the centre of the Milky Way; and a new method for discovering low mass extrasolar planets which are not detectable using available methods. Investigations into these problems make extensive use of a new formulism developed by Rosemary A. Mardling that predicts the long-term stability of three-body problem systems. This formulism predicts systems that are unstable to the eventual escape of one of the masses in a random walk process; it is referred to as the Mardling stability criterion (MSC) throughout this thesis.

The relevant dynamical theory covering the concerning the two-body and three-body problem as well as the stability in the three-body problem is outlined in Chapter 1. This chapter introduces the MSC as a method for quickly determining stability in the general three-body problem. It allows one to predict systems that will be unstable to the escape of one of the bodies; the most likely body that will eventually escape the system depends on the mass ratios between the three bodies. For globular clusters the three bodies are particles representing a star in the cluster, the cluster core and the galaxy. In this case the mass ratios between these bodies mean that the escaping body will be the star and therefore the MSC can be used to predict the escape of stars from globular clusters. In the case of a stellar binary encountering a massive black hole, close encounters will result in the loss of one of the binary components while distant encounters result in the escape of the black hole, which is equivalent to the escape of the binary.

The first project presented in Part I examines the escape of stars from globular clusters on eccentric orbits with the galaxy. Previous studies quantify the escape of stars from clusters using the tidal radius of the cluster. Two of these tidal radius estimates from the literature are given in Chapter 2 and are based on the tidal field of the galaxy balancing that of the cluster for various types of star-cluster orbits.

In Chapter 3 we introduce a globular cluster model which uses a Plummer potential as the cluster potential and investigates the effect this has on the Kepler elements for stellar orbits within the cluster. The MSC is applied to the star-cluster-galaxy system in Chapter 4 by approximating this system as three point masses. The predicted occurrence of unstable systems is compared to numerical results for the stability of three bodies taking the cluster potential as the Plummer potential. It was found that the Plummer potential stabilises the orbits of stars that come within the core of the cluster compared to the equivalent orbits in a point mass

potential.

Chapter 5 presents a more sophisticated cluster model than the three-body model which is also less computationally demanding than a direct N-body simulation. This model was actually developed before the three-body model presented in Chapter 4, when we thought that the galactic orbit of the cluster might be changed by the additional mass loss of stars on unstable orbits. The galactic orbit of the cluster was not found to significantly change on the timescales simulated, however the cluster model produced interesting results for escaping stars. The model presented in Chapter 5 is tested against an N-body simulation using the fraction of escaping stars as a function of the distance from the cluster centre. Similar results are found for this model as were found using the results from an N-body simulation provided by Holger Baumgardt. The cluster model developed in Chapter 5 is used to estimate the tidal radius for a range of eccentricities and perigalacticon distances that include clusters on very wide galactic orbits, which are not possible to model using N-body simulations for realistic numbers of stars. These tidal radius estimates from simulated clusters were then compared with estimates from the literature and with the predictions using the MSC determined in Chapter 4.

There was good agreement between the tidal radius estimates for simulated clusters, the more recent tidal radius estimates from the literature and the predictions using the MSC, which provided encouragement to apply these predicted tidal radii to real clusters. Chapter 6 compares the tidal radius estimates based on observations of clusters in the Milky Way globular cluster system to predicted radius estimates determined using the MSC. It was found that the different estimates for the tidal radius could not be distinguished using current cluster observations. A summary of results for Part I is given in Chapter 7 along with the ramifications for this work in the context of the capture of dwarf spheroidal galaxies by the Milky Way galaxy.

The second project presented in Part II is a continuation of previous work begun during my honours thesis (Kennedy 2001). The emphasis of this project has been substantially changed in the intervening years due to the discovery of hypervelocity stars in the Milky Way (Brown et al. 2005). The physical problem under investigation is the tidal disruption of a stellar binary if it encounters a massive black hole within a particular distance. Sufficiently close encounters result in the capture of one star and the ejection of the other for cases where the binary is initially on a parabolic orbit relative to the black hole. Thus the encounter between a stellar binary and the black hole can produce hypervelocity stars, as predicted by Hills (1988).

The conditions in the galactic centre are reviewed in Chapter 8 with particular emphasis on dynamical interactions that can result in binaries encountering the massive black hole or that can also produce hypervelocity stars. In Chapter 9 estimates from the literature are given for the maximum pericentre distance of the binary-black hole orbit for which the tidal disruption of the binary is expected. These maximum pericentre distances are then compared to detailed scattering experiments conducted by the author over a wide range of relative orbital inclinations and stellar binary eccentricities. We find that estimates of the cross-section for exchange in the literature are roughly consistent with the results from the scattering experiments presented here. However the theoretically estimated maximum pericentre distances fall short of the numerical values, and fail to explain the dependence of this distance on the inclination and orbital eccentricity of the stellar binary.

The dependence of the maximum pericentre distance on inclination and binary eccentricity for binary-black hole orbits with eccentricity of 0.9 is examined in Chapter 10. The dependence on inclination and binary eccentricity of the maximum pericentre distance for which the binary is disrupted is predicted using the MSC and confirmed by comparison with the results from scattering experiments. Future extension of the MSC to distinguish between which of the three masses will eventually be ejected will allow that criterion to be used to predict the maximum pericentre distance for parabolic binary-black hole orbits.

In Chapter 11 the velocities found for the ejected star from parabolic binary-black hole orbits are used to predict the distribution of hypervelocity stars as they leave the galactic centre. This velocity distribution is found to be insensitive to the orbital eccentricity of the stellar binary, but strongly dependent on the choice of distribution for its semi-major axis. A summary of the results for Part II is presented in Chapter 12.

The final project presented in Part III examines the possibility of detecting low-mass planets which have been captured into the 2:1 mean motion resonance. The first of two chapters in this part is an original paper submitted for publication in a peer reviewed journal by Rosemary Mardling and myself. The second chapter is original work conducted by the author on existing data using the theory presented in the submitted paper.

Chapter 13 uses the formulism that the MSC is based on to study the stability of planetary systems with a hypothetical planet in the internal 2:1 resonance and to provide simple expressions for the libration period and the change in the observed orbital period. Using simulated data it is shown in Chapter 13 that it is possible to identify the existence of a low-mass companion in the internal 2:1 resonance by calculating the orbital period using piecewise sections of radial velocity data.

In Chapter 14 preliminary results are presented for the existence of a low mass companion to the known Jupiter mass planet HD 121504 b. The existing data for this planetary system is analysed using the theoretical approach and a similar data analysis method introduced in Chapter 13. It is concluded that HD 121504 is likely to contain a low mass planetary companion with mass in the range of $14\mathrm{M}_\oplus \lesssim m_i \sin i \lesssim 30\mathrm{M}_\oplus$. It is strongly recommended that further observations for HD 121504 be made with as large a time resolution as possible to confirm these preliminary results. If this is confirmed it will represent a significant discovery and a vindication of the Mardling stability criterion that underlies this thesis.

Statement

This thesis contains no material which has been accepted for the award of any other degree or diploma in any University and, to the best of my knowledge, contains no material previously published or written by any other person, except where otherwise stated in the text.

Gareth F. Kennedy

Acknowledgements

Firstly I would very much like to thank my wife Belinda Bennett, who has had the unenviable role of being married to a PhD candidate. I would also like to thank my supervisor, Dr Rosemary A. Mardling, for suggesting these projects, correcting my English and science where appropriate and for providing the stability criterion this work is based upon. Without her help and guidance over the last few years this thesis would not have been possible.

I would like to thank my family and friends for their support during this candidature, particular my parents for an endless list of things. Thanks are also extended to the astrophysics group at Monash University, in particular Prof. John Lattanzio, for both interesting conversations, often having nothing to do with astrophysics, and for keeping the caffeine concentrations in my blood sufficiently high. Specific thanks in this capacity go to Carolyn Doherty and Simon Campbell. Recently I have been greatly aided by Pilar Gil-Pons and Juan Martinez-Olíveros for providing help with Spanish and decrypting official looking documents. Thanks also go to Keith Hsuan for keeping me in check in his role as a fellow PhD candidate and for deejaying at my wedding.

During my candidature I had the opportunity to attend workshops at the KITP, UCSB and IPAM, UCLA in 2004 and 2005 respectively. I am grateful to have been able to attend these and for many illuminating discussions, in particular with Eric Ford regarding statistical analysis.

This thesis could not have been possible without funding made available via an Australian Postgraduate Award and the computational resources available at the Victorian Partnership for Advanced Computing. I would also like to thank my employer Prof. Alan Bond and the rest of the electrochemistry group at the school of chemistry, Monash University for my time there over the past two years.

Contents

List of Tables

List of Figures

Chapter 1

Review of relevant theory

While the projects undertaken here involve different physical systems, they all share a common theoretical basis in the three-body problem. This is easy to see for the case of a binary system interacting with a massive black hole (Part II) and two planets orbiting a host star (Part III), but it is less obvious for the case of globular clusters (Part I). However, the latter can be considered as a superposition of three-body problems involving a single star, the cluster potential and a point mass galaxy since we will not include interactions between the stars themselves.

In order to cover the theory relevant for all these problems the concepts required are introduced in the context of the two-body problem in Section 1.1, then the general three-body problem is discussed in Section 1.2, and finally the stability of the three-body problem is examined in detail in Section 1.3.

1.1 Two-body problem

A summary of the two-body problem is presented in order to be able to refer back to fundamental concepts in later chapters. The bulk of this review comes from Murray and Dermott (2000), to which the reader is referred to for more detail.

The two-body problem consists of two point masses, m_1 and m_2, orbiting a common centre of mass. The problem can be reduced to solving the equations of motion for a single vector[1] $\mathbf{r}$, where $\mathbf{r} = \mathbf{x_2} - \mathbf{x_1}$ and $\mathbf{x_i}$ denotes the spacial coordinates of mass m_i relative to an inertial frame. The equations of motion for this problem are written as

$$\ddot{\mathbf{r}} = -\frac{Gm_{12}}{r^3}\mathbf{r} \tag{1.1}$$

where G is the gravitational constant, $m_{12} = m_1 + m_2$, $r = |\mathbf{r}|$ and $\ddot{\mathbf{r}}$ is used to denote the second time derivative of the position vector $\mathbf{r}$.

The two-body problem is analytically solvable and the solution is the familiar equation for

[1]Note that $\mathbf{x}$ is used to denote a vector and x its magnitude.

the distance between the two bodies

$$r = \frac{a\left(1 - e^2\right)}{1 + e\cos(\theta - \varpi)} \tag{1.2}$$

where e is the eccentricity, a is the semi-major axis, and the true longitude $\theta = \varpi + f$. The first of these two angles is a reference angle called the longitude of pericentre ϖ and the second is the true anomaly f. The angles used to describe the position of a mass in an arbitrary orbit relative to each other are shown in Figure 1.1.

The pericentre distance is the distance of closest approach between the two masses, given by

$$p = a\,(1 - e)\,. \tag{1.3}$$

The semi-major axis a is related to the orbital period T via Kepler's third law

$$T = 2\pi\sqrt{\frac{a^3}{Gm_{12}}}, \tag{1.4}$$

which is equivalent to the radial period for a Keplerian orbit. The orbital period in terms of the mean motion frequency of the orbit is

$$\nu = \frac{2\pi}{T} = \sqrt{\frac{Gm_{12}}{a^3}}, \tag{1.5}$$

which represents the average angular velocity of the two bodies about the centre of mass.

Another useful angle for describing the motion of m_1 and m_2 about the centre of mass is the mean anomaly M. This angle increases linearly over time with a single orbit spanning $0 \leq M < 2\pi$. The mean anomaly is given by $M = \nu(t - \tau)$ where τ is the time at pericentre. It is used in Equation (1.2) by solving the following relations for the true anomaly. The first of these is

$$M = E - e\sin E \tag{1.6}$$

where E is the eccentric anomaly. The eccentric anomaly is in turn related to the true anomaly by

$$\cos f = \frac{\cos E - e}{1 - e\cos E}. \tag{1.7}$$

Equations (1.6) and (1.7) must be solved iteratively for f for any given orbit with eccentricity e at time t.

The two-body point mass problem is completely constrained by seven integrals of the motion (fives of which are independent), these being the total energy and the three spatial components of the angular momentum and the Laplace-Runge-Lenz vector. For ease of use in later chapters, the energy of an orbit is written in two different forms

$$E = \frac{-G(m_1 + m_2)}{2a} = \frac{1}{2}\left(\dot{\mathbf{r}}.\dot{\mathbf{r}}\right) - \frac{Gm_{12}}{r} \tag{1.8}$$

with the first form valid for unbound orbits if one used Equation (1.3) to replace a with $p/(1-e)$. The angular momentum of the system is also conserved and can be written as

$$\mathbf{J} = \mu\sqrt{Gm_{12}a\,(1-e^2)}\hat{\mathbf{z}} \tag{1.9}$$

where the reduced mass of the system $\mu = m_1m_2/m_{12}$, and $\mathbf{k}$ is a unit vector normal to the orbit ($\hat{\mathbf{z}} = \hat{\mathbf{x}} \times \hat{\mathbf{y}}$ in the context of Figure 1.1).

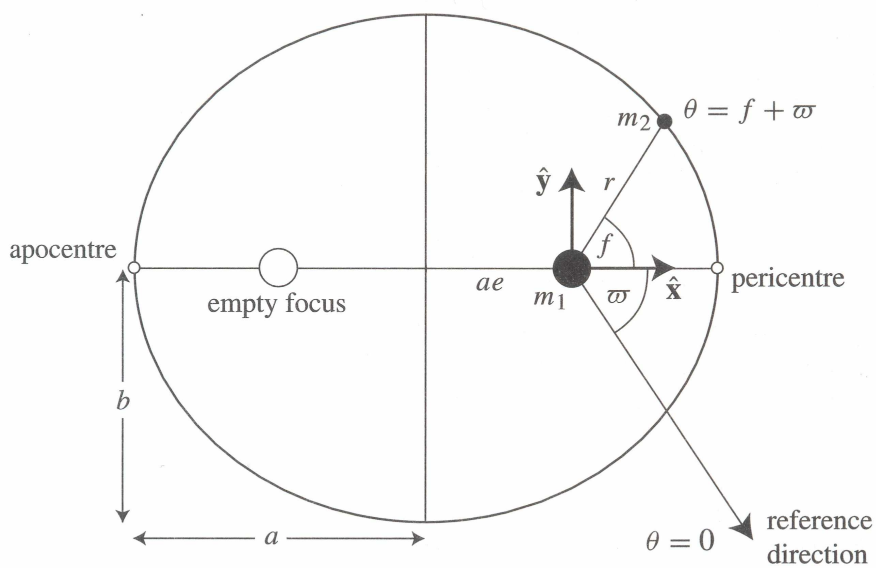

Figure 1.1: Illustration of orbital phase angles for a two-body orbit. Reproduced from Figure 2.5 of Murray and Dermott (2000).

To completely specify an orbit the masses of the two components, as well as six quantities are required. These quantities are either the initial position and velocity vectors, or another independent collection of parameters and angles. It is often useful to specify an orbit by the semi-major axis (a), the eccentricity (e), the true anomaly ($f = \theta - \omega$), and three angles relative to a reference plane. The orientation of an orbit is described by the Euler angles (Goldstein 1959) inclination (I), longitude of ascending node (Ω), and the argument of pericentre (ω), which are shown relative to a reference plane in Figure 1.2.

The quantities introduced here are continually referred to throughout this thesis. Of particular interest are changes in the binding energy (Equation 1.8) and orbital period (Equation 1.4), caused by the introduction of a third mass.

1.2 General three-body problem

The three-body problem presents an interesting paradox in mathematics, namely that it is one of the easiest problems to write down (see Equation 1.15 for the equations of motion), yet the general case is impossible to solve analytically.

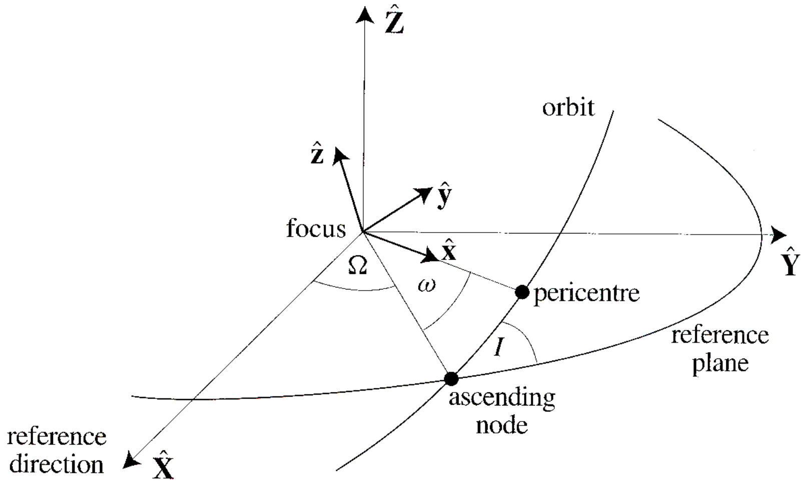

Figure 1.2: Orientation angles for a two-body orbit relative to a fixed reference plane and direction. Reproduced from Figure 2.13 of Murray and Dermott (2000).

Perturbation methods allow approximate solutions to be found in some cases, for example the case of a comet interacting with Jupiter's orbit approximated as a circle. Often the restricted three-body problem is used to study these scenarios, in which one of the bodies can be considered as a test particle ($m_3 = 0$). For a detailed description and some applications of this problem the reader is referred to Chapter 3 of Murray and Dermott (2000).

The assumption that $m_3 = 0$ cannot be made in any of the work presented here because the third mass is a galaxy in Part I, a massive black hole in Part II, and a Jupiter mass planet in Part III. Nor can any other parameter be assumed to be negligible for these applications, therefore approximate solutions to the three-body problem are put aside and the general three-body problem is discussed.

Jacobian coordinates are useful because we can represent the three-body system as the interaction of two binaries (Murray and Dermott 2000). A schematic diagram of this set up is shown in Figure 1.3 in both centre of mass and Jacobian coordinates. The inner orbit refers to the orbit containing m_1 and m_2, while the outer orbit consists of m_3 and the combined mass of the inner orbit ($m_1 + m_2$). Quantities relating to the inner or outer orbits are denoted with subscript i or o respectively, for example a_o refers to the outer semi-major axis.

The position and velocity vectors are defined in terms of the centre of mass coordinates by the following equations

$$\mathbf{r} = \mathbf{x_2} - \mathbf{x_1} \tag{1.10}$$

$$\mathbf{R} = \frac{m_{123}}{m_{12}}\mathbf{x_3} \tag{1.11}$$

where $m_{123} = m_1 + m_2 + m_3$, $\mathbf{x_i}$ denotes the centre of mass position of particle i, making $\dot{\mathbf{x}}_\mathbf{i}$ the

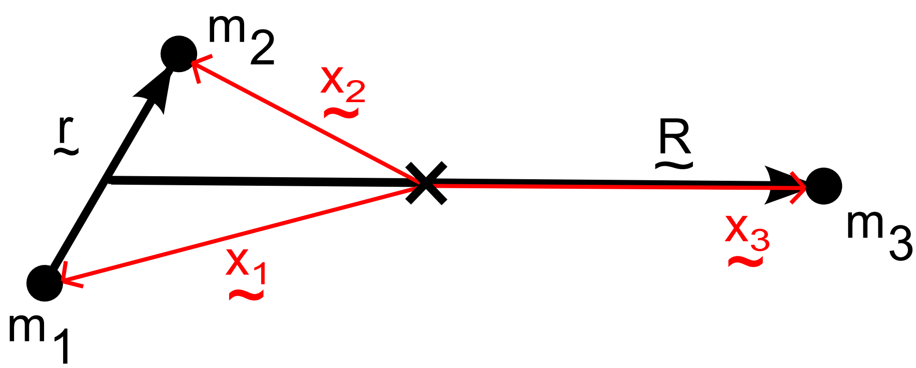

Figure 1.3: Schematic of the Jacobian coordinate system ($\mathbf{r}$ and $\mathbf{R}$) and centre of mass coordinates ($\mathbf{x_i}$) for three masses.

associated centre of mass velocity. It is also useful to write this in centre of mass coordinates

$$\mathbf{x_1} = -\frac{m_2}{m_{12}}\mathbf{r} - \frac{m_3}{m_{123}}\mathbf{R} \tag{1.12}$$

$$\mathbf{x_2} = \frac{m_1}{m_{12}}\mathbf{r} - \frac{m_3}{m_{123}}\mathbf{R} \tag{1.13}$$

$$\mathbf{x_3} = \frac{m_{12}}{m_{123}}\mathbf{R}. \tag{1.14}$$

The equations of motion for mass one can be written in centre of mass coordinates as

$$\ddot{\mathbf{x}}_\mathbf{1} = \frac{Gm_2\left(\mathbf{x_2} - \mathbf{x_1}\right)}{\left|\mathbf{x_2} - \mathbf{x_1}\right|^3} + \frac{Gm_3\left(\mathbf{x_3} - \mathbf{x_1}\right)}{\left|\mathbf{x_3} - \mathbf{x_1}\right|^3} \tag{1.15}$$

and similarly for masses two and three. It is worth noting that by adding extra terms this can be extended to $N > 3$ bodies, for example $N = 10^6$ stars for a typical globular cluster (refer to Part I). In Jacobian coordinates, the equations of motion for the inner orbit becomes

$$\ddot{\mathbf{r}} = -\frac{Gm_{12}}{r^3}\mathbf{r} + Gm_3\left[\frac{\left(\mathbf{R} + \frac{m_1}{m_{12}}\mathbf{r}\right)}{\left|\mathbf{R} + \frac{m_1}{m_{12}}\mathbf{r}\right|^3} - \frac{\left(\mathbf{R} - \frac{m_2}{m_{12}}\mathbf{r}\right)}{\left|\mathbf{R} - \frac{m_2}{m_{12}}\mathbf{r}\right|^3}\right] \tag{1.16}$$

where the second term is the perturbation of the two-body orbit as a result of the third mass. This term vanishes if $m_3 = 0$ and Equation (1.1) is recovered. The equation of motion for the outer orbit is

$$\ddot{\mathbf{R}} = -\frac{Gm_{123}}{m_{12}}\left[\frac{m_1\left(\mathbf{R} - \frac{m_2}{m_{12}}\mathbf{r}\right)}{\left|\mathbf{R} - \frac{m_2}{m_{12}}\mathbf{r}\right|^3} + \frac{m_2\left(\mathbf{R} + \frac{m_1}{m_{12}}\mathbf{r}\right)}{\left|\mathbf{R} + \frac{m_1}{m_{12}}\mathbf{r}\right|^3}\right]. \tag{1.17}$$

This reduces to the equation of motion of a test particle, i.e. the restricted three-body problem, if $m_3 = 0$. Equation (1.17) can be written as

$$\ddot{\mathbf{R}} = -\frac{Gm_{123}}{R^3}\mathbf{R} + \frac{Gm_{123}}{m_{12}}\left[\frac{m_{12}\mathbf{R}}{R^3} - \frac{m_1\left(\mathbf{R} - \frac{m_2}{m_{12}}\mathbf{r}\right)}{\left|\mathbf{R} - \frac{m_2}{m_{12}}\mathbf{r}\right|^3} + \frac{m_2\left(\mathbf{R} + \frac{m_1}{m_{12}}\mathbf{r}\right)}{\left|\mathbf{R} + \frac{m_1}{m_{12}}\mathbf{r}\right|^3}\right]. \tag{1.18}$$

where the term in brackets is the perturbation to the outer orbit.

Equations (1.16) and (1.18) can be written as

$$\mu_i\ddot{\mathbf{r}} + \frac{Gm_{12}}{r^3}\mathbf{r} = \frac{\partial\mathcal{R}}{\partial\mathbf{r}} \tag{1.19}$$

$$\mu_o\ddot{\mathbf{R}} + \frac{Gm_{123}}{R^3}\mathbf{R} = \frac{\partial\mathcal{R}}{\partial\mathbf{R}} \tag{1.20}$$

where $\mu_i = \frac{m_1 m_2}{m_{12}}$ and $\mu_o = \frac{m_{12} m_3}{m_{123}}$ are the reduced masses for the inner and outer orbits respectively. The disturbing function contains all the information pertaining to the interaction between the inner and outer orbits and is given by

$$\mathcal{R} = -\frac{Gm_{12}m_3}{R} + \frac{Gm_2m_3}{\left|\mathbf{R} - \frac{m_1}{m_{12}}\mathbf{r}\right|} + \frac{Gm_1m_3}{\left|\mathbf{R} + \frac{m_2}{m_{12}}\mathbf{r}\right|}. \tag{1.21}$$

Note that the disturbing function utilised here has dimensions of energy and not energy per unit mass as is the convention used for the restricted three-body problem (see, for example, Murray and Dermott 2000). The total energy of the three-body system can be written as

$$E = E_i + E_o + \mathcal{R} \tag{1.22}$$

where $E_{i/o}$ are the inner/outer binding energies of the unperturbed orbits as calculated by Equation (1.8).

The main advantage of setting the three-body system up in Jacobian coordinates is that interactions between the inner and outer orbits can be readily examined both analytically and numerically. For example by considering the inner and outer orbits independent of each other the eccentricities and semi-major axes for the inner (e_i and a_i) and outer orbits (e_o and a_o) can be determined in the same way as in Section 1.1.

To simplify matters the *initial* plane of motion for the inner binary orbit is used as the reference plane and the position of m_2 relative to m_1 at pericentre specifies the direction $\hat{\mathbf{x}}$ in Figure 1.2. This convention is reversed for the case of orbits in a globular cluster (Part I) where the initial orbit of the cluster about the galaxy is taken as the reference plane. Therefore the orientation angles (I, Ω and ω) are the initial angles between the outer and inner orbits.

1.3 Stability in the three-body problem

In this thesis we are interested in Laplace stability, which describes whether a given system is stable against the escape of one of the bodies to infinity. When the escaping body was a former member of the inner binary then the system has undergone an exchange. Unstable systems are defined as those where one body escapes and requires the transfer of energy to the escaping mass, while the total energy of the system remains negative. The escape of one of the bodies is a random walk process, a fact that is included in the stability criterion below. For a comparison between Laplace and Hill stability, which concerns the possibility of close encounters, the reader is referred to Kubala et al. (1993).

To determine whether a given three-body system is stable against the escape of one of the bodies we use two approaches, one numerical and the other analytical. Numerical examinations of stability have traditionally used long-term integrations, but here the sensitivity to initial conditions is taken advantage of, as described in Section 1.3.1. Stability predictions for systems are made using an analytical method referred to as the Mardling stability criterion (MSC) (Mardling 2008b), which is reviewed in Section 1.3.2.

1.3.1 Numerically defining a stable system

The precise definition of a stable system has long been a problem in dynamics. While the two-body system is inherently stable, determining the stability in the general three-body problem has been difficult. Recent work by Rosemary Mardling allows the stability of these systems to be determined. A summary of this work as it applies to this thesis is discussed in the next section.

Since all of the physical processes examined throughout this work occur on dynamical timescales ($\lesssim 10^3\ T_o$), a stable system is taken to mean a dynamically stable system. This is equivalent to saying that stability is governed by the mean motion resonances (e.g. a 2:1 ratio between the outer and inner binary periods) and not by combinations of mean motion and secular resonances. A dynamically stable system is defined to be any system that is insensitive to changes in the initial conditions (e.g. Mardling 2008b). This definition allows unstable and stable systems to be easily distinguishable using quick numerical integrations. The speed of this method is essential since each of the physical problems examined here involves large parameter space searches.

The procedure for determining the sensitivity of systems to initial conditions is as follows: Two sets of numerical integrations are carried out for a given system, differing only by a small change ϵ in one of the initial parameters (e.g. e_i or a_i). All numerical stability integrations are run using a Bulirsch-Stoer integrator (Press et al. 1986) for long enough to allow orbits to present as chaotic (100 to 1000 T_o depending on the significance of secular changes), or until the escape of one of the bodies.

At the end of the simulation, the difference between the inner semi-major axes for the two slightly different orbits (Δa) is compared. The condition for stable systems is

$$\Delta a = |a_{i,1} - a_{i,2}| < \epsilon N \tag{1.23}$$

where $a_{i,j}$ denotes the inner semi-major axis for simulation j, N is the number of time-steps in the simulation and we take $\epsilon \equiv 10^{-5}$. Note that the maximum value of Equation (1.23) is also monitored (refered to as Δa_{max}) and is compared with ϵ as an additional stability constraint.

Any system that this method finds as unstable will indeed be unstable, however the same cannot be said for stable systems. Mathematically it is impossible to prove that any three-body system is stable for all time, in fact even the long term stability of the Solar system remains unknown (e.g. Batygin and Laughlin 2008). An in-depth examination of the nature of stability is outside the scope of this work, so from hereon a stable system means stable over the dynamical timescale taken as $100T_o$ for simplicity and computational efficiency.

(a) Stable system (b) Unstable system

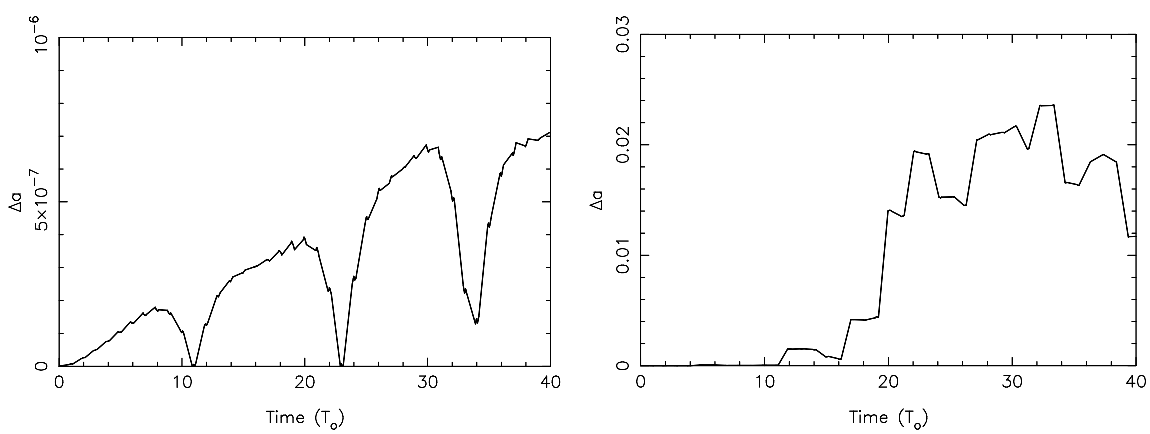

Figure 1.4: The difference in inner semi-major axis between nearly identical initial conditions for stable (a) and unstable (b) systems over time. The time evolution of the semi-major axis of the unstable system is seen to be a random walk process that will eventually end in the total dissolution of the binary. Note the substantially different scales for the semi-major axes of each plot.

To demonstrate the usefulness of the criterion in Equation (1.23), the difference between stable and unstable systems are shown in Figure 1.4. This figure is an example of the planetary system HD 216770 with an additional hypothetical planet (studied in Part III). The details of this system are not pertinent here and this figure is included to demonstrate two points. Firstly the stable orbit in panel (a) of Figure 1.23 shows the difference between simulations growing in proportion to the initial separation ϵ. Secondly the difference between systems with nearly identical initial conditions has noticeably diverged for the unstable system in panel (b) after 12 outer orbits. For further discussion of the behavioural differences between unstable and stable orbits see Mardling (2008b).

1.3.2 Determining stability using the Mardling stability criterion

The stability of the three-body problem is essential to each of the physical problems investigated in this thesis. The previous section outlined a computational method for determining the stability of a given three-body system, however the CPU time required for large parameter spaces is prohibitive. Therefore a method for quickly determining the stability in the general three-body problem by Mardling (2008b) is reviewed here. The aim is to summarise the Mardling stability criterion (MSC) and to outline the algorithm used to determine the stability of any coplanar three-body system. The more general case where the inner and outer orbits are relatively inclined by an angle I is examined in Section 1.3.3.

Recall that the interaction between the inner and outer orbits is given by the disturbing function $\mathcal{R}$ (Equation 1.22). This function contains all of the information relevant to the stability of the system and has the units of energy. The disturbing function is expanded in spherical harmonics and Fourier series to be expressible as a multiple sum over the cosine of the resonance angle associated with the $n : n'$ resonance (Mardling 2008b)

$$\phi_{mnn'} = n'M_i - nM_o + m\left(\varpi_i - \varpi_o\right) \tag{1.24}$$

where $M_{i/o}$ are the mean anomalies for the inner/outer orbit (Equation 1.6) and m is the spherical harmonic order. The angle from the pericentre direction to a reference plane for the inner/outer orbits $\varpi_{i/o}$ is shown in Figure 1.1 for a two-body orbit.

Rates of change of the semi-major axes for the inner and outer orbits are derived using Lagrange's planetary equations resulting in a pendulum equation for the resonance angles. There are two kinds of motion possible for the deflection angle ϕ of a forced pendulum, libration and circulation. If a pendulum is librating then the angle ϕ oscillates with a maximum magnitude $\phi_m \leq \pi$. Circulation for a forced pendulum means that the defection angle will increase or decrease indefinitely depending on initial conditions. The boundary between these kinds of motion is referred to as the separatrix.

Each of these types of motion are indicated in Figure 1.5 (a) with the separatrix marked by the black curves, circulation as the green curves and libration as the red curves. The resonance angle ϕ is shown along the horizontal axis and the time derivative of this angle $\dot{\phi}$ along the vertical axis. For the resonance angle associated with the three-body system (Equation 1.24) the time derivative is given by

$$\dot{\phi}_{mnn'} = n'\nu_i - n\nu_o + m\left(\dot{\varpi}_i - \dot{\varpi}_o\right) \tag{1.25}$$

where $\dot{M}_{i/o} = \nu_{i/o}$ from Section 1.1. Throughout this analysis the longitude of pericentre (ϖ) is assumed to be independent of time, thus $\dot{\varpi}_{i/o} = 0$. Figure 1.5 (a) shows this angle with $n' = 1$ in arbitrary units to demonstrate the types of motion for the three-body system.

The two types of motion, circulation and libration, are described as follows. The circulation of a resonance angle is equivalent to the inner and outer orbits being weakly coupled, i.e. the mean motions of each orbit can vary independently. This means that the resonance angle $\phi_{mnn'}$ will smoothly move along the horizontal axis, e.g. if $\phi_{mnn'} = 0$ initially and M_i was directed positively then $\phi_{mnn'}$ will increase with time. The time derivative $\dot{\phi}_{mnn'}$ will oscillate around the initial value of $\nu_i - n\nu_o$. This results in sinusoidal time dependence in the inner and outer orbital periods, and equivalently in the semi-major axes of the orbits.

For resonant systems the orbital periods of the inner and outer orbits are commensurate. For librating systems this means that the resonance angle $\phi_{mnn'}$ remains between some minimum and maximum values of $\phi_{mnn'}$, as seen for the red curves in Figure 1.5 (a). Taking the example system with initial conditions of $\phi_{mnn'} = 0$ and M_i directed positively then the system will smoothly move in a clockwise direction along one of the red paths indicated in Figure 1.5 (a). Note that $\dot{\phi}_{mnn'}$ also varies between a minimum and maximum $\dot{\phi}_{mnn'}$, which results in the inner and outer orbital periods having a large amplitude sinusoidal time dependence. The variation of the outer orbital period is used in Part III to show that it is possible to indirectly detect terrestrial planets orbiting interior to an observed Jupiter-mass planet. For further discussion of the physics of resonance the reader is referred to Mardling (2008b).

Since the resonance angles for the three-body problem satisfy a pendulum-like equation then a resonant system means that the resonance angle librates about a given value (usually $\phi_{mnn'} = 0$). Note that we will use the common terminology of a system being in resonance if the ratio of the outer to inner periods ($\sigma = T_o/T_i$) is within a distance $\Delta\sigma$ of a particular $n : n'$ resonance. When a system has initial conditions such that $\phi_{mnn'}$ and $\dot{\phi}_{mnn'}$ reside in two resonances simultaneously then it is possible for the resonance angles to librate inside either resonance at any time. This jumping between resonances can occur at any time and means that two three-body systems with initially very close conditions will quickly diverge once one jumps to a different resonance, leaving the other behind. This sensitivity to changes in the initial conditions is characteristic of chaotic motion and is used by the MSC to predict unstable systems.

The situation of two neighbouring resonances (n and $n+1$) overlapping is shown in Figure 1.5 (b). The libration regions for each resonance are coloured green while the region where the two

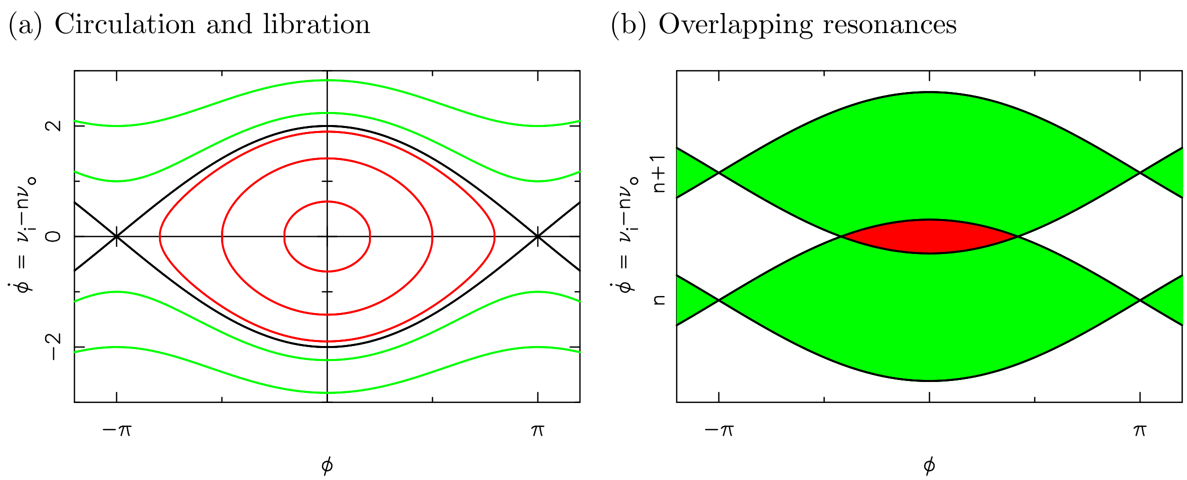

Figure 1.5: The left panel shows libration (green curves) and circulation (red curves) for the three-body problem. The separatrix between these types of motion is shown as the black curve in both panels. The same types of motion are seen in forced pendulums and the location of the separatrix is found by considering the three-body problem as a superposition of forced pendulums. This analysis is used by the MSC to predict unstable systems for which the regions of libration for neighbouring resonances overlap. The right panel illustrates the librating regions of each resonance in green and regions which reside in two resonances is red.

resonances overlap is coloured red. The shape of the separatrix (black curves) associated with each resonance is determined using Equation (1.28) with $\mathcal{A}_{mnn'}$ chosen such that the widths just overlap. Note that unstable orbits are not just found in the region where the two resonances overlap. Chaotic orbits can also occur near the separatrix where the system is librating in one resonance and circulating in a neighbouring resonance. This occurs when the variation in the orbital periods due to circulation is greatest, i.e. near the separatrix of the non-librating resonance.

The equations describing the time evolution of the resonance angles $\phi_{mnn'}$ for a coplanar system are of the form (Mardling 2008b)

$$\ddot{\phi}_{mnn'} = -n'^2 \nu_o^2 \mathcal{A}_{mnn'} \sin(\phi_{mnn'}), \tag{1.26}$$

which is a pendulum-like equation. As with a forced pendulum, chaotic motion occurs in the three-body problem when the system exists in two or more resonances simultaneously. To determine if a system of three point masses exists in a given $n : n'$ resonance the widths associated with the separatrix (black curves in Figure 1.5) for a given $\phi_{mnn'}$ must be calculated. For coplanar three-body systems in a resonance of the form $n : n'$ the resonance width is given by (Mardling 2008b)

$$\Delta\sigma_{mnn'} = 2\sqrt{\mathcal{A}_{mnn'}} \tag{1.27}$$

where $\mathcal{A}_{mnn'}$ is a function of all the orbital parameters. The equation for the separatrix is given by

$$\dot{\phi}_{mnn'} = n'\nu_i + n\nu_o + \Delta\sigma_{mnn'}\left(1 + \cos(\phi_{mnn'})\right) \tag{1.28}$$

where $\phi_{mnn'}$ is given by Equation (1.24).

For the cases of interest the $m = 2$ terms dominate for resonances of the form $n : 1$, so Equation 65 of Mardling (2008b) becomes

$$\mathcal{A}_{2n1} \approx -6c_{22}^2 s_1^{(22)}(e_i) F_n^{(22)}(e_o) \left[\frac{m_3}{m_{123}} + n^{2/3} \left(\frac{m_{12}}{m_{123}} \right)^{2/3} \left(\frac{m_1 m_2}{m_{12}^2} \right) \right]. \tag{1.29}$$

where $c_{22}^2 = 3/8$. The dependence of Equation (1.29) on the outer eccentricity is approximated by the asymptotic expression

$$F_n^{(22)}(e_o) \approx \frac{8\pi\sqrt{2\pi}}{3} \frac{(1-e_o^2)^{3/4}}{e_o^2} n^{3/2} e^{-n\xi(e_o)} \tag{1.30}$$

where

$$\xi(e_o) = \left(\mathrm{Cosh}^{-1}(\frac{1}{e_o}) - \sqrt{1-e_o^2} \right). \tag{1.31}$$

Resonances of the form $n : 1$ are frequently used in later chapters, so we introduce the notation of $\phi_n \equiv \phi_{2n1}$ and $\mathcal{A}_n \equiv \mathcal{A}_{2n1}$. Note that a different form for Equation (1.30) is used for the 2:1 resonance discussed in Chapter 13 for planetary systems.

The approximate functional dependence of Equation (1.29) on the inner eccentricity is

$$s_1^{22}(e_i) \approx -3e_i + \frac{13}{8}e_i^3 + \frac{5}{192}e_i^5 - \frac{227}{3072}e_i^7 \tag{1.32}$$

which is valid for $0 \le e_i \le 1$. The errors between this approximate expression and the exact integral expression are less than 1% for $e_i < 0.8$ and $< 0.1\%$ for $e_i < 0.63$ (Mardling 2008b). These errors are not significant for the applications studied here, since orbits with $e_i > 0.8$ are likely to be unstable regardless of the exact value of s_1^{22} (see for example Chapter 4).

As a system evolves on a secular timescale the resonance widths vary and are at their maximum when e_i is maximum. Therefore the inner eccentricity in Equation (1.32) needs to be modified for induced eccentricity in the inner orbit due to the outer orbit and the secular octopole term. The maximum eccentricity that can be dynamically induced in the inner eccentricity by the outer orbit following one passage is given by

$$e_i^{ind} = \left[e_i(0)^2 - 2\beta_n e_i(0)\sin(\phi_{2n1}) + \beta_n^2\right]^{1/2} \tag{1.33}$$

where $e_i(0)$ denotes the initial inner eccentricity, and

$$\beta_n = \frac{9\pi}{2n}\left(\frac{m_3}{m_{123}}\right)(1-e_o)^3\, F_n^{(22)}(e_o) \tag{1.34}$$

where $F_n^{(22)}(e_o)$ is given by Equation (1.30). The eccentricity correction due to the secular octopole term, non-zero if $m_1 \neq m_2$, is

$$e_i^{(oct)} = \begin{cases} (1+\alpha)e_i^{eq}, & \alpha \le 1 \\ e_i(0) + 2e_i^{eq}, & \alpha > 1 \end{cases} \tag{1.35}$$

where

$$\alpha = \left|1 - \frac{e_i(0)}{e_i^{eq}}\right| \tag{1.36}$$

and in the limit $e_i << 1$

$$e_i^{eq} = \frac{(5/4)e_o m_3(m_1-m_2)(a_i/a_o)^2\sigma(1-e_o^2)^{-1/2}}{\left|m_1m_2 - m_{12}m_3\sqrt{a_i/a_o}\sigma\sqrt{1-e_o^2}\right|}, \tag{1.37}$$

which is sufficiently accurate to determine the stability boundary for all values of e_i throughout this thesis. The inner eccentricity will also be affected by the Kozai effect for inclined systems, as discussed in the next section. For further expansion and explanations of these expressions the reader is referred to Mardling (2008b).

Before validating the predictions of unstable systems using the MSC with numerical simulations, it is timely to comment on the dependence of the resonance widths on high orbital eccentricities of the outer orbit. This is particularly appropriate for Part II of this thesis where the outer orbit is composed of the centre of mass of the stellar binary (composed of m_1 and m_2)

and the massive black hole (m_3). Encounters between the binary and the black hole are likely to occur on nearly parabolic orbits (see Chapter 8) and will either result in the exchange of the black hole for one of the binary components or the binary passing and escaping to infinity.

The mass ratios for this system are $m_2/m_1 = 1$ and $m_3/m_1 = 3 \times 10^6$ and taking the eccentricity of the inner stellar binary as $e_i = 0.4$ and the period ratio as $\sigma = 300$, the resonance widths as a function of the outer eccentricity e_o are shown in Figure 1.6 (a). The grey horizontal line at $\Delta\sigma = 1$ indicates roughly where all systems will be unstable, i.e. $e_o \gtrsim 0.9$ for $\sigma = 300$. The general shape of this curve does not change for higher values of σ which are equivalent to higher values of the pericentre distance of the outer orbit. Beyond a certain value of e_o (0.9 in this case) the resonance width depends more on factors like the mass ratio, inner eccentricity and relative inclination (see below) than the outer orbital eccentricity. This means that predictions using the MSC for $e_o = 0.9$ are expected to be very similar to $e_o = 0.99$ or 0.999.

(a) Resonance width against e_o (b) Possible unstable outcomes

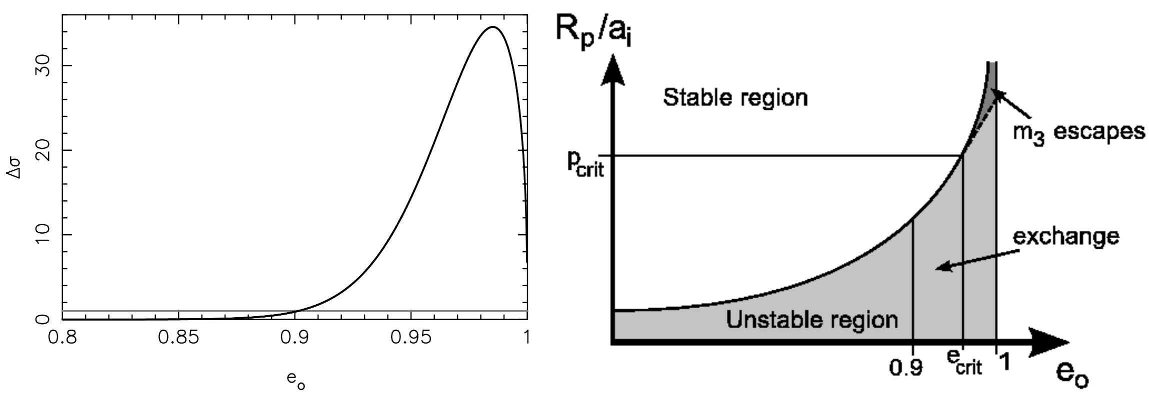

Figure 1.6: The left panel shows the resonance width as a function of e_o for the case of a stellar binary (m_1 and m_2) encountering a massive black hole (m_3), refer to Part II. The period ratio is $\sigma = 300$ and the orbital eccentricity of the inner binary (two stars in this case) is $e_i = 0.4$. The horizontal grey line at $\Delta\sigma = 1$ indicates where two neighbouring resonances will definitely overlap. The right panel is a schematic of the types of outcomes possible for unstable systems with binary-MBH mass ratios (shaded regions). The lightly shaded region indicates where m_1 or m_2 are expected to escape the system, resulting in an exchange between a star and the massive black hole (m_3). The darkly shaded region is where the system is still unstable to escape but in this case m_3 is expected to escape, i.e. the binary leaves the encounter intact. The critical values of pericentre distance (p_{crit}) and the associated eccentricity (e_{crit}) can be determined numerically (Mardling 2008, private communication).

The resonance widths indicated in Figure 1.6 mean that the MSC will *accurately* predict high e_o systems to be unstable to the escape of one of the masses. What the MSC does not do is distinguish between exchange (either m_1 or m_2 escapes) and the escape of the binary (equivalent to m_3 escaping). There will be a critical outer pericentre distance for a given outer eccentricity which marks the boundary between exchange for closer distances and the ejection of m_3 for wider distances, however this critical distance must be determined numerically (Mardling 2008, private communication).

Recall from Figure 1.4 that the escape of one of the masses from an unstable system is a random walk process. This creates a further complication for parabolic orbits since the first encounter must transfer energy from the outer orbit to the inner binary orbit to make the outer orbit bound. This is expected to occur half the time and is the only way of ensuring subsequent pericentre passages. In Part II numerical experiments are run with $e_o = 0.9$ and 1.0, but only the results for $e_o = 0.9$ are compared to predictions from the MSC. This ensures that all unstable systems predicted by the MSC will result in the escape of m_1 or m_2 and will therefore be equivalent to the disruption of the stellar binary.

The MSC predicts the stability of the three-body problem by determining the resonance width (using the formulae below) for the resonances n and $n+1$ that contain the period ratio of the system $\sigma = T_o/T_i = \nu_i/\nu_o$. For coplanar systems the width of each of these resonances depends on the masses of the three bodies (m_1, m_2 and m_3) the eccentricities of the inner and outer orbits (e_i and e_o), the period ratio σ and the orientation angles of the system via $\phi_{mnn'}$. The algorithm for determining if a system specified using these parameters is unstable is to test whether the system falls inside both the n and $n+1$ resonances, where the widths are defined in terms of these parameters below.

Note that this algorithm will not predict unstable orbits near the separatrix. Unstable orbits near the separatrix are particularly a problem for the algorithm when $\phi_{mnn'} \approx \pi$, since the resonances will both have zero width so no overlap is possible. This means that the algorithm based on the MSC will be less accurate when $\phi_{mnn'}$ deviates from zero, which is an issue when arbitrary phases between the inner and outer orbits are required. For the physical applications studied here we require a quick method for predicting the stability of a given three-body system. An algorithm that predicts a system to be unstable if it resides in two overlapping resonances (see Figure 1.5 b) fits this requirement well and produces good results throughout this work.

To illustrate the effectiveness of the MSC, the resonance widths for a coplanar, equal mass system ($m_i = 1$) with $e_i(0) = 0$ and $\phi_{mnn'} = 0$ are shown in Figure 1.7. Panel (a) is a reproduction of Figure 15 from Mardling (2008b) showing the resonance widths for $n = 4$ to $n = 20$, the dots representing unstable orbits found through numerical simulations. Note the general agreement found between these integrated orbits and the regions of resonance overlap. In Figure 1.7 (a) some unstable orbits are seen to trace out the left-hand separatrix, these systems are not in regions where two resonances overlap and so will not be predicted to be unstable by the MSC. Another point of interest is that the separatrix curves in Figure 1.7 do not coincide with the unstable systems for $\sigma \lesssim 8$. This is due to the neglect of the change in apsidal motion (ϖ) in the resonance angle (Equation 1.24). For further explanation of the discrepancy between unstable systems and regions where two resonances overlap the reader is referred to Mardling (2008b).

Figure 1.7 (b) shows the resonance widths for the same range of n with the shaded regions indicating where two or more resonances overlap. The kinks in the resonances in Figure 1.7 (b) are a plotting artefact occurring when the induced eccentricity exceeds unity. Since the algorithm implemented here successfully reproduces the stability boundary found by Mardling (2008b) (shown in panel a) it will be assumed to be a reliable diagnostic of unstable orbits for this thesis.

For further validation of the MSC in determining the stability of three-body systems the reader is referred to Mardling (2008b). From the point of view of this thesis, this criterion accurately predicts unstable orbits for all cases where $\sigma > 5$. This constraint is applicable to all physical problems of interest here except for extrasolar planets in a 2:1 type mean motion resonance where resonances of the form $n:2$ and $n:3$ may not be negligible. The effect of these resonances can be seen in the stability maps for planetary systems presented in Chapter 13 and is discussed further in that chapter.

1.3.3 Effect of inclination on the resonance width

For globular clusters (Part I) and binaries encountering the massive black hole in the galactic centre (Part II) the inclination between the inner and outer binary orbits is not restricted to the coplanar case. As such the method outlined above for calculating the resonance widths is incomplete and the inclination factors which include the effect of the relative inclination I must be included. The effect of inclination on the resonance width is under development (Mardling 2008a) and we present here a summary of the inclination factors relevant for this thesis.

For non-coplanar systems the disturbing function (Equation 1.21) also depends on the inclination of the inner and outer orbits to some reference plane. This dependence can be derived by making use of Wigner $\mathcal{D}$-functions developed to study arbitrary rotations in quantum mechanics (in particular, angular momentum), it is possible to find general expressions for spherical harmonics in terms of I, ω, Ω and f. In particular (Mardling 2008a)

$$Y_{lm}\,(\theta,\varphi) = \sum_{m'=-l,2}^{l} \mathcal{D}^{(l)}_{mm'}(I,\omega,\Omega)\, Y_{lm'}(\pi/2,f), \tag{1.38}$$

where the sum over m' is in steps of two and

$$\mathcal{D}^{(l)}_{mm'} = (-i)^{2l+m+m'} \gamma_{lmm'}(I)\, e^{i(m'\omega+m\Omega)} \tag{1.39}$$

is a Wigner $\mathcal{D}$-function with

$$\gamma_{lmm'}(I) = \sum_{n=n_{min}}^{n_{max}} \beta^{(n)}_{lmm'} \left(\cos\frac{I}{2}\right)^{2n-m-m'} \left(\sin\frac{I}{2}\right)^{2l-2n+m+m'} \tag{1.40}$$

and $\beta_{lmm'}$ are constants that depend on l, m and m'. Note that the form of Equation (1.39) has the three Euler angles siphoned off, which allows one to use the form of the resonance widths for coplanar systems given in the previous section.

As a consequence of the choice of spherical coordinates used to describe the inner and outer binary orbits the relative inclination between orbits is now separated out from the other Euler angles. The possible values for the new spherical harmonic index are $m' = -l, -l+2, \ldots, l-2, l$

where l is the index described in the previous section and the step size of two arises from the formulation (Mardling 2008a). Recall that $l = 2$ dominates for the physical applications of interest in this thesis, therefore the only non zero combinations are $m = 2$ with $m' = -2, 0, 2$ or $m = 0$ with $m' = 0$. In practice, the resonance width is given by

$$\sigma_{mnn'} = 2\sqrt{\mathcal{A}_{mnn'}} \tag{1.41}$$

where

$$\mathcal{A}_{mnn'} = \max(\mathcal{A}_{2n12}, \mathcal{A}_{2n10}, \mathcal{A}_{2n1-2}, \mathcal{A}_{0n10}) \tag{1.42}$$

and

$$\mathcal{A}_{mnn'm'} = -6c_{2m'}^2 s_n^{(2m')}(e_i) F_n^{(2m)}(e_o)\gamma_{2mm'}(I)\left[\frac{m_3}{m_{123}} + n^{2/3}\left(\frac{m_{12}}{m_{123}}\right)^{2/3}\left(\frac{m_1 m_2}{m_{12}^2}\right)\right], \tag{1.43}$$

with $c_{22}^2 = 3/8$ (as above) and $c_{20}^2 = 1/4$. The approximate dependence on the inner eccentricity are given by the functions

$$\begin{aligned} s_{-1}^{(22)}(e_i) &\approx -\frac{e_i^3}{15360}\left(4480 + 1880e_i^2 + 1091e_i^4\right) \qquad (1.44)\\ s_1^{(20)}(e_i) &\approx \frac{e_i}{9216}\left(-9216 + 1152e_i^2 - 48e_i^4 + e_i^6\right). \qquad (1.45)\end{aligned}$$

The dependence of Equation (1.43) on the outer eccentricity is approximated by the asymptotic expression

$$F_n^{(20)}(e_o) \approx \frac{1}{\sqrt{2\pi n}}\left(1 - e_o^2\right)^{-3/4} e^{-n\xi(e_o)} \tag{1.46}$$

where $\xi(e_o)$ is defined in Equation (1.31). The relevant inclination factors are

$$\begin{aligned} \gamma_{222}(I) &= \frac{1}{4}\left(1 + \cos(I)\right)^2 \qquad (1.47)\\ \gamma_{220}(I) &= \sqrt{\frac{3}{8}}\sin^2(I) \qquad (1.48)\\ \gamma_{22-2}(I) &= \frac{1}{4}\left(1 - \cos(I)\right)^2 \qquad (1.49)\\ \gamma_{200}(I) &= \frac{1}{2}\left(3\cos^2(I) - 1\right). \qquad (1.50)\end{aligned}$$

For inclined systems an additional secular effect is important, this is known as the Kozai effect (see for example Innanen et al. 1997) and involves a relationship between the eccentricity and inclination such that the maximum eccentricity induced by the Kozai mechanism is

$$e_K = \sqrt{\frac{1}{6}\left|Z + 1 - 4A^2 + \sqrt{D}\right|} \tag{1.51}$$

where

$$A = \cos I \sqrt{1 - e_i(0)^2} \tag{1.52}$$
$$Z = (1 - e_i(0)^2)(1 + \sin^2 I) + 5e_i(0)^2(\sin \varpi \sin I)^2 \tag{1.53}$$

and

$$D = 16A^4 - 20A^2 - 8A^2 Z - 10Z + Z^2 + 25, \tag{1.54}$$

which all depend on the initial eccentricity of the inner binary, $e_i(0)$, the initial relative inclination between the inner and outer orbits, I, and $\varpi = \varpi_o - \varpi_i$.

It turns out that it is the maximum possible eccentricity that comes out of this Kozai cycle that gives the maximum resonance width. This means that the maximum eccentricity induced by the Kozai mechanism (e_K) must also be included in the inner eccentricity functions given by Equations (1.32), (1.44) and (1.44). This is achieved by replacing e_i in these equations with the theoretical maximum inner eccentricity given by

$$e_i = \max(e_i^{ind}, e_i^{oct}, e_K) \tag{1.55}$$

where e_i^{ind} is the induced eccentricity due to the outer binary orbit (Equation 1.33) and e_i^{oct} is the eccentricity correction due to the octopole term (Equation 1.35). As the Kozai mechanism relates the eccentricity and inclination then the inclination used in Equation (1.47)-(1.50) must be replaced by the maximum possible inclination over a Kozai cycle (I_K). The maximum inclination is given by

$$\cos(I_K) = \frac{A}{\sqrt{1 - e_K}} \tag{1.56}$$
$$\sin(I_K) = \sqrt{1 - \cos^2 I_K}. \tag{1.57}$$

Each resonance width is calculated using the maximum e_i and inclination I_K and used by the stability algorithm, based on the MSC, for inclined systems in this thesis.

The resonance widths associated with each of the terms defined by Equation (1.43) are shown in Figure 1.8 for the cases of interest to this thesis. Each resonance width is calculated using Equation (1.41) and appears in Figure 1.8 as $\Delta\sigma(m = 2, m' = 2)$ (black curves), $\Delta\sigma(m = 2, m' = -2)$ (red), $\Delta\sigma(m = 2, m' = 0)$ (green) and $\Delta\sigma(m = 0, m' = 0)$ (blue). The mass ratios used in Figure 1.8 are $m_1 = m_2 = m_3$ for panel (a), $m_2/m_1 = 3.34 \times 10^{-5}$ and $m_3/m_1 = 6.89 \times 10^{-4}$ for panel (b), $m_2/m_1 = 10^{-6}$ and $m_3/m_1 = 10^5$ for panels (c) - (e), and $m_2/m_1 = 1$ and $m_3/m_1 = 3 \times 10^6$ for panel (f).

Note from Figure 1.8 that a discontinuity in the resonance widths at $I = \pi/2$ is seen for $m' = \pm 2$ (black and red curves). This occurs in the predicted resonance widths due to the form of the induced eccentricity of the inner binary due to the Kozai mechanism given by Equation (1.51). The discontinuities are genuine and are reproduced in scattering experiements (see for example Figure 10.2).

Future chapters make frequent use of the overlap of resonance widths of the form $n:1$ in both coplanar and inclined systems. The notation of $\phi_n \equiv \phi_{2n1}$ and $\mathcal{A}_n \equiv \mathcal{A}_{2n1}$ has already been introduced and we now add the qualification for inclined systems that $\mathcal{A}_{2n1}$ is replaced by $\mathcal{A}_{mnn'm'}$ given by Equation (1.42).

(a) Reproduction of Figure 15 from Mardling (2008b)

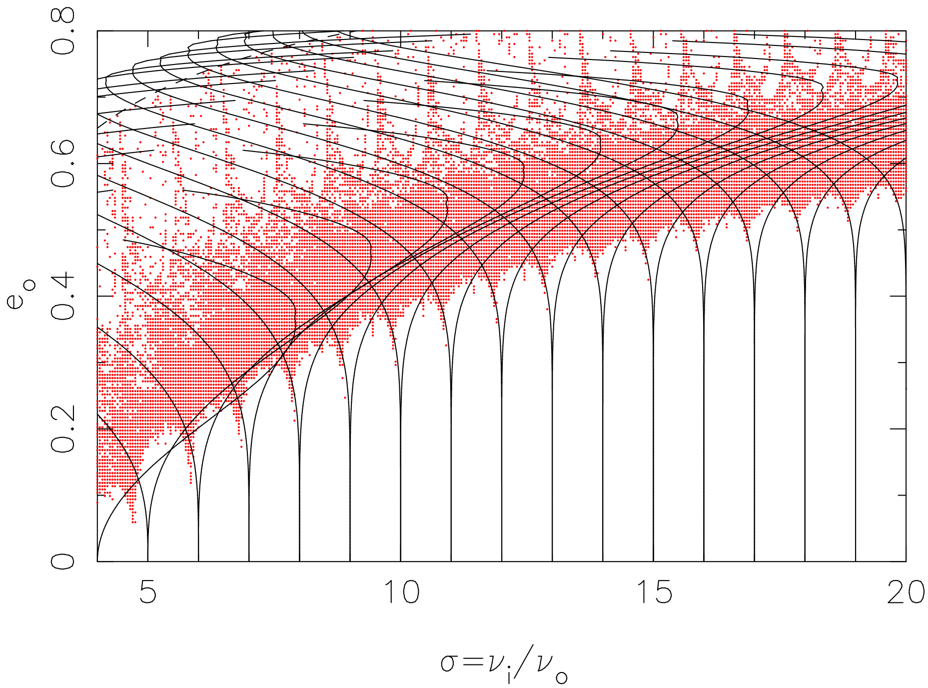

(b) Resonance widths determined using Section 1.3.2

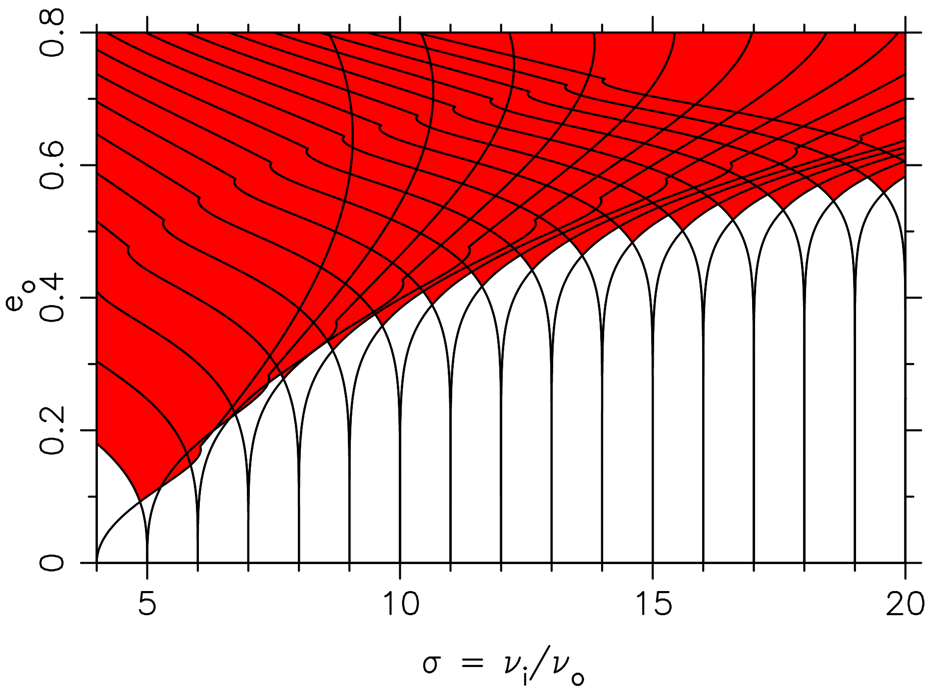

Figure 1.7: Comparison of stability boundary in Figure 15 of Mardling (2008b) for a coplanar system composed of equal masses with $e_i(0) = 0$, $M_i(0) = 0$ and $M_o(0) = \pi$. The data points in the top panel indicate unstable systems determined from numerical three-body experiments. The shaded region in the bottom panel indicates regions where two neighbouring resonances overlap and are predicted by the algorithm based on the MSC to be unstable. See text for further discussion.

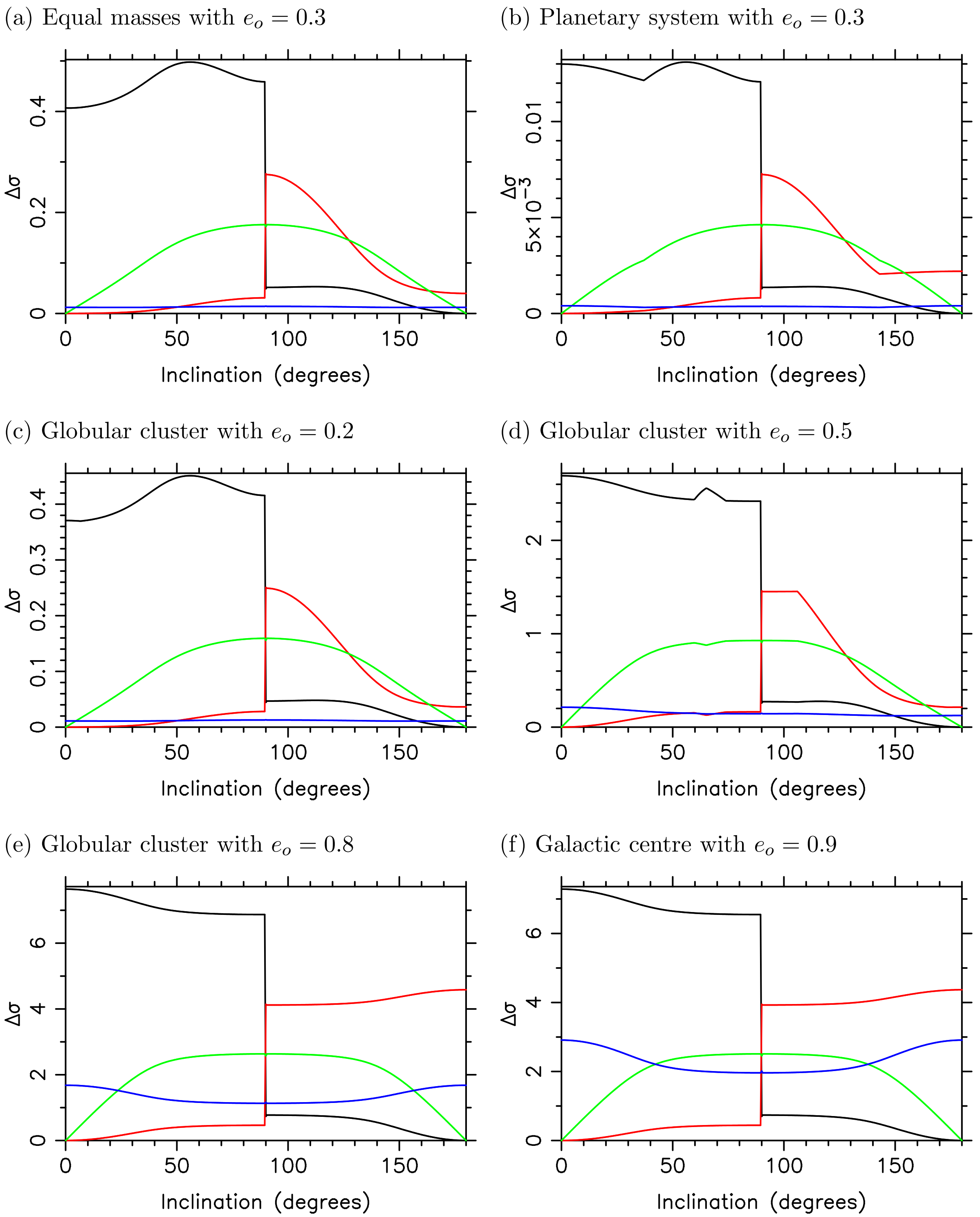

Figure 1.8: The effect of the relative inclination between the inner and outer binary orbits for a range of mass ratios described in text. All resonance widths $\Delta\sigma$ are calculated for individual terms defined by Equation (1.43) with $\phi_{mm'nn'} = 0$, $\varpi_i = \varpi_o = 0$, $\sigma = 10$ and $e_i(0) = 0.3$ before being corrected as per Equation (1.55). Curves are coloured differently for each term with $\Delta\sigma(m = 2, m' = 2)$ (black), $\Delta\sigma(m = 2, m' = -2)$ (red), $\Delta\sigma(m = 2, m' = 0)$ (green) and $\Delta\sigma(m = 0, m' = 0)$ (blue).

Part I

Dynamics of Globular Clusters

Chapter 2

Introduction

2.1 Summary

The aim of this project is to predict the escape of stars from globular clusters (GCs) on eccentric orbits using the Mardling stability criterion (MSC) described in Chapter 1. We will also utilise numerical models of increasing sophistication to test the results of the MSC against and finally apply it to predict the tidal radii for clusters in the Milky Way globular cluster system

A globular cluster is a bound system of stars of total mass between 10^5 and 10^7 $M_\odot$ in a roughly spherical shape orbiting within approximately 100 kpc of the host galaxy. The majority of these clusters formed more than 10 Gyr ago during similar processes that formed the galaxy, with recent galaxy mergers contributing relatively small numbers of GCs (Fall and Rees 1985; Forbes and Spitler 2008).

The stellar densities in the core of globular clusters can reach 1000 stars per cubic parsec and provide a fertile ground for stellar interactions. These interactions between stars are responsible for the internal dynamical processes occurring in clusters, which are discussed below. Recent work has also found that such dense environments have a detrimental effect on the stability of planetary systems (Spurzem et al. 2006).

From previous studies, a GC is expected to be truncated by the tidal field of the galaxy at a particular radius corresponding to equal accelerations due to cluster and the tidal field of the galaxy. A similar distance associated with the escape of stars from the cluster is predicted here using the stability boundary between unstable and stable orbits in the outer regions of the cluster. This approach was inspired by an analogue between a cluster orbiting a galaxy and a star orbiting a point mass star. The latter of these is referred to as the binary tides problem.

The existence of a stability boundary was found in the binary tides problem by modelling the structure of the primary star as an $n = 3$ polytrope and the companion star as a perturbing point mass (Mardling 1995a; Mardling 1995b). Using this model Mardling (1995a,b) found a sharp boundary beyond which chaotic energy exchange (see Section 1.3.1) takes place between the tides and the binary orbit.

The structure of a globular cluster can be approximated by an $n = 5$ polytrope (Spitzer 1987). Therefore a stability boundary is expected between stars on unstable and stable orbits in the outer regions of the cluster by analogue. By the discussion of stability in Section 1.3, unstable orbits are systems for which one body will be ejected. From energy considerations the galaxy and the cluster cannot be ejected, so stellar masses orbiting the cluster must be ejected.

Three numerical models of increasing sophistication are used to examine the escape of stars from a globular cluster. The first model is presented in Chapter 3 and consists of a particle in a Plummer potential, i.e. a star moving in an isolated cluster. This is used to examine the eccentricity distribution of stars in a cluster modelled by a Plummer potential. The relationship between the orbital period of a star in this potential and its binding energy and apocentre distance from the cluster centre are determined. Stars can only escape from the cluster through evaporation (see below) in this model. Chapter 3 serves to introduce the Plummer sphere potential and how the period of orbits inside this gravitational potential are calculated.

The second numerical model treats the interaction between stars in the outer regions, the cluster and the galaxy as a superposition of three-body systems. This model assigns a Plummer potential to the cluster particle, while the star and galaxy particles have point mass potentials. By neglecting the mutual interaction between particles most of the dynamical processes at work in globular clusters are neglected. These processes are discussed below, along with the justifications behind leaving them out of the model. The most significant of these processes are two-body relaxation and evaporation discussed in Sections 2.2 and 2.3.

The third numerical model is referred to as the simplified cluster model and consists of N particles orbiting a cluster core particle, which itself orbits a galaxy particle. The core particle is associated with the centre of the Plummer potential and can move in response to the positions of the N particles. This results in a mixing process in the cluster core that continually replenishes the regions in the cluster where stars escape. The simplified cluster model presented in Chapter 4 is an extension of the Plummer model presented in Chapter 3 and allows the computationally efficient treatment of GCs on eccentric orbits at the cost of excluding the mutual interaction between stars. In Chapter 4 the fraction of escaping stars as a function of distance from the cluster centre from the simplified cluster model is tested against the results from a direct N-body simulation, made available by Holger Baumgardt.

The fraction of escaping stars as a function of the distance from the cluster centre from the last two models is compared to the predicted values using the MSC. By using the period relationships from Chapter 3 and the MSC introduced in Section 1.3.2 the existence of a stability boundary between stars on orbits stable or unstable to escape GCs is examined in Chapter 4. Previous studies have also applied chaotic dynamical approaches to the escape of stars from star clusters. A recent study found a fractal structure exists in the phase space associated with the escape of stars from the cluster potential (Ernst et al. 2008). This study was limited to star clusters on circular orbits with the galactic centre, whereas the MSC is applied to eccentric cluster-galaxy orbits up to $e_o = 0.9$ in Chapter 4.

In Chapter 4 the MSC used to predict the range of distances from the cluster centre where stars are unstable to escape from the cluster. The predicted range is analogous to the tidal radius of a cluster, except that it is a continuum rather than a single distance. Predictions for the distances at which stars can escape the cluster using the MSC are compared to the fraction of escaping stars from the simplified cluster model in Chapter 5.

The fraction of unstable orbits expected by the MSC in Chapter 4 is used to predict the tidal truncation radii of different clusters in the Milky Way globular cluster system in Chapter 6. This tidal radii is found to have a greater dependence on the eccentricity of the cluster-galaxy orbit than other theoretical radii from the literature (see Section 2.4). We find that the orbital parameters of the Milky Way clusters are too strongly affected by the observational uncertainties to compare the accuracies of the eccentricity dependence between theoretical tidal radii. Finally in Chapter 7 a summary and discussion of the relevance of this work is presented.

2.2 Internal dynamical evolution globular clusters

Our discussion of the dynamics of globular clusters around the galaxy begins with a review of the internal dynamics of clusters. The influence of the parent galaxy is discussed in the context of destructive processes in Section 2.3. An excellent review of the literature for the internal dynamics of globular clusters can be found in Meylan and Heggie (1997) and more recently Heggie and Hut (2003). This section summarises the relevant parts of these reviews.

This project is focussed on the orbits of stars in the outer regions of the cluster. So it is necessary to know what processes are and are not at work beyond the cluster half-mass radius. The half-mass radius has special significance for the dynamics of globular clusters since it remains fairly constant for the early evolution of the cluster (see the N-body results in Meylan and Heggie 1997) and is a convenient boundary between the collapsing core and the expanding outer regions (see below).

The process of two-body relaxation acts to produce major changes in the radial structure of a cluster and is analogous to the thermal timescale in stars. This process is responsible for accelerating some stars to velocities greater than the escape velocity of the cluster and can be understood in the following way. For a star orbiting within a dense stellar environment two types of interactions are possible, close and distant encounters. While more dramatic, close encounters between two stars are greatly outnumbered by distant encounters and can be ignored when discussing the evolution of a cluster. Each distant encounter between two bodies produces a small velocity change in the trajectories of each star about the centre of the cluster. Repeated encounters redistribute the energy of the component stars leading to a Maxwellian distribution of energies. This process is called two-body relaxation and is characterised by the timescale at the half-mass radius of a cluster $R_{1/2}$, given by (Spitzer 1987)

$$t_{rh} = 1.7 \times 10^5 N^{1/2} \left(\frac{R_{1/2}}{pc}\right)^{3/2} \left(\frac{m}{\mathrm{M}_\odot}\right)^{-1/2} \tag{2.1}$$

where N is the number of stars of average mass m in the cluster. For globular cluster orbits of interest in this project (Section 2.5) the half-mass relaxation timescale is approximately 1 Gyr.

The dependence of the relaxation timescale on radius can be determined from

$$T_{relax} \propto \frac{v^3}{\rho} \tag{2.2}$$

where ρ and v are the stellar density and typical velocity, both of which depend on radius (Athanassoula et al. 2001). For a star on a circular orbit in a Plummer sphere, the density is given by Equation (3.7) and the velocity by Equation (3.18) (this potential is further discussed in Section 3.1). Using these equations the radial dependence of the relaxation time is found to be $R^{1/2}$ for stars in the outer regions of the cluster.

Since the orbital period of clusters on wide orbits about the galaxy is less than the relaxation timescale in the outer regions of the cluster, the relaxation process can be separated from the affect of the galactic tidal field. This is an important result for the simplified cluster model presented in Chapter 5, which does not include any relaxation processes. The assumption that relaxation processes can be separated from the tidal stripping of stars in the outer regions of the cluster is vindicated by comparing our model to results from an N-body simulation supplied by Holger Baumgardt in Chapter 5. The N-body simulation includes interactions between particles, and therefore two-body relaxation, in the cluster as it orbits inside a point mass galactic potential.

This relaxation process is also responsible for mass segregation (Fregeau et al. 2002 and references therein) and there is observational evidence that the timescale for mass segregation does indeed occur on a comparable timescale to two-body relaxation (Sosin 1997). Mass segregation results in high mass stars and binaries being over represented in the central cluster regions. Low mass stars will therefore overpopulate the outer regions of a cluster.

Stars orbiting in the outer regions of a cluster will have a distribution of velocities, some of which will be greater than the escape velocity of the cluster. These stars will leave the cluster in a process known as evaporation. Since the tidal field of the galaxy plays a major role here we delay discussion of this until next section.

The core of the cluster plays a crucial role in the later phases of the dynamical evolution of GCs. As a result of relaxation the density in the core increases while the outer regions expand by the virial theorem (Spitzer 1987). This causes the rate of evaporation to increase, reducing the total mass of the cluster and leading to further density increases in the core, again by the virial theorem. This situation is called core-collapse and can be observed in the cluster density profile as an almost pure power law without a flat region in the centre (Meylan and Heggie 1997).

Core-collapse does not continue indefinitely with the globular cluster collapsing to a point of infinite density. A number of mechanisms have been suggested to prevent core-collapse (Hut et al. 1992) of which only one is mentioned here. As previously discussed mass segregation leads to an increased fraction of binary systems in the core. These binaries may already exist from formation with observational evidence supporting a primordial binary fraction ranging from 10% to 50% (Sollima et al. 2007). Due to the dense environment only hard binaries[1]

[1] A discussion of hard binaries in the context of another dense stellar environment, the galactic centre, is given in Section 8.2.

with very small orbital periods, will survive in the core.

Interactions between passing stars and binaries is a major topic in astrophysics in its own right and the reader is referred to Heggie (1975), Hut and Bahcall (1983) and others in this series for details. Generally a single star encountering a binary system will extract some energy from the binding energy of the binary, making the binary more tightly bound. This interaction increases the kinetic energy of the single star, which is equivalent to increasing the orbital energy of the single star about the cluster centre. Therefore the orbit of the scattered single star about the cluster has a larger semi-major axis. Repeated encounters between single stars and binaries in the core of the GC result in a heating source for the cluster, which opposes the effects of relaxation.

The effect of binaries on the evolution in the outer regions can be neglected and as can other complications present in the core such as high mass stars, close encounters and possible intermediate mass black holes. For the cluster models presented here the core is defined as all mass inside of the half-mass radius and is simplified by a point-mass.

This project aims to predict the tidal truncation of GCs on eccentric orbits. So far the neglect of binary systems and close encounters for our purposes has been justified based on their strong association with the cluster core. Also the lack of two-body relaxation in the cluster model presented in Chapter 5 has been justified based on it having a long timescale in the outer regions of the cluster. It remains to discuss the influence of tidal field of the galaxy on the evaporation and eventual destruction of globular clusters.

2.3 Effect of a galaxy on the internal dynamics of cluster

For our purposes the orbits of GCs about the galaxy are divided into two classes. The first class concerns the tidal shocking of a cluster as it passes through the disk of the galaxy. These clusters are subject to the additional destructive processes outlined below. The second class of cluster orbit is widely orbiting clusters, which do not pass through the galactic disk. For these clusters the affect of the galaxy is confined to the tidal truncation of the cluster and is discussed in the next section.

The tidal field acting on a cluster due to the galactic disk and/or bulge will change over for the motion of close GCs, which causes the cluster to undergo tidal distortion (Ostriker et al. 1989; Kundic and Ostriker 1995; Gnedin et al. 1999). These two tidal processes are collectively referred to as tidal shocking and act to remove mass from the cluster.

Clusters that orbit close to the galactic centre are subject to another destructive process known as dynamical friction. Dynamical friction refers to the drag force caused by the combined gravitational interactions acting on a mass as it moves through a background of lower masses (such as a star field) (Chandrasekhar 1943; Chandrasekhar 1949). The timescale for a globular cluster to decay into the galactic centre treating the galactic potential as an isothermal sphere is (Binney and Tremaine 1987)

$$t_{DF} \approx 2.64 \times 10^{10} \left(\frac{R}{2kpc}\right)^2 \left(\frac{v_c}{250km/s}\right) \left(\frac{10^6 \mathrm{M}_\odot}{M_C}\right) yr \tag{2.3}$$

where R is the distance of a cluster of mass M_C from the galactic centre and v_c is the circular speed about the galactic centre. From Equation (2.3) any GC whose original orbit lay within 2 to 3 kpc of the galactic centre will already have merged with the galactic bulge.

Both dynamical friction and tidal shocking result in the loss of mass from the outer regions of the cluster and cause the orbit of the GC to decay. Orbital decay will inevitably result in the cluster merging with the galactic bulge as first suggested by Tremaine et al. (1975) and expanded upon by Capuzzo-Dolcetta (1993). In-falling clusters may also result in a super-cluster forming near the galactic centre (Capuzzo-Dolcetta and Vicari 2005). This has consequences for the fraction and distributions of binary systems in the galactic centre, which is studied in Part II of this thesis.

In summary the evaporation of clusters orbiting close to the galaxy is accelerated due to additional disruptive processes. The focus of this work is on GC orbits not subject to dynamical friction or tidal shocking, where the main affect of the tidal field of the galaxy is to truncate the cluster.

2.4 Tidal truncation of clusters by the galaxy

The tidal field of the galaxy truncates the radial density profile of the globular cluster at the tidal radius. This radius is analogous to the Roche Lobe in binary stellar systems, where the tidal field from the perturbing mass is sufficient to unbind a test particle from the surface of a star. This causes mass transfer in binary systems and stars to escape from globular clusters.

Recall from Section 2.2 that mass loss from the cluster will occur due to two-body relaxation accelerating some stars to velocities greater than the cluster escape velocity. Relaxation continually replenishes stars in the outer regions of the cluster, which can then be removed by the tidal field of the galaxy. The radius at which this occurs is independent of the two-body relaxation process, but the total mass loss of the cluster is not. This makes it very difficult to separate evaporation due to relaxation away from tidal stripping. We overcome this in the simplified cluster model presented in Chapter 5 by focussing on cluster orbits where the relaxation timescale in the outer regions of the cluster is large than the orbital period of the orbit.

Consider a star positioned on the line of centres at a distance r_t from the cluster in a coordinate frame moving with the cluster as it orbits the galaxy. The distance r_t corresponds to the position of a star such that the accelerations on the star due to the galaxy and cluster balance each other. A schematic diagram of this configuration is shown in Figure 2.1.

The simplest case to determine analytically is to consider a star located where the acceleration on the star in the rotating frame is zero and the velocity of the star is also zero. Such a star will be on a radial orbit with respect to the centre of the cluster. For a star on a radial orbit and using point mass potentials for the cluster and galaxy the tidal radius is given by (King 1962)

$$r_t = k\left(\frac{M_C}{M_G(3+e)}\right)^{1/3} R_p \tag{2.4}$$

where M_C and M_G are the masses of the cluster and galaxy respectively, e is the eccentricity of the clusters orbit around the galaxy, and R_p is the distance of closest approach to the galaxy, referred to as perigalacticon. The constant $k \sim 0.7$ was introduced by Keenan (1981) to better fit observations of the galactic globular clusters. The King radius will be used to denote the maximum theoretical tidal radius of a GC by using Equation (2.4) with $k = 1$ and $e = 0$.

Recently the analysis of King (1962) has been extended to stars on circular orbits on either prograde or retrograde orbits (Read et al. 2006). The velocities of stars with prograde or retrograde orbits is shown in Figure 2.1 along with the indicated motion of the cluster relative to the galaxy. A star has zero acceleration in a coordinate frame rotating with the motion of a point mass cluster if the distance from the cluster is given by (Read et al. 2006)

$$r_t \simeq R_p\left(\frac{M_c}{M_g}\right)^{1/3}\left(\frac{1}{1+e}\right)^{1/3}\left(\frac{\sqrt{\alpha^2+1+\frac{2}{1+e}}-\alpha}{1+\frac{2}{1+e}}\right)^{2/3} \tag{2.5}$$

where $\alpha = 0$ denotes a star on a radial orbit inside the cluster and reduces to Equation (2.4) in this case. Non-radial motion is restricted to the case of stars on circular orbits and is described in the tidal radius by setting $\alpha = 1$ or -1 for prograde and retrograde orbits respectively. For later comparison in Chapter 6 the Read radius is defined by Equation (2.5) with $\alpha = 1$, representing an easily tidally stripped cluster. The Read radius compared well with two N-body simulations of $10^7 \mathrm{M}_\odot$ satellite clusters using $N = 10^5$ particles with orbital parameters of perigalacticon $R_P/R_{1/2} = 267$ and eccentricity $e_o = 0.0$ and perigalacticon $R_P/R_{1/2} = 77$ and eccentricity $e_o = 0.57$ (Read et al. 2006). A summary of alternate equations for the tidal radius designed to fit observations can be found in Bellazzini (2004).

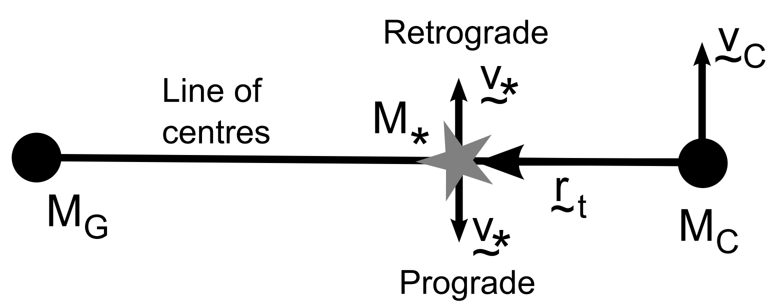

Figure 2.1: Schematic diagram of the position of the star (M_*) at a distance r_t from the cluster (M_C) along the line of centres of the galaxy (M_G) and cluster used in the literature to calculate the tidal radius. The vector $\mathbf{r_t}$ is always directed towards the galaxy in the coordinate system centred on the cluster as it moves through its orbit in the direction indivated with $\mathbf{v_C}$. The direction of the velocity for a star in a prograde or retrograde orbit is indicated by $\mathbf{v}_*$.

A cautionary note is required here. The dangers of assuming that the tidal radius acts as an instant remover of stars has been pointed out by Fukushige and Heggie (2000). They found for GCs on circular orbits that the escape timescales for stars beyond the tidal radii could be long enough to allow some stars to stay in this region indefinitely.

Now that the effect of the galaxy on an individual cluster has been discussed the effect on a distribution of clusters is examined.

2.5 The Milky Way globular cluster system

The Milky Way globular cluster system (MWGCS) is the only system for which orbital characteristics are known, although spatial distributions in other galaxies are known. Chapter 6 compares the observed tidal radii for the MWGCS to theoretical estimates from the previous section and from the resonance overlap stability criterion (Chapter 4). Future work based on the tidal radii estimates presented in Chapter 6 could be used to predict the initial population of globular clusters based on the observed MWGCS. Similar studies examining the survival of the galactic globular clusters based on an assumed initial MWGCS distribution are found in the literature (Aguilar et al. 1988; Gnedin and Ostriker 1997) and it would be interesting to see how a future study based on our results compares.

Direct comparison between the theoretical and observed tidal radii is complicated by the following factors. Firstly, the observed tidal radii depend on the distance between the Earth and the cluster so this is a source of error for the spatial distribution. Secondly the orbital parameters are subject to large uncertainties in the tangential velocity components for each GC. Finally the combined effect of the internal and external processes on individual clusters leads to clusters having less mass than at formation. This last point also means that the tidal radii of clusters on close orbits around the galactic centre may be larger than theoretical predictions. Any clusters where the observed tidal radius is surprisingly large could be due to tidal stripping having had insufficient time to remove all stars up to the theoretical tidal radius.

The dependence of the orbital parameters on uncertainties in the tangential velocities has been discussed in detail for the MWGCS elsewhere (Allen et al. 2006; Allen et al. 2008). The perigalacticon and eccentricities for the MWGCS are discussed in detail in Chapter 6, along with their relevance to the tidal radii of globular clusters.

Positions on the sky of globular clusters around the galaxy are well known, but require accurate distance measurements to fix the spatial coordinates. Spatial coordinates for the MWGCS are taken from Harris (1996), which is regularly updated online, and are used to show the MWGCS relative to the disc of the galaxy in Figure 2.2. Where available cluster velocities are used with the spatial coordinates to generate the previous 10 orbits about the galaxy for each GC, using the equations of motion given by Equation (6.6) and integrated using the method described in Section 6.1. The galactic potential used includes the galactic disk, bulge and the dark matter halo (Fellhauer et al. 2007). A sample of cluster orbits later studied in Chapter 6 is given in Figure 2.3. Note that NGC 6144 is a good example of a cluster that may have fallen into the galactic bulge, as discussed in Section 2.3.

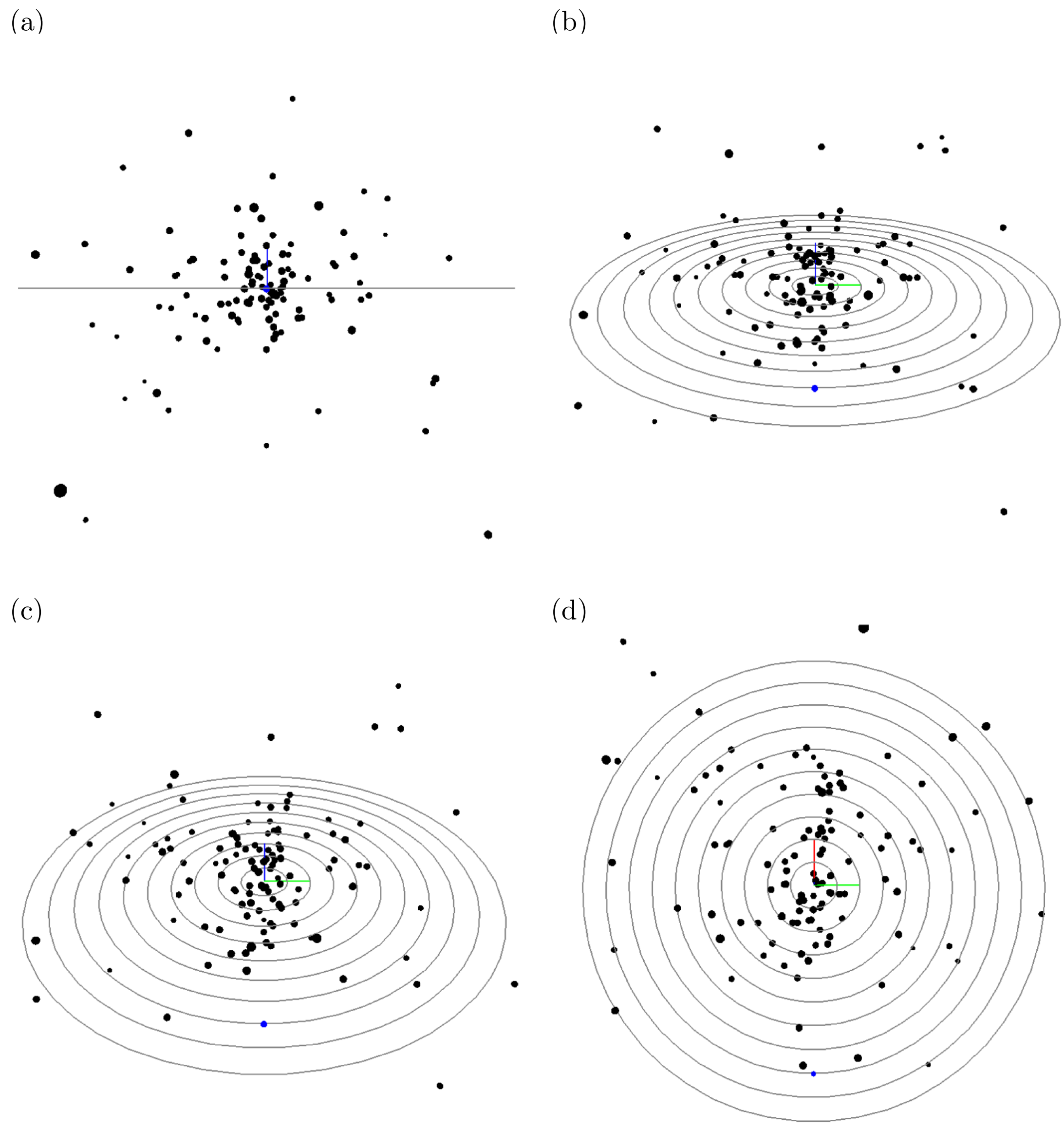

Figure 2.2: Milky Way globular cluster system shown from outside the galaxy, above the disk, looking in towards the galactic centre past the Sun (blue sphere). Each circle represents 1 kpc distance from the galactic centre in the galactic plane. Panels (a) to (d) show the same distribution from an angle above the plane of 0°, 30°, 60° and 90° respectively.

A summary of the orbital parameters found for clusters in the MWGCS using the available velocities and a realistic galactic potential is given in Table 6.1. Clusters with observed tidal radii and total masses are used to compare the theoretical tidal radii to observed values in Table 6.3.

For reference through out this part we require a representative GC orbit, which satisfies the requirement that the galactic potential affects the cluster only by tidal stripping. Based on GC orbits that satisfy this condition from the structural and orbital parameters for the

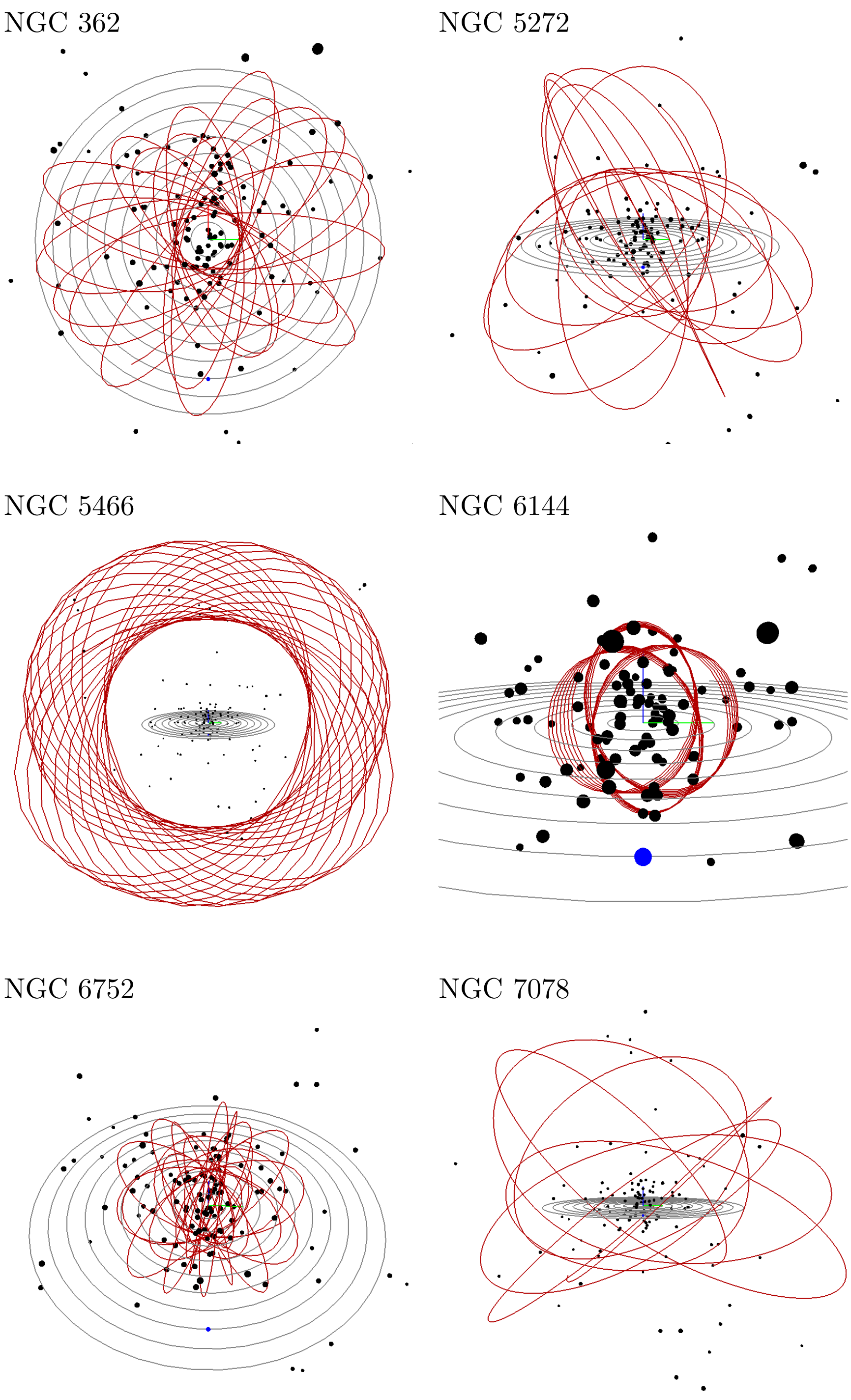

Figure 2.3: A sample of orbits integrated backwards in time from the Milky Way globular cluster system shown from different angles above the galactic plane. The Sun is shown as a blue sphere at 8 kpc from the galactic centre. Orbits are integrated using the galactic potential including a disk, bulge and dark matter halo described in Section 6.1 using spatial data from Harris (1996). Velocity data is from Meziane and Colin (1996) and references therein, Dinescu et al. (1999) and references therein, and Dinescu et al. (2001) for each cluster as indicated by Table 6.1.

MWGCS (Table 6.1) a cluster mass of 10^6 $M_\odot$ and a half-mass radius of $R_{1/2} = 4.3$ pc is chosen. This mass is consistent with the natural initial size of GCs for a simple galactic model (Fall and Rees 1985). A suitable orbit for this cluster is chosen as having perigalacticon $R_p = 6.2$ kpc, eccentricity of $e = 0.5$ and therefore an orbital period of order 1 Gyr. Note from Section 2.2 that this is approximately the same as the half-mass relaxation time given by Equation (2.1), and so is significantly shorter than the relaxation time near the tidal radius. The relaxation time is compared to our cluster model in Section 5.2 along with a comparison to a direct N-body simulation.

From the large orbital period it is clear that such a cluster will only have completed roughly 10 orbits about the galaxy. It is unclear if 10 perigalacticon passages will provide sufficient time for stars to escape from beyond the tidal radius. The timescale for stars to escape from beyond the tidal radius might be very large for the long orbital period clusters of interest here as suggested by Fukushige and Heggie (2000). Indeed this is what is observed in Table 6.3 when theoretical estimates for the tidal radii are consistently lower than observed values.

Chapter 3

Particle in a Plummer potential

Our ultimate aim is to determine a relationship between the effective tidal radius of a cluster and the eccentricity of its galactic orbit. This will also depend on the pericentre distance of the cluster in units of its characteristic radius.

The Mardling stability criterion (MSC, introduced in Section 1.3.2) uses the Kepler elements of the inner and outer orbits (a, e, I, ϖ and Ω) to determine the stability of a given three-body configuration. In order to use this to estimate the tidal radii of GCs on eccentric orbits, we need to determine the equivalent Kepler elements for orbits in a Plummer potential. This chapter addresses the determination of these elements, particularly the radial period, as well as the methodology used to set the initial conditions for a globular cluster modelled by particles in a Plummer potential.

Orbits in spherical potentials exist on invariant planes so the angles describing the spatial orientation of an orbit in a point mass potential (I, ϖ and Ω) are equivalent to those for a Plummer potential. This leaves equivalent quantities for the semi-major axis and eccentricity to be determined for the Plummer sphere. For ease of use with the MSC, the radial period of an orbit in a Plummer potential will be determined rather than the semi-major axis. For point mass potentials the instantaneous Kepler elements can be calculated from the position and velocities vectors. This is not possible for a Plummer potential and so the orbital period and eccentricity must be found by other means.

For the sake of simplicity the galactic potential is taken to be that of a point mass in the next chapter, thus the galactic period of the cluster is Keplerian. Note that by treating the galactic potential as a point mass tidal shocking effects are ignored. This is not a problem since we are concerned with large period globular clusters as discussed in the previous chapter.

The gravitational potential of a globular cluster is modelled here by a Plummer sphere using Binney and Tremaine (1987). The procedure for assigning positions and velocities to N particles such that a Plummer sphere with a Maxwellian velocity distribution is satisfied is described in Section 3.1. This cluster model consisting of N particles is used in Chapter 5 to examine the effect of a galactic potential on particle orbits.

To use the MSC to predict effective tidal radius of a cluster requires the ratio of the outer (cluster-galaxy) orbital period to the inner (particle in cluster potential) orbital period

($\sigma = T_o/T_i$). An integral expression for the radial period of a particle orbiting inside a spherical potential exists (Binney and Tremaine 1987), however this must be solved numerically for each set of initial binding energy and angular momentum for a particle in a Plummer sphere. Instead the orbits of test particles in a Plummer potential are examined by integrating its initial distance and velocity forward in time. This approach is given in Section 3.2 and allows the calculation of the radial period and eccentricity for a given set of initial radius (set as the apocentre distance) and velocity. The procedure for determining the radial period adopted here is more straightforward than solving the integral expression given in Binney and Tremaine (1987) for the chosen form of our initial conditions.

To compare the period ratio used by the MSC to numerical results for the stability of particle orbits in a Plummer sphere (Chapter 4) the procedure given in Section 3.2 is used. However subsequent chapters are concerned with all of the particle orbits in a cluster and so must take the isotropic distribution of velocities into account.

Chapters 5 and 6 require formulae for mapping the initial binding energy and apocentre distance to the radial period for a particle in a Plummer potential. The ultimate purpose of these formulae is to determine an effective tidal radius of a cluster from the ratio of the clusters galactic period to the period of a particle in the Plummer potential. This particular period ratio is associated with the boundary between unstable and stable particle orbits as predicted by the MSC (see next chapter). The statistical approach and resulting formulae for mapping the orbital period of particles in a cluster to binding energy and radial distance are given in Section 3.3. The essential results from this chapter are summarised in Section 3.4.

3.1 Initial conditions for particles in a Plummer sphere

The motion of a star inside a globular cluster is modelled as a point mass m_i orbiting inside a spherical gravitational potential. Recall from Section 2.5 that we are interested in globular clusters orbiting the galaxy at large distances so that the galactic potential can be approximated as a point mass and relaxation effects can be neglected. The assumption of a purely spherical potential is justified since any anisotropy due to tidal distortion and/or cluster rotation is expected to be suppressed for clusters at galactic distances of interest (Takahashi et al. 1997).

A globular cluster is modelled using a Plummer sphere with gravitational potential given by (Binney and Tremaine 1987)

$$\Phi = \frac{-GM_C}{\sqrt{b^2 + r^2}} \tag{3.1}$$

where G is the gravitational constant, M_C is the mass of the cluster, r is the radial distance, and b is a parameter chosen to describe the compactness of the cluster. For $b = 0$ the Plummer potential reduces to the potential for a point mass of mass M_C.

All physical quantities are scaled using

$$r = R_C r' \tag{3.2}$$

$$M = M_C M' \tag{3.3}$$

$$t = t'\sqrt{\frac{R_C^3}{GM_C}} \tag{3.4}$$

where a prime denotes a scaled quantity and R_C is a characteristic length scale of the cluster, which is later related to the cluster half-mass radius.

In scaled units the Plummer potential becomes

$$\Phi' = \frac{-1}{\sqrt{b^2 + r'^2}} \tag{3.5}$$

where the minimum value is given by $-1/b$. The affect of b on the steepness of the gravitational potential is shown in Figure 3.1. Note that by $r' = 5$ the Plummer potential has converged to approximately the same value as that of a point mass potential ($b = 0$). From herein all quantities are written as scaled quantities and the prime notation is dropped.

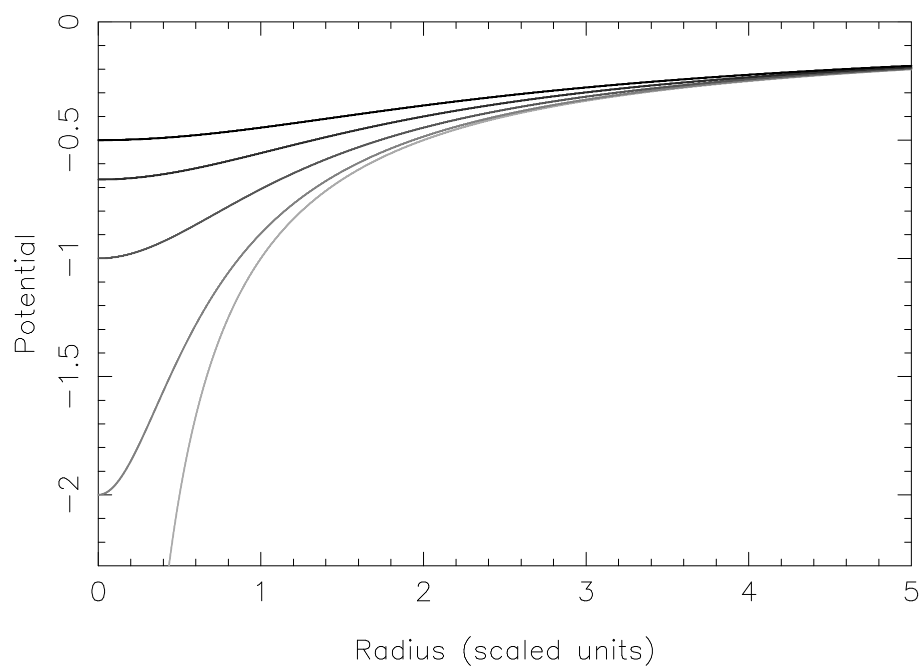

Figure 3.1: Potential energy of a Plummer sphere in scaled units for a range of the compactness parameter b as given by Equation (3.5). The increasing divergence from a point mass potential is demonstrated using darker lines for larger values of b in the range $b = 0.0$, 0.5, 1.0, 1.5 and 2.0.

In Chapter 5 the effect of the galaxy on the orbits of stars inside a globular cluster over time is examined. This requires N particles be distributed such that the combined gravitational potential is equivalent to the Plummer potential and the velocities satisfy a Maxwellian distribution. The distribution of particles is achieved by using the mass enclosed within a particular radius along with von Neumann's rejection technique for random sampling from a distribution to determine the velocities (Aarseth et al. 1974).

To determine the enclosed mass for a given radius we first solve Poisson's equation

$$\nabla^2\Phi = 4\pi\rho \tag{3.6}$$

for the density, which gives

$$\rho = \frac{3b^2}{4\pi}\left(b^2 + r^2\right)^{-5/2}. \tag{3.7}$$

The mass internal to radius r is found by

$$M(r) = 4\pi\int_0^r \rho r^2 dr = \frac{r^3}{(b^2 + r^2)^{3/2}} \tag{3.8}$$

where the total mass $M(\infty) = 1$ in scaled units. The half-mass radius of the cluster is found by setting $M = 1/2$ in Equation (3.8) and is

$$R_{1/2} = \frac{bR_C}{\sqrt{2^{2/3} - 1}}. \tag{3.9}$$

For our representative cluster (Section 2.5) $M_C = 10^6 M_\odot$ and $R_{1/2} = 4.3$ pc, which for $b = 1$ gives a characteristic length of $R_C = 3.3$ pc.

Now that the enclosed mass for a Plummer sphere is known from Equation (3.8) and the total mass is scaled to unity, the distribution of radii and velocities for a system of N particles can be determined. We follow the same procedure as that of Aarseth et al. (1974), except for the alterations made to account for the compactness parameter b.

By rearranging Equation (3.8) the radius in terms of the enclosed mass is given by

$$r = \frac{bM^{1/3}}{\sqrt{1 - M^{2/3}}} \tag{3.10}$$

where $0 \leq M \leq 1$ is the enclosed mass in scaled units. To select the radius of a single particle the mass is equated to the random number Y_1, where all random numbers Y_i are uniformly generated in the range [0, 1]. In addition the radius is initially truncated at the King radius (Equation 2.4) to minimise the number of stars that can instantly escape the cluster.

The velocity magnitude V for a particle at radius r from the cluster centre is assigned by firstly calculating the escape velocity by

$$V_e = \sqrt{2}\left(b^2 + r^2\right)^{-1/4}. \tag{3.11}$$

Assuming the cluster is in a steady state and the velocity distribution is isotropic then the probability distribution is proportional to (Aarseth et al. 1974)

$$g(q) = q^2\left(1 - q^2\right)^{7/2} \tag{3.12}$$

where $q = V/V_e$ and $0 \leq q \leq 1$. This distribution has a maximum at $q = \sqrt{2}/3$ of $g = 0.092$, so

$g(q)$ is always less than 0.1. Individual values of q are chosen using von Neumann's comparison method whereby a particular q value is accepted if it satisfies $0.1Y_2 < g(Y_3)$, where Y_2 and Y_3 are independent random numbers.

The radius R and velocity V magnitudes are now distributed uniformly about a sphere to determine the position $\mathbf{r}$ and velocity $\mathbf{v}$ vectors for particles in an isotropic Plummer sphere. This is achieved by taking a magnitude X as either R or V and determining the vector $\mathbf{X} = (x_1, x_2, x_3)$ by

$$x_1 = \left(X^2 - x_3^2\right)^{1/2} \cos(2\pi Y_3) \tag{3.13}$$

$$x_2 = \left(X^2 - x_3^2\right)^{1/2} \sin(2\pi Y_3) \tag{3.14}$$

$$x_3 = (1 - 2Y_4)\, X \tag{3.15}$$

where Y_3 and Y_4 are random numbers and $\mathbf{r}$ or $\mathbf{v} = \mathbf{X}$. The positions for $N = 10^4$ particles relative to the cluster centre are shown in Figure 3.2.

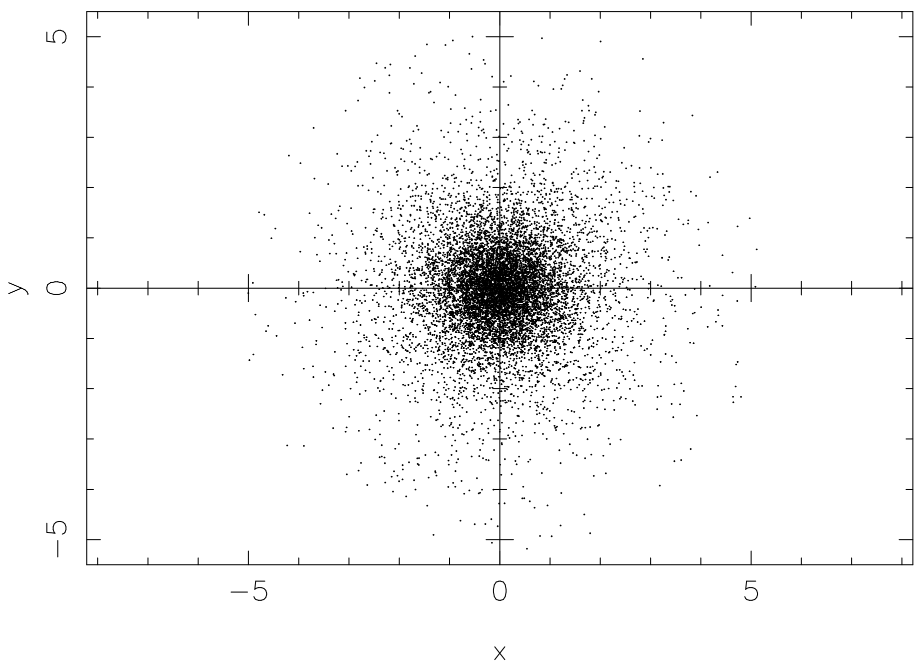

Figure 3.2: Initial positions of stars in a Plummer potential given by the procedure described in Section 3.1. Note the truncation at $r \sim 5$ corresponding to the maximum theoretical tidal radius (Equation 2.4) for a GC orbiting the galaxy with eccentricity $e_o = 0.5$ and perigalacticon $R_p = 500R_C$.

3.2 Particle orbits in a Plummer potential

For this section we consider a single particle in a Plummer potential and not the distribution of particles described in the previous section. This analysis of a single particle in a Plummer potential allows us to clearly see the difference in orbits in a Plummer sphere to those in a point mass potential. By concentrating on a single particle the framework for setting up orbits for comparison with unstable orbits predicted by the MSC in Chapter 4.

Unlike the Kepler potential, the Plummer potential produces apsidal motion. There are also no closed form solutions to the equations of motion as there are for the point mass two-body problem (Section 1.1). This means that we must use numerical means to determine the equivalent Kepler elements for a Plummer potential. The shape of the orbit is fully specified by the equivalent quantities to the orbital period and eccentricity. The remaining Kepler elements give the orientation of the orbit relative to a reference plane and are the same as for a point mass, since the orbital plane is invariant for spherical potentials.

Using the scaled quantities from the previous section, the equations of motion for a single test particle in a Plummer sphere are

$$\ddot{\mathbf{r}}_{\mathbf{i}} = -\frac{\mathbf{r}_{\mathbf{i}}}{\left(b^2 + r_i^2\right)^{3/2}} \tag{3.16}$$

where $\mathbf{r}_{\mathbf{i}}$ is the position vector of particle i relative to the centre of the Plummer sphere. The corresponding energy per unit mass of such a particle is

$$E_i = \frac{1}{2}v_i^2 - \frac{1}{\sqrt{b^2 + r_i^2}} \tag{3.17}$$

where v_i is the magnitude of the velocity vector of the particle relative to the cluster centre. While the motion of a particle in a Plummer potential can not be solved analytically from Equation (3.16), one property that can be analytically determined is the circular velocity given by

$$v_{circ} = \sqrt{r\frac{\partial \Phi}{\partial r}} = \frac{r}{\left(b^2 + r^2\right)^{3/4}}. \tag{3.18}$$

Our aim here is to determine the equivalent orbital period T_i and eccentricity e_i for a single particle i in a Plummer potential. We require a general way of writing the position and velocity of a particle in a Plummer sphere and not the distribution associated with a cluster in equilibrium described in the previous section.

The orbital period and eccentricity of the motion of a particle in a Plummer potential is easiest to examine when $\mathbf{r}$ and $\mathbf{v}$ correspond to apocentre and $\mathbf{r}$ is initially aligned with the x-axis. At this point the velocity is set as some fraction f of the circular velocity in the positive y-direction (i.e. the radial component of velocity equals zero) and $0 \leq f \leq 1$. A schematic diagram of this configuration is shown in Figure 3.3 a) with the magnitude of the velocity vector given by $v = f v_{circ}$. By choosing the velocity in this manner the initial radial distance is ensured to occur at apocentre and will be denoted as $R_{a,i}$. This form of the velocity also means that $f = 0$ and $f = 1$ correspond to radial ($e_i = 1$) and circular ($e_i = 0$) orbits respectively. The spatial orientation of the orbital plane for a single particle in a Plummer potential is not needed due to spherical symmetry. Thus the shape of the orbit is completely specified by choosing f and $R_{a,i}$.

Describing the orbital parameters for non-circular orbits in a Plummer sphere can only be done numerically and the following procedure is adopted. A particular set of initial radius and velocity (see mass m at $t = 0$ in Figure 3.3 a) are evolved in time using Equation (3.16) until the radius returns to apocentre ($t = T_i$ in Figure 3.3 a). To calculate the orbits a Bulirsch-Stoer integrator (Press et al. 1986) was used in a computer code developed by the author for this problem.

The radial period of the orbit is found using the time taken for the particle to return to the original distance from the cluster centre (compare $t = 0$ to $t = T_i$ in Figure 3.3 a). The eccentricity is calculated by

$$e_i = \frac{R_{a,i} - R_{p,i}}{R_{a,i} + R_{p,i}} \tag{3.19}$$

where $R_{a,i}$ is the initial apocentre and $R_{p,i}$ is the first pericentre of the particle. A particle on an eccentric orbit with $e_i \sim 0.5$ is shown in panel (b) of Figure 3.3. For the orbit shown in Figure 3.3 (b) the particle spends a lot of time inside the core of the Plummer sphere ($|\mathbf{r}| \lesssim b = 1$), which produces substantial apsidal motion.

The method of assigning initial apocentre distances and velocities for a single particle is used to compare the stability of a particle-cluster-galaxy system with predictions from the MSC in Section 4.2. Later chapters include more than one particle in the cluster-galaxy system and require a statistical approach to the period.

(a) Period determination (b) Eccentric orbit

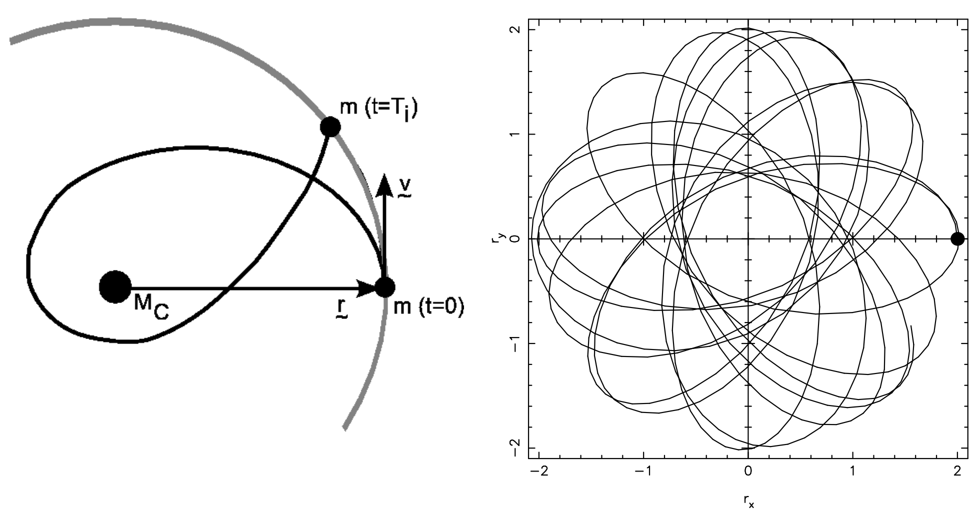

Figure 3.3: Illustration of how the radial period of a test particle in a Plummer potential is determined in panel (a). Panel (b) shows a numerically determined orbit of a test particle in a Plummer potential with $e_i \sim 0.5$, initially at $R_{a,i} = 2$ (marked as a dot) and moving in the positive y-direction.

3.3 Orbital distributions for a realistic cluster

Later chapters require formulae relating the radial period, initial binding energy and apocentre distance of a particle in a Plummer sphere. Specifically applying the MSC to a globular cluster with prescribed orbital parameters (Chapter 4) results in an maximum orbital period for particles in a Plummer potential that are expected to be stable against escape from the cluster. This maximum orbital period provides an estimate of the tidal radius for a given globular cluster. To compare this period to the results of escaping stars from a simulated cluster in Chapter 5 requires a formula relating the binding energy to the orbital period of a particle in a Plummer potential. While comparison to the tidal radii of observed clusters requires the apocentre distance (Chapter 6). Note that both of these require the average behaviour of a cluster modelled by a Plummer potential. Therefore the aim of this section is to describe the average behaviour of particles in the cluster and not the behaviour of all possible types of behaviour.

Chapters 5 and 6 both assume that a globular cluster can be modelled using a Maxwellian velocity distribution for particles in a Plummer sphere. Since each initial radial position of a particle will have a distribution of velocities the eccentricities and periods will be scattered around an average value. This section uses a statistical approach to determine the average value for the orbital period in particular as a function of apocentre distance or initial binding energy. These are then summarised by fitting formulae for use in later chapters.

The procedure adopted here is as follows. Firstly a globular cluster model is constructed for a Plummer potential with compactness b with $N = 10^4$ particles according to the initial conditions described in Section 3.1. The positions and velocities of this cluster are distributed as an isothermal sphere so the initial radius is not equivalent to the apocentre, unlike the previous section. Secondly each particle is integrated in time until at least one radial period is completed. Finally the radial period and eccentricity are calculated from the minimum and maximum distances from the cluster centre using the procedure outlined in the previous section.

The distribution of eccentricities for particle orbits in a cluster is shown in Figure 3.4. An integrable function that fit the eccentricity distribution was sought and by trial and error the Beta distribution was used. The Beta distribution is given by

$$f(e_i) = \frac{1}{B(\alpha,\beta)} e_i^{\alpha-1} \left(1 - e_i\right)^{\beta-1} \tag{3.20}$$

where $B(\alpha,\beta)$ is the Beta function and the mean of the distribution is given by $\alpha/(\alpha+\beta)$. For the fitting function plotted as a grey curve in Figure 3.4 $\alpha = 2.691732$, $\beta = 3$, and $B(\alpha,\beta) = 0.042898$. These values ensure the same mean eccentricity value of $\bar{e_i} = 0.47$ for the fitting function as for the distribution. The cumulative probability distribution for Equation (3.20) is

$$F(e_i) = \int_0^{e_i} f(e)de = \frac{1}{B(\alpha,\beta)} \left(0.371508 e_i^{\alpha} - 0.541751 e_i^{\alpha+1} + 0.213141 e_i^{\alpha+2}\right), \tag{3.21}$$

which is used when averaging over the eccentricity distribution to derive the fraction of unstable orbits in Chapter 4. Three values useful for Sections 4.2 and 4.3 are that the probability of

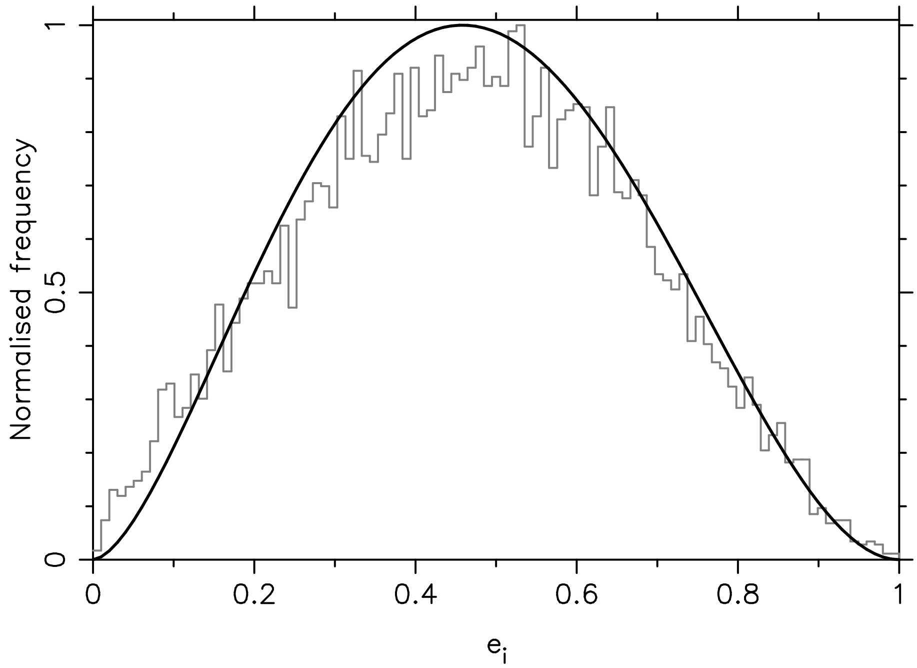

Figure 3.4: The distribution of eccentricities for stellar orbits in a Plummer sphere with $b = 1$ and using an isotropic velocity distribution described in Section 3.1. A Beta distribution is fit to the data of the form given in Equation (3.20) and is shown as a grey curve for the best fit. The eccentricity distribution has a mean of $\bar{e_i} = 0.47$ for both the data and the fitting function.

$e_i > 0.6$, 0.9 and 0.95 are 0.2739, 0.0068 and 0.0009 respectively.

The stability analysis using the MSC (Section 1.3.2) requires the radial period of a particle in a Plummer potential. In particular the MSC is used in Chapter 4 to determine a maximum orbital period for a particle in a cluster that is stable to escaping the cluster. We use this period to estimate the tidal radius of a globular cluster and compare to numerical simulations and observed clusters in later chapters.

Chapter 5 examines the fraction of escaping stars found from numerical cluster simulations as a function of the initial binding energy of each star (E_i). To compare the maximum orbital period where a star is expected to be stable to these results requires an approximate relationship between the period and binding energy.

Using the integrated particle orbits in a Plummer sphere the relationship between the period and the initial binding energy of a particle in a Plummer potential is seen in Figure 3.5 (a). The solid line represents the fitting function

$$T_{Fit}(E_i) = A\sec(\frac{\pi}{2}(E_i + 1)) + C \tag{3.22}$$

where $A = 10.5$ and $C = -7.2$ are fitted constants. The energy per unit mass of the particle E_i is defined by Equation (3.17) for an isolated cluster and Equation (5.8) for a cluster orbiting the galaxy. From Figure 3.5 (a) some particle orbits with $E_i \gtrsim -0.4$ have radial periods significantly above the solid line. These occur in discrete groups and are due to particles on nearly circular

(a) Relationship between orbital period and initial binding energy

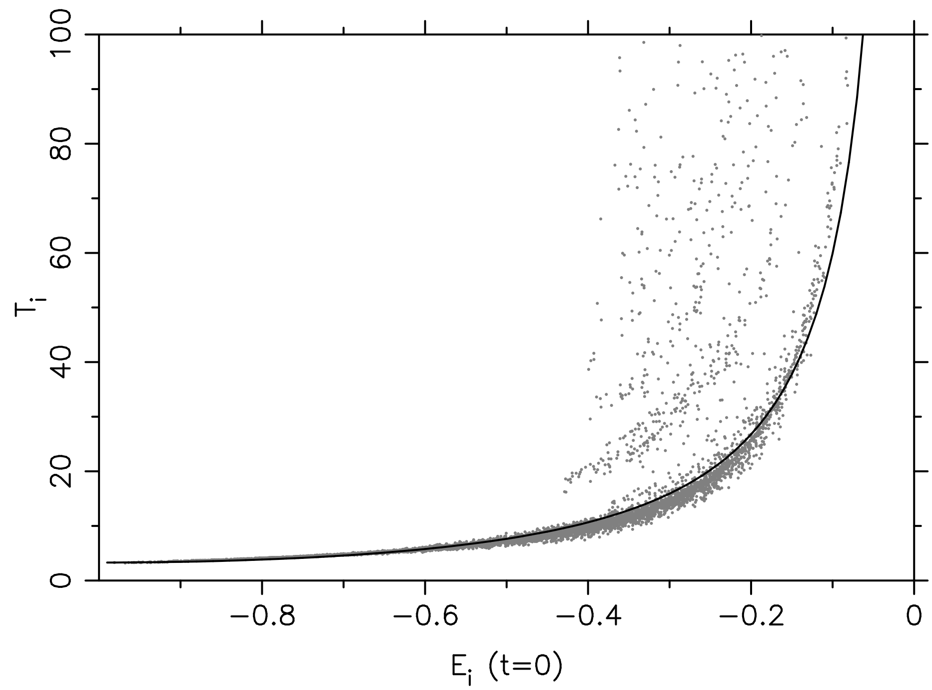

(b) Relationship between orbital period and apocentre distance

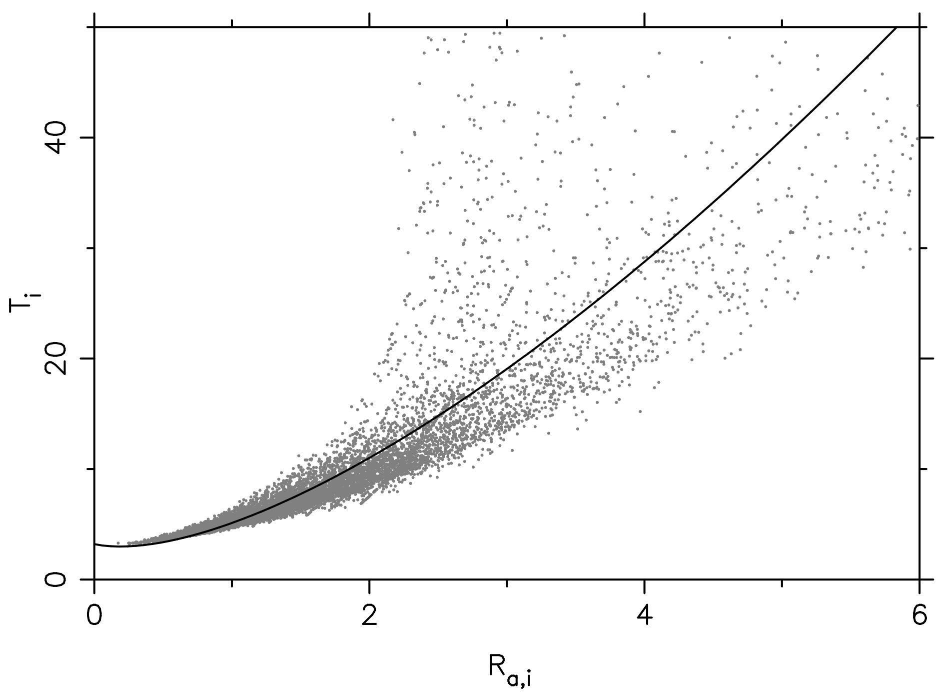

Figure 3.5: The relationship between the orbital period T_i and the initial binding energy per unit mass E_i (top panel) and apocentre $R_{a,i}$ (bottom) for bound cluster stars. Data is produced using the time integrated orbits for $N = 10^4$ particles in a Plummer potential with an isotropic velocity distribution described in Section 3.1. Fitting functions to the data are shown as solid lines and are given by Equation (3.22) for panel (a) and Equation (3.22) for panel (b).

orbits. The discrete nature of the outlying points in Figure 3.5 (a) is due the low numbers of particles in the outer regions of the cluster. The precise origin of this fine structure is not critical to the statistical description given in Equation (3.22), since these abnormally large period orbits only represent a small number of particles. The fitting formula Equation (3.22) is only used in relation to simulated clusters in Chapter 5 and therefore does not need to be completely accurate.

Chapter 6 compares the maximum orbital period where a star is expected to be stable to the tidal radius of observed globular clusters in the Milky Way globular cluster system. We therefore use the integrated particle orbits to show the radial periods T_i for $N = 10^4$ particles as a function of their initial apocentre radius ($R_{a,i}$) in Figure 3.5 (b). The spread in the orbital periods against E_i and $R_{a,i}$ seen in Figure 3.5 reflects the range of eccentricities for particles of a given cluster distance. The solid line in this figure shows the fit to the period as a function of the apocentre radius and is given by

$$T_{Fit}(R_{a,i}) = 2\pi \left(\frac{R_{a,i}}{1+\bar{e}_i} \right)^{3/2} + \frac{3.21}{1+R_{a,i}} \tag{3.23}$$

where the first term is the Keplerian period in scaled units and the second is a correction term based on the period data in Figure 3.5 (b). The Keplerian period is calculated for an apocentre of $R_{a,i}$ using the mean eccentricity of particle orbits in a Plummer potential given by $\bar{e}_i = 0.47$ from Figure 3.4. This relationship given in Equation (3.23) allows the ratio of periods $\sigma = T_o/T_i$ and the tidal radius to be quickly compared in Section 6.2.

The period-radius fitting formulae will be required for very close and very distant particle orbit, thus it must behave physically as $R_{a,i} \to \infty$ and $R_{a,i} \to 0$. Equation (3.23) is constructed such that it reduces to the Keplerian period in the limit of $R_{a,i} \to \infty$ and to the minimum Plummer period (from Figure 3.5 $T_i = 3.21$ in scaled units) as $R_{a,i} \to 0$. Finite periods as $R_{a,i} \to 0$ occur for particles moving in a constant density sphere. In the limit $r/b \to 0$ the circular velocity of a particle in a Plummer potential given by Equation (3.18) becomes $v_{circ} = r/b^{3/2}$. Thus the angular velocity is constant and the particles are undergoing rigid body rotation. The fitting function Equation (3.23) can now be used for all $R_{a,i}$, since it gives the correct physical behaviour in both distance extremes and is a good fit to the radial period of a Plummer potential where $R_{a,i} \sim 1$.

The formulae relating the radial period, initial binding energy and apocentre distance of a particle in a Plummer sphere are now expressed by Equations (3.22) and (3.23).

The fitting formulae and the distribution of eccentricities will be used in later chapters to apply the MSC to the tidal radii of globular clusters on eccentric orbits.

3.4 Summary

The aim of this chapter was to determine the equivalent Kepler elements for orbits in a Plummer potential. This has been done for a single particle with a given radial distance and assigned velocity in Section 3.2. This particular method is used in Chapter 4 when comparing the numerically determined stability of particles in a Plummer potential to the predicted stability using the MSC.

A prescription for setting up a realistic steady-state cluster with an isotropic velocity distribution was outlined in Section 3.1 and will be used in subsequent chapters. The distribution of eccentricities for particles in this cluster was approximated by a Beta distribution in order to be integrable and provide an analytical form of the associated cumulative distribution function.

Due to the distribution of eccentricities for particles of a given distance to the cluster centre a statistical approach to determining the orbital period was developed. By integrating the orbits of these particles relationships between the radial period, the initial binding energy and the apocentre distance were found (see Figure 3.5). For later use empirical relationships between the radial period of a particle in a Plummer potential and the initial binding energy (Equation 3.22) and apocentre radius (Equation 3.23) based on these integrated orbits have been approximated.

By determining the equivalent Kepler elements (particularly the orbital period) for a Plummer potential with an isotropic distribution of velocities we can now use the MSC (Chapter 1) to estimate the tidal radii in globular clusters on eccentric orbits. The empirical relationships for the orbital period will be used to compare maximum period that a particle is predicted to be stable using the MSC to cluster simulations in Chapter 5 and to the tidal radii of observed clusters in Chapter 6.

Chapter 4

Application of the Mardling stability criterion to globular clusters

The aim here is to apply the Mardling stability criterion (MSC) to determine the boundary between tidally stable and unstable orbits in a cluster potential, where an unstable orbit refers to a star orbiting inside the globular cluster that will eventually escape the cluster. This stability boundary is analogous to the tidal radius of a globular cluster and is predicted using the MSC as a ratio of the cluster-galaxy to star-cluster orbital periods.

For the purposes of applying this simple stability analysis, the star-cluster-galaxy system is approximated as follows. A star of mass m_i orbits a particle representing the total cluster mass M_C which itself orbits the galaxy, taken as a particle of mass M_G. Each of these particles is treated as a point mass so that we can treat the system can a three-body problem.

Simplifying the star-cluster-galaxy system to a single three-body problem also removes mutual interactions between stars in the cluster. As previously discussed, neglecting mutual interactions between particles results in two-body relaxation being ignored. This means that in a real cluster stars will be able to diffuse over the predicted tidal radius and escape the cluster from orbits that were initially in stable regions. The effect of relaxation on globular clusters at galactic distances of interest to this work is discussed in Chapter 5.

Note that for all other chapters the cluster potential is treated as a Plummer potential and we only use a point mass potential when applying the MSC. By approximating the cluster potential as a point mass we have assumed that particles spend most of their time outside of the cluster core, this is discussed in detail in Section 4.1.2.

By treating the galaxy as a point mass the discussion is limited to GCs, which spend most of their time at distances greater than approximately 5 kpc. This is true for many of the galactic globular cluster system analysed in Chapter 6 and is certainly true for the characteristic GC orbit described in Section 2.5. The assumption of a point mass potential for the galaxy for distant cluster orbits is also justified since the mass inside 6.4 kpc is consistent with that of a point mass of roughly 10^{11} $M_\odot$, based on the reasonably well known orbits of the globular clusters NGC 2419 and NGC 7006 (Bellazzini 2004). To test this assumption a realistic treatment of actual globular clusters orbiting in a galactic potential is discussed in Section 6.1.

This chapter will apply the MSC to stellar orbits within globular clusters on eccentric galactic orbits and is structured in the following way. A stability analysis of the three-body system corresponding to a point mass approximation for the star, cluster and galaxy system is presented in Section 4.1. Numerical experiments modelling the cluster using a Plummer potential are compared to the predicted fraction of unstable orbits from the MSC in Section 4.2. Finally a summary of the relevant results of this chapter for subsequent chapters is given in Section 4.4.

4.1 Theoretically stable regions

We wish to use the stability analysis outlined in Section 1.3.2 to look at how stability depends on the proximity of a star to the centre of the cluster. The MSC uses a stability analysis which recognises that particles (stars here) random walk their way out of the cluster. Therefore stars on orbits that are found to be unstable are predicted to eventually escape the cluster.

For this analysis point mass potentials are assumed for the galaxy and cluster. We take the three body system to consist of a star $m_i = 1$ M$_\odot$, the globular cluster $M_C = 10^6$ M$_\odot$ and the galaxy $M_G = 10^{11}$ M$_\odot$. We refer to the orbit of the star-cluster as the inner orbit ($m_1 = M_C$ and $m_2 = m_i$) and the orbit of the cluster-galaxy as the outer orbit ($m_3 = M_G$). Refer back to Figure 1.3 for a schematic diagram of the position vectors associated with the inner and outer orbits.

Using the MSC a boundary between predominately unstable orbits and stable orbits is sought, separated by a period ratio σ_u. This boundary value is defined below using the predicted fraction of unstable orbits for a cluster with a distribution of particle eccentricities given in the previous chapter.

The transition between the unstable exterior of the cluster and stable interior is characterised by two additional period ratio values σ_{min} and σ_{max}. The difference between σ_{max} and σ_{min} represents the width of the transition region and is used to calculate the maximum and minimum tidal radii for observed globular clusters in Chapter 6. A conceptualisation of the stability of stellar orbits within a cluster is shown in Figure 4.1. Note that the distance from the cluster centre can be expressed in terms of the ratio of outer to inner periods σ, the apocentre distance $R_{a,i}$ and the initial binding energy of a particle E_i.

4.1.1 Coplanar systems

The MSC is applied to a co-planar system with outer eccentricity $e_o = 0.5$ following the method given in Section 1.3.2. The resonance widths for $n : 1$ type resonances[1] are determined from Equation (1.27) with $\phi_n = 0$ and are shown in Figure 4.2 (a) as a function of $\sigma = \nu_i/\nu_o = T_o/T_i$ for $m_2/m_1 = 10^{-6}$ and $m_3/m_1 = 10^5$. Regions where two or more resonances overlap are shaded in red to indicate theoretically unstable orbits. In the context of globular clusters, stars on these orbits are expected to eventually escape from the cluster.

[1]Recall that n is the lower integer part of σ.

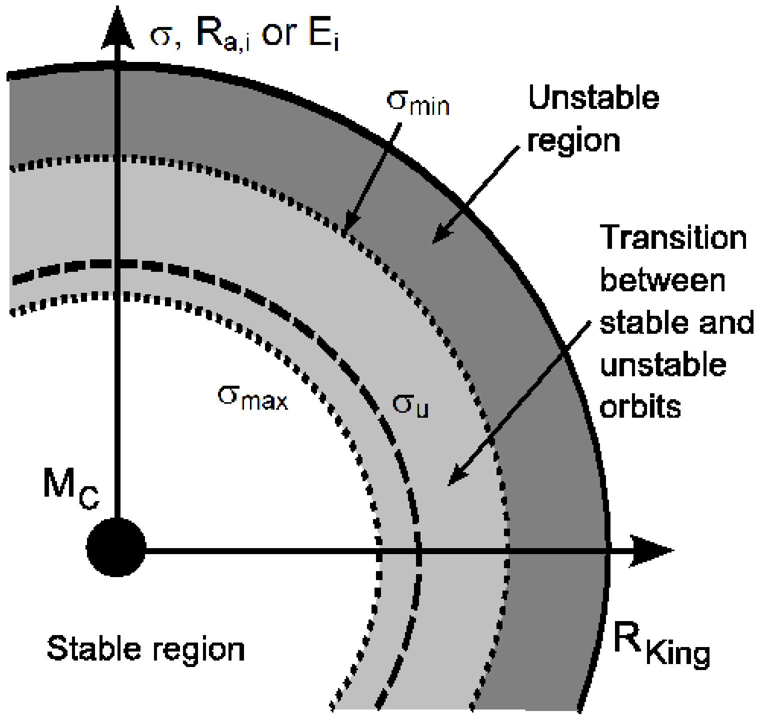

Figure 4.1: Conceptualisation of the stability of stellar orbits in a globular cluster. The distance from the cluster centre associated with the transition from unstable (dark shading) to stable (unshaded inner region) orbits is indicated by the ratio of outer to inner periods σ_u (defined in text). The region where orbits can be found in either unstable or stable configurations is shown as a light shading between σ_{min} and σ_{max}. The cluster is truncated at the maximum theoretical tidal radius (equivalent to R_{King} given by Equation (2.4)), which is shown here at a larger distance than the stable to unstable transition.

Regions where the resonance angle ϕ_n librates are shaded green in Figure 4.2 and the boundary of this region (the separatrix) is indicated by a black curve. The resonance width calculated by Equation (1.27) is the distance of the separatrix from exact resonance ($n:1$). A diagrammatical representation of circulation and libration for the three-body program was shown in Figure 1.5.

Recall from Section 1.3.2 that unstable orbits can occur outside the regions of resonance overlap near the separatrix. This is particularly problematic for $\phi_n \approx \pi$ since the resonance has zero width at this point, so the MSC predicts no unstable systems. Unstable systems can still occur near the separatrix, which has ramifications when we average over the relative phase between orbits in Section 4.1.2. The criterion of an unstable systems being a system that resides in two resonances simultaneously is adopted as a quick diagnosis and gives a good estimate as to where most unstable regions of σ-e_i space occur.

By averaging over the inner eccentricity using Equation (3.21) the fraction of unstable orbits as a function of σ can be determined. This averaging is realised by numerically determining the minimum (e_{min}) and maximum (e_{max}) values for the unstable region shown in Figure 4.2 (a) for a particular σ. The fraction of unstable orbits predicted for a coplanar system with a fixed

(a) Regions of overlapping resonances for $m_2/m_1 = 10^{-6}$ and $m_3/m_1 = 10^5$.

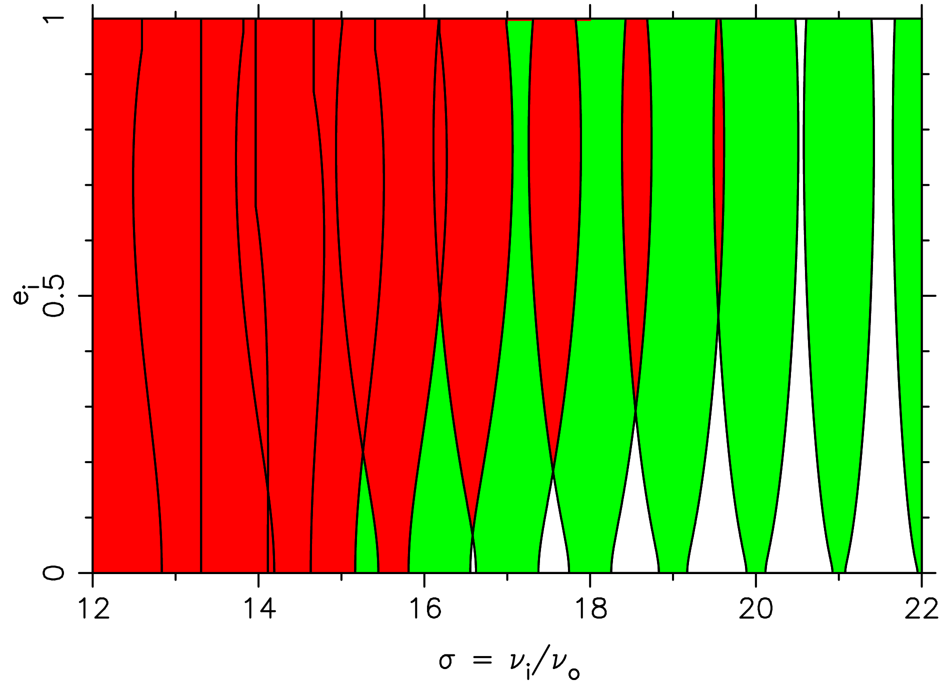

(b) Fraction of unstable orbits after including the distribution of e_i.

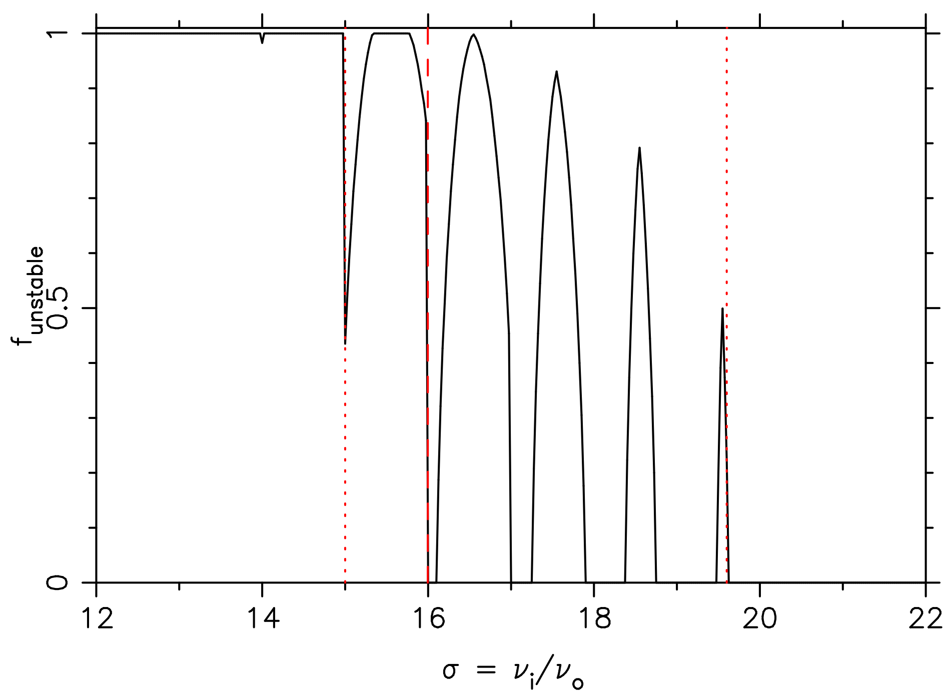

Figure 4.2: Resonance widths for a particle orbiting the cluster core with a perturbing galaxy on a coplanar $e_o = 0.5$ orbit. Regions of resonance overlap are shaded in red to show the predicted unstable orbits in panel (a), while regions inside a single resonance widths are shaded in green. Panel (b) shows the predicted fraction of unstable orbits as a function of the ratio of outer to inner orbital periods after averaging over the distribution of eccentricities in a cluster (shown in Figure 3.4).

outer eccentricity is then

$$f_{unstable}(\sigma) = Pr(e_{min} < e_i < e_{max}) = F(e_{max}) - F(e_{min}) \tag{4.1}$$

where $F(e)$ is the cumulative distribution function for the eccentricities of particles in a Plummer sphere given by Equation (3.21).

The fraction of unstable orbits for the co-planar $e_o = 0.5$ system with $\phi_n = 0$ is shown in Figure 4.2 (b). The dashed red line in this figure indicates σ_u, which is the lowest σ value where the fraction of unstable orbits drops beneath 10%. This value is a representative value for characterising the transition from stable orbits inside the cluster to unstable orbits in the outer regions of the cluster, as illustrated in Figure 4.1. We will later use σ_u as an estimate of the tidal radius of a globular cluster with simulated clusters (Chapter 5) and observed clusters (Chapter 6).

The dotted line in Figure 4.2 (b) at $\sigma_{min} \approx 15$ indicates the lowest σ value where $f_{unstable} < 0.95$, while the second line at $\sigma_{max} \approx 19.6$ indicates the greatest σ value where $f_{unstable} > 0.05$. Together these dotted lines show the width of the transition from stable to unstable orbits in units of the period ratio σ for a given e_o (the lightly shaded region in Figure 4.1). The minimum and maximum σ vales are used to give the dispersion of the tidal radius for observed clusters in the Milky Way globular cluster system in Chapter 6.

For the period ratios not shown in Figure 4.2, all $\sigma < 12$ are predicted to be unstable for this set of parameters and $\sigma > 22$ are stable. As discussed in Section 1.3.2 the MSC accurately predicts unstable orbits for $\sigma > 5$, which is well below the period ratios of interest here. Therefore the MSC is expected to accurately predict the transition between unstable and stable orbits; in as far as the point mass approximation used in the analysis is valid.

4.1.2 Inclined systems and the effect of orbital phase

Stellar orbits in globular clusters will have a distribution of relative inclination and phase with respect to the orbit of the cluster-galaxy. This section investigates the effect of the relative inclination and phase on the transition from unstable to stable orbits (σ_u).

For orbits with relative inclination I the inclination terms presented in Section 1.3.3 are used to calculate the resonance width and hence the stability of orbits. The effect of the inclination on the resonance widths are shown in Figure 1.8 for the mass ratios of interest here with a star-cluster orbital eccentricity of $e_i = 0.3$, $\sigma = T_o/T_i = 10$ and cluster-galaxy eccentricities of $e_o = 0.3$ (panel c), 0.5 (panel d) and 0.8 (panel e).

The fraction of unstable orbits as a function of the period ratio σ is determined by averaging Equation (4.1) across the range of relative inclinations between the star-cluster and cluster-galaxy orbits. The probability distribution function for the relative inclination uniformly distributed across a sphere is

$$g(I) = \frac{1}{\pi}(1 + \cos 2I) \tag{4.2}$$

where $0 \leq I \leq \pi$. The probability of the inclination being in the range $I_j - \Delta I/2 \leq I \leq I_j + \Delta I/2$

is then given by

$$P(I_j) = \left| \int_{I_j - \frac{\Delta I}{2}}^{I_j + \frac{\Delta I}{2}} g(I) dI \right|, \tag{4.3}$$

except at the end points where it is given by

$$P(I_j = 0) = \left| \int_0^{\frac{\Delta I}{2}} g(I) dI \right| \qquad P(I_j = \pi) = \left| \int_{\pi - \frac{\Delta I}{2}}^{\pi} g(I) dI \right| \tag{4.4}$$

where we choose $\Delta_I = \pi/6$. The resonance widths for determining the stability of the star-cluster-galaxy system are now calculated using Equation (1.27) with $\phi_n = 0$ and $\mathcal{A}_n$ given by Equation (1.42), which includes additional terms to allow for a variable inclination.

Using the probability distribution given by Equations (4.3) and (4.4), the fraction of unstable orbits becomes

$$f_{unstable}(\sigma) = \sum_{j=1}^{N_{Inc}} \left[F(e_{max}) - F(e_{min}) \right] P(I_j) \tag{4.5}$$

where N_{Inc} is the total number of inclination values (set at 12 here) spaced in increments of $\Delta I = 2\pi/N_{Inc}$ and $F(e)$, e_{max} and e_{min} have been defined in the previous section.

The fraction of unstable orbits after averaging over the relative inclination and eccentricities of stellar orbits within a cluster, as determined by Equation (4.5), is shown in Figure 4.3 (a) to (c) for $e_o = 0.2$, 0.5 and 0.8 respectively. The dashed vertical line in this figure again indicates the lowest σ value where the fraction of unstable orbits drops beneath 10% (σ_u). The dotted lines indicate σ_{min}, the lowest σ value for which $f_{unstable} < 0.95$, and σ_{max}, the highest σ value for which $f_{unstable} > 0.05$.

The effect that the outer eccentricity has on the transition from unstable to stable orbits is seen in Figure 4.3 where we see that σ_u increases as e_o increases. This is due to the dependence of the resonance width on the combination $n\xi(e_o)$ in Equation (1.30), where n refers to the $n:1$ resonance. This quantity is always positive and as it increases the resonance width rapidly falls to zero. Unstable systems therefore require $n\xi(e_o)$ to be as close to zero as possible, which is achieved for high values of n (and σ) if e_o is also high. Physically, this reflects the fact that an exponentially small amount of energy is exchanged between the inner (star-cluster) and outer (cluster-galaxy) orbits when their orbits are very wide (Mardling 2008b).

The width of the transition from unstable to stable orbits also increases with e_o as seen in the progression of panels (a) through (c) of Figure 4.3. Note that the basic structure of peak stability occurring at integer values of σ and stability increasing with increasing σ is consistent for all eccentricities. This phenomenon is expected since resonance widths from the $n:1$ and $n+1:1$ resonances (where $n < \sigma < n+1$) overlap at the mid point between these resonances, as seen previously in Figure 4.2 (a) for the coplanar case.

The results for all eccentricity values are shown in Figure 4.4 (a) from which a near exponential dependence of σ_u on e_o is seen. This is also true for the width of the transition between unstable and stable orbits as represented by $\sigma_{min/max}$ and shown as dotted curves on each side of σ_u in Figure 4.4 (a). Note that the coarseness in the curves for all σ values for low eccentricities

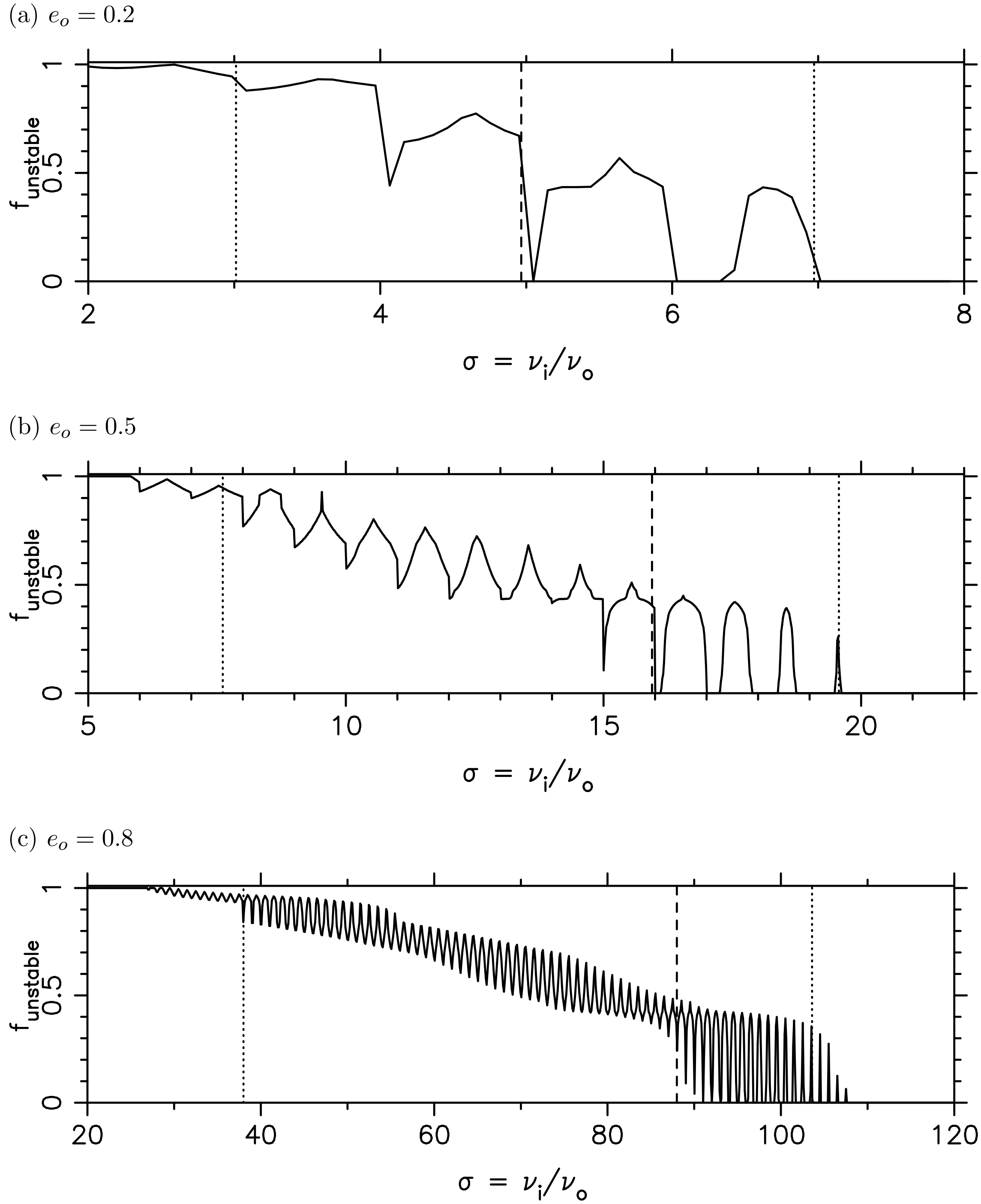

Figure 4.3: The effect of the outer eccentricity on the fraction of unstable orbits against the ratio of outer to inner periods. The transition from unstable to stable orbits σ_u is shown as a vertical dashed line and is the lowest σ value where the fraction of unstable orbits drops beneath 10%. The minimum and maximum σ values associated with the width of this transition are shown as dotted lines. Note the increase in the range of σ as e_o increases.

is due to a resolution of 1 σ when producing this figure. For high eccentricities it is clear that there is a large range in period ratios from which stars can potentially escape the cluster. This is an important result for understanding the differences between $e_o = 0.5$ and $e_o = 0.8$ in the numerical results for Plummer potential, as presented in Section 4.2.

The transition value of σ_u will be used to calculate the tidal radius for a given perigalacticon and eccentricity of the cluster orbit about the galaxy in later chapters. The width of the transition from unstable to stable orbits, given by $\sigma_{min/max}$, will be used to provide approximate error bars associated with the tidal radius.

With reference to the galactic orbits of globular clusters it is informative to show an estimate of how close a cluster can come to the galactic centre before being destroyed. We will judge a cluster to be destroyed when the tidal radius estimated using σ_u is equal to the half mass radius. The formula for relating the apocentre distance of the star-cluster orbit to its period (Equation 3.23) gives a period of $T_i = 4.96$ in scaled units for $R_{a,i} = 1$. Using the scaling from Section 3.1 the orbital period for motion of the cluster around the galaxy in scaled units is

$$T_o = 2\pi \left(\frac{p_o}{1-e_o}\right)^{3/2} (1+q)^{-1/2} \left(\frac{\sqrt{2^{2/3}-1}}{b}\right)^{3/2} \tag{4.6}$$

where $b = 1$ and $q = M_G/M_C = 10^5$ for the galaxy and cluster masses used here. The quantity $p_o = R_p/R_C$ is introduced as a shorthand description, where R_C is the characteristic length scale of the cluster and is related to the half-mass radius of the cluster by Equation (3.9).

With the inner period given by $T_i = 4.96$ the perigalacticon distance in scaled units is found from $\sigma_u = T_o/T_i$ for a given galactic orbital eccentricity e_o using Equation (4.6). The minimum perigalacticon distance for a cluster to have particles orbits stable to escape at the half mass radius is shown against eccentricity in Figure 4.4 (b). This figure shows how close a cluster can come to the galactic centre before half of the stars are predicted to be on orbits unstable to escaping the cluster. We will later use Figure 4.4 (b) to discuss the orbits of observed clusters in the Milky Way globular cluster system in Chapter 6.

The resonance angle used by the MSC to determine stability is taken as $\phi_n 0$ in the above analysis. For resonances of the form $n : 1$ the $m = 2$ terms dominate and resonance angle is given by (Equation 1.24)

$$\phi_n = M_i - nM_o + 2(\varpi_i - \varpi_o) \tag{4.7}$$

where $M_{i/o}$ are the mean anomalies and longitude of pericentre for the star-cluster (inner) and cluster-galaxy (outer) orbits. For the orbits of stars in a globular cluster these quantities will result in ϕ_n being randomly distributed from 0 to 2π. Recall from Section 1.3.2 that the resonance widths are at a maximum at $\phi_n = 0$ and are zero at $\phi_n = \pi$. The MSC is based on the overlap of neighbouring resonances and therefore predicts no unstable orbits for $\phi_n = \pi$. A diagrammatical representation of the overlap or resonances and the resonance width as a function of ϕ_n is shown in Figure 1.5.

As discussed in Section 1.3.2 unstable orbits are not confined to regions where two resonances

(a) Effect of eccentricity on the transition from unstable to stable orbits

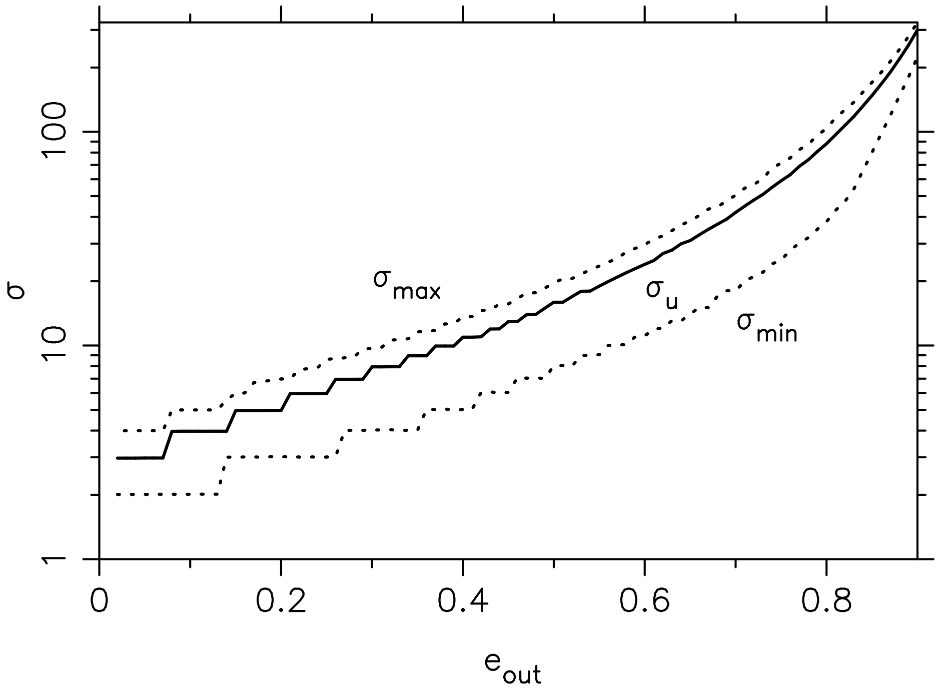

(b) Estimated perigalacticon distances associated with σ_u, σ_{min} and σ_{max}

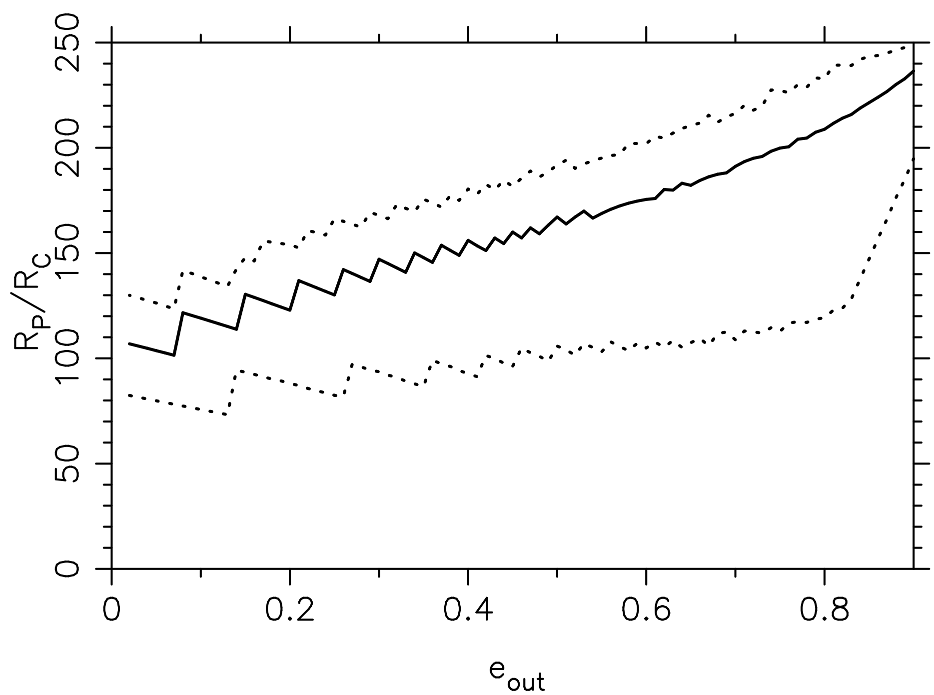

Figure 4.4: The effect of the galactic orbital eccentricity of the cluster on the transition from unstable to stable star-cluster orbits (top panel). The transition σ_u is shown as a solid line and is used as an estimate for the tidal radius, while the associated transition width values $\sigma_{min/max}$ are shown as dotted lines. The bottom panel shows the minimum perigalacticon distance as a function of eccentricity for a cluster to have particles orbits stable to escape at the half mass radius.

overlap. They can also occur near the separatrix between circulation and libration, which is what the resonance width actually specifies. This results in the MSC overestimating the stability of the star-cluster-galaxy system, which leads to the differences between the predicted fraction of unstable systems and those for a point mass system in Section 4.3. Unstable systems are found to occur away from regions of resonance overlap for high star-cluster orbital eccentricities (see Figures 4.10 and 4.11 below). Interestingly the leakage of unstable systems from regions of resonance overlap is not as significant for clusters modelled using the Plummer potential than it is for point mass clusters. This point is returned to in Section 4.3.

Aside from the orbital phase, apsidal advance will also alter the resonance widths. Apsidal advance means that the time derivatives of the longitude of pericentre for both orbits are no longer zero. This complicates the analysis used by Mardling (2008b) to determine the resonance widths as $\dot{\phi}_n$ no longer depends on the periods of the orbits (Equation 1.25). This simplification is not expected to alter the period ratio associated with the transition from unstable to stable orbits (σ_u) since it occurs far from the cluster centre where apsidal advance is weakest. A rule of thumb is that the pericentre distance of the star-cluster orbit must satisfy $R_{p,i} > b$ in order for apsidal advance to be negligible, where b is the compactness parameter of the Plummer sphere (previous chapter).

The transition between unstable and stable orbits σ_u, and the associated width, are used in later chapters to determine the tidal radii of globular clusters. The tidal radius represents the boundary between unstable orbits, associated with stars that will eventually escape the cluster, and stable orbits, which remain bound. The tidal radii corresponding to this transition will be compared to other theoretical estimates given in Section 2.4. Since σ_u is used as part of a statistical approach to determine the tidal radius the neglect of the orbital phase is justified by the associated error in σ_u being less than other sources of error, such as the point mass approximation to a Plummer potential.

4.2 Comparison to numerical experiments

The previous section used the MSC to determine the stability of the three-body system that approximates the star-cluster-galaxy system. This section examines the accuracy of this stability analysis by comparison with numerical experiments using a realistic cluster potential.

To model the gravitational potential of the cluster the core particle is no longer assumed to be a point mass and instead is assigned the Plummer potential (Equation 3.1). This core particle is free to orbit the galaxy, which again is a point mass of mass M_G. A mass-less particle placed in the outer regions of the cluster is used to model the star's motion in response to the cluster and galaxy.

The equations of motion for the test particle are

$$\ddot{\mathbf{x}}_\mathbf{i} = \frac{GM_G\left(\mathbf{x_g} - \mathbf{x_i}\right)}{\left|\mathbf{x_g} - \mathbf{x_i}\right|^3} - \frac{GM_C\left(\mathbf{x_i} - \mathbf{x_c}\right)}{\left(b^2 + r_i^2\right)^{3/2}} \quad, i = 1, \ldots, N \tag{4.8}$$

where $M_G = 10^{11}$ M$_\odot$, $M_C = 10^6$ M$_\odot$, the cluster compactness parameter (introduced in Section 3.1) is fixed as $b = 1$ for this section. The position vectors for the stellar halo particle i, cluster core, and galaxy in centre of mass coordinates are denoted by $\mathbf{x_i}$, $\mathbf{x_c}$, and $\mathbf{x_g}$ respectively and are shown in Figure 4.5. The radial distance of the particle from the cluster r_i is the magnitude of $\mathbf{r_i} = \mathbf{x_i} - \mathbf{x_c}$.

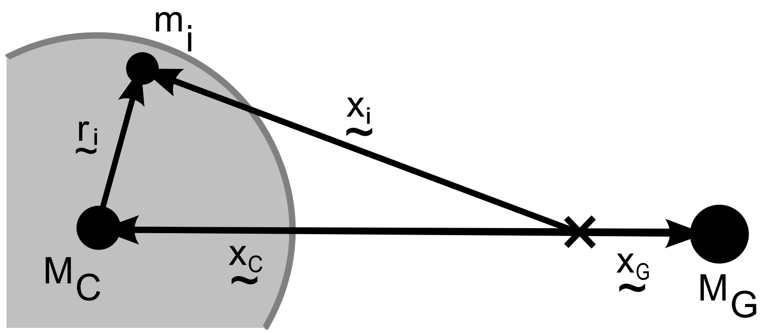

Figure 4.5: Schematic diagram showing the configuration of the test particle $m_i = 0$, cluster core particle M_C using a Plummer potential and the galaxy particle M_G. The centre of mass of the particle-cluster-galaxy system is shown as a cross.

The equations of motion for the cluster core and galaxy particles are given by

$$\ddot{\mathbf{x}}_\mathbf{c} = \frac{GM_G\left(\mathbf{x_g} - \mathbf{x_c}\right)}{\left|\mathbf{x_g} - \mathbf{x_c}\right|^3}, \qquad \ddot{\mathbf{x}}_\mathbf{g} = -\frac{GM_C\left(\mathbf{x_g} - \mathbf{x_c}\right)}{\left|\mathbf{x_g} - \mathbf{x_c}\right|^3}, \tag{4.9}$$

i.e. two-body motion. The general form of these equations for N particles is discussed in the context of the cluster model presented in Section 5.1.

The cluster core particle orbits the galaxy particle with eccentricity e_o and perigalacticon R_p, and the cluster is initially at apogalacticon. To reduce the number of free parameters we take the cluster compactness parameter as $b = 1$, the mass ratio of the galaxy to the cluster as $q = M_G/M_C = 10^5$ and the perigalacticon as $p_o = 500$, where $p_o = R_p/R_C$. Recall that R_C is the characteristic length scale of the cluster and is related to the half-mass radius and compactness parameter of the cluster by Equation (3.9).

The orbital period T_i and eccentricity e_i for the particle-cluster orbit are found by assigning a radial distance and tangential velocity following the procedure in Section 3.2. This period is in scaled units defined in Section 3.1 so the period ratio of the outer (cluster-galaxy) to the inner (particle-cluster) orbits ($\sigma = T_o/T_i$) requires T_o in the same units, given previously by Equation (4.6). We can now directly compare particle orbits integrated in time using Equations (4.8) and (4.9) to stability predictions using the MSC from the previous section.

The stability of a particular stellar orbit described by the equations of motion above is determined by exploiting the sensitivity to initial conditions of unstable systems (Section 1.3.1). Two simulations are run with initial inner semi-major axes differing by $\epsilon = 10^{-5}$ until the difference between them diverges in the sense of Section 1.3.1, or until the time exceeds $\approx 2T_o$

($\lesssim 60T_i$)[2].

The fraction of unstable orbits is shown in Figure 4.6 as a function of σ and the eccentricity of the particle-cluster orbit. The fraction of unstable orbits for each set of σ and e_i is shaded according to the scale on the right hand side of each figure and is calculated by

$$f_{unstable}(\sigma, e_i) = \frac{N_{unstable}}{N_{phase}} \tag{4.10}$$

where $N_{unstable}$ is the number of unstable orbits found for N_{phase} values of the inner orbital phase ($N_{phase} = 12$) and the relative inclination between orbits (I) is indicated above each plot. The minimum and maximum values of σ, over which the simulation shown in Figure 4.6 was done, were chosen to show where particle orbits were mostly unstable and stable for moderate values of e_i. This range was determined from low-resolution runs and spans orbits beyond the tidal radius for this cluster ($\sigma \sim 9$) and very close to the core (apocentre distance $\approx 2.4R_C$ for $\sigma = 30$ and $e_o = 0.5$). The hatched region in Figure 4.6 indicates that no simulations were run for those values of e_i and σ.

Since the cluster-galaxy orbit is fixed in space, the relative inclination I is defined using the plane of this orbit as the reference plane (compare to Section 1.2). The fraction of unstable orbits as a function of σ for a fixed inclination is found numerically by

$$f_{unstable}(\sigma) = \sum_{j=1}^{N} \left[F(e_{i,j}) - F(e_{i,j-1})\right] f_u(\sigma_j, e_{i,j})\delta(\sigma, \sigma_j) \tag{4.11}$$

where $f_u(\sigma_j, e_{i,j})$ is equivalent to $f_{unstable}(\sigma, e_i)$ from Equation (4.10) with $\sigma = \sigma_j$ and $e_i = e_{i,j}$. These N data points of index j are ordered by increasing $e_{i,j}$ for approximately equal value of σ_j to ensure that $e_{i,j} > e_{i,j-1}$. For the cases where $e_{i,j} = 0$, $F(e_{i,j-1})$ is set to zero. Thus $F(e_{i,j}) - F(e_{i,j-1})$ is the probability of e_i being found between $e_{i,j}$ and $e_{i,j-1}$ for all j. To select only those sets of σ_j and $e_{i,j}$ close to a particlular period ratio σ we define $\delta(\sigma, \sigma_j)$ to be

$$\delta(\sigma, \sigma_j) = \begin{cases} 1 & \text{if } |\sigma - \sigma_j| \leq \sigma_{bin} \\ 0 & \text{otherwise} \end{cases} \tag{4.12}$$

where σ_{bin} is the bin size chosen to give sufficient resolution to show the behaviour of $f_{unstable}(\sigma)$ ($\sigma_{bin} \approx 0.75$ for $N = 4000$ in Figure 4.6). This approach is similar to the procedure used in the previous section, except that the spacing between e_i and σ values in Figure 4.6 is irregular because of how the initial conditions for the particle in the Plummer potential are determined in Section 3.2. Regions of e_i and σ where no simulations were conducted (hatched lines) are taken as unstable for lower σ than shown and stable for high σ. Sets of parameters for which $e_i > 0.95$ are also taken as unstable. This will not significantly effect $f_{unstable}(\sigma)$ as the probability of $e_i > 0.95$ is approximately 0.1%, as determined previously in Section 3.3.

[2]Test simulations were also run for $100T_o$ to check the robustness of the stability results presented here. Longer simulations were found not to alter the conclusions and were judged not to be worth the significant additional computational expenditure.

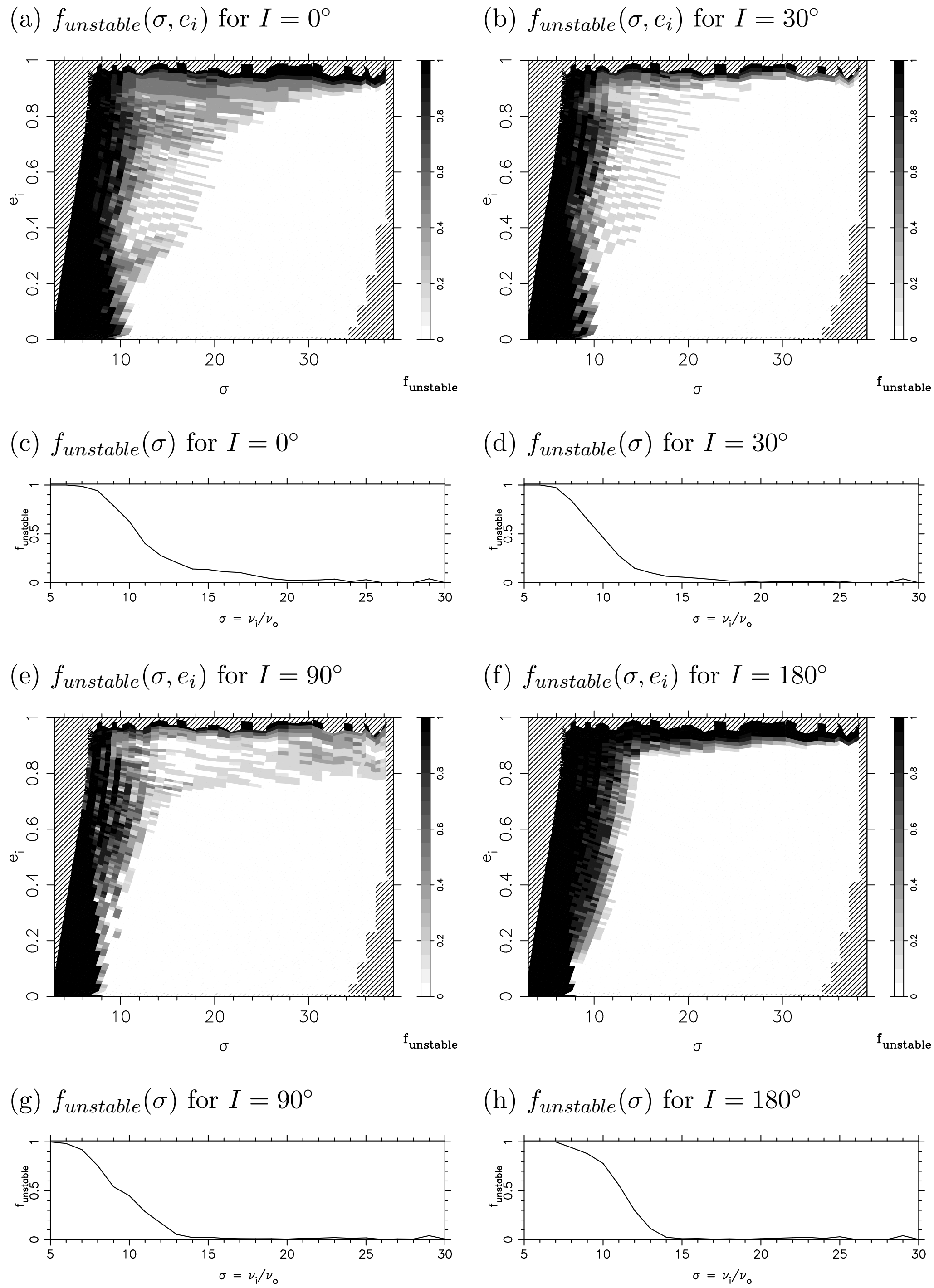

Figure 4.6: The effect of the relative inclination between the particle-cluster and cluster-galaxy orbits on the fraction of particle orbits unstable to cluster escape. All fractions of unstable orbits are found numerically using the equations of motion given by Equations (4.8) and (4.9) for a cluster of compactness $b = 1$ and a cluster-galaxy orbit of eccentricity $e_o = 0.5$ and perigalacticon $p_o = 500$. The fraction of unstable orbits as a function of the ratio of periods σ and inner eccentricity e_i is shown by the degree of shading in panels (a), (b), (e) and (f) for increasing inclinations. The effect of increasing the inclination on the fraction of unstable orbits as a function of σ only is shown in panels (c), (d), (g) and (h).

The effect of the inclination on the stability of test particles in a Plummer potential is shown for $I = 0°$, $30°$, $90°$ and $180°$ in Figure 4.6 (a), (b), (e) and (f) respectively. The corresponding fraction of unstable orbits as a function of σ is presented in panels (c), (d), (g) and (h) of Figure 4.6, as determined from Equation (4.11). As expected from the sharp decline in the resonance widths at inclinations $> 90°$ (shown in Figure 1.8), $I = 90°$ has more stable orbits than $I = 0°$ for low values of σ.

Also note the fine structure in Figure 4.6 seen as bands of unstable regions where $10 \lesssim \sigma \lesssim 20$ and $e_i \lesssim 0.9$ for prograde orbits ($I = 0°$ and $30°$). The progression from prograde to retrograde orbits causes the fraction of unstable orbits to decrease, as seen in Figure 4.6. We find that particles on retrograde orbits (Figure 4.6 f and h) are less likely to escape the cluster than particles on prograde orbits (Figure 4.6 a and c). We return to the difference between prograde and retrograde orbits in a Plummer potential in Section 4.3 where the stability of such orbits is compared to a point mass potential. This result confirms the conclusions of Read et al. (2006) who found that particles on prograde orbits are easier to strip from clusters than those on retrograde orbits.

Before comparing these numerical stability results to the predicted fraction of unstable orbits determined using the MSC in the previous section, we need to average the inclination over a uniform sphere. The fraction of unstable orbits as a function of σ and e_i is adjusted to include the inclination by

$$f_{unstable}(\sigma, e_i) = \sum_{j=1}^{N_{Inc}} P(I_j) f_u(\sigma, e_i, I_j) \tag{4.13}$$

where the probability of the inclination satisfying $I_j - \Delta I/2 \leq I \leq I_j + \Delta I/2$ is given by $P(I_j)$ in Equation (4.3) with $\Delta I = \pi/6$. The fraction of unstable orbits $f_u(\sigma, e_i, I_j)$ is equivalent to $f_{unstable}(\sigma, e_i)$ in Equation (4.10) for inclination I_j. The resulting fraction of unstable orbits as a function of σ and e_i for $e_o = 0.5$ is shown in Figure 4.7 (a). Note the sharp boundary between mostly unstable and mostly stable orbits at $\sigma \sim 10$ in Figure 4.7 (a) remains after averaging over the inclinations. The increase in unstable orbits for high star-cluster orbital eccentricities is also preserved and results in the fraction of unstable orbits never completely falling to zero as σ increases.

The fraction of unstable orbits as a function of σ is determined using the distribution of eccentricities for particle orbits in a Plummer potential (Equation 4.11) using the same procedure as for Equation (4.11). This fraction of unstable orbits from the numerical stability results is shown for $e_o = 0.5$ in Figure 4.7 (b). The corresponding fraction of unstable orbits predicted using the MSC for the same e_i and I distribution is shown in Figure 4.7 (c).

Comparison between the predicted fraction of unstable orbits using the MSC and the numerical stability results are shown in Figure 4.8 for a range of galactic orbit eccentricities. This figure shows the predicted fraction of unstable orbits (dashed curve) and the numerical results (solid curve) as a function of σ for $e_o = 0.2$, 0.5 and 0.8 with $p_o = 500$. The resolution used to display the fraction of unstable orbits predicted by the MSC for $e_o = 0.8$ in Figure 4.8 (c) has been decreased so as not to obscure the numerical results the original high resolution version

(a) Fraction of unstable orbits for $p_o = 500$ and $e_o = 0.5$ as a function of σ and e_i.

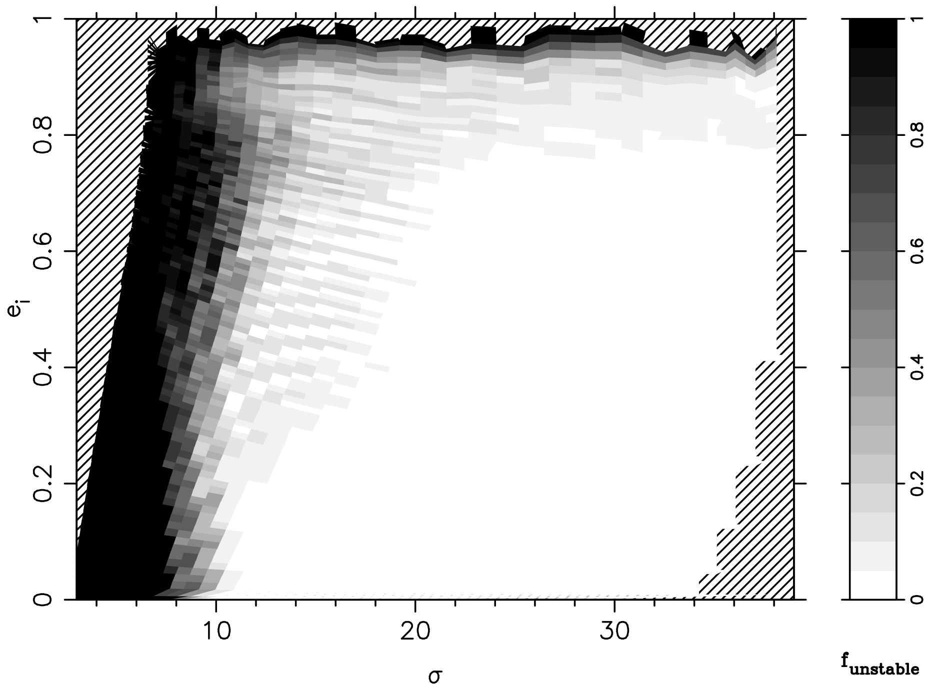

(b) Fraction of unstable orbits given in (a) after including the eccentricity distribution.

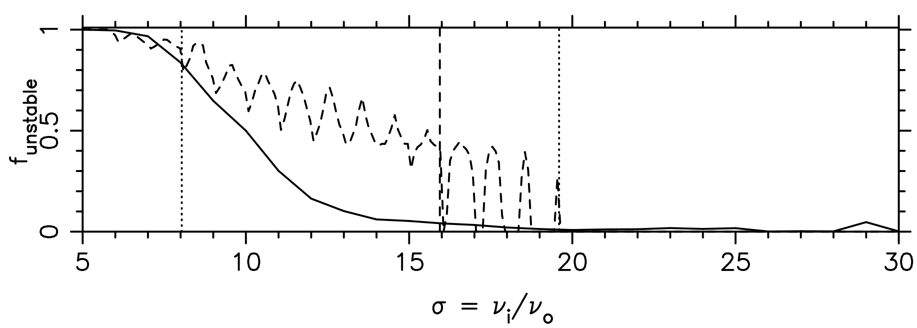

Figure 4.7: The fraction of unstable orbits from numerical stability tests as a function of the period ratio σ and the eccentricity of the particle-cluster orbit e_i is shown in panel (a) for $e_o = 0.5$ and $p_o = 500$. For a distribution of eccentricities given by Equation (3.20), the unstable fraction is reduced to a function of σ, shown as the solid line in panel (b). The fraction of unstable orbits predicted by the MSC is shown as the dashed line in panel (b).

was shown in Figure 4.3 (c). The period ratio corresponding to the transition between unstable and stable orbits σ_u is shown as a vertical dashed line in Figure 4.8 and the $\sigma_{min/max}$ values associated with the width of this transition are shown as dotted lines.

Generally good agreement between the predicted fraction of unstable orbits and the fraction determined from numerical integrations of a particle in a Plummer potential is seen in Figure 4.8. The main difference is that the fraction of unstable orbits predicted by the MSC is consistently higher than the numerically determined fraction for $e_o = 0.8$ (Figure 4.8 c). This discrepancy can be explained by considering the how the distance from the cluster centre depends on the ratio of periods σ.

To determine the radius from $\sigma = T_o/T_i$ we need to know the orbital period of the cluster-galaxy orbit T_o and a function relating the radius to the particle-cluster orbital period T_i. To be consistent with the numerical simulations we take the perigalacticon as $p_o = R_P/R_C = 500$ and allow the eccentricity of the cluster-galaxy orbit e_o to vary.

From Equation (4.6) the period of the particle-cluster orbit in terms of σ is given by

$$T_i = \frac{2\pi}{\sigma}(1+q)^{-1/2}\left(\frac{p_o}{1-e_o}\right)^{3/2} \tag{4.14}$$

where $q = 10^5$ as before. Note that Equation (4.14) does not depend on the compactness parameter b of the cluster, since the same b dependence appears in the time scaling for both T_i and T_o. This equation is solved iteratively for the apocentre distance by rearranging Equation (3.23) to give

$$R_{a,i}^{k+1} = \left(\frac{T_i(1+\bar{e}_i)^{3/2}}{2\pi} - \frac{3.21(1+\bar{e}_i)^{3/2}}{2\pi(1+R_{a,i})}\right)^{2/3} \tag{4.15}$$

where the mean eccentricity and is given by $\bar{e}_i = 0.47$ for N particles in a Plummer potential with a Maxwellian distribution of velocities. Equation (4.15) is solved iteratively by setting $R_{a,i}^1 = T_i(1+\bar{e}_i)^{3/2}/(2\pi)$ and typically requires $k = 5$ iterations to converge. The apocentre distance as a function of σ is shown as solid curves in Figure 4.9 (a) for galactic orbital eccentricities of $e_o = 0.2$ (red lines), 0.5 (green) and 0.8 (blue). The dashed lines in this figure also show the pericentre distances calculated by $R_{p,i} = R_{a,i}(1-\bar{e}_i)/(1+\bar{e}_i)$, for the same values of e_o.

The enclosed mass for the Plummer potential as a function of the period ratio is determined by setting the radius in Equation (3.8) equal to the semi-major axis of the particle-cluster orbit, i.e. $r = a_i = R_{a,i}(1-\bar{e}_i)$. This enclosed mass is shown in Figure 4.9 (b) and is in scaled units where the total cluster mass equals unity. The enclosed mass gives a measure of how close the Plummer potential is to a point mass potential for a given period ratio. We will return to this topic in Section 4.3, where numerical stability results from a point mass cluster potential are compared to the Plummer potential results for $e_o = 0.5$.

There are two key questions that arise from the comparison between the MSC stability predictions and the numerical stability results. Firstly, why is the fraction of unstable orbits predicted by the MSC close to the numerical stability results at all? Secondly, why does the MSC overestimate the occurrence of unstable orbits for high values of σ when $e_o = 0.8$? Both

(a) Fraction of unstable orbits for $e_o = 0.2$

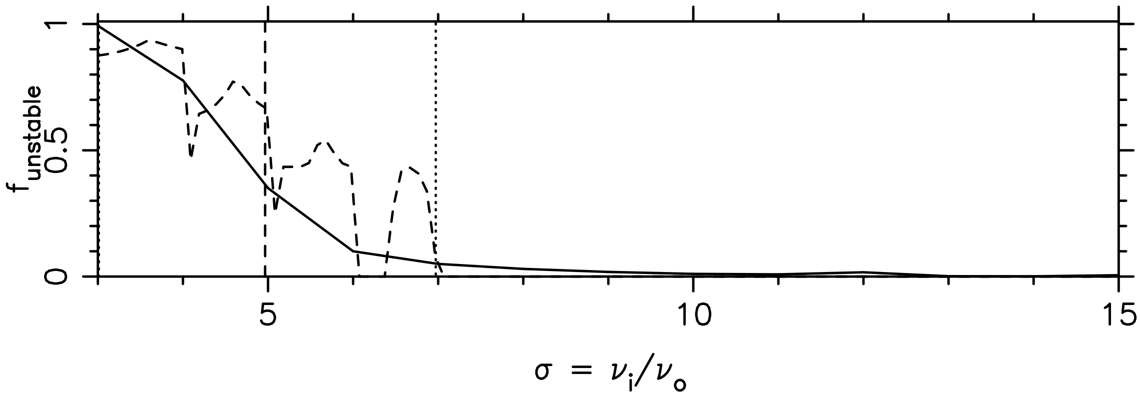

(b) Fraction of unstable orbits for $e_o = 0.5$

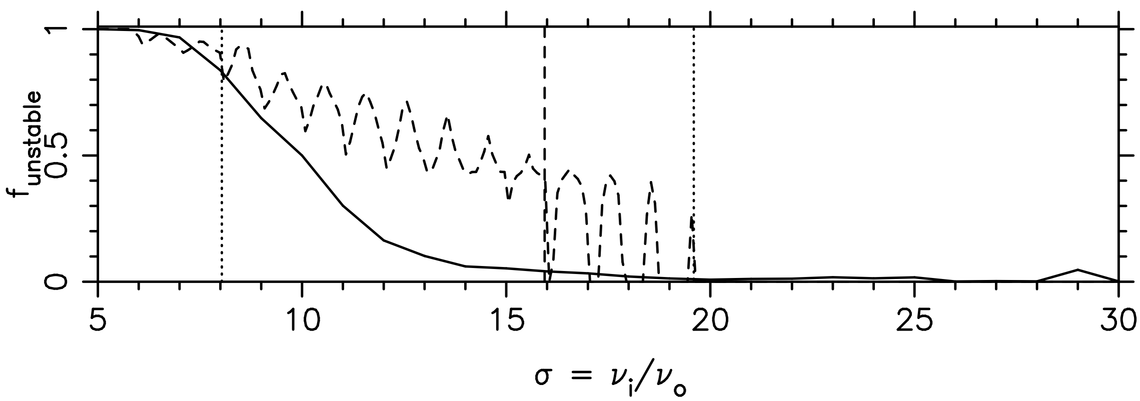

(c) Fraction of unstable orbits for $e_o = 0.8$

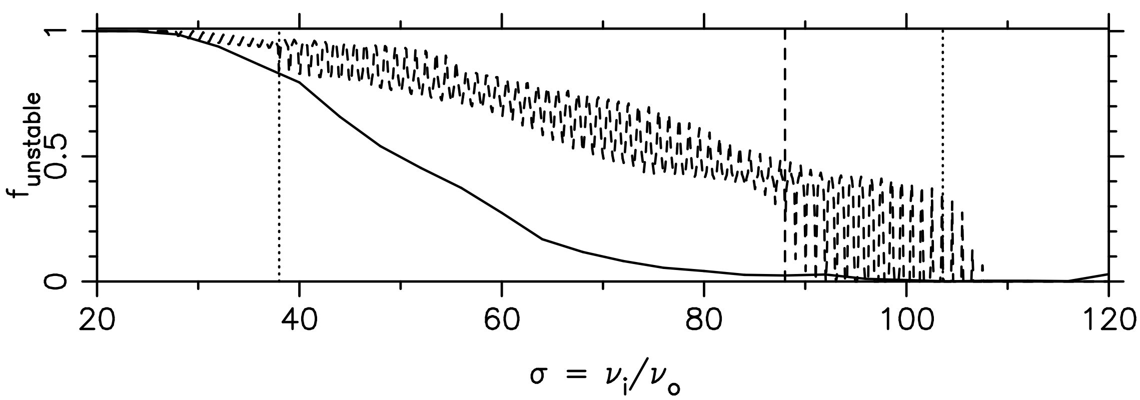

Figure 4.8: The fraction of unstable orbits predicted by the MSC assuming a point mass cluster potential (dashed curves) as reproduced from Figure 4.3 and the fraction found using numerical stability results for a Plummer cluster potential (solid curve). The eccentricity of the cluster's orbit around the galaxy is $e_o = 0.2$, 0.5 and 0.8 in panels (a), (b) and (c) respectively. The dashed vertical lines show the transition between unstable to stable orbits σ_u and the dotted lines show the associated $\sigma_{min/max}$ values determined using the MSC.

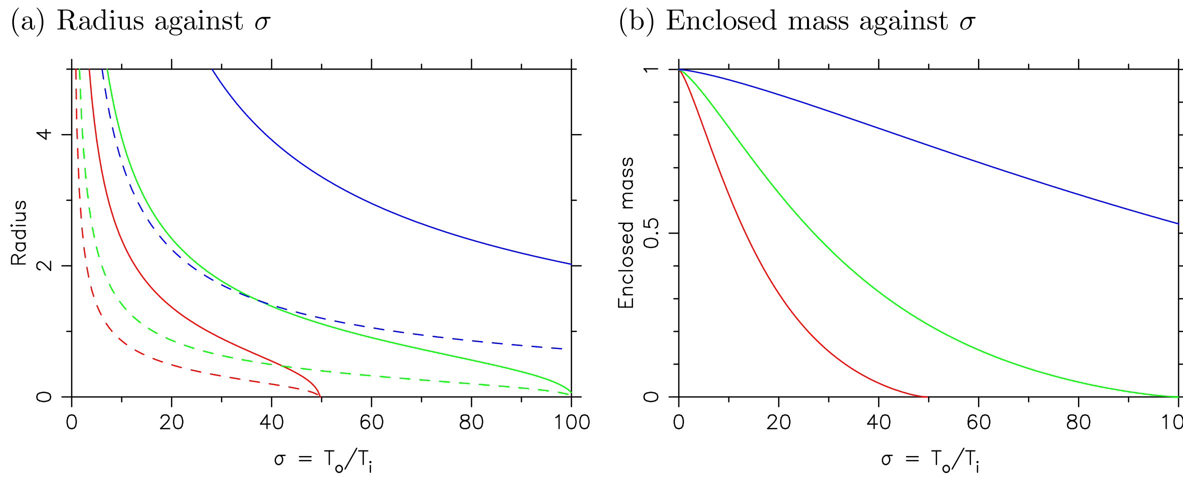

Figure 4.9: The apocentre (solid curves) and pericentre radius (dashed curves) of a particle in the Plummer sphere determined from $\sigma = T_o/T_i$ for the galactic orbital period T_o with perigalacticon 500 and particle-cluster orbital period T_i (panel a). For simplicity the eccentricity of the particle-cluster orbit is taken as the mean eccentricity ($\bar{e_i} = 0.47$) for the isotropic velocity distribution, shown previously in Figure 3.4. The enclosed mass is determined using the semi-major axis of the particle-cluster orbit and is shown in panel (b). The effect of the galactic orbital eccentricity is shown in both panels for $e_o = 0.2$ (red lines), 0.5 (green) and 0.8 (blue). Recall from Figure 3.5 that T_i does not decrease to zero as the particle distance decreases to zero.

of these questions can be addressed using Figure 4.9.

The MSC predicts the stability of particle orbits in a Plummer potential reasonably well because in the transition region from unstable to stable orbits the Plummer potential is closely approximated by a point mass potential. This is seen in Figure 4.9 (b) where the enclosed mass values associated with σ_{max} are approximately 70%, 60% and 50% of the total cluster mass for $e_o = 0.2$, 0.5 and 0.8 respectively. The higher the amount of mass enclosed by the semi-major axis associated with a particular value of σ the more like a point mass potential the cluster potential will appear. As σ decreases then the distance from the cluster increases and eventually the cluster-particle orbits are indistinguishable from Kepler orbits. Where the particle-cluster orbits are close to Keplerian for all $\sigma \leq \sigma_{max}$ the MSC will describe the stability of the three-body orbit well, as expected from Section 1.3.2.

The enclosed mass for the semi-major axis of particle-cluster orbits does not explain why the MSC predicts less stable orbits than seen in the numerical results for e_o. To explain this discrepancy we examine how the pericentre distance relates to the core of the cluster.

We put forward the hypothesis that if the pericentre of a particle-cluster orbit lies within the cluster core, i.e. $R_{p,i} < b$, then the orbit is made more stable than if the cluster potential was a point mass potential. This hypothesis is tested in the next section by comparing numerical stability results from particles in a Plummer potential to particles in a point mass potential for the representative cluster-galaxy orbit of $e_o = 0.5$ and $p_o = 500$. Here we will examine the ramifications of this hypothesis for the fraction of unstable orbits as a function of σ for different cluster-galaxy orbital eccentricities.

From Figure 4.9 (a) the pericentre distance satisfies $R_{p,i} = b = 1$ at $\sigma = 8.2$, 16.4 and 64.8 for $e_o = 0.2$, 0.5 and 0.8 respectively. For comparison the maximum period ratios associated with the transition from unstable to stable orbits predicted by the MSC are given by $\sigma_{max} = 7.0$, 19.6 and 103.6 for the same eccentricities. Therefore for $e_o = 0.2$ all period ratios associated with the transition from unstable to stable orbits ($\sigma \leq \sigma_{max}$) have pericentre distances beyond the cluster core and the stability is expected and observed to be well described by the MSC. The predicted stability transition for particle-cluster orbits with $e_o = 0.5$ has some particle-cluster orbits satisfying $\sigma \approx \sigma_{max}$ whose pericentre distances take them inside the cluster core. For $e_o = 0.8$, the transition between unstable and stable orbits falls well inside the range where $R_{p,i} < 1$ and so the fraction of unstable orbits is expected to be less for particles in a Plummer potential than if they were in a point mass potential. Since the MSC is based on the overlapping resonance widths for point mass potentials it too is expected to overestimate the fraction of unstable orbits for $e_o = 0.8$.

By comparing numerical stability results to the fraction of unstable orbits predicted be the MSC in Figure 4.8 we have shown that the transition from $f_{unstable} \approx 100\%$ to $f_{unstable} \approx 0\%$ occurs across the same range indicated by σ_{min} and σ_{max}. This gives weight to using σ_{min} and σ_{max} to indicate the range of tidal radii from which stars are predicted to escape the cluster, as first discussed in Section 4.1. The use of the predicted σ_u and $\sigma_{min/max}$ in regards to more sophisticated cluster models and to observed clusters will be discussed below in Section 4.4.

4.3 Comparison of stability between Plummer and point mass potentials

In the previous section we put forward the hypothesis that if the pericentre distance of a particle-cluster orbit lies within the cluster core, i.e. $R_{p,i} < b$, then the orbit is made more stable than if the cluster potential was a point mass potential. In this section this hypothesis is tested by comparing numerical stability results from particles in a Plummer potential to particles in a point mass potential, for the representative cluster-galaxy orbit of $e_o = 0.5$ and $p_o = 500$.

If pericentre distances of a particle-cluster orbit in a Plummer potential which satisfy $R_{p,i} < b$ are more stable than the equivalent orbits in a point mass potential then we will expect that for a fixed e_i there will be more stable orbits at lower σ values for particles in a Plummer sphere compared to particles in a point mass cluster potential. This effect will be particularly evident for high particle-cluster orbital eccentricities (e_i) since these orbits have lower pericentre distances that are more likely to satisfy $R_{p,i} < 1$. If e_i is too high then the apocentre distance will be sufficiently far from the cluster centre for the particle to be directly stripped by the galaxy potential for either potential type.

The effect of the Plummer potential on the stability of particle-cluster orbits is investigated for a fixed orbital phase and the particle-cluster-galaxy system in a coplanar configuration. The orbits of the particle-cluster and the cluster-galaxy are integrated in time using Equations (4.8) and (4.9) with $b = 0$ (corresponding to a point mass) and stability is determined by the procedure

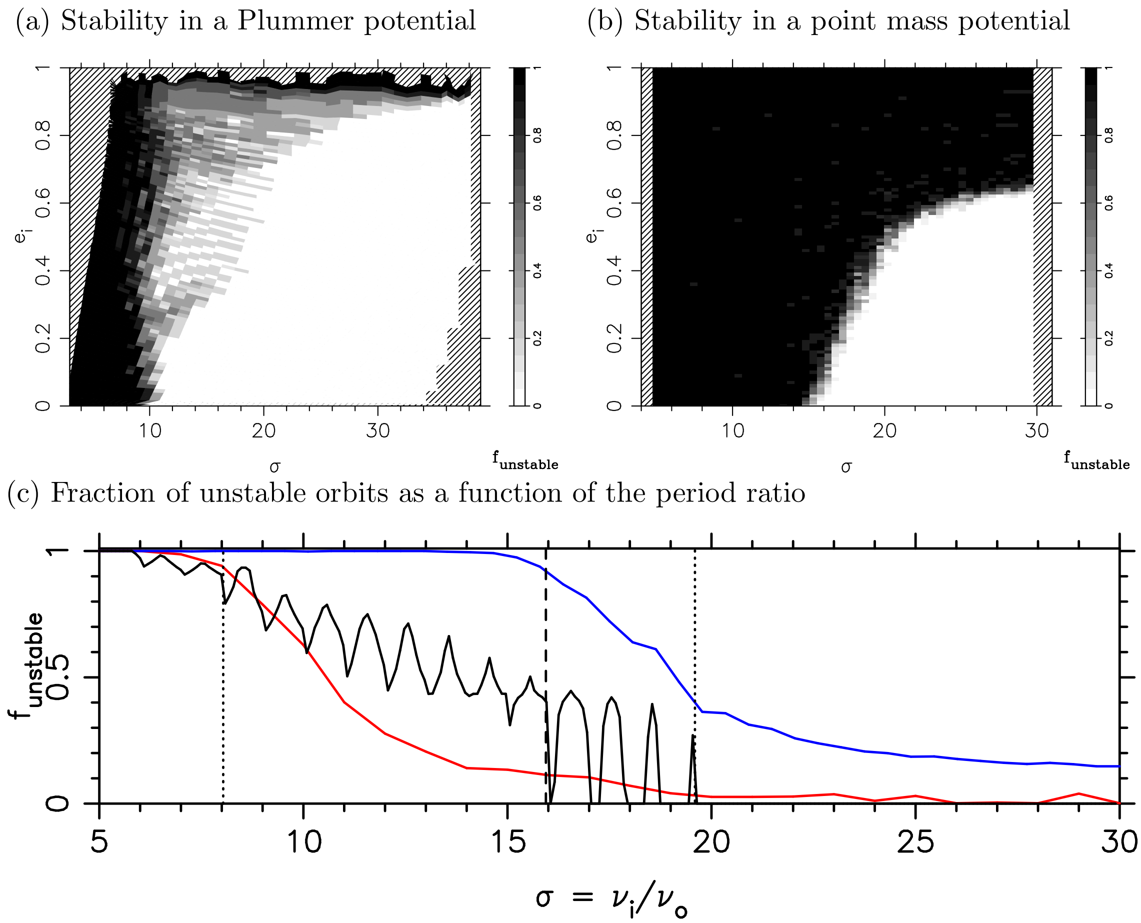

Figure 4.10: Numerically determined stability results for a particle in a Plummer potential (panel a) and a point mass potential (panel b) for a cluster-galaxy orbit of $e_o = 0.5$ and $p_o = 500$ with a fixed orbital phase and zero relative inclination between the orbits. The lower panel compares the fraction of unstable orbits between a particle in a Plummer potential (red curve), a particle in a point mass potential (blue) and the fraction predicted by the MSC (black) is shown in the bottom panel. All particles are on prograde orbits inside the cluster.

in Section 4.2. The stability results for a cluster-galaxy orbit of $e_o = 0.5$ and $p_o = 500$ are shown in Figure 4.10 (b). The stability results for a particle in a Plummer potential are reproduced from Figure 4.6 (a) for the prograde coplanar case ($I = 0$) in Figure 4.10 (a). A comparison of the fraction of unstable orbits is shown in Figure 4.10 (c) between a particle in a Plummer potential (red curve), a particle in a point mass potential (blue) and the fraction predicted by the MSC (black).

Similar stability results for a Plummer and point mass potential are shown in Figure 4.11 for the retrograde coplanar case ($I = 180°$). As previously commented upon, more stable systems are seen in the Plummer potential for retrograde orbits than for prograde orbits. This is also true of the stability results for a point mass cluster potential. Interestingly the stability results for the point mass potential shown in Figure 4.11 (b) show a lot more structure corresponding to overlapping resonances than seen for prograde orbits in Figure 4.10 (b).

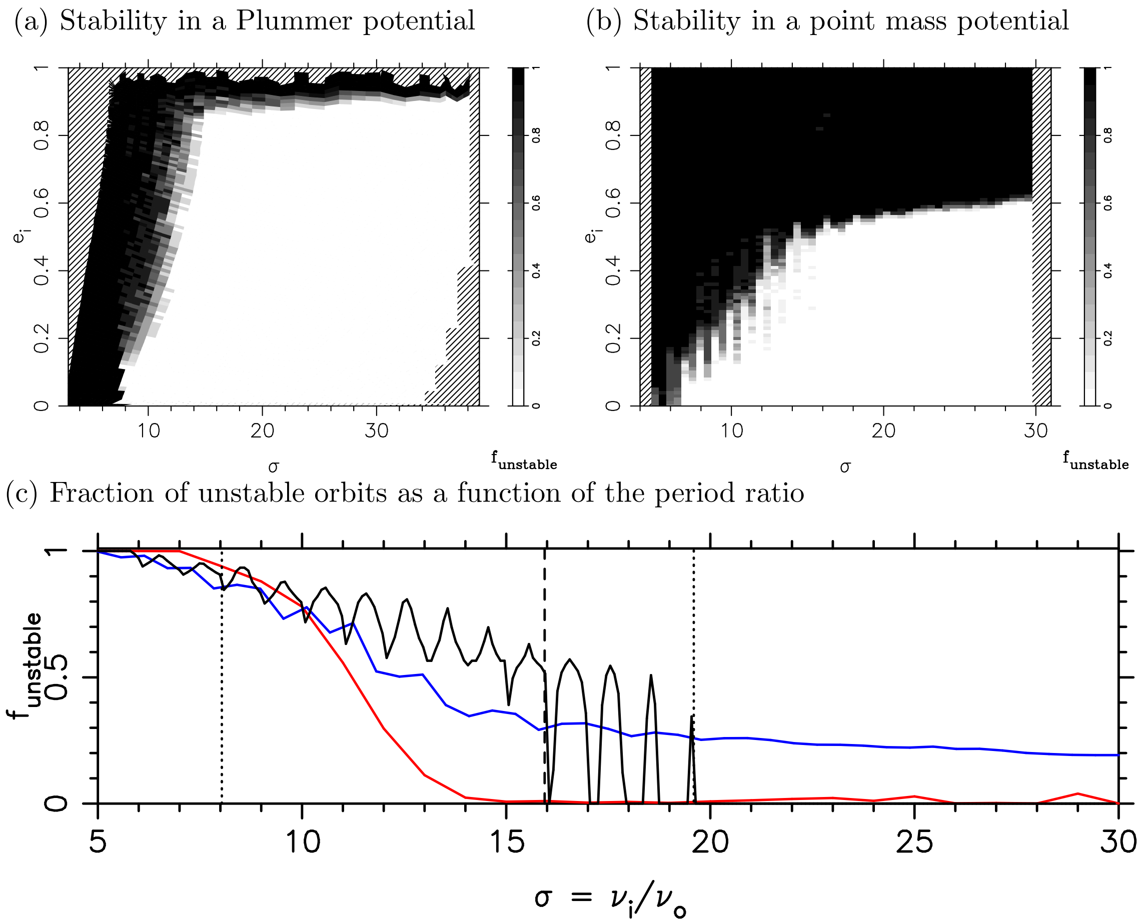

Figure 4.11: Same as Figure 4.10 but for a particle on a retrograde orbit. Stability results for the Plummer potential are reproduced from Figure 4.6 (f).

The predictions of core entry increasing the stability of particle orbit are confirmed in Figures 4.10 and 4.11 for prograde and retrograde orbits. In fact particle orbits in the point mass potential are still mostly unstable for $\sigma = 30$ when $e_i \gtrsim 0.6$, whereas they are mostly stable for the Plummer potential. This eccentricity range represents approximately 27.4% of all e_i values for particles in a Plummer potential (Figure 3.4) and results in an increased fraction of unstable orbits for the point mass potential seen for high values of σ in Figure 4.10 (c). Comparing this result to the predicted fraction of unstable orbits using the MSC shows the MSC correctly predicting the stability of particle orbits in the Plummer potential, but not in the point mass potential.

This counter-intuitive result is due to how the MSC is used to predict stable orbits in Section 1.3.2. Any orbit written as an eccentricity e_i and a ratio of periods σ is expected to be unstable if and only if the resonance widths associated with the resonance angles ϕ_n and ϕ_{n+1} overlap, where n is the lowest integer part of σ. This definition of unstable orbits does not include instabilities occurring close to the separatrix (see Section 1.3.2), which is used to calculate the resonance width. This explains why the MSC does not predict the occurrence of unstable systems for the point mass potential but does not explain why orbits in the Plummer potential are more stable.

For particle-cluster orbits with pericentre distances satisfying $R_{p,i}/b < 1$ apsidal motion will be significant, as seen in Figure 3.3 (b). However, as commented in Section 4.1.2, this is not likely to be the cause of increased stability. The increase in stability seen for particle orbits in a Plummer potential compared to a point mass potential is most likely the caused by the resonance widths associated with libration (see Figure 1.5) for a Plummer potential are thinner than for a point mass potential. To confirm or refute this would require the MSC to be modified for a Plummer potential.

By comparing the stability of particles in a Plummer potential to a point mass potential the following conclusions can be drawn. Firstly, to correctly predict the stability of particle orbits in a point mass potential the MSC must be modified to include unstable orbits occurring near the separatrix of the resonance. Secondly, the Plummer potential is a stabilising influence on orbits whose pericentre distance satisfies $R_{p,i}/b < 1$. This second conclusion is important when discussing the stability and eventual escape of particles from a globular cluster modelled by a Plummer potential, in particular for high eccentricity galactic orbits as found in Section 4.2.

4.4 Summary

The aim of this chapter has been to apply the MSC to determine the boundary between tidally stable and unstable orbits in a cluster potential, where an unstable orbit refers to a particle orbiting inside the globular cluster that will eventually escape the cluster.

The stability of particle orbits in a cluster is summarised by the fraction of unstable orbits as a function of the period ratio σ of the cluster-galaxy orbit to the particle-cluster orbit. This fraction as a function of σ is determined by averaging across a distribution of particle-cluster orbital eccentricities (shown in Figure 3.4) and assuming the relative inclination to the cluster-galaxy is distributed over a uniform sphere.

The fraction of unstable orbits against σ is summarised for galactic orbital eccentricities of the cluster of $e_o = 0.2$, 0.5 and 0.8 in Figure 4.8. This figure compares numerical stability results for a particle in a Plummer potential to the predicted fraction of unstable orbits using the MSC for a point mass cluster potential. From Figure 4.8 the transition from unstable to stable orbits occurs in the region defined by $\sigma_{min} \lesssim \sigma \lesssim \sigma_{max}$, where σ_{min} is the lowest σ value where $f_{unstable}$ is predicted by the MSC to be less than 95% and σ_{max} is the greatest σ value where $f_{unstable} > 0.05$. The transition from unstable to stable orbits is characterised by σ_u, which is defined as the lowest σ value where the fraction of unstable orbits is predicted to be less than 10%. The transition between unstable and stable orbits σ_u is used to estimate the tidal radius of a globular cluster in later chapters.

The predicted period ratios σ_u and $\sigma_{min/max}$ are shown as a function of the cluster-galaxy orbital eccentricity e_o in Figure 4.4 (a). These predicted values were found to underestimate the stability of particles in a Plummer potential for high eccentricities, as seen for $e_o = 0.8$ in

Figure 4.8 (c). Particle orbits that come within the core of the Plummer potential were found to be more stable than predicted.

We found that particle-cluster orbits whose pericentre distances satisfied $R_{p,i}/b < 1$ where more stable than expected for point mass cluster potentials and therefore predicted to be unstable by the MSC. This was confirmed in Section 4.3 by numerical stability results for the particle-cluster-galaxy system using a point mass cluster potential. Importantly most particles that orbit near the tidal radius of a cluster do not enter the core. Thus, this effect is ignored from herein as we require a representational σ_u value to convert into an apocentre radius in subsequent chapters. In addition the range of tidal radii given by σ_{min} to σ_{max} is accurate for all e_o values and the difference between these serves as an estimate of the error.

Recall that unstable orbits are used as a predictor the escape of stars from a cluster. This assumes that particles on unstable orbits will escape the cluster faster than other processes at work in the cluster, such as two-body relaxation. The effect of cluster relaxation on these results is examined in the next chapter and is found to negligible in the outer regions of long galactic orbital period clusters.

Despite the complications of this model, using the MSC to estimate the tidal radius of a globular cluster on an eccentric galactic orbit has two significant advantages. Firstly, the transition between unstable and stable orbits σ_u, and the associated range given by $\sigma_{min/max}$, provide a good estimate of the stability of particle orbits as determined numerically. Secondly, using the MSC is far less computationally expensive than determining the stability numerically. For example a single stability plot with the resolution shown in Figure 4.7 (a), required the numerical integration of over 500000 individual three-body systems. This would have to be repeated for every combination of perigalacticon and eccentricity for the cluster-galaxy orbit since the cluster compactness parameters b introduces a length scale. This task would be completely unfeasible using direct N-body simulations, particularly for clusters on large period galactic orbits. By contrast the tidal radii predicted using the MSC is not dependent on b since it is based on the period ratio for an equivalent point mass system. The cluster compactness parameter b is only used to convert σ_u into physical units.

The transition from unstable to stable orbits σ_u as a function of the cluster-galaxy orbital eccentricity (Figure 4.4 a) is compared to results from a more sophisticated cluster model presented in the next chapter and to the observed tidal radius of clusters in the Milky Way globular cluster system in Chapter 6.

Chapter 5

Simplified cluster model

The aim of this chapter is to develop and validate a more sophisticated globular cluster model than the modified three-body cluster system presented in the previous chapter. This model will allow the tidal radius to be estimated using the fraction of escaping stars as a function of their initial distance from the cluster centre. The tidal radius estimated from a simulated cluster is then compared to the location of orbits predicted by the Mardling stability criterion (MSC) to be stable or unstable to escape from the cluster. The radius past which orbits are unstable to escape is referred similar to the tidal radius for globular clusters on eccentric galactic orbits. This chapter serves as a test of the MSC to predict the tidal radii of simulated clusters on known galactic orbits with reasonable accuracy. Therefore providing a measure of its reliability for estimating the tidal radii in observed clusters in Chapter 6, where the orbital parameters are not known with certainty.

The model presented in this chapter was developed before the three-body model presented in Chapter 4, when we thought that energy exchange between the cluster stars and the cluster orbit might be an important factor for tidal stability. The galactic orbit of the cluster was not found to significantly change on the timescale that the cluster model was valid for. The main difference between the model presented in Chapter 4 and the model presented below is that the previous three-body model takes the mass of the stars in the cluster to be zero.

A "simplified cluster" model (SCM) is developed in this chapter, which does not include the mutual gravitational interactions between particles and therefore excludes relaxation processes. This reduces the number of operations required to simulate N particles to $\mathcal{O}(N)$ rather than $\mathcal{O}(N^2)$ for direct N-body simulations. For comparison the simulation with the longest period examined here ($p_o = R_P/R_C = 1000$ and $e_o = 0.8$) only took 101 CPU hours on a single 2.3 GHz processor. The SCM allows for the study of escaping stars in clusters with large galactic orbital periods, which is not possible for direct N-body models due to impractical simulation times.

The SCM consists of N particles orbiting a cluster core particle which is endowed with 50% of the total cluster mass, the core particle itself orbits the galaxy (see Section 5.1). Using a core particle consisting of half the cluster mass means that the orbits of particles in the innermost regions of the cluster do not need to be integrated forward in time. This results in a large reduction of the CPU time taken to integrate the cluster through a galactic orbit by increasing the time-step required to resolve the innermost particle orbit. We later show in Section 5.2 that neglecting these innermost orbits does not effect the tidal radius unless the cluster loses most of the particles. To better simulate a realistic cluster the cluster is modelled by a Plummer potential centred on the core particle, while the N particles and the galaxy particles are treated as point masses. The equations of motion for the particles in this model are derived from the Lagrangian of the system in Section 5.1.

The core particle will move within the cluster in response to the spatial distribution of halo particles. This results in the core wandering in the inner regions of the cluster and is responsible for altering the orbits of particles close to the core. This mixing of particles in the core may result in particles migrating out from the centre of the cluster where they can subsequently escape the cluster. This process is similar to, but not the same as, two-body relaxation and is examined in Section 5.1.

By removing the mutual interactions between particles the SCM does not include two-body relaxation. As discussed in Section 2.2, globular clusters on galactic orbits with perigalacticon distance $R_P = 6.2$ kpc and eccentricity $e = 0.5$ (Section 2.5) have long relaxation timescales $t_{rx} \gtrsim 1Gyr$ at the half mass radius of the cluster (Equation 2.1), which is of the same order as the orbital period. The radial dependence of the relaxation timescale is shown later in Figure 5.6 (b) and shows the relaxation timescale near the tidal radius is significantly larger than the galactic orbital period the cluster. Therefore we have assumed that neglecting two-body relaxation in the SCM does not change the tidal radius results for the cluster orbits of interest. This assumption is tested in Section 5.2 by comparing the cluster model with results from a direct N-body code including relaxation run by Holger Baumgardt, then at the University of Tokyo.

The single set of N-body simulation results for perigalacticon distance $R_P/R_C = 500$ and eccentricity $e_o = 0.5$ is also used to test that the core particle treatment used by the SCM does not effect the tidal radius. The N-body results for the fraction of escaping stars against distance from the cluster centre also serves as a benchmark for the SCM for determining how well the tidal radius can be estimated.

However there is another way to examine the tidal radius estimates using the SCM without having N-body simulations of all galactic eccentricities and perigalacticon distances available. The theoretical tidal radius referred to here as the Read radius (Equation 2.5) was found by Read et al. (2006) to be consistent with the results from two N-body simulations of a $10^7 M_\odot$ satellite clusters modelled by $N = 10^5$ particles and using a galactic potential similar to that used in Chapter 6. Converting the orbital parameters for the two N-body simulations into similar units to our own means that these two orbits had perigalacticon $R_P/R_{1/2} = 267$ and eccentricity $e_o = 0.0$ and perigalacticon $R_P/R_{1/2} = 77$ and eccentricity $e_o = 0.57$ (Read et al. 2006). These are at the low period end of the parameter space used in this chapter (see below). Where the parameter space overlaps we find that the tidal radius estimated from the SCM results and predicted by the MSC compare well with the Read radius. In this region by checking the tidal radius results from the SCM and predicted by the MSC against the Read radius we have effectively checked them against N-body simulations. This means that we can use our results from the SCM and the MSC to extrapolate to higher galactic periods.

Comparisons between the fraction of escaping stars seen in numerical results of the SCM and the predicted transition from unstable to stable orbits from the MSC are made in Section 5.3. The fraction of escaping stars over time and the MSC predictions are also used to examine the tidal radii for a range of eccentricities and perigalacticon distances for globular clusters in this section. It is found that the tidal radii predicted by the MSC are consistent with the Read radius values and with tidal radii estimated from the SCM.

These results are summarised and discussed in Section 5.4 emphasising the tidal radii predictions based on the MSC and their comparison to existing theoretical determinations. An extension of this work on the tidal radius into the domain of clusters on extremely long galactic periods is discussed in Chapter 7 in the context of capturing dwarf spheroidal galaxies into orbits bound to the Milky Way.

5.1 Derivation of the simplified cluster model

The aim of this section is to develop a simplified cluster model that adequately reproduces the behaviour of escaping stars as a function of their initial binding energy from clusters with large galactic orbital periods. Ideally this model will be as close to an N-body simulation as possible, without including the mutual interaction between particles. In particular, this model will retain a form of mixing in the inner regions of the cluster due to the movement of the core particle, see below. This model can then be used as a mid way point between the stability of the three-body problem discussed in Chapter 4 and direct N-body simulations.

The SCM consists of two parts: a core and a system of equal mass halo particles. The core particle moves in response to the halo particles and the galaxy. The particle is associated with the centre of the Plummer potential given by Equation (3.5). The halo particles move in response to the Plummer potential whose centre coincides with the position of the core particle and to the galaxy, itself modelled by a point mass. A schematic diagram of the system is shown in Figure 5.1 for a core particle of scaled mass f, a galaxy particle of scaled mass q, and a halo particle of scaled mass m_i.

The time-step used to resolve the system is taken as approximately a tenth of the smallest orbital period in the system, which is the orbital period of the innermost halo particle. The choice of a tenth here is to allow for the high eccentricities of orbits in the Plummer potential (Figure 3.4 shows the eccentricity distribution) and is found to be adequate for the Bulirsch-Stoer numerical integrator used here. The errors for the integrator are monitored and do not exceed one part in 10^{14} and 10^{13} per time-step for the total energy and angular momentum respectively.

The core is assigned a fraction f of the total mass of the cluster M_C, therefore each halo particle has the mass $m_i = (1 - f)/N$. A core fraction of $f = 0.5$ is chosen to ensure that halo orbits at the half mass of the cluster are included. Recall from Section 3.1 that the half mass

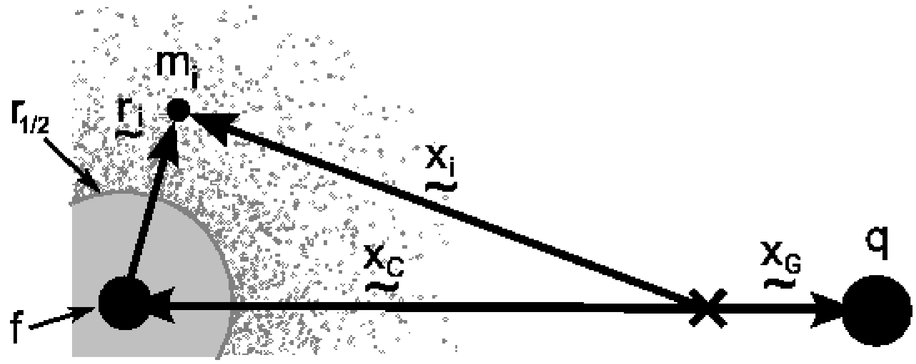

Figure 5.1: Schematic diagram of the simplified cluster model (SCM). The model consists of a cluster core particle of mass f, a galaxy particle of mass q, and N halo particles of mass m_i, of which one is shown. The masses in this figure are scaled such that the core is half the total initial mass of the cluster. The grey region denotes the inner region of the cluster of mass f which has been replaced by the core particle, while the grey points are the N halo particles which model the outer regions of the cluster.

radius is given in terms of the characteristic length of the cluster by Equation (3.9) for the scaling adopted here. Therefore the radius of the core will depend on the cluster compactness parameter b, but will always be equal to the half-mass radius of the cluster (shown as $r_{1/2}$ in Figure 5.1). The core fraction of $f = 0.5$ is consistent with findings by Giersz and Heggie (1994) indicating that the velocity distribution inside the half mass radius remains isotropic and therefore does not need to be resolved by individual particles.

To ensure that the equations of motion describing the system conserve energy they are derived from the Lagrangian of the system. The Lagrangian (L) is related to the total energy of the system (E) by

$$L = T - U \qquad\qquad E = T + U \tag{5.1}$$

where T and U are the total kinetic and potential energies of the system respectively. Recall that the particle masses are scaled by the total cluster mass M_C (Section 3.1), the total system consists of a cluster of N halo particles of mass $m_i = (1-f)/N$, a cluster core of mass f and a galaxy particle of mass $q = M_G/M_C$. This system has kinetic and potential energies given by

$$T = \sum_{i=1}^{N} \frac{1}{2} m_i \dot{\mathbf{x}}_\mathbf{i}.\dot{\mathbf{x}}_\mathbf{i} + \frac{1}{2} f \dot{\mathbf{x}}_\mathbf{c}.\dot{\mathbf{x}}_\mathbf{c} + \frac{1}{2} q \dot{\mathbf{x}}_\mathbf{g}.\dot{\mathbf{x}}_\mathbf{g} \tag{5.2}$$

$$U = -\sum_{i=1}^{N} m_i \frac{1}{\sqrt{b^2 + r_i^2}} - \sum_{i=1}^{N} \frac{m_i q}{|\mathbf{x_g} - \mathbf{x_i}|} - \frac{fq}{|\mathbf{x_c} - \mathbf{x_i}|} \tag{5.3}$$

with $\mathbf{x_g}$, $\mathbf{x_c}$ and $\mathbf{x_i}$ denoting the coordinates of the galaxy particle, cluster core particle and an individual halo particle i with respect to the centre of mass of entire system, as shown in Figure 5.1. The short hand of $\mathbf{r_i} = \mathbf{x_i} - \mathbf{x_c}$ and its magnitude r_i are used extensively throughout this chapter.

The equations of motion for each particle are derived using Euler-Lagrange's equation with no external forces (Goldstein 1959)

$$\frac{d}{dt}\left(\frac{\partial L}{\partial \dot{q}_j}\right) - \frac{\partial L}{\partial q_j} = 0 \tag{5.4}$$

where q_j and $\dot{q}_j$ denote a single position and velocity coordinate for any specified particle respectively. Solving these equations for each position coordinate of the halo, core and galaxy particles yields the corresponding equation of motion. For the cluster halo particle the equations of motion can be written as

$$\ddot{\mathbf{x}}_\mathbf{i} = \frac{q\left(\mathbf{x_g} - \mathbf{x_i}\right)}{\left|\mathbf{x_g} - \mathbf{x_i}\right|^3} - \frac{\mathbf{x_i} - \mathbf{x_c}}{\left(b^2 + r_i^2\right)^{3/2}}. \tag{5.5}$$

The equations of motion for the cluster core particle are

$$\ddot{\mathbf{x}}_\mathbf{c} = \frac{q\left(\mathbf{x_g} - \mathbf{x_c}\right)}{\left|\mathbf{x_g} - \mathbf{x_c}\right|^3} + \sum_{i=1}^{N} \frac{m_i\left(\mathbf{x_i} - \mathbf{x_c}\right)}{\left|\mathbf{x_i} - \mathbf{x_c}\right|^3} \tag{5.6}$$

and for the galaxy particle

$$\ddot{\mathbf{x}}_\mathbf{g} = -\sum_{i=1}^{N} \frac{m_i\left(\mathbf{x_g} - \mathbf{x_i}\right)}{\left|\mathbf{x_g} - \mathbf{x_i}\right|^3} - \frac{f\left(\mathbf{x_g} - \mathbf{x_c}\right)}{\left|\mathbf{x_g} - \mathbf{x_c}\right|^3}. \tag{5.7}$$

The binding energy of a particle relative to the cluster centre, specified by the core particle, is given by

$$E_i = \frac{1}{2} m_i \dot{\mathbf{x}}_\mathbf{i}.\dot{\mathbf{x}}_\mathbf{i} - \frac{1}{\sqrt{b^2 + r_i^2}} \tag{5.8}$$

with the initial binding energy of particle i is denoted by $E_0 \equiv E_i(t = 0)$.

Recall that the aim of this model is to be as physically meaningful as possible without including the mutual interaction between particles. The SCM described by Equation (5.5)-(5.7) achieves this by having the halo particles only respond to the galaxy particle and the core particle, which is used as the centre of the Plummer potential. The centre of the Plummer potential moves in response to the changing distribution of halo particles and the galactic potential (Equation 5.6). This configuration allows for feedback between the cluster potential as a whole and the halo particles.

The effect of the movement of the core in the central regions of the cluster is shown in Figure 5.2 for two cluster orbits with eccentricity $e_o = 0.5$ and perigalacticon distances $p_o = 500$ (left panels) and 1000 (right panels). The top panels of this figure show the energies of three particles, calculated by Equation (5.8), against the number of innermost particle orbits ($T_{1/2}$). The bottom panels show the movement of the core from its original position, after accounting for the orbit of the cluster with the galaxy. This distance is determined by

$$\mathbf{R_{core}} = \mathbf{x_c} - (1 - q)\mathbf{x_g}. \tag{5.9}$$

This distance quickly moves from zero once the simulation has started, which is not visible in Figures 5.2 (c) and (d). The peaks in $|\mathbf{R_{core}}|$ correspond to perigalacticon passages of the cluster, where the distribution of halo particles is at its most disturbed. For $p_o = 500$ (panel c) the cluster has lost enough mass for the core to be showing significant deviation from its initial position. This effect is not as clear for $p = 1000$ as there are some discontinuities visible as flat lines in the distance from the original cluster centre in Figure 5.2 (d).

The movement of the core causes the mixing of particles in the central cluster regions. This is clearly seen in Figure 5.2 (b) where the binding energies for two particles (shown as red and green curves) indicate that they are alternating with respect to which is the innermost particle. This mixing can result in particles initially close to the cluster centre migrating outwards to regions where they may escape the cluster, as indicated by the red curve in Figure 5.2 (a). For practical purposes the energy of the halo particles in the outermost regions of the cluster are unaffected by the movement of the core providing negligible mass has been loss, an example of this is the blue curve in Figure 5.2 b).

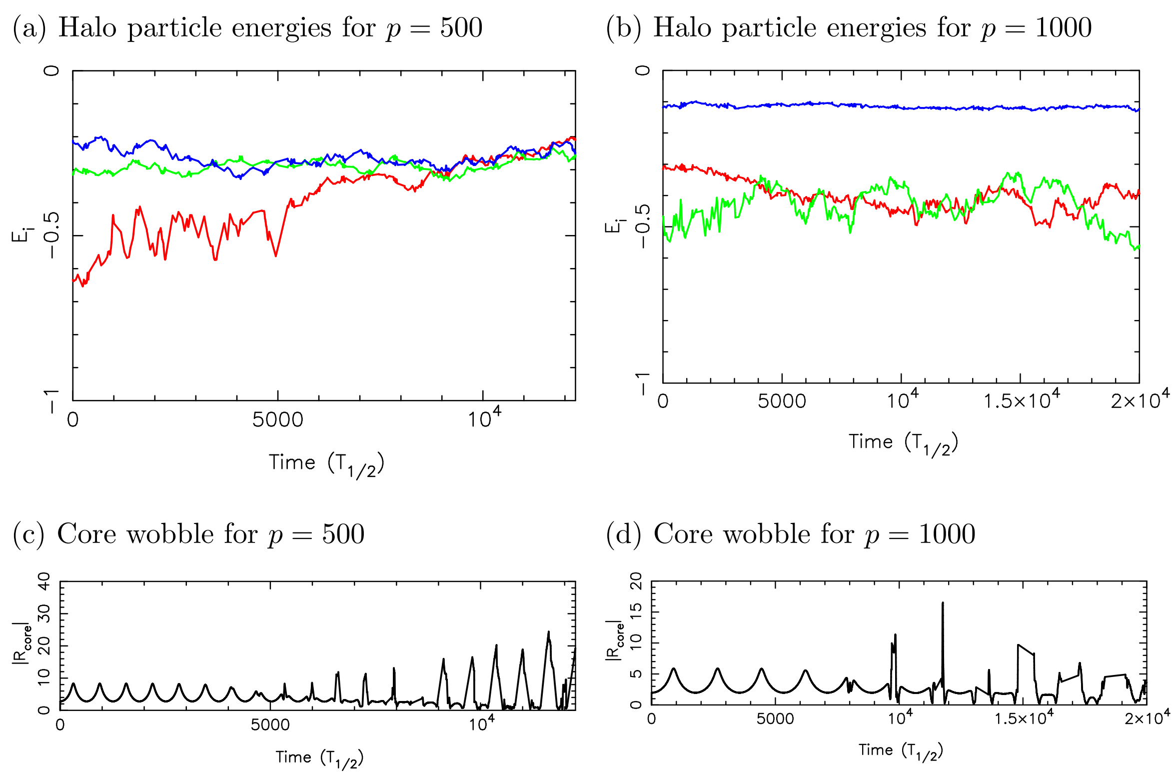

Figure 5.2: The effect of the movement of the core particle in the SCM is shown against time for two cluster orbits with eccentricity $e_o = 0.5$ and perigalacticon distances $p_o = 500$ (left panels) and 1000 (right panels). The top panels show the energies of three particles, calculated by Equation (5.8), against the number of innermost particle orbits ($T_{1/2}$). The bottom panels show the movement of the core from its original position (determined by Equation 5.9) against time. Note that the movement of the core has the least effect on the binding energies of halo particles at apogalacticon, which coincides with the throughs in bottom panels.

The galaxy particle also responds to changes in the distribution of halo particles, although this effect is infinitesimal. It sees the cluster as a system of point masses, with the effect of the core particle approximated by a point mass of mass f. This is justified even for the closest distance between the cluster and galaxy modelled in Section 5.3, since when $|\mathbf{x_g} - \mathbf{x_c}| >> b$ the Plummer potential reduces to the potential of a point mass (see Section 3.1).

Note that Equation (5.5) contains the implicit assumption that cluster does not lose mass over time. This assumption is reasonable as long as two conditions hold, namely that no significant mass loss occurs during the time span of interest and, that the distribution of particles in the inner regions of the cluster does not change much. The first of these is satisfied providing that not too many cluster orbits are followed. The second condition is essentially the Cowling approximation, which states that if the mass is centrally concentrated then variations in the density in the outer regions do not produce significant variations in the gravitational potential (Cowling 1941). This is the case provided that halo particles orbiting beyond the half mass radius of the cluster are the only ones that escape the cluster in significant numbers. This is found to be true for all numerical results found later in this chapter.

The halo particles are initially distributed with positions and velocities specified relative to the cluster core particle following the procedure set out in Section 3.1. The initial positions for a cluster of $N = 10^4$ halo particles for cluster-galaxy orbit of eccentricity $e_o = 0.5$ and perigalacticon distance $R_P/R_C = 500$ is seen in Figure 3.2. The position vectors of the halo particles relative to the cluster core particle initially sum to the null vector, however this symmetry is quickly broken and the core particle wanders around the central regions of the cluster relative to its initial position. This occurs more at perigalacticon where the tidal forces are strongest.

The movement of the core is a problem when determining the binding energy of particles in the central regions of the cluster. Incorrect determinations of the cluster centre can lead to incorrect estimates for the cluster density and velocity dispersion (Read et al. 2006) and the same is true for the binding energy. N-body simulations overcome the problem of defining the centre of the cluster by procedures similar to the shrinking spheres method proposed by Power et al. (2003). Defining the cluster centre is not a problem for the SCM as we are already using the core particle as the centre for the cluster. To minimise the effect of the movement of the core particle (see Figure 5.2), the energies of the halo particles (Equation 5.8) are calculated at apogalacticon.

In order to estimate the tidal radius for the cluster of interest we will monitor the fraction of particles that escape as a function of their initial binding energy (E_0). This approach allows for comparison between the results from the SCM and the results from the N-body simulation in the next section and to theoretical estimates in Section 5.3.

The cluster is initially placed at apogalacticon so the tidal forces on the halo particles are weak at the beginning of the simulation. All particles are integrated using Equation (5.5)-(5.7) with the Bulirsch-Stoer method (Press et al. 1986) until 20 galactic orbital periods are completed or until all of the halo particles escape the cluster. The Fortran 77 computer code implementation of this problem was found to conserve the total energy and angular momentum to one part in 10^{14} and 10^{13} per time-step respectively. This accuracy is more than adequate for all of the cluster orbits examined. Considering clusters with periods longer than 500 Myr and the age of the galaxy as approximately 10 Gyr, then a maximum of 20 galactic orbits is chosen. Recall that the representative cluster orbit described in Section 2.5 has a period of approximately 1 Gyr, so would only complete 10 orbits in the lifetime of the galaxy.

Before comparing the results of the simple cluster model with the results of the stability analysis in Chapter 4 the model itself must be tested against a direct N-body simulation.

5.2 Validation of simplified cluster model against N-body results

In order to validate the simplified cluster model derived in the previous section, an N-body simulation of a cluster using the same density profile is required. N-body simulations have long been used as a benchmark for large-scale dynamical models, for example with Fokker-Planck simulations in Kim et al. (2008). As well as validating the simple cluster model, comparison with an N-body simulation will also allow us to test two assumptions used as the basis of the model. These are that ignoring two-body relaxation in the model does not significantly alter the behaviour of particles in the outer cluster regions, and that this behaviour is also not affected by using a core particle instead of explicitly modelling particle orbits in the inner regions of the cluster.

Comparison between the SCM and an N-body simulation has been made for a cluster-galaxy orbit of $e_o = 0.5$ and $p_o = 500$ with a mass ratio of the galaxy to the cluster of $q = 10^5$. Results from a direct N-body simulation using these parameters has been made available by Holger Baumgardt for a cluster composed of $N = 50000$ equal mass particles in a Plummer potential of compactness $b = 0.45$ for two galactic orbits. Recall that we are using $N = 10000$ particles to model the outer 50% by mass of a globular cluster with the intention of extending the parameter space to high eccentricities (up to $e_o = 0.8$) and large perigalacticon distances ($p_o = 1000$) for 20 galactic orbits. For comparison Read et al. (2006) were able to complete 5 galactic orbits using an N-body simulation consisting of $N = 10^5$ particles for an orbit with eccentricity $e_o = 0.57$ and perigalacticon $R_P/R_{1/2} = 77$.

The model used by the N-body simulation consists $N = 50000$ particles initially distributed according to a Plummer density profile, refer to Section 3.1. Each particle moves in response to all other $N-1$ particles and to the galaxy, which is modelled as a point mass of q times the total mass of the cluster. This simulation used the NBODY6++ code (Spurzem and Baumgardt 2003), which is a massively parallel variant of NBODY6 (Aarseth 2007).

To allow for comparison with the escaping fraction of stars of a given binding energy used later with the SCM, the initial potential energy distribution for the particles in the N-body simulation needs to be matched to a particular compactness parameter b in the Plummer model. For the N-body cluster the initial conditions were consistent with a Plummer potential of compactness parameter $b = 0.45$ when the N-body units were converted to our scaled units.

Note that to directly compare the potential energy and radius between simulations, the length, mass and time scaling must be in the same units. To convert N-body units used in the cluster results supplied by Holger Baumgardt, three pieces of information concerning the physical cluster and common to both models are used[1]. The first common point between the SCM and the N-body model is that the total mass of the cluster components is unity. The second is that the minium binding energy of a particle in a Plummer sphere of compactness parameter $b = 0.45$ is given by $E_i = -1/b = -2.22$ in our units (for detailed of the scaling used by the SCM see Section 3.1). The minimum value for the binding energy for a particle in the Plummer sphere is found by putting the position (r_i) and velocity ($\mathbf{\dot{x}_i}.\mathbf{\dot{x}_i}$) to zero in Equation (5.8). The third point of comparison is that the half-mass radius for the particle distribution between the N-body cluster and the SCM should be equal for $b = 0.45$. Using these three points all velocities and positions for the N-body particles are converted into the scaled units used by the SCM, therefore all comparisons will be conducted in units of our model.

The potential as a function of radius is shown for a randomly selected sample of 1000 N-body particles in Figure 5.3 (a), along with the Plummer potential given by Equation (3.5) with $b = 0.45$. The residuals for the particles compared to the Plummer potential are shown in Figure 5.3 (b).

(a) Potential energy of cluster components (b) Residuals

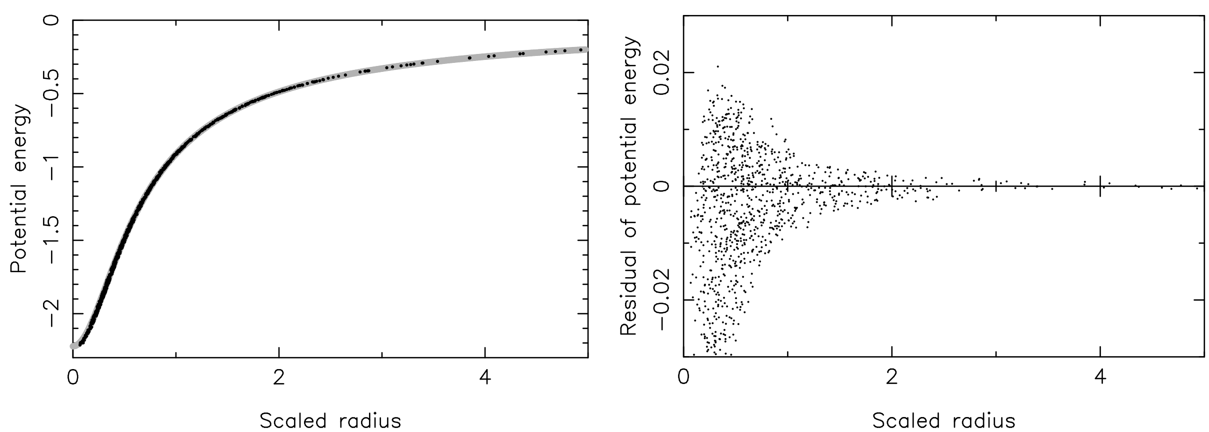

Figure 5.3: Initial potential energies of particles in an N-body simulation (dots) compared to the Plummer model with $b = 0.45$ (grey line). The potential energy against radius in scaled units is shown in panel (a), while panel (b) shows the residual between the Plummer potential with $b = 0.45$ and the N-body particle potentials.

In addition to the potential energy of particles from the N-body simulation results, we can derive the eccentricity and binding energy distributions from the position and velocity vectors. This is done using the position $\mathbf{r_i}$ and velocity $\mathbf{v_i}$ for each particle i measured relative to the cluster centre in either the N-body or the SCM clusters and integrating the motion of each particle in the absence of the galaxy. This is the same method used in Section 3.2, but with the initial particle position and velocity set using the cluster at a particular snap shot in time.

The binding energy (E_i) and eccentricity e_i distributions for all cluster particles are shown

[1]For a detailed description of how the physical quantities in this N-body simulation are scaled the reader is referred to Baumgardt (2001).

as red curves in Figure 5.4 (a) and (b) respectively. The time evolution of these distributions is indicated by the colour with red, green and blue curves indicating the distributions after 0, 1 and 2 galactic orbits. Both of these panels in Figure 5.4 show the distributions of particles in the N-body cluster as dashed lines and in our model of the cluster as solid lines. All distributions in Figure 5.4 are normalised using the peak values in the distributions to allow direct comparison between cluster models.

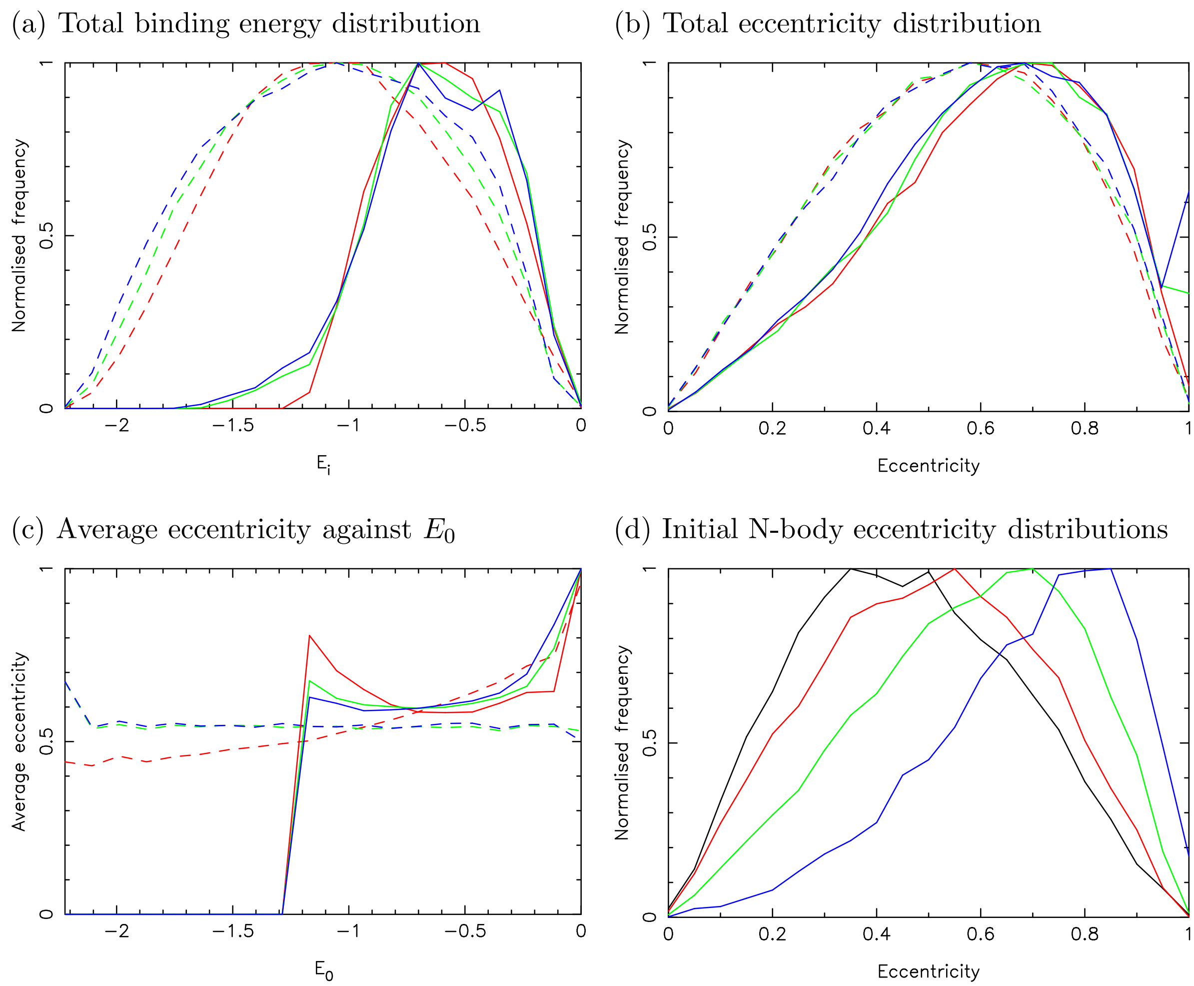

Figure 5.4: Normalised distributions for the binding energy and orbital eccentricity of particles in the N-body and simplified cluster models. Binding energy and eccentricity distributions for all cluster particles are shown in panels (a) and (b) respectively against time. The mean orbital eccentricity against the initial binding energy $E_0 \equiv E_i(t = 0)$ for particles of both models is shown in panel (c). For panels (a), (b) and (c) N-body particles (dashed lines) and SCM particles (solid lines) are shown initially (red), and after one (green) and two (blue) apogalacticon passages. The initial eccentricity distribution for particles in the N-body cluster, as broken down by binding energy, is shown in panel (d). The binding energy groupings used in panel (d) are $E_0 < -1.5$ (shown as the black curve), $-1.5 < E_0 < -1.0$ (red), $-1.0 < E_0 < -0.5$ (green) and $-0.5 < E_0 < 0.0$ (blue).

Figure Figure 5.4 (a) shows the binding energy of particles in the N-body cluster is distributed across the total possible range of $-1/b \leq E_0 < 0$ with a peak at $E_0 \approx -1.1$. The binding energies for the SCM particles has a minimum of $E_0 = -1.35$, which is the energy associated with the Plummer potential of compactness $b = 0.45$ at the half-mass radius in scaled units ($R_{1/2} = 0.59$ by Equation 3.9). This energy cut-off in the SCM exists because no particle orbits are simulated inside the half-mass radius and the inner cluster regions are instead modelled by a core particle. Since the innermost particle is specified by radius and not its binding energy then there is not a sharp cut-off in the energy seen in Figure 5.4 (a).

We later use the initial binding energy E_0 to discuss results for escaping stars from both the SCM and N-body models. To give a sense of the mass fraction associated with initial binding energy ranges for the distribution shown in Figure 5.4 (a) the following numbers are useful. The fraction of the total cluster mass distributed across particles with $E_0 > -0.2$ is 1.91% for the N-body model and 5.53% for the SCM. For particles with $E_0 > -0.1$ the mass fractions are 0.47% and 0.60% for the N-body and SCM clusters respectively. Note that a mass fraction of 1% is equivalent to 100 particles for the SCM and 500 particles for the N-body simulation.

The initial eccentricity distributions for particles in a Plummer potential are shown in Figure 5.4 (b) for positions and velocities given by the N-body simulation (dashed red lines) and the SCM (solid red lines). Note that the eccentricity distribution for the N-body particles is similar to the eccentricity distribution for the cluster with compactness parameter $b = 1$ shown previously in Figure 3.4. The bias towards high eccentricities seen in the eccentricity distribution of the SCM relative to the N-body results can be understood by considering the average eccentricity as a function of the initial binding energy for the N-body cluster particles, shown as a dashed red line in Figure 5.4 (c).

The dependence of the initial eccentricity distribution on the binding energy for N-body cluster particles is shown in greater detail in Figure 5.4 (d). This figure shows the initial eccentricity distribution binned by the initial binding energy using the ranges $E_0 < -1.5$ (black curve), $-1.5 < E_0 < -1.0$ (red), $-1.0 < E_0 < -0.5$ (green) and $-0.5 < E_0 < 0.0$ (blue). The initial binding energies of particles in the SCM are restricted to $E_0 > -1.35$ as a result of the core particle approximation for the inner 50% of the cluster mass. Therefore the distribution of eccentricities for the SCM is expected to be closest to the N-body distributions for $-1.0 \approx E_0 < 0.0$, i.e. the green and blue curves in Figure 5.4 (d). Comparison to Figure 5.4 (b) confirms that the the SCM and N-body simulations have similar eccentricity distributions when the distribution of binding energy (panel a) for the SCM is allowed for.

Further discussion of the binding energy and eccentricity distributions as they evolve over time is delayed until the results for escaping stars from both models are discussed. Recall that it is the tidal radii of globular clusters that is of interest in this study, thus the number of escaping stars will be compared between the models.

A star is defined as escaping the cluster if its binding energy is positive, measured when the cluster is at apogalacticon by Equation (5.8). The behaviour of escaping stars is examined for both models, which focuses on the escape of stars as a function of their initial binding energy. Figure 5.5 shows the fraction of escaping stars as a function of their initial binding energy binned into equal increments for the N-body model and the SCM after one (top panels) and two (bottom panels) cluster-galaxy orbits. The solid vertical lines in Figure 5.5 denote the lowest initial binding energy bin E_S where at least 90% of the particles have escaped the cluster. This value gives an estimate of the tidal radius, and the evolution of E_S over time provides a point of comparison between the cluster models.

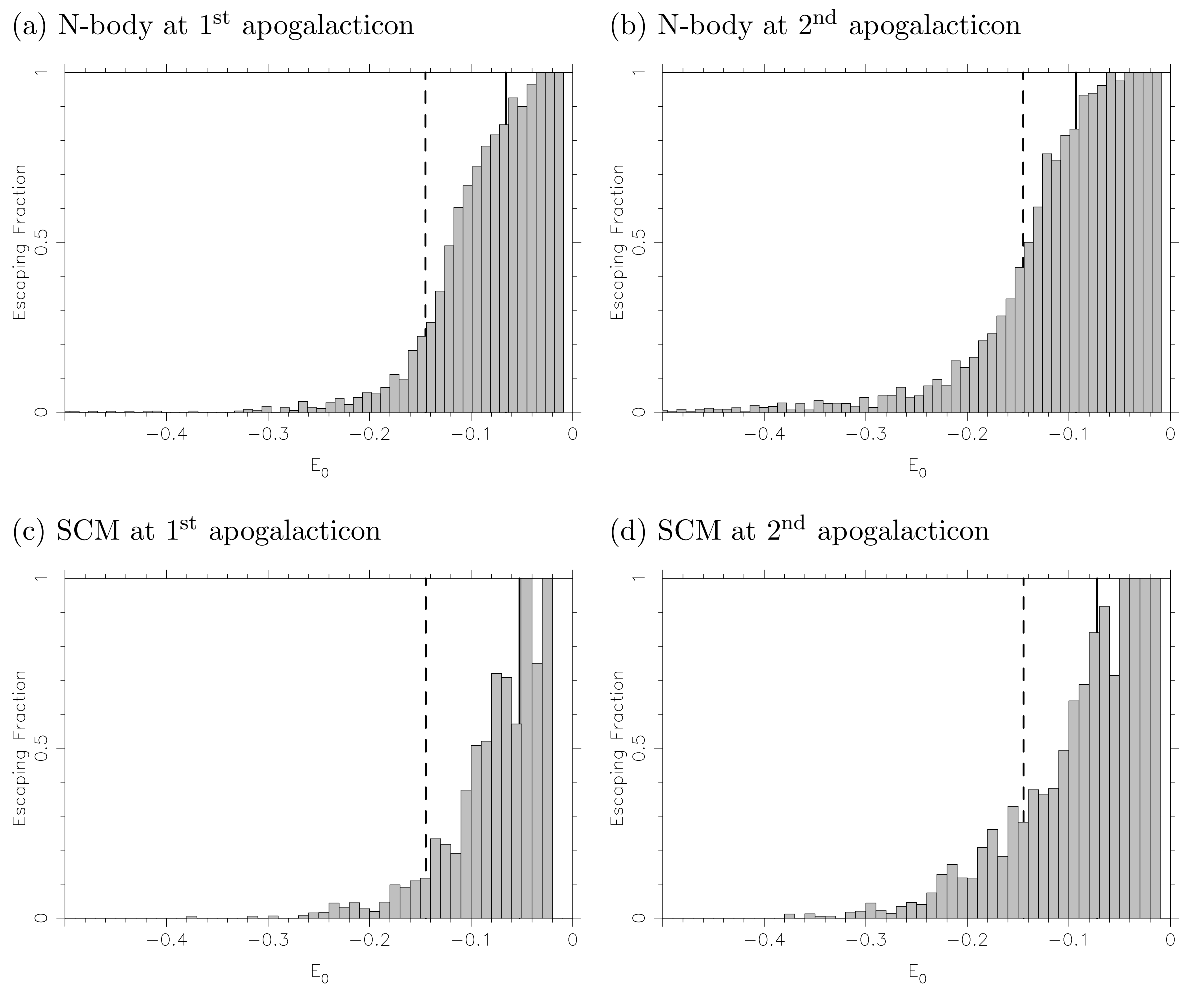

Figure 5.5: The fraction of stars escaping a cluster as a function of the initial binding energy (E_0) after the cluster has completed one (left panels) and two (right panels) apogalacticon passages. Results from N-body simulations and the SCM are shown in the top and bottom panels respectively. The dashed vertical line represents the boundary between stable and unstable orbits E_U predicted using the MSC. The solid vertical line indicates the binding energy associated with an escaping fraction of 90% (E_S) from the cluster simulation. The mass fraction of particles with $E_0 > E_S$ is given in Table 5.1 for both cluster models.

The dashed lines in Figure 5.5 indicate a characteristic binding energy representing the transition from unstable to stable orbits. This binding energy value is an estimate for the tidal radius of a cluster, as predicted by the MSC in Chapter 4. It is determined from the orbital period of the cluster-galaxy orbit and by using the relation between the period and binding energy for a particle-cluster orbit (Equation 3.22).

Recall that Equation (4.14) used the period of the cluster-galaxy orbit to determine the

Model	Time (t/T_o)	E_S	$M(E_0 > E_S)$
N-body	1	-0.066	0.21%
	2	-0.093	0.41%
SCM	1	-0.052	0.17%
	2	-0.072	0.28%

Table 5.1: The initial binding energy associated with an escaping fraction of 90% (E_S) after one and two galactic orbits (with period T_o), for both cluster simulations. Column 4 shows the mass fraction of particles with initial binding energies $E_0 > E_S$, referred to as $M(E_0 > E_S)$, as determined from the distribution shown in Figure 5.4 (a). A mass fraction of 0.1% is equivalent to 10 particles for the SCM and 50 particles for the N-body cluster simulation.

period of the particle-cluster orbit as

$$T_{fit} = \frac{2\pi}{\sigma_u(e_o)} (1+q)^{-1/2} \left(\frac{p_o}{1-e_o}\right)^{3/2}, \tag{5.10}$$

where $\sigma_u(e_o)$ is the representative value for characterising the transition from unstable to stable orbits, predicted by the MSC and defined in Section 4.1.1 for a cluster with galactic orbital eccentricity e_o. The dependence of σ_u on e_o was shown in Figure 4.4 (a), and was seen in Figure 4.8 to be accurate for describing the stability of particles in a Plummer sphere for moderate eccentricities ($e_o \lesssim 0.8$).

The binding energy associated with σ_u for a cluster-galaxy orbit with $p_o = 500$ and $e_o = 0.5$ is given by $E_U = -0.145$, using Equation (3.22) to convert the particle-cluster period given by Equation (5.10) into an estimate for the binding energy. The binding energy E_U marks the transition from unstable to stable orbits and physically means that stars with initial energies of $E_0 > E_U$ are expected to be unstable to escape from the cluster. This value of E_U is used as a estimate of the cluster tidal radius in this section since the relation used to convert the particle-cluster period to a binding energy (Equation 3.22) was determined for a cluster with compactness $b = 1$, not $b = 0.45$ used here.

From Figure 5.5 some stars with initial binding energies $E_0 < E_U$ are seen to escape the cluster for the N-body (top panels) and the SCM (bottom) cluster simulations. This may be due to the small number of particles escaping after each period of the cluster-galaxy orbit T_o, as demonstrated in Table 5.1. The fraction of the total cluster mass associated with initial binding energies greater than the characteristic energy E_S is shown in column 4 as $M(E_0 > E_S)$. These mass fractions never exceed 0.5% and indicate a small statistical sample when we recall that a mass fraction of 0.1% is equivalent to 10 particles for the SCM and 50 particles for the N-body cluster simulation.

The two assumptions used as a basis for the SCM can now be tested. These were that ignoring two-body relaxation and using the core particle to simplify the inner regions of the cluster does not affect the outer regions where particles escape the cluster.

We will firstly deal with the more straightforward of these assumptions, which is that using a core particle has negligible effect on the escape of particles from the outer regions of the cluster.

This can be demonstrated by the following simple argument. For a cluster with compactness parameter $b = 0.45$, the half mass radius in units of R_C is ≈ 0.59 which is equivalent to a binding energy of $E_{1/2} \approx -1.35$ using Equation (3.22). As seen in Figure 5.5, $E_{1/2}$ occurs far below the initial binding energies associated with any significant fraction of escaping particles. Therefore the assumption that using a core particle to model the inner 50% by mass of the cluster has little effect on the outer regions of the cluster is valid. Note that this argument also applies to a cluster of compactness parameter $b = 1$, which used in the next section, the relevant values being $R_{1/2} \approx 1.30 R_C$ and $E_{1/2} \approx -0.61$.

By removing the inner half of the cluster, the core particle significantly alters the eccentricity of tightly bound particle orbits. This produces a peak in eccentricity at $E_0 \approx -1.0$, as seen in the mean eccentricity as a function of the initial binding energy (Figure 5.4 c). This peak is the result of removing particles from the inner regions of the cluster using their distance from the centre, rather than their binding energies. This can be understood by considering a particle initially at apocentre relative to the cluster centre with its radius at the half-mass radius. This particle will have a high eccentricity and semi-major axis less than the half-mass radius; therefore it will have an initial binding energy lower than a circular orbit at the same radius. This results in particles orbits with low binding energy having higher than average eccentricities. The effect of the core particle increasing the mean orbital eccentricity of cluster halo particles is seen to be negligible for $E_0 \gtrsim -0.5$. Once again we can conclude that the core particle does not affect the orbits of particles in the outer regions of the cluster.

We now test the second assumption made by the SCM, which is that ignoring two-body relaxation does not affect particles that eventually escape the cluster. The theoretical relaxation timescale as a function of radius can be determined using the half-mass relaxation timescale (Equation 2.1) and using the radial dependence of this timescale of $R^{1/2}$, found for the Plummer model in Section 2.2. It is more useful for our study of the fraction of escaping stars (Figure 5.5) to discuss the initial binding energies of particles, rather than their radii. A plot of the initial binding energy against radius is shown for the N-body cluster in Figure 5.6 (a) as a reminder of the relationship between these quantities for particles in a Plummer potential. The minimum binding energy E_{min} as a function of radius for a particle in a Plummer potential is found be setting the velocity to zero in Equation (5.8). This minimum energy is indicated as a grey curve in Figure 5.6 (a) and is used to determine the relaxation timescale as a function of binding energy.

Rearranging Equation (5.8) for r allows us to plot the relaxation time as a function of the minimum energy E_{min} in Figure 5.6 (b). The relaxation time in this figure is shown in units of the galactic orbital period of the cluster (T_{GC}). From Figure 5.6 (b) it is concluded that after two galactic orbits two-body relaxation is only effective at redistributing energy between particles with binding energies $E_0 \lesssim -0.5$. This is an important result for interpreting the differences seen between models in Figure 5.5, since it means that stars with initial binding energies satisifying $E_0 < -0.4$ can migrate out to regions where they can escape the cluster. However, the mixing of particles due to two-body relaxation cannot explain the difference between the models seen

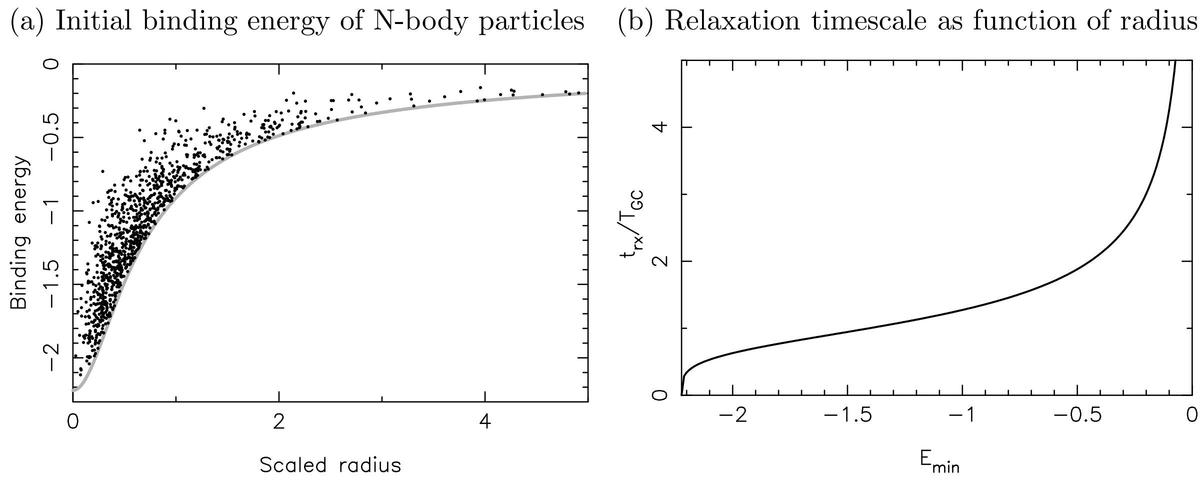

Figure 5.6: Initial binding energy against radial distance from the cluster centre for 1000 randomly selected particles from the N-body cluster (left panel). The minimum possible binding energy E_{min} as a function of radius is indicated as a grey curve in this plot and is the Plummer potential with $b = 0.45$, shown previously in Figure 5.3. The relaxation timescale (t_{rx}) in units of the cluster-galaxy orbital period (T_{GC}) is shown against E_{min} in the right panel, as determined using the procedure described in text. The minimum binding energy is given by $-1/b$ and the initial binding energy associated with a circular orbit at the half mass radius is $E_i(t = 0) = -1.35$. Note that $t_{rx}/T_{GC} = 2$ for a minium binding energy of $E_{min} \approx -0.5$.

for escaping stars with $E_0 > -0.2$.

From Figure 5.5 the fraction of escaping stars in the SCM is consistently less than the escaping fraction in the N-body model for $E_0 > -0.2$. This discrepancy also causes the binding energy associated with 90% of particles escaping the cluster, E_S, to be lower for the N-body model than that for the SCM (as seen in Table 5.1). Both two-body relaxation and the influence of the core particle have already been shown to be ineffective in this binding energy range (see Figure 5.6 b), so an alternate explanation is sought.

Another possible explanation for why there are proportionately fewer stars escaping from the SCM than from the N-body model, is the difference in the average eccentricity for particles with $E_0 > -0.2$. From Figure 5.4 (c), the average eccentricity is much higher in this energy range for the SCM particle orbits than for the N-body particle orbits. However, this difference is actually an artefact of how the N-body simulation deals with particles that escape the cluster. Such particles are removed from the N-body cluster over time to reduce the number of operations needed per time-step. The eccentricity information of these particles is then lost after $t = 0$, although they are still counted as having escaped from the cluster, so the fraction of escaping stars results presented in Figure 5.5 is unaffected. It has been pointed out by Fukushige and Heggie (2000) that stars with energies greater than zero can remain bound to the cluster for many cluster-galaxy orbits. By instantly removing such particles they are not given the chance to rejoin the cluster and therefore reduce the computed fraction of escaping stars.

This effect is amplified when we consider the low number of particles in the outer regions of the cluster. The initial distribution of particles as a function of the initial binding energy is shown in Figure 5.4 (a). For $E_0 > -0.2$ this is equivalent to 553 and 955 particles in the SCM and N-body simulations respectively, and for $E_0 > -0.1$ the particle numbers become 60 and 235. For comparison the number of particles removed during the N-body simulation is 711 after the first cluster orbit and an additional 468 after the second cluster orbit. This makes a total of 1179 particles removed from the entire cluster ($E_0 < 0$), out of the original 50000, over the two cluster-galaxy orbits modelled here.

Very similar results are obtained for the escape of stars in the outer regions of the cluster between the SCM and the N-body cluster model. The small discrepancies in the fraction of escaping stars in the outer regions are likely to be caused by either small N statistics or by the removal of escaping stars from the N-body cluster. The overall similarity between these cluster models is typified by the results for E_S shown in Table 5.1. Therefore the SCM is assumed to be suitable for simulating the dynamical evolution of particle orbits in the outer regions of the cluster.

5.3 The application of the stability criterion to simulated clusters

In the previous section the fraction of escaping stars against the initial binding energy from the simplified cluster model were tested against the equivalent results for an N-body cluster simulation. It was shown for $p_o = 500$ and $e_o = 0.5$ that the method developed in Section 5.1 to model the escape of stars from a Plummer sphere was accurate for particles in the outer regions of the cluster. As we are interested in estimating the tidal radius of a cluster using the escape of stars in this region, it is assumed that the SCM is suitable for this purpose.

The SCM will now be used to examine the escape of particles from a cluster of compactness parameter $b = 1$ on a range of galactic orbits, specified by the perigalacticon distance $p_o = R_P/R_C$ and eccentricity e_o. This section will focus on comparing the predicted transition from unstable to stable orbits using the MSC, as summarised by E_U (previous section), to the initial binding energy E_0 of particles that escape from the SCM over time.

The initial distribution of binding energies and eccentricities for $N = 10^4$ particles orbiting in a Plummer potential with compactness $b = 1$ is shown in Figure 5.7. For clusters with large galactic orbital periods the distribution of particles is independent of p_o and e_o. The only qualifier to this is that the cluster is truncated using the King radius (Equation 2.4), which makes little difference since it is extremely rare for any particle to be near the truncation radius initially (see Section 3.1 for how the cluster is constructed).

From Figure 5.7 (a) the total number of particles with initial binding energies satisfying $E_0 > -0.2$ is 2917 and for $E_0 > -0.1$ is 607 particles. These mass fractions are higher than those for a $b = 0.45$ cluster (Figure 5.4 a), since the cluster mass is not as centrally condensed for a $b = 1$ cluster[2].

The behaviour of halo particles over time can be studied by considering the fraction of

[2]The reader is referred to Figure 3.1 for the dependence of the potential energies on b.

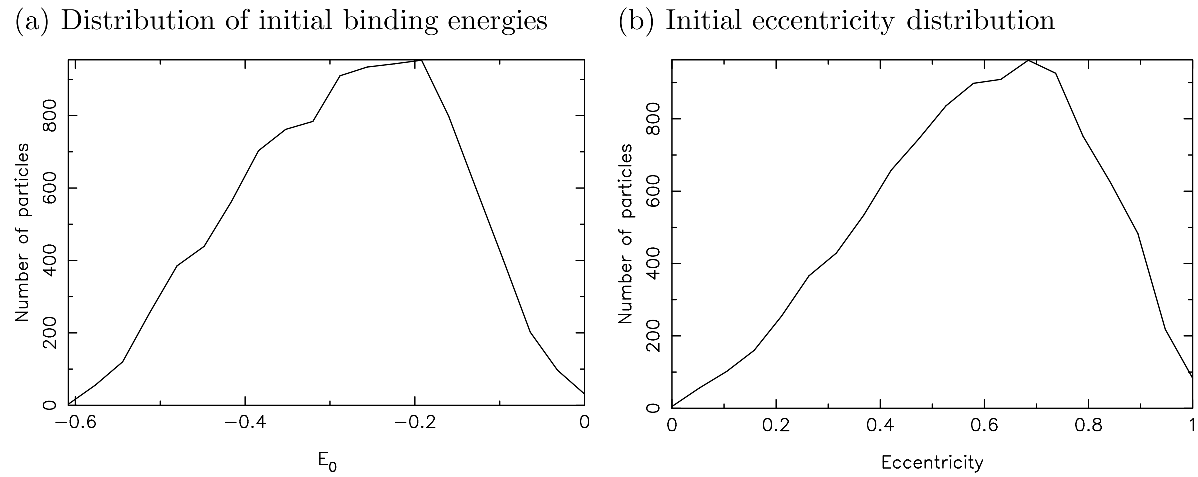

Figure 5.7: The initial binding energy (left panel) and eccentricity (right panel) distributions for $N = 10^4$ particle orbits in a Plummer potential with compactness parameter $b = 1$. Distributions are for a cluster simulated using the SCM with a core particle of 50% the total cluster mass. The total number of particles with initial binding energies satisfying $E_0 > -0.2$ is 2917 and for $E_0 > -0.1$ is 607 particles.

particles that escape from a given initial binding energy range. A particle is said to have escaped the cluster if its binding energy becomes positive when the cluster is at apogalacticon, where the binding energy is given by Equation (5.8). This method is detailed in the previous section in the context of comparing the N-body and SCM results.

The fraction of escaping particles against initial binding energy E_0 for a cluster in a galactic orbit with $e_o = 0.5$ and $p_o = 500$ is shown in Figure 5.8 (a)-(d) after 1, 2, 5 and 15 cluster orbits. Recall from Section 5.1 that the cluster is initially placed at apogalacticon, so the time at the 1$^{\text{st}}$ apogalacticon is equivalent one cluster-galaxy orbit.

Note that the gap in fraction of escaping stars at $E_0 \approx -0.04$ in Figure 5.8 is due to a lack of particles of that initial binding energy, see Figure 5.7 (a). The lowest initial binding energy associated with 90% of the simulated particles escaping the cluster, E_S, characterises the evolution of the halo particles over time, and is shown as the solid vertical lines in Figure 5.8. The transition from unstable to stable orbits as predicted by the MSC, E_U, is shown as the dashed vertical lines in Figure 5.8. The procedure for obtaining E_U from σ_u is described in the previous section. Briefly, σ_u is a function of the galactic orbital eccentricity e_o only (shown in Figure 4.4 a), and the perigalacticon distance effects E_U through the period of the cluster-galaxy orbit.

Figure 5.8 shows the time evolution for stellar orbits in the outer regions of a cluster with orbit $e_o = 0.5$ and $p_o = 500$ using the SCM. Similar results for the fraction of escaping stars are shown for $e_o = 0.2$ and 0.8 in Figure 5.9.

The effect of increasing e_o for a fixed p_o is that the total number of escaping stars increases and that these stars come from a range of initial binding energies E_0. Recall from the distribution of binding energies, shown in Figure 5.7, that the distribution does not depend on the cluster-galaxy orbit provided they are sufficiently wide, for example $p_o = 500$. The increase in the

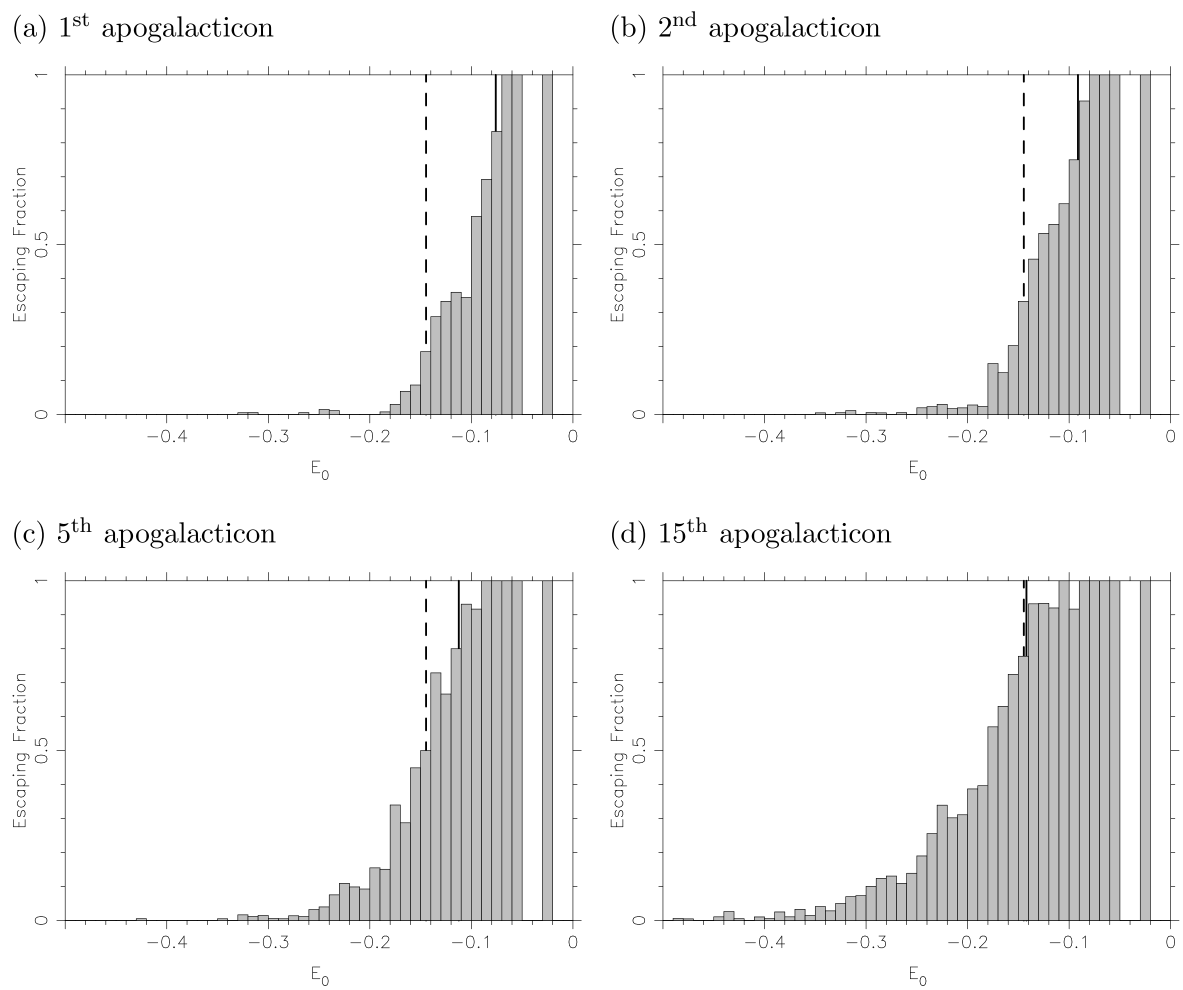

Figure 5.8: The fraction of escaping stars as a function of initial binding energy E_0 for $e_o = 0.5$ and $p_o = 500$, as simulated using the SCM. The solid line is the energy associated with an escaping fraction of 90% (E_S) and the dashed line represents the boundary between stable and unstable orbits (E_U) predicted using the MSC. Both of these values are used to estimate the tidal radius of a cluster. The binding energy E_U is determined using the period ratio $\sigma_u(e_o)$, which is the lowest σ value predicted by the MSC where the fraction of unstable orbits drops beneath 10%. The dependence of σ_u on the orbital eccentricity of the cluster-galaxy orbit is shown in Figure 4.4. This period ratio is then used in Equation (5.10) to obtain the equivalent orbital period of a particle in the cluster, which is converted into an equivalent binding energy E_U via Equation (3.22). The value for E_S is seen to converge to E_U after 15 galactic orbits, however this is misleading since E_S will continue to decrease as the cluster eventually loses all of its particles. Note that the gaps in these results reflect the lack of stars in the distribution for $E_0 \gtrsim -0.05$ (see Figure 5.7 a).

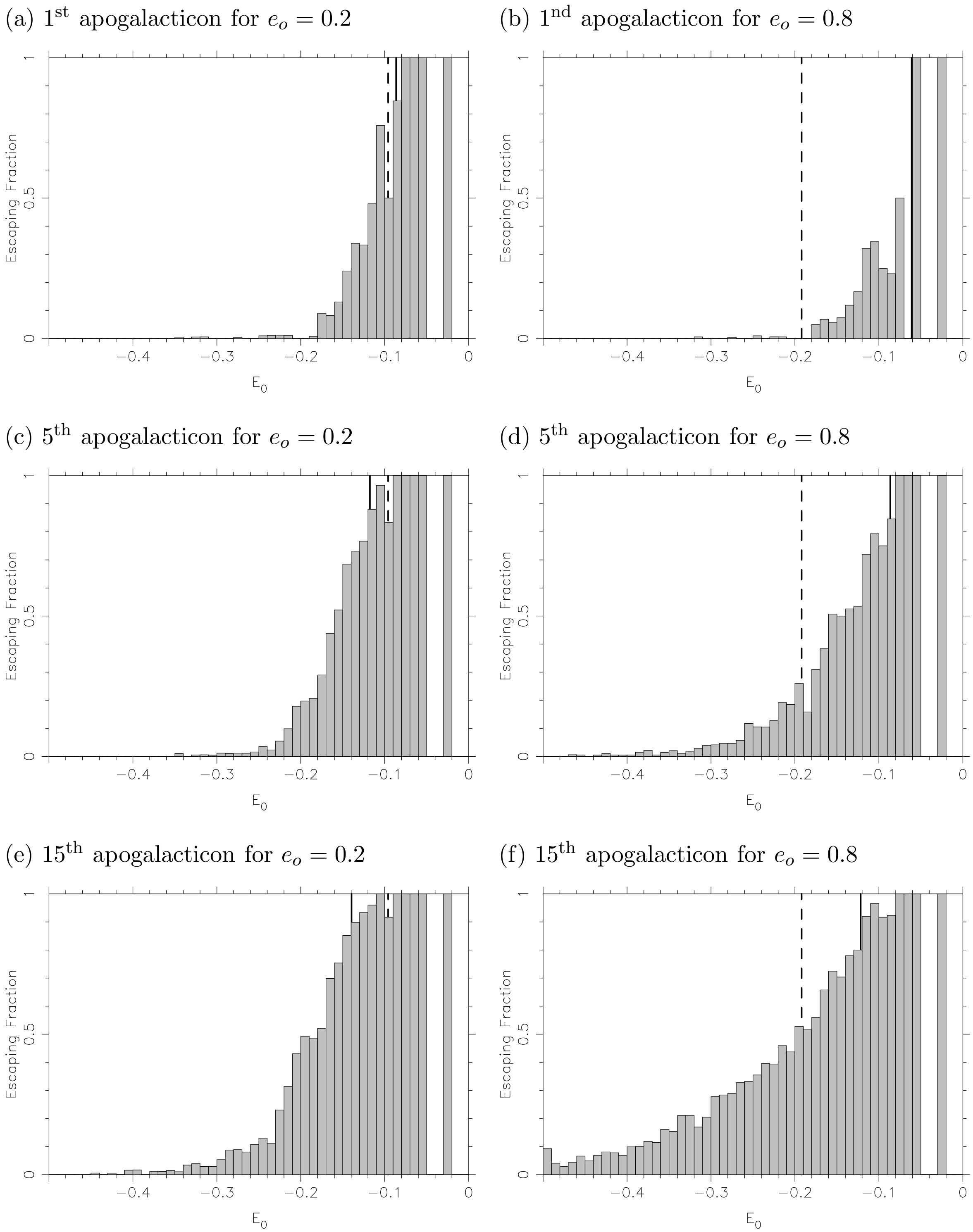

(a) 1$^{\text{st}}$ apogalacticon for $e_o = 0.2$

(b) 1$^{\text{nd}}$ apogalacticon for $e_o = 0.8$

(c) 5$^{\text{th}}$ apogalacticon for $e_o = 0.2$

(d) 5$^{\text{th}}$ apogalacticon for $e_o = 0.8$

(e) 15$^{\text{th}}$ apogalacticon for $e_o = 0.2$

(f) 15$^{\text{th}}$ apogalacticon for $e_o = 0.8$

Figure 5.9: The escaping fraction of stars against the initial binding energy E_0 for $p_o = 500$ with $e_o = 0.2$ (left panels) and $e_o = 0.8$ (right panels) using the SCM. As with Figure 5.8, the binding energies E_U and E_S are indicated by dashed and solid vertical lines respectively.

range of E_0 from which stars can escape is particularly evident when comparing the results for $e_o = 0.5$ (Figure 5.8 d) to $e_o = 0.8$ (Figure 5.9 f) after 15 cluster-galaxy orbits.

The MSC predicts that stars will eventually escape the cluster from a range of initial distances from the cluster centre. This is characterised by the minium and maximum period ratios $\sigma_{min/max}$, which are shown as a function of e_o in Figure 4.4 (a). Using the same method as for σ_u (described in Section 5.2) these period ratio can be converted into the corresponding range in the initial binding energy $E_{min/max}$. For a cluster on a galactic orbit of $p_o = 500$ and $e_o = 0.5$ the minimum and maximum binding energies associated with the transition from unstable to stable orbits are given by $E_{min} = -0.219$ and $E_{max} = -0.092$. This range of binding energies still falls short of explaining the range of E_0 for which stars are seen to escape the cluster in Figure 5.9 (f). As demonstrated in Section 5.1 and shown in Figure 5.2, it is possible that the movement of the core particle over time is causing particles initially on these orbits to move into particle-cluster orbits that are unstable to escape.

The distance that the core moves from its initial position increases as more particles are lost to the cluster. The magnitude of the cores movement depends on the number of perigalacticon passages, and also increases with the number of orbital periods that the innermost particle has completed in the cluster ($T_{1/2}$). After 15 galactic orbits the number of orbital periods that the innermost particle has completed is larger for the cluster with orbital eccentricity $e_o = 0.8$ than for $e_o = 0.5$ or $e_o = 0.3$ for a fixed pericentre distance. This means that more particles that were initially in the central regions of the cluster will reside in the outer regions due to the mixing caused by the movement of the core particle. This has been observed for a particle originally having a binding energy of $E_0 \approx -0.6$ moving out to a binding energy of $E_i \approx -0.3$ after $10^4 T_{1/2}$, refer to the red curve in Figure 5.2 (a). It is likely that since the cluster orbit with e_o is longer than $e_o = 0.5$ then the core particle will have had more of an effect on the halo particles, and therefore more particles will have escaped from lower initial binding energy orbits.

A parameter search across three values of the eccentricity ($e_o = 0.2$, 0.5 and 0.8) and nine of the perigalacticon distance ($p_o = 200$, 300, ..., 1000) of the galactic orbit of the cluster using the SCM has been conducted. The results are shown in Table 5.2 where the initial binding energy E_0 associated with an escaping fraction of 90% (E_S) after 1, 5 and 15 cluster orbits appear in columns 3-5. The binding energies associated with the transition from stable to unstable orbits predicted by the MSC for each orbit are shown in columns 6 and 7. The representative energy value E_U and the minimum binding energy E_{min} are determined from the σ dependence on e_o as shown in Figure 4.4 (a). The binding energy E_U is the estimate for the tidal radius of a globular cluster determined in Chapter 4, while E_{min} gives an indication of the error in this estimate. The final column in Table 5.2 shows the Read radius given by Equation (2.5) converted to a binding energy E_R using the fitting formulae Equations (3.23) and (3.22) (Section 3.3). Recall from Section 2.4 that the Read radius is an estimate of the tidal radius of a globular cluster based on analytic calculations for a particle orbiting a cluster at perigalacticon (Read et al. 2006).

From Table 5.2 the tidal radius estimates from the simulated cluster (E_S) and predicted

e_o	p_o	E_S ($1\times T_o$)	E_S ($5\times T_o$)	E_S ($15\times T_o$)	E_U	E_{min}	E_R
0.2	200	-0.269	-0.375	-0.403	-0.302	-0.385	-0.399
	300	-0.153	-0.231	-0.274	-0.187	-0.246	-0.251
	400	-0.104	-0.163	-0.179	-0.130	-0.173	-0.167
	500	-0.087	-0.118	-0.140	-0.096	-0.130	-0.117
	600	-0.088	-0.101	-0.112	-0.075	-0.102	-0.086
	700	-0.056	-0.085	-0.101	-0.060	-0.083	-0.065
	800	-0.055	-0.074	-0.077	-0.050	-0.069	-0.051
	900	-0.041	-0.071	-0.073	-0.042	-0.058	-0.041
	1000	-0.043	-0.045	-0.045	-0.036	-0.050	-0.034
0.5	200	-0.197	-0.353	-0.402	-0.419	-0.481	-0.420
	300	-0.126	-0.211	-0.271	-0.270	-0.315	-0.269
	400	-0.094	-0.142	-0.170	-0.192	-0.227	-0.181
	500	-0.076	-0.112	-0.142	-0.145	-0.172	-0.128
	600	-0.001	-0.098	-0.111	-0.114	-0.136	-0.094
	700	-0.053	-0.081	-0.095	-0.093	-0.111	-0.072
	800	-0.055	-0.074	-0.075	-0.077	-0.093	-0.057
	900	-0.044	-0.044	-0.074	-0.065	-0.079	-0.046
	1000	-0.041	-0.043	-0.056	-0.056	-0.068	-0.037
0.8	200	-0.234	-0.348	-0.386	-0.523	-0.581	-0.437
	300	-0.124	-0.183	-0.223	-0.346	-0.388	-0.285
	400	-0.052	-0.142	-0.154	-0.250	-0.284	-0.194
	500	-0.061	-0.087	-0.122	-0.192	-0.219	-0.138
	600	-0.001	-0.085	-0.088	-0.152	-0.175	-0.102
	700	-0.053	-0.056	-0.092	-0.125	-0.144	-0.078
	800	-0.051	-0.063	-0.066	-0.104	-0.121	-0.062
	900	-0.042	-0.055	-0.071	-0.089	-0.103	-0.050
	1000	-0.032	-0.042	-0.042	-0.077	-0.089	-0.041

Table 5.2: Tidal radius estimates expressed as the initial binding energy of a particle-cluster orbit from the SCM (E_S), predicted by the MSC (E_U and E_{min}) and using the theoretical estimate referred to as the Read radius (E_R). The results for the entire range of cluster-galaxy orbital eccentricities e_o and perigalacticon distances p_o are given. The tidal radius estimates from the simulated clusters are defined using the initial binding energies above which 90% of stars from the SCM become unbound from the cluster (E_S) after 1, 5, or 15 apogalacticon passages. The binding energy corresponding to the transition from mostly unstable to mostly stable orbits as predicted by the MSC is characterised by a maximum depth (i.e. minimum energy) that orbits can be unstable to escape from cluster (E_{min}) and the representative binding energy value E_U. The definitions of these energies are described in text and accompanying Figure 5.8. The final column shows the energy associated with the Read radius E_R given by Equation (2.5).

using the MSC (E_U) are in good agreement after 15 galactic orbits, particularly for $e_o = 0.5$ (see also Figure 5.8 d). This reflects the fact that the MSC predicts orbits to be unstable if they eventually escape the cluster via a random walk process. The discrepancy at low perigalacticon ($p_o \approx 200$) may be a result of the tidal radius being too close to the core radius for the SCM to simulate correctly, as discussed below. The E_U values are also in general agreement with the binding energy associated with the Read radius E_R. The advantage of applying the MSC to the problem of stars escaping a cluster in an eccentric galactic orbit is that it predicts a range of binding energies that allow stars to escape from the cluster. This is evident in the difference between E_U (column 6) and E_{min} (column 7), which itself reflects the behaviour of the transition of unstable to stable orbits as a function of e_o, shown in Figure 4.4 (a).

The validity of results for escaping stars in the SCM depend on having enough particles in the correct binding energy range to capture the behaviour of E_S over time. Correctly modelling the escape process using the SCM requires that two assumptions hold. Firstly the tidal radius of the cluster is sufficiently distant from the core radius, which is associated with the innermost particle orbit that is modelled by the SCM. Discussion of the core radius is returned to in the context of the time dependence of the tidal radius below. The second assumption is that very few particles escape which initially had binding energies close to the core particle. This requires that the binding energy associated with the removal of the inner 50% of the cluster be significantly less than the E_S values given in Table 5.2. Recall that for $b = 1$ the half mass radius in scaled units is $R_{1/2} \approx 1.30R_C$ and the associated binding energy is $E_{1/2} \approx -0.61$. The lowest initial binding energy associated with an escaping fraction of 90% after 15 apogalacticon passages was $E_S = -0.403$, which is significantly higher than $E_{1/2}$. However the time dependence of the tidal radius must now be examined before the core particle assumption can be validated.

The lowest energy associated with 90% of particles escaping the cluster, E_S, is seen to decrease over time in Table 5.2. Further investigation of the time evolution of E_S is shown in Figure 5.10 (a), for a representative sample of orbits given by $p_o = 200$ (solid lines), 500 (dashed) and 1000 (dotted) for $e_o = 0.2$ (red curves), $e_o = 0.5$ (green) and $e_o = 0.8$ (blue). The initial binding energies associated with a 90% escaping fraction, E_S, are converted to an equivalent tidal radius, R_T, using the fitting formulae Equations (3.23) and (3.22). The resulting tidal radii from the SCM are shown in Figure 5.10 (b) for the same orbital parameters as panel (a). Note that the occasional roughness in the data presented in Figure 5.10 is due to the small number of particles satisfying $E_0 > E_S$ (see Figure 5.7).

Figure 5.10 shows that E_S has settled to an approximate equilibrium value after 15 apogalacticon passages and can be compared with the tidal radius estimate using the MSC, E_U. Using Figure 5.10 (b) the discrepancy between the predicted E_U and the equilibrium values for E_S can now be understood. After 15 cluster-galaxy orbits the tidal radii for all clusters with perigalacticon $p_o = 200$ is given by $R_T \approx 2R_C$ while for comparison the half-mass radius for this cluster is $R_{1/2} = 1.3R_C$. Inspection of Figure 5.7 (a) shows that more than half of the halo particles (a quarter of the total cluster mass) have escaped the cluster for this radius (equivalent to $E_0 \approx -0.61$). This significant mass loss violates the basic assumptions upon which the SCM

(a) Initial binding energy associated with a 90% fraction of escaping particles against time

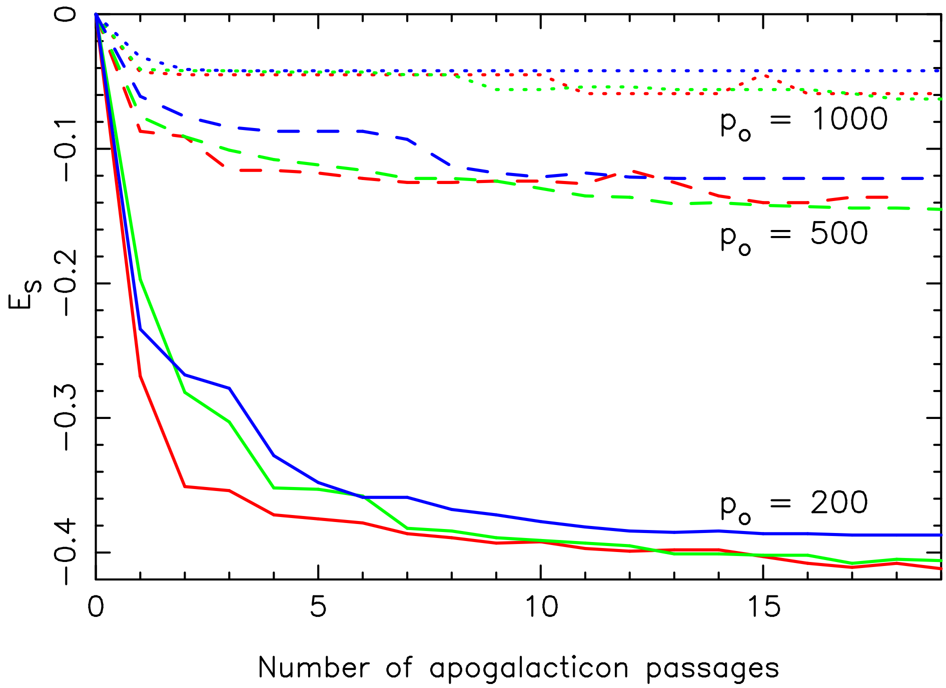

(b) Corresponding radii against time

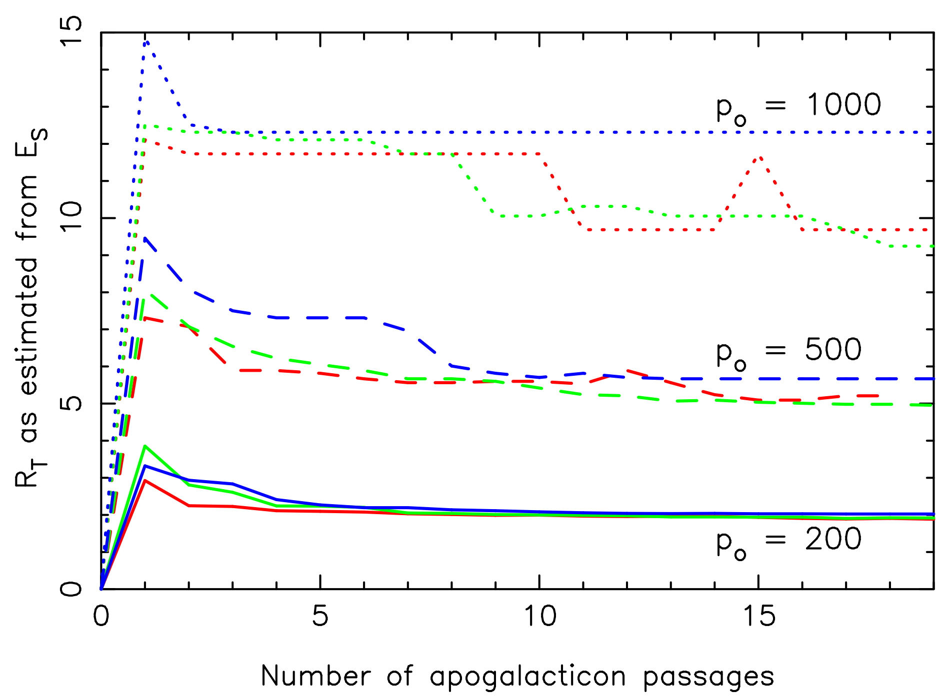

Figure 5.10: Time evolution of the initial binding energy associated with a 90% fraction of escaping particles E_S from the SCM (top panel) and the corresponding tidal radius estimate R_T (bottom panel) as a function of the number of apogalacticon passages. The corresponding radii serve as approximations to the tidal radii for clusters with $R_P/R_C = p_o = 200$ (solid lines), 500 (dashed) and 1000 (dotted) for the eccentricities $e_o = 0.2$ (red curves), $e_o = 0.5$ (green) and $e_o = 0.8$ (blue). Note from panel (a) that E_S has settled to an approximate equilibrium value after 15 apogalacticon passages.

is based (see Section 5.1) and thus the model results can not be trusted for clusters with such short perigalacticon distances. The assumptions of no significant mass loss and no changes to the potential in the inner regions of the cluster do hold for larger perigalacticon, such as $p_o = 500$ in Figure 5.10.

The equivalent tidal radii for all clusters on galactic orbits simulated using the SCM, R_T, are shown in Figure 5.11. The tidal radius for each cluster is estimated using the binding energy E_S after 15 apogalacticon passages by the same method used to convert the energies in Figure 5.10 (a) into distances in Figure 5.10 (b). The tidal radii for all clusters presented in Table 5.2 are plotted against $p_o = R_P/R_C$ as filled circles in Figure 5.11, with the colour indicating the eccentricity of the cluster-galaxy orbit ($e_o = 0.2$ is red, $e_o = 0.5$ is green and $e_o = 0.8$ is blue). The predicted tidal radius using the MSC is shown against the perigalacticon distance in Figure 5.11 as solid lines, with the eccentricity coloured as before. Theoretical tidal radii from the literature are shown as dashed lines for the Read radius R_{Read} (Read et al. 2006) and dotted lines for the King radius R_{King} (King 1962).

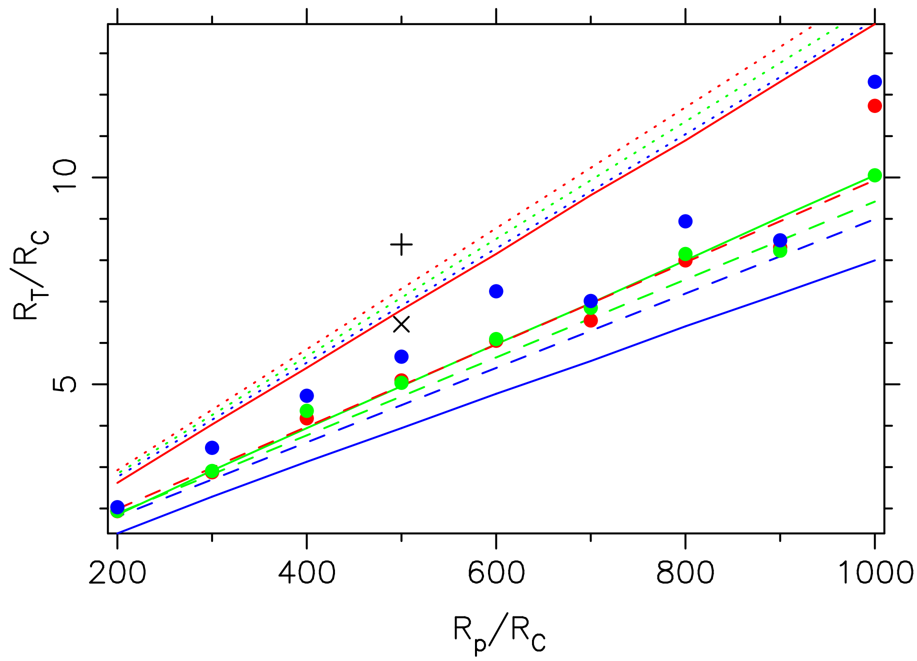

Figure 5.11: Tidal radii of theoretical estimates (lines) and from simulated clusters using the SCM (dots) against the perigalacticon distance. The tidal radii from simulated clusters, R_T, are determined from the E_S binding energy values after 15 apogalacticon passages (given in Table 5.2) using the fitting formulae Equations (3.23) and (3.22). Data points represent the SCM results for cluster compactness parameter $b = 1$ for all cluster-galaxy orbits simulated in Table 5.2. Predictions for the tidal radii based on the MSC (R_U) are indicated with solid curves, while theoretical determinations are also shown using the King radius (dotted line) and the Read radius (dashed line). The data points and theoretical curves are colour coded by eccentricity as $e_o = 0.2$ (red), $e_o = 0.5$ (green) and $e_o = 0.8$ (blue). The results from Section 5.2 for a cluster of compactness $b = 0.45$ after two apogalacticon passages are shown for the SCM (black plus) and N-body simulations (black cross).

General agreement is seen in Figure 5.11 between the tidal radii from clusters simulated using the SCM value for R_T and the theoretical tidal radii, particularly R_U and R_{Read}. However from the simulation results presented in Figure 5.11 none of the theoretical tidal radius estimates examined here match the dependence on the eccentricity see in the SCM values. All theoretical estimates predict that the lower eccentricity cluster orbits should have the largest tidal radii, for a fixed perigalacticon distance. The data points for the SCM appear to follow the opposite trend in Figure 5.11, with lower eccentricities having lower tidal radii. This is the opposite trend from what it expected if the movement of the core particle had a significant effect on the escape of stars in the outer cluster regions. The movement of the core would lower the tidal radius estimate using the SCM relative to the theoretical estimates since more particles with initial orbits in the central regions will be mixed outwards and subsequently escape the cluster (recall the red curve in Figure 5.2 a).

There are two explanations that may account for the tidal radius estimates of the SCM being lower than expected by theory. The first of these that there may be too few particles to adequately resolve the fraction of escaping stars in the outer regions of the cluster. For example after 15 cluster orbits $E_S \approx -0.1$ for $e_o > 0.2$, this initial binding energy is associated with $\lesssim$ 1000 particles (as discussed previously). These particles are spread across approximately 15 energy bins so that the fraction of escaping particles from each bin can be determined, therefore the bin with at least 90% of particles escaping (E_S) will contain $\sim$ 10 particles. Despite the potential lack of resolution in the outer regions, the general agreement between the simulated cluster and the theoretical results show that the SCM provides a good estimate of the tidal radius for long period cluster orbits.

The second explanation for why the tidal radius estimated by the SCM may be lower than expected is that the SCM uses a Plummer potential while all theoretical estimates are based on point masses. In the previous chapter the Plummer potential was found to stabilise the orbits of particles compared to the corresponding orbits in a point mass potential, refer to Figures 4.10 and 4.11 for prograde and retrograde particle orbits respectively. The largest effect of this stabilisation was seen for higher eccentricities where the MSC overestimated the proportion of unstable orbits as a function of the period ratio σ, see Figure 4.8 (c) for $e_o = 0.9$.

From Figure 5.11 the tidal radius estimates based on the MSC are seen to have a stronger dependence on the eccentricity of the cluster-galaxy orbit than the Read or King tidal radius estimates. The data for simulated clusters presented in this figure are not sufficient to discriminate between these theoretical estimates. Tidal radii estimated by the Read radius (dashed lines) and the MSC (solid lines) are in reasonable agreement for low perigalacticon distances (p_o), but diverge as p_o increases. Recall that the Read radius was tested against N-body simulations for two cluster orbits, one with $e_o = 0.57$ and $p_o = 77$ in these units and the other with $e_o = 0.0$ and $p_o = 267$ (Read et al. 2006). These distances barely overlap with the parameter space examined here, but where they do the Read and MSC tidal radius estimates are in agreement.

In Chapter 4 the MSC successfully predicted the range of period ratios for which unstable orbits could occur. Particles on these orbits are predicted to eventually escape the cluster via a random walk in their orbital binding energy. The predicted occurrence of these unstable orbits compared well with three-body simulations in Section 4.2, despite the difference between the Plummer and point mass potentials (investigated in Section 4.3). For each of the cluster eccentricities used in this chapter ($e_o = 0.2$, 0.5 and 0.8) the fraction of unstable orbits against the period ratio σ has been shown in Figure 4.8. From the success of the MSC in Chapter 4 we argue that the tidal radius estimated using the MSC can be trusted.

The complications associated with comparing the tidal radii between theoretical estimates and simulated data will now be discussed. For the SCM there are three main complications that arise: the timescale of a particle to escape, whether escaping particles can rejoin the cluster, and if two-body relaxation will influence these results.

The tidal radius estimate R_U is based on the period ratio associated with unstable orbits that will eventually escape the cluster through a random walk in the binding energy of the particle. An example of the random walking process for a particle on an unstable orbit was shown for a different set of three-body masses in Figure 1.4. This timescale for escape means that the tidal radius estimates from the SCM should converge to the tidal radius estimate using the MSC. The convergence of the tidal radius estimates for the simulated cluster are seen in Figure 5.10, however they do not always converge to the radius predicted by the MSC. This is likely to be due to the increased stability of orbits in a Plummer potential compared to point mass potentials, which are used by the MSC and may result in lower tidal radius estimates.

To get an indication of how many cluster-galaxy orbits it takes for particles on unstable orbits to escape the cluster the following three-body integrations were conducted. A three-body system of point masses is set-up using the same mass ratios as the star-cluster-galaxy system, with an eccentricity of $e_o = 0.9$ for the cluster-galaxy orbit. The particle-cluster orbit is assigned an eccentricity from the eccentricity distribution for a particle in a Plummer potential given by Equation (3.20). The phase of the particle-cluster orbit relative to the cluster-galaxy orbit is taken from a uniform distribution across $[0, 2\pi]$ and the relative inclination is taken from the probability distribution function given by Equation (4.2). The semi-major axis of the particle-cluster orbit is specified by the period ratio $\sigma = T_o/T_i$, where each period is given by the Keplerian period (Equation 1.4). The period ratio σ is varied from 90 to 350 to capture the transition from mostly unstable to mostly stable orbits for this cluster-galaxy eccentricity.

Each set of initial orbital parameters is numerically integrated using a Bulirsch-Stoer method for ten cluster-galaxy orbits, or until the particle reaches ten times its initial apocentre distance. If the particle reaches this distance then its is assumed to have escaped the cluster and the time of escape is stored. After all 100 particles have been integrated the mean and standard deviation in the escape times for all escaping particles are computed for each σ. The resulting escaping fraction and average escape times against σ are shown in Figure 5.12.

The average escape times presented in Figure 5.12 are based on a simple point mass model and are included here to give an indication of the timescale for particles to escape from a Plummer potential. In the Section 4.3 the Plummer potential was found to stabilise particle orbits and resulted in the MSC overestimating the fraction of unstable orbits, particularly for high σ. This same stabilising effect will occur here, leading to many particles on unstable orbits

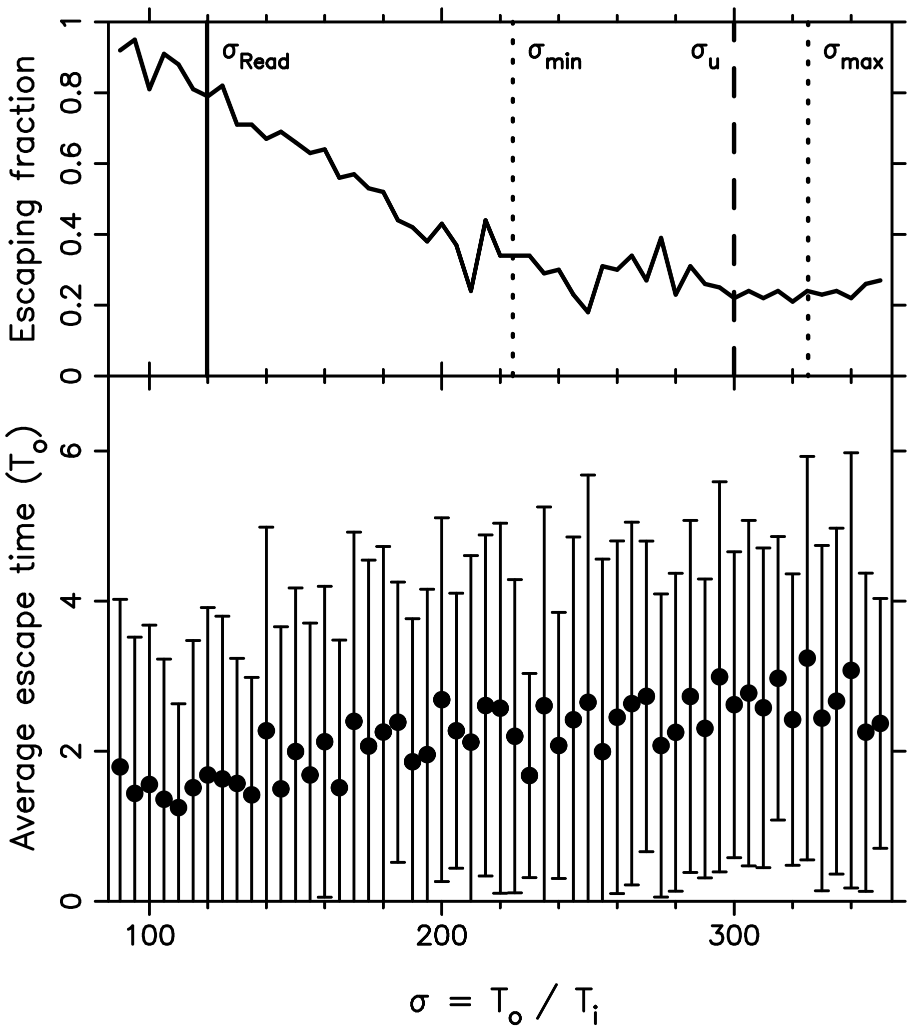

Figure 5.12: Escape timescale for a particle from a point mass cluster on an $e_o = 0.9$ galactic orbit. Top panel shows the escaping fraction of particles against σ. Each particle is assigned a different relative phase, inclination and eccentricity drawn from probability distributions for a particle in a Plummer potential. The top panel also indicates the minimum, maximum and representative σ values determined using the MSC, and the period ratio associated with the Read radius. For the escaping particles, the mean escape time and standard deviations are calculated and are shown against σ in the bottom panel.

not having sufficient time to escape the cluster. Since the tidal radius estimated using the MSC is associated with particles that will eventually escape the cluster then the estimate of the transition energy E_U is expected to be less than the initial binding energy associated with escaping stars E_S.

In the previous section the N-body simulation was found to produce more escaping stars than the SCM for $p_o = 500$ and $e_o = 0.5$ after two galactic orbits, this is also seen by comparing the black markers in Figure 5.11. For this set of initial conditions, neither two-body relaxation nor close encounters between particles had sufficient time to affect the escape of stars in the outer regions of the cluster. This discrepancy may be explained by the instantaneous removal of particles with positive binding energy from the N-body cluster or by poor statistics in the outer regions of the clusters. Particles that escape the cluster will still be on galactic orbits close to the cluster and can therefore be recaptured. For a more detailed discussion of the problems that arise when considering escaping stars the reader is referred to Fukushige and Heggie (2000). Particles that rejoin the cluster are likely to do so on unstable orbits, which are therefore predicted by the MSC to escape the cluster again. Thus this complication can be reduced to the timescale of a particle to escape the cluster, discussed above.

From Section 5.2 two-body relaxation was found not to affect results for the escape of stars from a cluster after two apogalacticon passages for that particular example. The same is not necessarily true after 15 apogalacticon passages. To investigate the effect of relaxation after 15 apogalacticon passages the relaxation timescale at the half-mass radius is shown against the perigalacticon distance in Figure 5.13 (a).

(a) Two-body relaxation time at $R_{1/2}$ (b) Relaxation time against binding energy

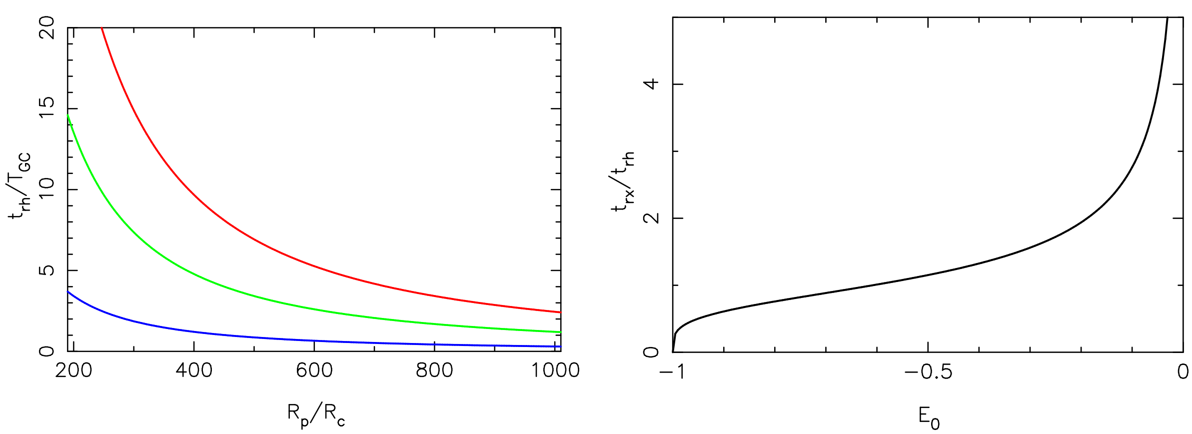

Figure 5.13: The half-mass relaxation timescale t_{rh} (Equation 2.1) in units of the galactic period of the cluster T_{GC} is shown against the perigalacticon distance R_P/R_C (left panel). The orbital eccentricities are coloured red for $e_o = 0.2$, green for $e_o = 0.5$ and blue for $e_o = 0.8$ in panel (a). The dependence of the two-body relaxation timescale, t_{rx}, on the binding energy for a cluster of compactness parameter $b = 1$ is shown in units of t_{rh} in the right panel. The method for determining the relaxation timescale for a given binding energy E_0 is described in relation to Figure 5.6 in Section 5.2.

Figure 5.13 shows the relative strength of two-body relaxation in units of the galactic orbital period of the cluster. This allows us to see how the relaxation timescale affects the tidal radius estimates from the SCM after 15 galactic orbit periods. Note that physically the relaxation timescale depends only on the properties of the cluster itself, and not on the galactic orbital parameters of the cluster (Equation 2.1). For the representative cluster discussed in Section 2.5 the half-mass relaxation time is approximately 1 Gyr.

In Section 2.2 the relaxation time was found to be proportional to the square root of the radial distance. This radius can be converted into the associated binding energy using the method described in relation to Figure 5.6 in Section 5.2. The dependence of the relaxation time t_{rx} on the binding energy of a cluster with compactness parameter $b = 1$ is shown in

Figure 5.13 (b). For binding energies greater than -0.2, we see that the relaxation timescale is at least twice the half-mass relaxation timescale. This minimum binding energy is indicative of a typical tidal radius, determined from E_S after 15 cluster-galaxy orbits from Table 5.2.

By combining this result with Figure 5.13 (a) we can determine the minimum perigalacticon distance where the relaxation timescale is less than 15 T_{GC} for energy values near E_S. Note that for globular clusters on long period orbits 15 T_{GC} is approximately the age of the galaxy for low cluster-galaxy eccentricities. Using the condition $t_{rx} > 2t_{rh}$ the minimum perigalacticon distances are given by $p_o \approx 450$ for $e_o = 0.2$ and $p_o \approx 300$ for $e_o = 0.5$ and for $e_o = 0.8$ the minium distance is below 200 (not shown in Figure 5.13 a). Therefore the tidal radius estimates of clusters simulated using the SCM will be unaffected by two-body relaxation, for clusters on long galactic period orbits.

While relaxation does not change the results for simulated clusters presented in this section, it can be important for clusters in the Milky Way globular cluster system (studied in the next chapter). For a cluster with an orbital period of 1 Gyr the cluster will only have completed roughly 10 orbits in its lifetime. If the half-mass relaxation timescale is approximately 1 Gyr for a cluster then the relaxation timescale is greater than 2 Gyr near the tidal radius. For this example these timescales mean that the observed cluster can be in a state of energy equilibrium, even in the outer regions of the cluster from which stars can escape the cluster. The overall effect of relaxation on real clusters is that E_U will overestimate the tidal radius, i.e. it is easier for stars to escape from inside the cluster than predicted by the MSC.

The effect of the complications faced when comparing tidal radii estimated from clusters simulated by the SCM (R_T) to the predicted tidal radii using the MSC (R_U) are summarised as follows. Firstly, the timescale for particles to escape the cluster means that the tidal radius estimated using the SCM is expected to converge to the theoretical estimates. This trend is generally seen in Figures 5.8 and 5.9 for the simulated E_S (solid lines) and theoretical E_U (dashed) binding energy values associated with the tidal radius estimates. Secondly, particles that escape the cluster, only to later rejoin it, does not effect either R_T or R_U determinations here. Finally, two-body relaxation does not effect the results presented here but will result in the predicted value underestimating the tidal radii in real clusters (expect $R_T < R_U$).

We conclude that tidal radii predicted using the MSC are consistent with the tidal radii estimated from simulated clusters using the SCM. Discrepancies between these radii have been discussed and are mostly the result of the theoretical estimates being based on point mass potentials, whereas the simulated cluster uses a Plummer potential. Contributions to the discrepancy in the tidal radius estimates between theoretical and simulated cluster may also be due to poor statistics in the SCM results, or the tidal radii being too close to the half-mass radii in the case of close (e.g. $p_o = 200$) galactic orbits. Furthermore, the tidal radii predicted by the MSC are consistent with radii determined using a recent theoretical estimate by Read et al. (2006). This is an important result and will be discussed more in the next section.

5.4 Summary

The aim of this chapter has been to develop and validate a globular cluster model that can be used to estimate the tidal radius of globular clusters on eccentric orbits with long periods. The tidal radius estimated from a simulated cluster was then compared to the location of orbits predicted by the Mardling stability criterion (MSC) to be stable or unstable to escape from the cluster. The tidal radius estimated by the MSC was also checked against other theoretical estimates from the literature (see Section 2.4) and will be applied to the Milky Way globular cluster system in Chapter 6.

To simulate clusters on galactic orbits with wide separations and high eccentricities a simplified cluster model (SCM) was developed in Section 5.1. This model consists of N particles orbiting a cluster core particle which is endowed with 50% of the total cluster mass, the core particle itself orbits the galaxy. The SCM was tested against an N-body simulation of a cluster on a galactic orbit with perigalacticon distance $R_P/R_C = 500$ and eccentricity $e_o = 0.5$, provided by Holger Baumgardt. The behaviour of these simulations differed only by more stars escaping from deeper within the cluster for the N-body simulation, but not so deep as to invalidate the core particle assumption used by the SCM. This is likely the result of escaping stars being instantly removed from the N-body cluster or of low numbers of particles in the outer regions of the cluster, and not two-body relaxation as first thought.

Two-body relaxation did not have an appreciable effect on any of the results presented for the SCM, since the associated timescale is very large in the outer regions of the clusters modelled here. This will become an issue when we apply the MSC to predicting the tidal radii of clusters in the Milky Way, as relaxation has had time to redistribute the energy inside these clusters.

For the star-cluster-galaxy system an unstable orbit is equivalent to an orbit that will result in the star eventually escaping the cluster. In the previous chapter, the MSC was used to predict the location of the transition from unstable to stable orbits for mass ratios consistent with the star-cluster-galaxy system. Using the fitting formulae given by Equations (3.23) and (3.22), the predicted ratio of periods (σ_u) was converted into an equivalent binding energy and radius in a Plummer potential, E_U and R_U respectively.

The fraction of stars escaping with a particular initial binding energy was used to characterise the results from the SCM for galactic orbits with eccentricities $e_o = 0.2$, 0.5 and 0.8 and perigalacticon distances $R_P/R_C = 200, 300, ..., 1000$. The tidal radius estimated from these clusters was defined using the lowest binding energy for which more than 90% of particles escaped the cluster E_S. By using the fitting formulae Equations (3.23) and (3.22) this was converted into a tidal radius R_T and compared to theoretical estimates. The tidal radii for all simulated clusters are shown in Figure 5.11, and compared particularly well to the Read radius and to the radius R_U predicted by the MSC. Note that the theoretical estimates indicate that all particles outside these radii will eventually escape. Thus it was expected that the energy associated with the tidal radius estimate from simulated clusters (E_S) would converge on the theoretical estimates using the MSC (E_U) and the Read radius (E_R). This trend was generally observed after 15 galactic periods in Table 5.2, except for some sets of parameters which are commented on in Section 5.3.

The predicted tidal radii using the MSC compared remarkably well in Figure 5.11 with the Read radius, given by Equation (2.5). The Read radius is a recent theoretical estimate of the tidal radius and found excellent agreement with two N-body simulations with $R_P/R_{1/2} = 267$ and eccentricity $e_o = 0.0$ and perigalacticon $R_P/R_{1/2} = 77$ and eccentricity $e_o = 0.57$ (Read et al. 2006). We have explicitly tested our tidal radii estimate against a single N-body simulation, but by comparing to the Read radius we are in effect testing it against more N-body simulations in the short galactic period range. Unlike the Read et al. (2006) analysis the MSC takes the orbital characteristics of a cluster star into account. By comparison their analysis considered only circular or radial orbits of stars inside a cluster. Read et al. (2006) found that the escape of a star from the cluster depended on the orbit of the star within the cluster. We confirm this result and add that it depends specifically on the star's orbital eccentricity and orbital period, neither of which is included in detail in their analysis.

Estimates of the tidal radius using the MSC and using the Read radius are in disagreement over the dependence on eccentricity, particularly for clusters with long galactic period orbits. This is seen in Figure 5.11 where the range of tidal radii is very spread out as the perigalacticon distance increases. Note that in this region the Read radius has not been tested against N-body simulations and so this does not disprove our analysis. Future N-body simulations for clusters on a variety of wide galactic orbits will allow for comparisons to be made between the tidal radii estimated using the MSC and using the Read radius.

Two complications were found that did not affect the results presented for clusters simulated in this chapter, but may affect the tidal radii in real clusters. The first of these is two-body relaxation will contribute to the MSC overestimating the tidal radius by making it easier for stars to escape from deep within the cluster. This occurs by the diffusion of stars from inside the cluster to replace those lost from unstable orbits.

The second complication is that the MSC assumes that particles on unstable orbits will instantly escape the cluster. As seen in Figure 1.4 the particles escapes the cluster in a random walk process and typically takes multiple perigalacticon passages of the cluster to completely escape the cluster. This results in the MSC underestimating the tidal radius by predicting that stars on unstable orbits escape the cluster when they are likely to still be bound during the lifetime of the cluster.

Overall the findings of this chapter indicate that the tidal radius estimated using the stability of stars in a cluster is accurate for globular clusters on eccentricity galactic orbits with a wide range or periods. In the next chapter the observed tidal radii of clusters in the Milky Way globular cluster system will be examined and compared to the predicted value.

Chapter 6

The Milky Way globular cluster system

In this chapter we use the Mardling stability criterion (MSC) to estimate the tidal radius of observed globular clusters. This theoretical estimate, along with two other estimates from the literature for the tidal radii, is compared to the observed tidal radii of globular clusters with a range of masses.

The tidal radius of a GC depends on the parameters of its orbit around the galaxy. However, the observed tidal radius is determined by using the distance from the cluster centre where the light falls below a particular threshold. This means that the observed tidal radii used in this chapter are estimates of the tidal radius for each cluster.

This chapter will only consider the Milky Way globular cluster system (MWGCS), as position and velocity observations are unavailable for other galactic systems. The orbital parameters for known clusters from the MWGCS are determined in Section 6.1 by integrating the cluster orbits backwards in time through a realistic galactic potential for the Milky Way.

Globular clusters for which the mass, tidal radius and orbital parameters are known are compared in Section 6.2 with theoretical tidal radii predicted by the MSC and from the literature (King 1962; Read et al. 2006). This section also highlights the discrepancies between the theoretical and observed tidal radii for the group of GCs with high orbital eccentricities.

A simple procedure for using the theoretical tidal radius estimates to constrain the orbital parameters of GCs is given in Section 6.2. Such an approach is required because of the significant range of eccentricities that result from the large velocity uncertainties obtained from the proper motion of individual GCs. Some of the discrepancies between the theoretical and observational tidal radius estimates for individual clusters are further discussed in the next chapter. This format is chosen so that the conclusions from previous chapters, relating to applying the MSC to the tidal radius of globular clusters, can be summarised and discussed along with possible future directions of this work.

6.1 Orbital parameters of the Milky Way globular clusters

Spatial information for clusters in the MWGCS has been available for many decades now, although GCs in the inner regions of the galaxy are still being discovered (e.g. Froebrich et al. 2007 and Bica et al. 2007). A continually updated catalogue of spatial coordinates for globular clusters in the MWGCS can be found online (Harris 1996) and is used extensively throughout this chapter. The positions of the clusters in galactic coordinates assume a distance of the Sun to the galactic centre of 8 kpc (consistent with 7.9 ± 0.4 kpc from Eisenhauer et al. 2003) and on distance determinations for each cluster based on the position of the main sequence turn-off in the Hertzsprung-Russell diagram (Harris 1996).

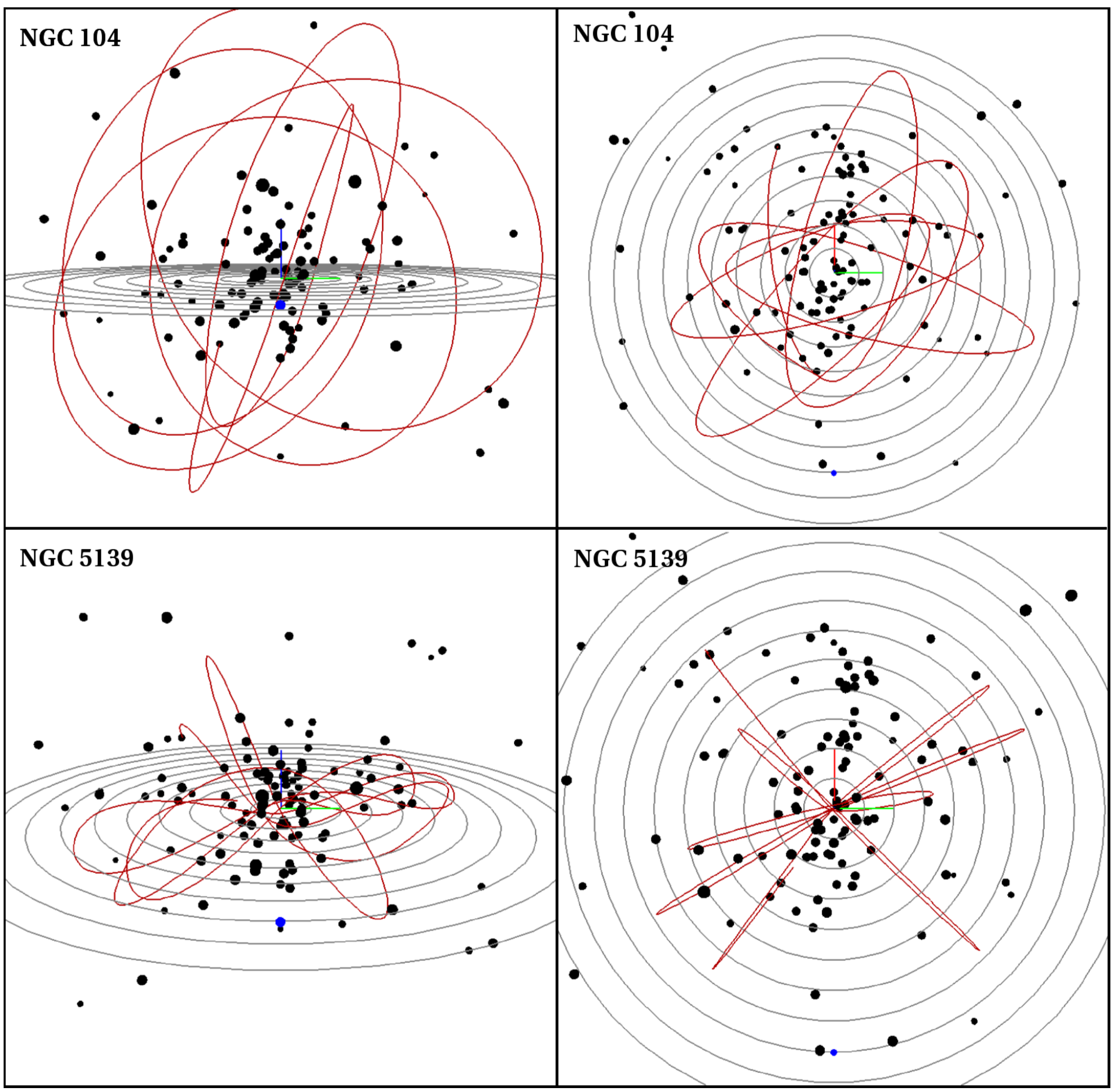

Figure 6.1: Orbits of 47 Tucanae (top) and ω Centauri (bottom) shown from different angles looking past the Sun (blue sphere). The disk of the galaxy is indicated using concentric circles with radii of 1, 2, ..., 10 kpc.

The eccentricities and perigalacticon distances for clusters in the MWGCS are required to determine the tidal radii using theoretical approaches. These orbital parameters depend on the three-dimensional velocity for each cluster, as well as the gravitational potential of the Milky Way. The difficulty in observing the tangential velocity components for globular clusters makes precise determinations of these orbital parameters difficult, as previously discussed in Section 2.5.

The most recent velocity and distance values for each cluster are used in conjunction with the galactic potential used by Fellhauer et al. (2007). This gravitational potential consists of a Miyamoto-Nagai potential (Miyamoto and Nagai 1975) combined with a logarithmic potential. The total galactic potential Φ is given as a sum of the galactic halo Φ_h, disc Φ_d and bulge Φ_b potentials by (Fellhauer et al. 2007)

$$\Phi(x, y, z) = \Phi_h(r) + \Phi_d(R, z) + \Phi_b(r) \tag{6.1}$$

where

$$r = \sqrt{x^2 + y^2 + z^2} \qquad R = \sqrt{x^2 + y^2} \tag{6.2}$$

and x, y and z are galactic coordinates with units in kpc. In this coordinate system the Sun is located at (-8,0,0) at which a particle with velocity directed in the positive $\mathbf{y}$ direction is moving in the direction of Galactic rotation. It follows that $\mathbf{z}$ points in the direction of the northern galactic pole. The gravitational potentials for the galactic halo Φ_h, disc Φ_d and bulge Φ_b are

$$\Phi_h(r) = \frac{1}{2} v_o^2 \ln\left(1 + \frac{r^2}{a^2}\right) \tag{6.3}$$

$$\Phi_d(R, z) = \frac{-GM_d}{\sqrt{R^2 + \left(b + \sqrt{z^2 + c^2}\right)^2}} \tag{6.4}$$

$$\Phi_b(r) = \frac{-GM_b}{r + d} \tag{6.5}$$

where $a = 12.0$ kpc, $b = 6.5$ kpc, $c = 0.26$ kpc, $d = 0.7$ kpc, $v_o = 181$ km/s and G is the gravitational constant. The masses of the galactic disc and bulge are $M_d = 10^{11}$ $M_\odot$ and $M_b = 3.5 \times 10^{10}$ $M_\odot$ respectively. The equations of motion for a cluster moving in this potential are given by

$$\mathbf{r} = -\nabla\left(\Phi_h + \Phi_d + \Phi_b\right). \tag{6.6}$$

For globular clusters with velocity data, Equation (6.6) is integrated back through time for approximately 10 cluster-galaxy orbits, using the Bulirsch-Stoer numerical integration method (Press et al. 1986). A sample of these orbits for six globular clusters, five of which are later used in Table 6.3, appeared previously in Figure 2.3. In addition to this sample, the orbits for 47 Tucanae (NGC 104) and ω Centauri (NGC 5139) are shown in Figure 6.1. These two clusters are highlighted since 47 Tuc is a well studied close globular cluster, while ω Cen shows evidence of a different formation history (Fellhauer and Kroupa 2003). The origin and formation of clusters in the MWGCS will be returned to in the next chapter.

Table 6.1 lists the orbital parameters resulting from the simulated sample of galactic globular clusters. The observed cluster mass M_C and half-mass radius $r_{1/2}$ are shown in columns 2 and 3. During the time integration of each cluster using Equation (6.6), the minimum distance from the galactic centre R_{min} and the maximum distance R_{max} averaged over the first few orbits are recorded. This information is used to estimate the eccentricity by

$$e = \frac{R_{max} - R_{min}}{R_{max} + R_{min}} \tag{6.7}$$

and perigalacticon distance $R_p = R_{min}$, both of which are presented in columns 4 and 5 of Table 6.1. The orbital periods for globular clusters determined from the numerical simulations are shown in column 6, clusters for which no mass determination was found in the literature are taken as 10^5 $M_\odot$. References for the velocity, mass and half-mass radius for each cluster are given in column 7, with all spatial coordinates from Harris (1996). The half-mass radii (in pc) quoted in Table 6.1 are based on recent estimates of the cluster distance taken from the references given in column 7. The orbital parameters R_p, e and P in Table 6.1 generally agree with a similar study conducted by Allen et al. (2006) which used a different galactic potential.

Table 6.1: Structural and orbital parameters for a sample of the Milky Way globular cluster system (MWGCS). Observational data is obtained from the literature while R_p, e and orbital period P are determined from numerical integration of the model given in Section 6.1. All spatial coordinates for globular clusters are from Harris (1996) with velocities, masses and half-mass radii from: (1) Meziane and Colin (1996) and references therein, (2) Dinescu et al. (1999) and references therein, (3) Dinescu et al. (2001), (4) Dinescu et al. (2003), and (5) Casetti-Dinescu et al. (2007).

System	log($\mathbf{M}_c$)	$R_{1/2}$ **(pc)**	R_p **(kpc)**	e	P **(Myr)**	**Reference(s)**
NGC 104 (47 Tuc)	6.03	3.79	5.2	0.17	147	1,2
NGC 288	4.64	5.76	1.7	0.74	157	1,2
NGC 362	5.45	1.64	0.8	0.85	116	1,2
NGC 1851	-	1.65	5.7	0.69	740	2
NGC 1904	-	2.38	4.2	0.65	390	2
NGC 2298	-	2.48	1.9	0.78	238	2
NGC 2808	-	-	2.6	0.65	190	5
NGC 3201	-	-	9.0	0.42	574	5
NGC 4147	4.39	2.52	4.1	0.72	526	1,2
NGC 4372	-	-	2.8	0.45	108	5
NGC 4590	-	4.02	8.6	0.48	631	2,3
NGC 4833	-	-	0.7	0.84	86	5
NGC 5024	5.68	6.11	15.5	0.4	1232	1,2

Continued on next page...

Table 6.1 – Continued

System	log($\mathbf{M}_c$)	$R_{1/2}$ **(pc)**	R_p **(kpc)**	e	P **(Myr)**	**Reference(s)**
NGC 5139 (ω Cen)	6.38	7.41	1.2	0.67	65	1,2
NGC 5272	5.81	3.41	5.5	0.42	274	1,2
NGC 5466	4.85	9.48	9.0	0.84	3960	1,2,3
NGC 5897	-	7.4	2.0	0.64	123	2
NGC 5904	5.66	3.81	2.5	0.87	792	1,2
NGC 5927	-	-	4.5	0.1	105	5
NGC 5986	-	-	0.6	0.79	45	5
NGC 6093	-	1.68	0.6	0.73	31	2
NGC 6121	4.83	2.87	0.6	0.8	49	1,2
NGC 6144	-	4.03	1.8	0.25	35	2
NGC 6171	4.8	3.25	2.3	0.21	47	1,2
NGC 6205	5.59	3.48	5.0	0.62	448	1,2
NGC 6218	5.07	2.61	2.6	0.34	73	1,2
NGC 6254	-	2.39	3.4	0.19	81	2
NGC 6266	-	-	0.5	0.59	13	4
NGC 6304	-	-	0.3	0.82	20	4
NGC 6316	-	-	0.7	0.66	25	4
NGC 6341	5.34	2.24	1.4	0.76	132	1,2
NGC 6362	-	4.23	2.4	0.39	73	2
NGC 6397	4.63	1.94	3.1	0.34	96	1,2
NGC 6522	-	-	0.5	0.2	4	4
NGC 6528	-	-	0.5	0.17	4	4
NGC 6553	-	-	1.2	0.32	23	4
NGC 6584	-	3.11	0.9	0.87	171	2
NGC 6626	5.36	2.53	2.1	0.19	39	1,2
NGC 6656	5.53	3.1	2.9	0.53	144	1,2
NGC 6712	4.98	2.6	0.9	0.75	64	1,2
NGC 6723	-	-	0.7	0.69	28	4
NGC 6752	5.1	2.23	4.8	0.08	112	2
NGC 6779	-	3.09	0.9	0.86	153	2
NGC 6809	-	4.17	1.9	0.51	72	2
NGC 6838	4.29	-	4.8	0.17	131	1,2
NGC 6934	-	2.83	9.0	0.81	3060	2,3
NGC 7006	-	4.5	17.0	0.71	4213	2,3
NGC 7078	5.85	3.01	5.4	0.32	210	1,2

Continued on next page...

Table 6.1 – Continued

System	$\log(\mathbf{M}_c)$	$R_{1/2}$ **(pc)**	R_p **(kpc)**	e	P **(Myr)**	**Reference(s)**
NGC 7089	5.78	3.28	6.4	0.68	840	1,2
NGC 7099	-	2.39	3.0	0.39	102	2
Pal 3	-	17.89	82.5	0.67	37102	2
Pal 5	-	20	2.3	0.74	247	2
Pal 13	-	2.67	12.0	0.78	3781	2,3

The orbital parameters derived in Table 6.1 are intended as estimates for use in calculating tidal radii in the next section. Most of the uncertainty in the parameters is due to the poorly constrained cluster velocity components directed tangential to our line of sight. Such measurements are difficult to obtain and rely on comparing the current positions of globular clusters on the sky with older position data found on photographic plates. The motion of each cluster is then determined from the change in positions (in milli-arcseconds, mas) over time, with the positions calibrated using "fixed" distant objects, such as quasars (e.g. Dinescu et al. 1997).

Some contribution to the error in orbital parameters is from cluster distance estimates, which primarily affects the half-mass radii. This distance also affects the velocity determinations when they are converted from the observed sky motions ($\sim$ 1 - 10 mas yr^{-1}) to proper motions tangential to our line of sight ($\sim$ 100 km/s).

The relative errors in the velocity measurements of some clusters in the MWGCS are shown in Table 6.2, which is based on a compilation of other sources presented in Table 2 of Dinescu et al. (1999). The velocity magnitudes in galactic coordinates are listed in column 4 for the systems given in column 1. Column 2 shows the line of sight velocities V_{RV}, determined using the radial velocity. The relative errors for the radial velocity and total velocity of each cluster are listed in columns 3 and 5 respectively.

The velocity magnitude of each cluster (column 4 in Table 6.2) is calculated by

$$V_{GC} = \sqrt{U^2 + V^2 + W^2} \tag{6.8}$$

where U, V and W are the cluster velocity components (km/s) in galactic coordinates presented in Table 2 of Dinescu et al. (1999). The radial velocities V_{RV} and associated uncertainties are taken from the same table, with the relative errors given by the magnitude of $\Delta V_{RV}/V_{RV}$ in column 3 of Table 6.2. The relative error for the total cluster velocity (column 5) is determined by

$$\left|\frac{\Delta V_{GC}}{V_{GC}}\right| = \sqrt{\left(\frac{\Delta U}{U}\right)^2 + \left(\frac{\Delta V}{V}\right)^2 + \left(\frac{\Delta W}{W}\right)^2} \tag{6.9}$$

where ΔU, ΔV and ΔW are the associated uncertainties (in km/s) for U, V and W taken from

System	V_{RV} km/s	$\frac{\Delta V_{RV}}{V_{RV}}$	V_{GC} km/s	$\frac{\Delta V_{GC}}{V_{GC}}$
NGC 104	-18.7	0.011	121.7	0.42
NGC 288	-46.4	0.009	253.1	0.57
NGC 362	223.5	0.002	290.0	1.31
NGC 1851	320.5	0.002	332.8	0.35
NGC 1904	207.5	0.002	223.1	4.87
NGC 2298	149.4	0.009	237.7	0.81
NGC 4147	183.0	0.005	244.1	0.91
NGC 4590	-95.1	0.006	191.1	4.45
NGC 5024	-79.1	0.052	92.3	3.15
NGC 5139	232.5	0.003	262.0	2.51
NGC 5272	-147.1	0.003	172.1	1.43
NGC 5466	107.7	0.003	351.7	0.54
NGC 5897	101.7	0.010	324.7	1.11
NGC 5904	51.8	0.010	406.9	0.26
NGC 6093	7.3	0.562	296.5	0.90
NGC 6121	70.4	0.006	201.4	0.64
NGC 6144	189.4	0.006	310.9	2.34
NGC 6171	-33.8	0.009	78.0	11.02
NGC 6205	-246.6	0.004	288.8	0.37
NGC 6218	43.5	0.014	152.8	0.30
NGC 6254	75.5	0.015	155.0	0.34
NGC 6341	-120.5	0.014	152.7	1.05
NGC 6362	-13.3	0.045	143.1	0.44
NGC 6397	18.9	0.005	138.7	0.25
NGC 6584	222.9	0.067	405.2	0.41
NGC 6626	15.8	0.063	74.6	0.57
NGC 6656	-149.1	0.004	194.0	0.86
NGC 6712	-107.7	0.006	163.8	0.37
NGC 6752	-32.1	0.047	49.0	0.51
NGC 6779	-135.9	0.007	133.1	11.01
NGC 6809	174.9	0.002	295.3	0.20
NGC 6838	-22.9	0.009	96.4	7.00
NGC 6934	-412.2	0.004	537.7	1.03
NGC 7078	-106.6	0.006	270.6	0.46
NGC 7089	-3.1	0.290	392.5	0.49
NGC 7099	-184.3	0.005	313.4	0.42
Pal 3	83.4	0.101	203.7	4.09
Pal 5	-55.0	0.291	266.0	1.84
Averages		0.045		1.83

Table 6.2: Velocities and associated uncertainties for a subset of clusters from the MWGCS, taken from Dinescu et al. (1999). The radial velocities V_{RV} are shown to be significantly more reliable than the total cluster velocities V_{GC}. This is due to uncertainties in the velocity components tangential to our line of sight dominating the overall relative error (final column).

Dinescu et al. (1999).

Table 6.2 shows that the radial velocities V_{RV} are significantly more reliable than the total cluster velocities V_{GC}. In many cases the uncertainties in the cluster velocity V_{GC} are greater in magnitude than the measurement itself. This is slightly misleading when we consider the case of a hypothetical cluster with $W = 10$ km/s, $U = V = 100$ km/s and $\Delta U = \Delta V = \Delta W = 20$ km/s. For this hypothetical case Equation (6.9) is almost entirely due to $\Delta W/W$ and the relative error is found to be 2.02. Such large relative errors also occur for the radial velocity measurements, particularly for NGC 6093. It is still meaningful to compare the difference between the average relative errors for the radial velocity (0.045) and for the total cluster velocity (1.83). A similar factor of ~ 100 between the relative errors is found for individual clusters, typical values for which are 0.002 for the radial velocity and 0.2 for the total velocity. This discrepancy in the relative errors between the radial and total velocities is the result of uncertainties in the velocity components tangential to our line of sight dominating the overall relative error.

Another factor that can cause uncertainty in the orbits of globular clusters is the choice of the galactic potential. For example, the inclusion of a central bar of 3 kpc scale length in the galactic potential model resulted in significant variation in globular cluster orbits near the galactic centre (Allen et al. 2006; Allen et al. 2008). The perigalacticon and eccentricities for 46 clusters in Allen et al. (2006) and 6 in Allen et al. (2008) were obtained using orbital integrations similar to those presented here. These studies determined the errors in orbital parameters for galactic potentials with and without the bar, by integrating two additional orbits for each cluster. They found that variations in the orbital parameters for the two additional cluster orbits were far larger than the variations in the orbital parameters of clusters moving through galactic potentials with or without a bar. Therefore the presence of a central bar can be ignored as a relatively minor source of uncertainty in the orbital parameters. Variations in the orbital parameters between clusters in Table 6.1 and those of Allen et al. (2006) and Allen et al. (2008) were also found to be less than the range of orbital parameters produced for each cluster due to the velocity uncertainties.

Of the globular clusters presented in Table 6.1 those with quoted cluster masses will be used to study the tidal radii. The mass is required to accurately determine the orbital period which is in turn needed to determine the period ratio between the cluster-galaxy and the star-cluster orbits, σ. This sub-set of the Milky Way globular clusters is shown in Table 6.3 and is used to compare the observed tidal radii to theoretical estimates in the next section.

6.2 Tidal radius comparisons

The aim of this section is to compare the tidal radius predictions using the MSC from Chapters 4 and 5 with MWGCS observations. Application of the MSC to GCs in Chapter 4 found that a transition between unstable and stable orbits exists for stars orbiting within a cluster, itself orbiting a galactic potential. This transition was characterised by the period ratio of the cluster-galaxy and star-cluster orbits, σ_u, and is equivalent to the predicted tidal radius R_U.

System	R_{GC} (kpc)	R_p (kpc)	e	N_{orbits}	$\|\Delta V_{GC}/V_{GC}\|$	R_T	R_U	R_{min}	R_{max}	X_{err}	R_{Read}	R_{King}
NGC 6121	5.9	0.6	0.80	205	0.64	8.90	0.00	0.00	1.38	1.00	0.77	1.18
NGC 362	9.4	0.8	0.85	87	1.31	19.89	2.95	2.70	4.18	0.85	2.86	4.40
NGC 6712	3.5	0.9	0.75	156	0.37	5.43	1.59	1.33	2.87	0.71	1.43	2.19
NGC 5139	6.4	1.2	0.67	154	2.51	13.64	2.41	2.08	3.97	0.82	1.99	3.03
NGC 6341	9.6	1.4	0.76	76	1.05	13.92	3.70	3.34	5.74	0.73	3.41	5.22
NGC 288	12	1.7	0.74	64	0.57	5.83	0.76	0.39	1.86	0.87	0.94	1.44
NGC 6626	2.7	2.1	0.19	255	0.57	7.22	6.90	5.82	8.91	0.05	5.06	7.43
NGC 6171	3.3	2.3	0.21	214	11.02	6.46	3.99	3.65	5.75	0.38	2.79	4.11
NGC 5904	6.2	2.5	0.87	13	0.26	13.46	4.27	4.00	5.48	0.68	4.50	6.94
NGC 6218	4.5	2.6	0.34	136	0.30	8.15	5.77	5.24	8.74	0.29	4.72	7.03
NGC 6656	4.9	2.9	0.53	70	0.86	8.89	6.57	5.97	9.38	0.26	6.11	9.23
NGC 6397	6	3.1	0.34	105	0.25	6.79	6.42	5.83	9.69	0.05	5.40	8.05
NGC 4147	21.3	4.1	0.72	19	0.91	14.67	4.57	4.17	7.05	0.69	4.30	6.57
NGC 6752	5.2	4.8	0.08	89	0.51	23.65	12.49	11.12	17.59	0.47	10.98	15.97
NGC 6838	6.7	4.8	0.17	77	7.00	5.43	8.41	7.21	10.86	-0.55	6.73	9.87
NGC 6205	8.7	5.0	0.62	22	0.37	16.90	9.07	8.23	13.65	0.46	9.69	14.72
NGC 104	7.4	5.2	0.17	68	0.42	15.36	14.72	12.65	18.94	0.04	14.03	20.59
NGC 7078	10.4	5.4	0.32	48	0.46	20.28	14.89	12.89	20.94	0.27	15.53	23.09
NGC 5272	12.2	5.5	0.42	37	1.43	34.10	12.87	11.15	17.41	0.62	13.30	19.93
NGC 7089	10.4	6.4	0.68	12	0.49	23.06	12.41	11.30	18.35	0.46	15.08	23.00
NGC 5466	16.2	9.0	0.84	3	0.54	15.22	3.56	3.26	5.20	0.77	3.51	5.40
NGC 5024	18.3	15.5	0.40	8	3.15	19.59	16.41	14.71	24.28	0.16	19.00	28.43

Table 6.3: Tidal radii comparisons between the observed (R_T) and theoretical values for Milky Way globular clusters with masses quoted in Table 6.1. The cluster distance for the galactic centre (R_{GC}) from Harris (1996) is included in column 2 and column 5 shows the number of orbits completed in 10 Gyrs, based on a constant orbital period P given in Table 6.1. The orbital parameters in columns 3 and 4 are reproduced from Table 6.1. The relative error for the cluster velocities are also presented as taken from Table 6.2. All tidal radii are in units of the half-mass radius for each cluster, determined from Harris (1996). Columns 8-10 shown the predicted tidal radii using the MSC as characterised by R_U and the range of radii $R_{min/max}$. The relative difference $X_{err} = (R_T - R_U)/R_T$ is shown in column 11. Other theoretical estimates from the literature are denoted by R_{Read} (Read et al. 2006) and R_{King} (King 1962). Clusters are listed in order of ascending perigalacticon distance for ease of comparison with Figure 6.3. The orbital and structural parameters for each cluster are listed in Table 6.1, along with references from the literature.

Chapter 4 found that the tidal radius of a given cluster would not be a single value rather it is characterised by σ_u and associated with the range σ_{min} to σ_{max}, which are predicted using the MSC. The behaviour of the period ratio as a function of the eccentricity of the cluster orbit is shown in Figure 4.4. The maximum galactic orbital eccentricity (e) of a cluster for which σ_u is determined is $e = 0.9$, which is greater than any of the values presented in Table 6.3.

The results from previous chapters can be applied by making the assumption that a globular cluster can be modelled using a Plummer potential of compactness parameter $b = 1$ with the same mass as the observed cluster mass. This assumption allows us to use the fitting formula, given by Equation (3.23), to convert any period for a star-cluster orbit into an apocentre distance from the cluster centre assuming an average eccentricity of $\bar{e_i} = 0.47$ (refer to the eccentricity distribution in Figure 3.4). For a star on the edge of the region predicted by the MSC to be unstable to escape, the orbital period of the star is given by $T_i = P/\sigma_u$ where P is the orbital period of the cluster-galaxy orbit in Myr given in Table 6.1 and σ_u is a function of e only. The period T_i is converted into a radius in units of the half-mass cluster radius ($R_{1/2}$) for a Plummer potential using the fitting formula Equation (3.23) and using the relation of the length scale to the half-mass radius given in Equation (3.9). The predicted tidal radii using the MSC are now in units of the half-mass radii, with the representative radius given as R_U and the expected range of radii for which stars can escape the cluster given by $R_{min/max}$. These predicted tidal radii can now be compared to a sub-set of clusters from the MWGCS previously listed in Table 6.1.

A summary of the tidal radii of observed globular clusters is listed in Table 6.3, for clusters with mass determinations given in column 7 of Table 6.1. Accurate mass determinations are a prerequisite for inclusion in Table 6.3 since the orbital period of the cluster needs to be as accurate as possible and this period is used to predict the tidal radius using the MSC (R_U, $R_{min/max}$). These clusters are listed in order of ascending perigalacticon distance (column 3) to aid comparison with Figure 6.3, discussed later in this section. The orbital eccentricity in column 4 has been reproduced from Table 6.1, while column 5 shows the number of cluster orbits (N_{orbits}) completed during in the age of the galaxy (taken as 10 Gyr) if the orbital period for the cluster (P in Table 6.1) were constant over this time. To give an indication of the current orbital phase of the cluster its distance to the gala lactic centre (R_{GC}) is given in column 2, these values are taken from Harris (1996). Since the period depends on the orbital parameters and the mass of the cluster then N_{orbits} can vary even for similar e and R_p values, as is the case for NGC 6121 and NGC 362 in Table 6.3. The relative error in the measured cluster velocities (Equation 6.9) for each cluster are listed in column 6.

The observed tidal radius in Table 6.3 is the ratio of the tidal radius in arcminutes to the half-mass radius (also in arcminutes) taken from Harris (1996). Note that the observed tidal radius (column 7) is itself an estimate based on the light fall off for each cluster. Using this procedure the observed tidal radius (R_T) is in units of the physical half-mass radius presented in Table 6.1. This ratio of the tidal radius to the half-mass radius is chosen since it is directly observed from the angular projection on the sky, rather than dependent on the cluster distance.

Theoretical tidal radii estimates in Table 6.3 are divided into two parts, those predicted by the MSC using Chapter 4 and those from the literature. The radii corresponding to the transition from unstable to stable orbits R_U, R_{min} and R_{max} are given in columns 8-10 in units of the half-mass radius $R_{1/2}$. The relative difference between the observed tidal radius R_T and the predicted radius R_U is given by $X_{err} = (R_T - R_U)/R_T$ and appears in column 10 of Table 6.3.

Theoretical estimates from the literature are given in columns 12 and 13 of Table 6.3 these are the Read radius R_{Read} (Equation 2.5) and the King radius R_{King} (Equation 2.4). The Read radius was determined by considering particles on circular prograde orbits in a point mass cluster potential (Read et al. 2006), while the King radius represents the maximum radius for a particle on a radial orbit within a cluster (King 1962). The approaches used by these studies to determine the Read and King radii have been discussed in detail in Section 2.4. The tidal radii predicted by the MSC are generally found be between the Read and King tidal radii, i.e. $R_{Read} \lesssim R_U \lesssim R_{King}$, for the cluster eccentricities presented in Table 6.3. However the accuracy of these eccentricities is questionable, as will now be discussed.

Two factors are expected to affect the relative difference between the observed tidal radius and the predicted tidal radius using MSC for each cluster (X_{err}), these being the orbital eccentricity and phase of the cluster-galaxy orbit. The orbital eccentricity is expected to be more dependent on the observed cluster velocity than the perigalacticon distance. This can be demonstrated by considering a GC on a nearly circular galactic orbit. If the velocity components were changed by a small amount consistent with the average relative velocity errors in Table 6.2 then, on average, the new orbit will be more eccentric than it was originally. The same argument applies to GCs on orbits with moderate eccentricity and therefore velocity errors will tend to increase the eccentricities determined for the MWGCS shown in Tables 6.1 and 6.3. Therefore the relative difference X_{err} is expected to increase with the orbital eccentricity. This is behaviour is shown in Figure 6.2 (a) for the clusters presented in Table 6.3. Note that the size of each data point indicates the observed cluster mass for which no correlation is seen to $|X_{err}|$.

The second factor expected to affect the relative difference between observed and theoretical estimates of the tidal radius is the phase of the cluster-galaxy orbit. The orbital phase is defined here as the ratio of the perigalacticon distance determined from orbital integrations of the cluster to the observed distance from the galactic centre, i.e. R_p/R_{GC}. A cluster observed close to the perigalacticon ($R_p/R_{GC} \approx 1$) means that R_p is more likely to be correct and thus the theoretical tidal radius estimates should be in better agreement with the observational tidal radius estimates. Thus the relative difference X_{err} is expected to decrease as R_P/R_{GC} increases, i.e. the theoretical and observational estimates will converge as the cluster is observed closer to perigalacticon. This is seen to occur in Figure 6.2 (b) for the clusters listed in Table 6.3. From Figure 6.2 we conclude that the relative difference between the observational and theoretical tidal radius estimates depend on both the orbital eccentricity and phase.

The tidal radii for the globular clusters in Table 6.3 are plotted against the perigalacticon of the cluster orbit in Figure 6.3. The observed tidal radii are shown as data points in this figure and are colour coded by eccentricity depending on whether it is closest to $e = 0.2$ (red), $e = 0.5$ (green) or $e = 0.8$ (blue). The theoretical tidal radii as a function of perigalacticon distance also

(a) Relative difference $|X_{err}|$ against the orbital eccentricity

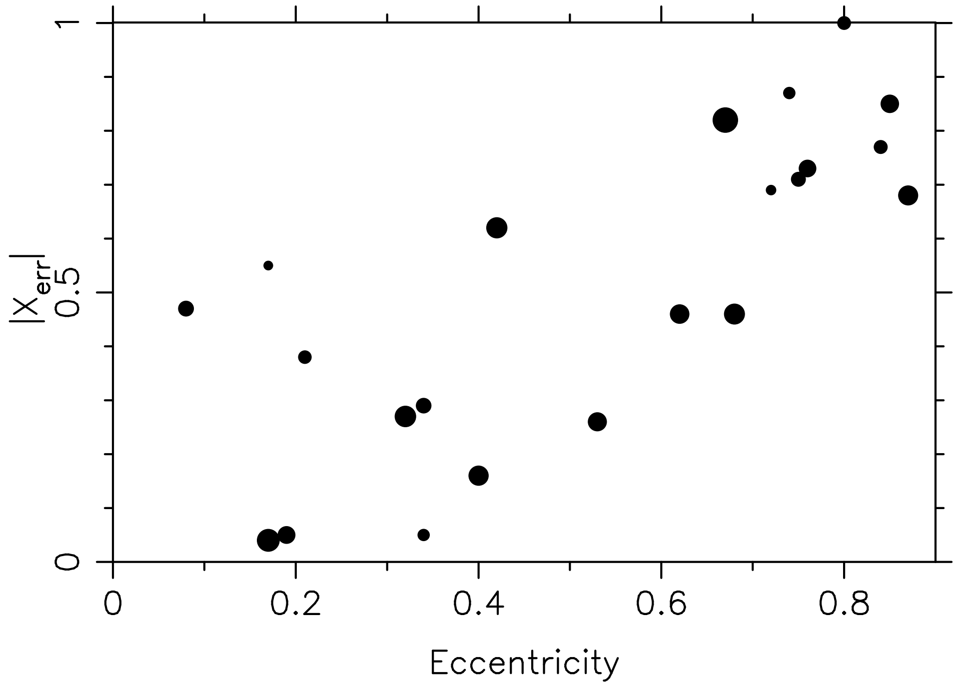

(b) Relative difference $|X_{err}|$ against the orbital phase

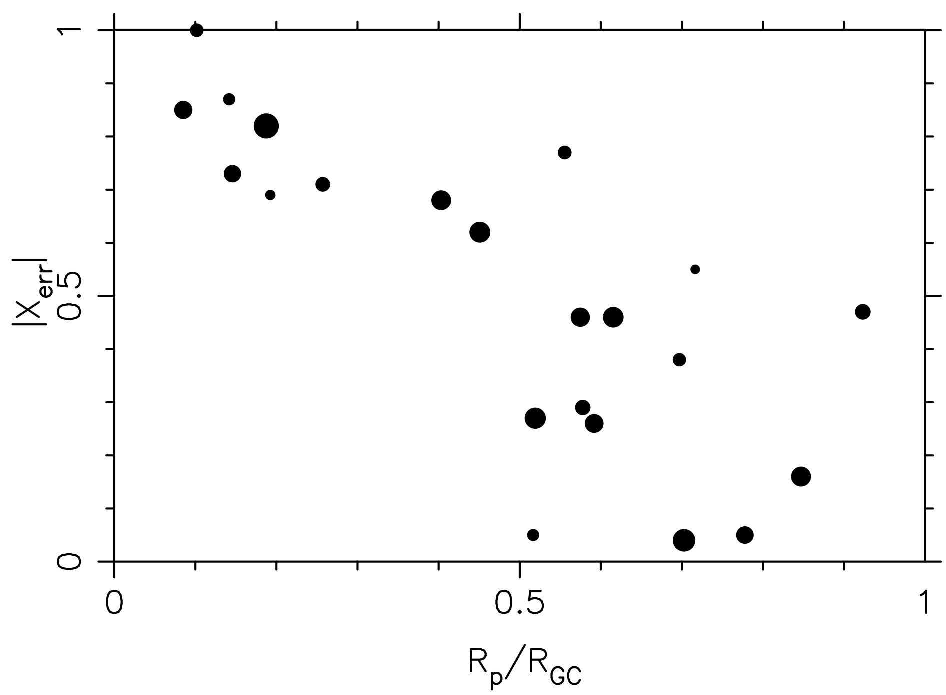

Figure 6.2: The dimensionless relative difference between the observed tidal radii and the predicted tidal radii using MSC, $|X_{err}|$, against the orbital eccentricity (top panel) and orbital phase (bottom panel) for the clusters presented in Table 6.3. The sizes of the data points indicate the observed mass of the cluster for which no correlation is seen to $|X_{err}|$. A correlation is seen between $|X_{err}|$ and the orbital eccentricity of GCs. The bottom panels shows $|X_{err}|$ decreasing as the cluster is observed closer to perigalacticon ($R_p \approx R_{GC}$).

appear in Figure 6.3 using the same colour code for eccentricity but are determined for a cluster of $M_C = 10^6$ rather than each individual cluster mass for simplicity. The tidal radii associated with the MSC prediction are shown as solid lines, the Read radius as dashed lines and the King radius as dotted lines. This figure is similar to Figure 5.11 which examined the tidal radii of simulated clusters compared to theoretical estimates.

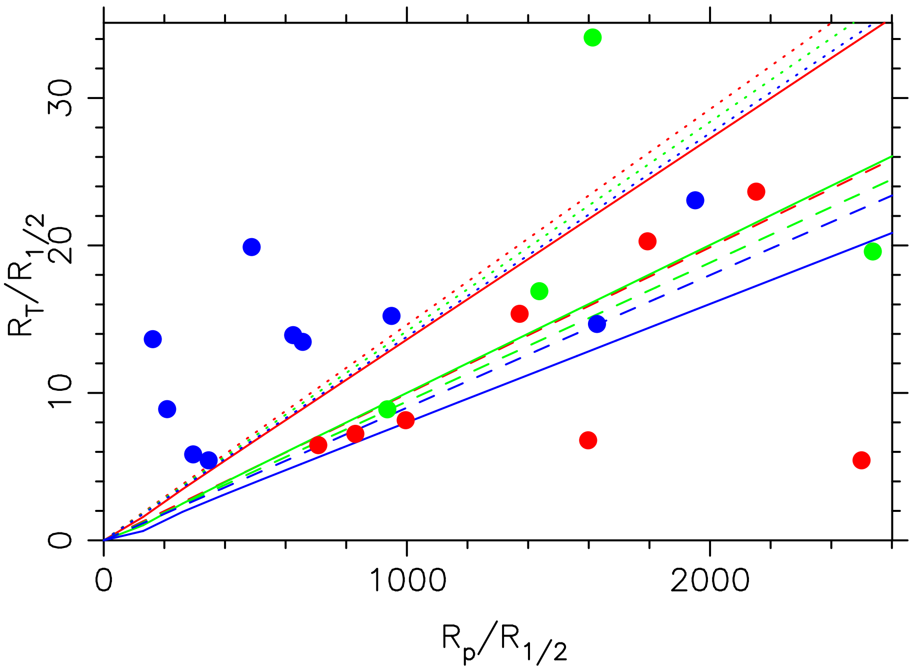

Figure 6.3: Tidal radii for observed clusters in the MWGCS from Table 6.3 (data points) compared to theoretical determinations (lines) for a cluster mass of $10^6 M_\odot$. Both the tidal radii and perigalacticon distances are in units of the half-mass radii, $R_{1/2}$. Predictions for the tidal radii based on the MSC are indicated with solid curves, while theoretical determinations from the literature are shown using the King radius (dotted line) and the Read radius (dashed line). The theoretical curves for eccentricity $e = 0.2$ (red), $e = 0.5$ (green) and $e = 0.8$ (blue) are determined for a cluster mass of $10^6 M_\odot$ rather than the individual cluster masses used for the estimates given in Table 6.3. Observed cluster tidal radii are colour coded by the closest eccentricity $e = 0.2$, 0.5 or 0.8 to the orbital eccentricity given in Table 6.3.

It is convenient to divide the clusters into two groups by their galactic eccentricities. The boundary between these groups is set at $e = 0.65$, which means that the high eccentricity clusters are the blue dots in Figure 6.3. The low eccentricity group of globular clusters have tidal radii that are generally consistent with the theoretical estimates, including the tidal radii predicted using the MSC.

In contrast, most of the high eccentricity clusters have significantly larger tidal radii than predicted by any of theoretical estimates for these orbital parameters, as seen in Figure 6.3. Clusters in this group with tidal radii far exceeding the theoretical estimates are NGC 288, NGC 362, NGC 5139 (ω Cen) and NGC 6121.

There are two possible explanations for the observed tidal radii of clusters to be larger than the theoretical estimates. These are that the orbital parameters are in error, or that stars have had insufficient time to escape the cluster. All theoretical tidal radii discussed here assume an instantaneous removal of stars, which is equivalent to treating particles on unstable orbits predicted using the MSC as instantly escaping particles. Estimates of the tidal radii in the literature examined here (Section 2.4) are determined from the distance from the cluster centre where the acceleration of the particle from the cluster and galaxy cancel. Such particles are then assumed to be lost to the cluster for all time, an assumption that is highly questionable as discussed by (Fukushige and Heggie 2000). The timescale argument is more applicable to clusters orbiting close to the galactic centre where the cluster orbit may be changing faster than stars can escape the cluster, thus leading to anomalously large observed tidal radii.

For clusters on long period orbits, such as those of interest to this study, the discrepancy between the observed tidal radii and the theoretical tidal radii are most likely the result of errors in the orbital parameters R_P and e. This conclusion is supported by the correlations found for the relative difference in observational and theoretical tidal radius estimates X_{err}. Firstly, this difference was found to increase with increasing orbital eccentricity, as expected by the uncertainties in the tangential velocity components discussed in Section 6.1. Secondly, the relative difference X_{err} increased the further the cluster was from perigalacticon in its orbit with the galaxy.

Unfortunately the lack of clarity in the orbital parameters of clusters in the MWGCS means that we cannot use the observed tidal radii to distinguish between different theoretical models. In particular the dependence of the tidal radius on galactic orbital eccentricity is predicted to be stronger by the MSC than by the Read radius (Read et al. 2006). This is clearly seen in Figure 6.3 with the spread of tidal radii from the MSC estimates (solid line) being much larger than for the Read radius (dashed lines). Future N-body simulations may be able to distinguish between these models, using a similar methodology based on the fraction of escaping stars over time as described in Chapter 5. We will return to this topic in the next chapter and discuss the relative merits of using the MSC to estimate the tidal radii against the Read radius.

Both the Read radius and the MSC predicted radius were found to be good estimates of the tidal radii for simulated clusters in the previous chapter; see Figure 5.11. Therefore if we assume that these radii accurately predict the tidal radii for clusters with known galactic orbits, then we can use them to comment on the probability of a given set of orbital parameters to be correct. This analysis can only be used as a guide since the difference between observational and theoretical tidal radius estimates was also found to depend on the phase of the cluster-galaxy orbit.

We outline a simple procedure for rejecting unlikely sets of orbital parameters based on observational quantities with relatively low uncertainties. Beginning with the observed cluster mass and the tidal radius an equivalent period of a star-cluster orbit is estimated. The estimate for the period of the star-cluster orbit T_i can be based on any potential model for the cluster, such as the $b = 1$ Plummer model used to determine the fitting formulae for the period given by Equation (3.23). The tidal radius is typically at large distances from the centre of the cluster where the cluster potential can sufficiently be described by a point mass potential. Next perform orbital integrations for the cluster using a range of velocities drawn from within the error range of the observed velocities. Combinations of the cluster's orbital period P and eccentricity e are rejected if $P < \sigma_u T_i$, where σ_u is the transition from unstable to stable orbits predicted by the MSC and is function of e only. The behaviour of σ_u is based on the three-body point mass problem, so is not dependent on the choice of the cluster potential. The dependence of σ_u on the eccentricity of the cluster-galaxy orbit is shown in Figure 4.4 (a), along with the associated transition width values $\sigma_{min/max}$.

This chapter has compared the tidal radius of observed clusters from the Milky Way to estimates using the MSC and theoretical estimates from the literature (King 1962; Read et al. 2006). We favour the idea that the discrepancies between the theoretical and observed tidal radius estimates are likely caused by two factors: (1) the generally high eccentricities determined due to uncertainty in the observed cluster velocities (discussed in Section 6.1) and (2) observing GCs far from pericentre which compounds the uncertainties in the orbital parameters of the GCs. A procedure for constraining the orbits of GCs using the MSC predictions has been outlined.

The tidal radii predicted by the MSC and the Read radius (Read et al. 2006) have a different dependence on eccentricity that cannot be distinguished using current cluster observations. Differences between these models were tested using simulated clusters in Chapter 5 and will be discussed along with a summary of this work in the next chapter.

Chapter 7

Summary and discussion

The aim of this project was to estimate the tidal radius of globular clusters (GCs) on eccentric orbits using the Mardling stability criterion (MSC) described in Chapter 1. The tidal radius estimated using the MSC was compared with theoretical estimates from the literature, numerical cluster models and observational estimates for clusters from the Milky Way globular cluster system.

Traditionally the tidal radius for a cluster has been estimated by the distance from the cluster centre corresponding to equal accelerations on a star from the cluster and the tidal field of the galaxy. Stars at this distance from the cluster centre are considered to be instantly stripped from the cluster by the tidal field of the galaxy. The dangers of assuming that the tidal radius acts as an instant remover of stars has been pointed out by Fukushige and Heggie (2000). They found that for GCs on circular orbits the escape timescales for stars beyond the tidal radii could be long enough to allow some stars to stay in this region indefinitely. Two tidal radius estimates from the literature were used in this study for comparison with predictions using the MSC, these were the classical result referred to as the King radius (King 1962) and a recent determination for particles on prograde orbits referred to as the Read radius (Read et al. 2006). The King radius considered a particle on a radial orbit in the rotating frame of the cluster and used point mass potentials to determine where the acceleration on this star was zero in this frame. The Read radius extended this analysis to particles on circular prograde orbits. The Read radius was found to give good estimates compared to N-body simulations (Read et al. 2006), and is used as a benchmark estimate for GCs on short period galactic orbits.

The tidal radius has been estimated here using the stability boundary between unstable and stable orbits in the outer regions of the cluster. An unstable orbit refers to a star-cluster orbit that is unstable to the escape of the star from the cluster. Such stars will eventually escape the cluster via a random walk in their binding energies. Since the MSC approach does not assume that stars are instantly stripped from the cluster, as other theoretical approaches do, we take these predictions to be more reliable.

Using the MSC to estimate the tidal radius of a cluster has three main advantages over estimates based on equal accelerations. Firstly, the stability analysis that underlies the MSC is based on physical principles, as discussed in Section 1.3.2. Secondly, it predicts a range of distances from the cluster centre for which star-cluster orbits can be found that are unstable to escape. The range of distances also increases with the orbital eccentricity of the cluster-galaxy orbit, which in principal allows the tidal radius estimates using the MSC to be distinguished from previous studies. Finally, the MSC predicts that stars can be on unstable orbits interior to the tidal radius estimates from the literature. This final point means that more stars can potentially escape the cluster than through tidal stripping, which has implications for the orbital decay of GCs and dwarf spheroidal galaxies (discussed below).

The MSC was applied to the star-cluster-galaxy system in Chapter 4 by approximating the star, cluster and galaxy as point masses. This allowed the same method for determining the stability of systems given in Section 1.3.2 to be used for this system. To examine whether the gravitational potential of the cluster makes a difference to the stability of the star-cluster-galaxy system numerical stability experiments were conducted for the three-body system. For the numerical experiments the potential of the cluster was modelled by a Plummer potential, which was studied in detail in Chapter 3.

Unlike the point mass potential, the Plummer potential lacks a simple equation relating the orbital period and eccentricity to the position and velocity vectors. This meant that the orbital period of a star in a Plummer potential (T_i) in terms of the binding energy (E_i) and apocentre distance ($R_{a,i}$) had to be related using fitting formulae given by Equations (3.22) and (3.23) respectively. The orbital eccentricity (e_i) was determined from the minimum and maximum cluster distances using numerical orbit integrations using Equation (3.19) and the distribution of eccentricities was shown in Figure 3.4.

The fraction of unstable orbits predicted using the MSC as a function of the ratio of the periods (σ) for the cluster-galaxy orbit (T_o) to the star-cluster orbit (T_i) was found in Chapter 4 to compare favourably to numerical stability results for a star in a Plummer potential. Comparison to the predicted stability results required that the numerical stability results be presented as a function of σ and e_i, which was made possible by the fitting functions determined in Chapter 3.

The tidal radius was estimated using the stability predictions of the MSC in the following way. Firstly, the fraction of unstable orbits ($f_{unstable}$) as a function of σ was determined by averaging over the distribution of eccentricities for particles in a Plummer sphere using the cumulative distribution function given by Equation (3.21). The fraction of unstable orbits was then characterised by the lowest σ for which $f_{unstable} < 0.95$ (σ_{min}), the greatest σ for which $f_{unstable} > 0.05$ (σ_{max}) and the lowest σ for which $f_{unstable} < 0.10$ (σ_u). The last of these, σ_u, is used as a representative value to estimate the tidal radius of the cluster with the other values indicating the range over which stars may also escape the cluster. The dependence of these values on the orbital eccentricity of the cluster-galaxy orbit can be seen in Figure 4.4. Using the fitting formulae provided in Chapter 3, the period ratio σ_u is converted into an associated binding energy E_U or apocentre radius R_U for a known period of the cluster-galaxy orbit T_o; similarly for σ_{min} and σ_{max}.

This study was particularly interested in the tidal radii of GCs on long period and eccentric galactic orbits. Currently such orbits are not possible to simulate using direct N-body models with realistic numbers of stars (N). These orbits are also very difficult to get observations of their tangential velocities and so their orbital parameters are largely unknown (see below). So while their tidal radii can be observed we cannot make meaningful comparisons with theoretical estimates since their orbital eccentricities and perigalacticon distances are unknown. In order to study GCs with such long periods, a simplified cluster model (SCM) was developed, which neglects the mutual interaction between particles and treats the galaxy as a point mass. As we are interested in orbits with wide perigalacticon distances then the point mass galaxy approximation is valid since the clusters are not subject to other destructive processes, such as dynamical friction and tidal shocking, as discussed in Section 2.3.

The simplified cluster model presented in Chapter 4 was an extension of the Plummer model presented in Chapter 3 and allowed the computationally efficient treatment of GCs on eccentric orbits at the cost of excluding the mutual interaction between stars. It consists of N particles orbiting a cluster core particle, which itself orbits a galaxy particle. The core particle is associated with the centre of the Plummer potential and moves in response to the positions of the N particles. This feedback resulted in the mixing of particle orbits near the core (see Figure 5.2) but is not equivalent to two-body relaxation, which is ignored in the SCM since the N particles cannot mutually interact. Neither of these processes was found to alter the orbits of stars in the outer regions of the cluster, except for GCs on close galactic orbits. This approach meant that the number of operations required scales as $\mathcal{O}(N)$ rather than $\mathcal{O}(N^2)$ for N-body simulations.

The SCM was tested against a direct N-body cluster model provided by Holger Baumgardt, then at the University of Tokyo. The SCM used $N = 10000$ particles distributed in a Plummer sphere with compactness parameter $b = 0.45$ by the method given in Section 3.1, which had the same density profile as the $N = 50000$ particles used in the N-body model. Both models used a cluster on a galactic orbit with eccentricity 0.5, a perigalacticon distance of 500 times the half-mass radius of the cluster and a mass ratio of the galaxy to the cluster of 10^5. Two assumptions built into the SCM were also tested in Chapter 5. These were that particles on unstable orbits will quickly escape the cluster, and that ignoring relaxation does not affect the outer regions of the cluster. The first of these was found to be valid providing the cluster has time to complete approximately six galactic orbits, as shown in Figure 5.12. The relaxation timescale was shown not to affect the tidal radii comparisons between theory and simulated clusters, as indicated by Figure 5.13. However, the relaxation timescale in the outer regions is short enough to affect the escape of stars in observable clusters.

In Chapter 4 it was found that the SCM slightly underestimated the loss of stars from the outer regions of the GC compared to the N-body results. However, this may be due to the instantaneous removal of stars with positive binding energy by the N-body simulation. The average behaviour of escaping stars between the two models was very similar. Thus it was concluded that the core particle approximation and two-body relaxation did not affect the results for escaping stars on wide orbits for the first two cluster-galaxy orbits.

A parameter search across was conducted three values of the eccentricity ($e_o = 0.2$, 0.5 and 0.8) and nine of the perigalacticon distance ($p_o = R_P/R_C = 200$, 300, ..., 1000) of the galactic orbit of the cluster using the SCM. Each simulation was run for 20 galactic orbital periods of the cluster, which would be extremely computationally intensive for a direct N-body model. For comparison the simulation with the longest period examined here ($p_o = 1000$ and $e_o = 0.8$) took 101 CPU hours on a single 2.3 GHz processor. The fraction of escaping stars as a function of the initial binding energy of the star was used to estimate the tidal radius for each of these simulated clusters. The resulting tidal radius estimates were compared to the theoretical using the MSC, and from the literature, in Figure 5.11. These results showed that tidal radius estimates predicted using the MSC, and the Read radius (Read et al. 2006), were in good agreement to the tidal radius estimated from the escape of stars in the SCM.

Figure 5.11 showed the predicted tidal radii using the MSC (solid lines) and the Read radius (dashed lines) against the perigalacticon distance. The major difference between these theoretical estimates is the spread in tidal radius estimates caused by the eccentricity of the cluster-galaxy orbit. The MSC predicts this spread to be much larger than the Read radius does. Unfortunately, neither the tidal radii results from the simulated clusters nor for observed clusters (below) were able to indicate which of these theoretical estimates was more accurate. We expect that the tidal radius estimates using the MSC are more accurate since they were found to correctly predict the fraction of unstable orbits for three-body models of the star-cluster-galaxy system in Chapter 4 for a wide range of eccentricities and period ratios, as shown in Figure 4.8. By contrast the Read radius only compared to two N-body simulations, one with perigalacticon distance $R_P/R_{1/2} = 267$ and eccentricity $e_o = 0.0$ and the other with perigalacticon distance $R_P/R_{1/2} = 77$ and eccentricity $e_o = 0.57$ (Read et al. 2006). In this low galactic period regime tidal radius estimates for the MSC and the Read radius were in agreement. N-body simulations of wide separation clusters on eccentric orbits will be required to distinguish these models, but will only be possible when computing power increases.

In Chapter 6 the orbital parameters for the Milky Way globular cluster system (MWGCS) have been determined for 53 GC orbits by numerically integrating their observed positions and velocities through a realistic galactic potential. The positions and tidal radius estimates for each cluster were taken from Harris (1996), while the velocities and cluster masses were found from a variety of sources. For clusters with available velocity measurements, the orbital eccentricity, perigalacticon distance, mass and the corresponding references from the literature for each cluster were summarised in Table 6.1. The errors associated with the orbital parameters were found to be dominated by the observed tangential velocity components, as discussed in Section 6.1 and shown in Table 6.2. The orbital parameters presented in Table 6.1 are consistent with Allen et al. (2006) and Allen et al. (2008), within the uncertainties caused by the velocity measurements.

Observed tidal radii are themselves estimates based on the fall off of light from the centre of each cluster. The observed tidal radius estimates for 22 globular clusters with quoted masses in the literature were compared to theoretical tidal radius estimates in Table 6.3. The theoretical tidal radius estimates presented in this table were the King radius (King 1962), the Read radius (Read et al. 2006) and the three radii predicted by the MSC to cover the range of orbits that stars will eventually escape the cluster (R_U, R_{min} and $Rmax$). The observed GCs were divided into a high and low eccentricity group, using $e = 0.65$ as the boundary separating these groups. For the low eccentricity group the theoretical estimates are generally consistent with the observed tidal radius estimates for each cluster. The high eccentricity group has significantly larger observed tidal radii than predicted by any of theoretical estimates for these orbital parameters, as seen by the blue data points in Figure 6.3.

There are two possible explanations for the observed tidal radii of clusters being larger than the theoretical estimates, as was found for most of the high e group. These are that the orbital parameters are in error, or that stars have had insufficient time to escape the cluster. For most clusters the first of these is considered to be more likely since stars on unstable orbits will have had time to random walk out of the cluster, as indicated in Figure 5.12. Recall that the errors in the orbital parameters for GCs are dominated by uncertainties in the tangential velocity components. Therefore differentiating between theoretical models is difficult and requires more accurate cluster velocity determinations and/or wide field observations of globular cluster tidal tails, as discussed by Montuori et al. (2007). In the meantime, theoretical tidal radii determinations for these orbits can be used to constrain observations by rejecting improbable orbital parameters for clusters in the MWGCS. A procedure for achieving this using the MSC is given in Section 6.2.

The other possible explanation for observed tidal radii being larger than theoretical estimates is that stars have had insufficient time to escape the cluster. This is expected for some clusters since the escape timescales for stars beyond the tidal radii can be long enough to allow some stars to stay in this region indefinitely (Fukushige and Heggie 2000). This scenario is discussed by considering two of the more massive clusters in the MWGCS, NGC 104 (47 Tuc) and NGC 5139 (ω Cen), both of whose orbits are shown in Figure 6.1. The orbital parameters for these clusters differ greatly (Table 6.1) with ω Cen approaching closer to the galactic centre and having a higher eccentricity. The difference between the theoretical and observed tidal radius for 47 Tuc is small enough to be explained by a slight error in the orbital parameters of the cluster, but the same is not true of ω Cen. Even if ω Cen was on a circular orbit at its presently observed position (6.4 kpc from the galactic centre), it would still have an observed tidal radius (13.6 times its half-mass radius) greater than any theoretical estimate (e.g. 8.3 $R_{1/2}$ for the Read radius). Therefore the underestimation of the tidal radius for ω Cen may not be the result of velocity uncertainty alone.

Fellhauer and Kroupa (2003) first suggested ω Cen to be an ultra compact remnant of a dwarf spheroidal galaxy, captured by the galaxy from a near radial orbit. This scenario is also favoured by recent N-body simulations (Tsuchiya et al. 2004; Ideta and Makino 2004). We found that ω Cen fits this scenario well, since it must have had a far larger initial mass to have the observed mass and tidal radius at its galactic position. Current galaxy formation mechanisms are consistent with this origin of ω Cen. Hierarchical galaxy formation begins with numerous small galaxies combining to form larger galaxies through the process of galactic cannibalism (e.g. Burstein et al. 2004). The destruction of small galaxies is one explanation for the discrepancy between cosmological simulations and the lack of observed dwarf galaxies, referred to as the missing satellite problem (Kravtsov et al. 2004).

The transition between unstable and stable orbits predicted by the MSC and used to model the tidal radius for a cluster can be generalised to the problem of capturing dwarf spheroidal galaxies. Indeed the resonance stability criterion that underlies the MSC was originally developed for the binary tides problem (Mardling 1991), which has since been used to capture passing stars. Therefore it is a natural extension of this project to investigate the capture of a passing dwarf spheroidal galaxy by a larger galaxy.

Consider a dwarf spheroidal galaxy (DSG) on a parabolic orbit with respect to the Milky Way. At this point the MSC predicts that all stars within the DSG are on unstable orbits. As discussed in Section 1.3.2, while this statement is correct it does not allow us to distinguish between exchange and escape. For the star-DGG-galaxy system an unstable system will eventually end with the escape of a star (i.e. an exchange process) or the escape of the DSG and star (equivalent to the escape of the galaxy particle). There exists a critical pericentre distance (R_P) above which the escape of the DSG is favoured and below which a star is more likely to escape (Mardling 2008, private communication). This situation is illustrated in Figure 1.6 (b) with m_3 representing the galaxy in this case. If a star escapes the DSG then some energy is lost from the DSG-galaxy orbit, which may become bound if enough stars are lost during the encounter.

For now we will use the Read radius (Read et al. 2006) to estimate what happens to stars inside the DSG during the encounter with the galaxy. The Read radius (Equation 2.5) can be written as

$$R_{Read} = R_P \left(\frac{M_C}{M_G} \right)^{1/3} f(e) \tag{7.1}$$

where M_C and M_G are the mass of the DSG and galaxy respectively, R_P is the distance at closest approach, and $f(e) = 0.4061$ when $e = 1$ and $f(e) = 0.4116$ when $e = 0.9$. If a DSG on a parabolic orbit loses most of the stars beyond this radius then the DSG may become bound to the galaxy. Once the DSG is on a bound orbit we can use the MSC as presented in Section 1.3.2 to predict the boundary between stable stellar orbits in the interior and unstable orbits in the outer regions of the DSG. Assuming that the orbital period of a star at this distance is Keplerian, then the radius beyond which stars are unstable to escape from the cluster is estimated by the MSC as

$$R_U = R_P \left(\frac{M_C}{M_G} \right)^{1/3} g(e) \tag{7.2}$$

where

$$g(e) = \frac{[\sigma_u(e)]^{-2/3}}{1 - e} \tag{7.3}$$

and the dependence of σ_u on the eccentricity e for $M_C/M_G = 10^{-5}$ is shown in Figure 4.4. Note that the form of R_U in Equation (7.2) is equivalent to that of the Read radius, except for the dependence on the eccentricity. For $e = 0.9$ $g(e) = 0.2924$, which is approximately 70% of the Read radius value of $f(e) = 0.4116$. This means that once the galaxy has captured the DSG, there will be more stars able to escape the cluster from unstable orbits than expected by tidal striping.

From this simple case study we see that the tidal radius estimated using the MSC and using the Read radius can be used to understand the decay of DSG orbits. The MSC predicts that stars on unstable orbits will significantly contribute to the mass loss of a distant DSG. As more mass is lost from the cluster the binding energy decreases, i.e. the orbital period decreases, and the DSG is brought closer to the galactic centre.

Orbital decay via mass loss is also expected to occur for globular clusters on distant orbits. This process may allow GCs to be brought close to the galactic centre where they are subject to further orbital decay due to tidal shocks and dynamical friction. A detailed examination of this process is beyond the scope of this work. The decay of GC orbits will produce in-falling clusters which have been theorised to form part of the galactic bulge (Capuzzo-Dolcetta 1993). This argument is strengthened by numerical modelling of decaying globular cluster orbits in elliptical galaxies, whose conditions are similar to bulges in spiral galaxies (Capuzzo-Dolcetta 2004).

Part II

Dynamics of binary stellar systems in galactic centres

Chapter 8

Introduction

8.1 Summary

Sufficiently close encounters between a stellar binary and a massive black hole (MBH) will result in the tidal disruption of the binary. This causes one binary to be captured by the MBH and the other to be ejected from the system with high velocity. This is referred to as the Hills mechanism and is examined in this project using numerical scattering experiments and the Mardling stability criterion (MSC). The tidal disruption of binaries by a MBH was initially studied by Hills (1988) who predicted the ejection of hypervelocity stars (HVS), recently discovered in the Milky Way by Brown et al. (2005).

In recent years the existence of MBHs in the centres of galaxies has moved from being theoretically possible to almost certain. In previous decades most studies have concentrated on understanding the role of MBHs as the engines of active galactic nuclei. The observations of stars in galactic centre has only been possible in the past decade, making the stellar conditions in the centre of the Milky Way a fertile topic. In particular this renewed interest in the galactic centre has been fuelled by recent observational studies of stellar motions (Ghez et al. 2000, and Schödel et al. 2003), HVS (Brown et al. 2005) and stellar tidal disruption events from the inner regions of spiral galaxies (Komossa et al. 2004).

The observation of young stars on short period orbits with a dark mass of $3.4 \times 10^6 \mathrm{M}_\odot$, the S-stars (Schödel et al. 2003), poses particular difficulties for star formation theory. These stars have pericentre distances within 0.04 parsecs of the central mass, which is far closer than any other observable stellar population. Star formation is suppressed in regions of strong tidal fields, making the in situ formation of these stars in the galactic centre improbable. For a good general review of the theory of star formation the reader is referred to Phinney (1989).

The stellar populations in the galactic centre are discussed in Section 8.2 but can be summarised by three populations. These are the S-stars in the innermost 0.04 parsecs, the stellar disks observed from approximately 0.04 to 0.4 parsecs and the stellar cusp that includes many young clusters (Alexander 2005). The last of these populations is outside the dynamical sphere of influence of MBH, which is approximately 3 parsecs (Alexander 2005). Note that these populations should be taken as guides only since only young, bright stars can be observed in the inner 100 pc.

Star formation in dense gaseous disks (see, for example, Levin and Beloborodov 2003, Milosavljević and Loeb 2004 and Bonnell and Rice 2008) can explain the observed two disks of stars at ~ 0.1 pc (Paumard et al. 2006), but the Hills mechanism is still required to explain the extremely short period S-stars (Löckmann et al. 2008). Therefore the existence of the S-stars means that either star formation can occur in much stronger tidal fields than predicted by theory or that some mechanism can scatter stars and binary systems closer to the MBH.

Scattering experiments of the tidal disruption of a stellar mass binary system by a MBH are conducted in Chapter 9. The barycentre of the binary is taken to be on either parabolic ($e_o = 1.0$) or eccentric orbits ($e_o = 0.9$) and three values are adopted for the orbital eccentricity of the binary itself ($e_i = 0.0$, 0.4 and 0.7). All scattering experiments cover a wide range of pericentre distances and the full range of relative inclinations between orbits and examine their effect on the probability of binary disruption. This study is the most comprehensive numerical examination of the fine detail involved in the Hills mechanism known by the author.

The maximum pericentre distance for which the binary was disrupted is found to depend on the orbital eccentricity of the stellar binary and its relative inclination to the binary-MBH orbit. For parabolic orbits this distance is compared to two theoretical estimates from the literature (Hills 1992; Heggie et al. 1996), given in Section 9.1.

A similar study of parabolic binary-MBH orbits using binaries composed of massive stars to produce the S-stars appears elsewhere (Gould and Quillen 2003), however this study did not closely examine the effect of the pericentre distance of the binary-MBH orbit and the relative inclination between this orbit and the binary orbit. (Gould and Quillen 2003) did find some inclination dependence in their overall results but did not break this down by the stellar binary eccentricity or the pericentre distance of the binary-MBH orbit. Here we provide high-resolution scattering experiments for how the disruption of a binary depends on the orbital eccentricity of the binary and its relative inclination to the binary-MBH orbit.

The Mardling stability criterion (MSC), introduced in Section 1.3.2, is used to predict the stability for bound binary-MBH orbits with eccentricity $e_o = 0.9$ in Chapter 10. Detailed comparisons are made between the scattering results and the predicted fraction of unstable orbits using the MSC as a function of the pericentre distance and the relative inclination between orbits. Recall from Section 1.3.2 that the MSC predicts the stability of three-body systems but does not predict the final configuration of the system. For mass ratios in this region essentially all unstable systems will involve the exchange of one binary component for the MBH, thus forming a new star-MBH binary. Despite not explicitly covering exchange processes, the MSC is found to provide a good estimate of the maximum pericentre distance for bound orbits that can result in the disruption of the binary.

An orbital eccentricity for the binary-MBH orbit of $e_o = 0.9$ is chosen for two reasons. Firstly for a given pericentre distance the orbital period is ten times longer than $e_o = 0.9$ for $e_o = 0.99$ and 100 times longer for 0.999 etc. Secondly the resonance widths using in the MSC do not significantly change for high values of e_o (see Figure 1.6 a) and therefore the results are expected to be very similar between $e_o = 0.9$ and higher values (Mardling 2008, private communication). This choice of the binary-MBH eccentricity is expected to be indicative of repeat encounters between binaries and MBHs. Thus it will serve as an analogue to parabolic binary-MBH orbits when the effect of inclination and binary eccentricity are examine in Chapter 10.

We conclude this study into the Hills mechanism by using the scattering results for parabolic binary-MBH orbits to predict the distribution of velocities of hypervelocity stars (HVS) as they leave the Galactic centre. Comparing this distribution to the observed velocity distribution of HVS allows one to constrain the gravitational potential of the galaxy and the details of the dynamical interaction that ejected them.

Our investigation into the Hills mechanism is organised as follows. Firstly the conditions in the galactic centre are summarised in Section 8.2, then recent observations of the S-stars and HVS are summarised in Section 8.3 and their impact on constraining dynamical mechanisms are discussed in Section 8.4. Of these possible dynamical processes the Hills mechanism is selected as the simplest and most comprehensive. Two estimates are taken from the literature for the maximum distance of closest approach where the Hills mechanism can tidally disrupt an in-falling binary, and are discussed in Section 9.1.

Chapter 9 presents results from scattering experiments for an equal mass binary encountering the MBH on parabolic and bound ($e_o = 0.9$) orbits. This chapter also compares the maximum pericentre distances for which the binary is disrupted to theoretical estimates and finds a significant dependence on the binary eccentricity and relative inclination. To examine this dependence on a closely related system the MSC is applied to bound binary-MBH orbits in Chapter 10.

The results from Chapter 9 are combined with approximate distributions of the pericentre distance, the binary semi-major axis and the component masses to predict the velocity distribution of HVS in Chapter 11. Each chapter builds upon the results of the previous chapters, so all results are summarised and discussed in Chapter 12.

8.2 Galactic centre environment

This study is interested in encounters between stellar binaries and the MBH that occur within 0.04 parsecs at closest approach. Stars cannot be formed in this region as so a brief examination into the possible origin and orbital parameters of these binaries in the galactic centre is required.

The galactic centre is located 7.9 ± 0.4 kpc (Eisenhauer et al. 2003) from the Sun in the direction of the Sagittarius constellation. A MBH is thought to reside in this region and is associated with the radio source Sgr A*, which is known to experience sporadic X-ray events consistent with the accretion of comet mass objects (Bananoff et al. 2001). The stellar distribution in the galactic centre can be divided into three populations (Alexander 2005). The first of these is the stellar cusp that begins at a distance of 0.4 pc from the MBH and extends outwards into the galactic bulge stellar population. This population includes bound star clusters and contains significant quantities of gas from which more stars can form. The stellar cusp also extends beyond the dynamical sphere of influence of MBH, which is approximately 3 parsecs (Alexander 2005). Binaries scattered in from this stellar population on orbits whose pericentre distance is within 0.04 parsecs of the MBH must be on nearly radial orbit.

The second stellar population is located between 0.04 and 0.4 pc and consists of multiple stellar disks on eccentric orbits with respect to the central MBH (Paumard et al. 2006). Star formation is thought to be possible in gas disks themselves (Levin and Beloborodov 2003) or from in-falling giant molecular clouds Bonnell and Rice (2008) both of which may be responsible for the stellar disks. These disks orbit the MBH with eccentricities up to about 0.8 based on Figure 17 of (Genzel et al. 2003). This means that binaries scattered from these stellar disks can have a wide range of orbital eccentricities relative to the MBH and still have pericentre distances within 0.04 pc.

The final stellar population are indicated by the S-stars and reside within 0.04 pc from the MBH. The full extent of this population is not known since only bright stars can be observed in the inner 100 pc (Alexander 2005). By our current understanding of star formation these stars cannot form this close to the tidal field of the MBH and so must be produced by dynamical interactions. These stars are discussed in detail in Section 8.3.1 and the possible dynamical production mechanisms in Section 8.4.

Having looked at the origin of binaries in the galactic centre we now examine the range of orbital parameters, particular the semi-major axis, of binaries scattered into < 0.04 pc from the MBH. We will assume throughout this work that there is no preferred orientation of the stellar binary with respect to the initial orbit of the binary-MBH. Thus the relative inclination and phase are uniformly distributed across a sphere. The eccentricity is also assumed to be able to take the same values as binaries in the galactic field. This does not affect our results since the orbital eccentricity of the stellar binary is examined using three discrete values ($e_i = 0.0$, 0.4 and 0.7) and not an assumed distribution. The semi-major axis for these binaries is the greatest unknown for binaries encountering the MBH, this is again discussed when the velocity distribution of the HVS is predicted in Chapter 11.

To allow general comments to be made about the semi-major axis the conditions in the stellar cusp as a whole will be considered. Stellar densities within the central parsec of the galactic centre reach $\sim 10^6$ $M_\odot$ pc^{-3} and the velocity dispersion in this region is characterised by relative stellar velocities of $\sigma \sim 150$ km/s (Genzel et al. 2003). This velocity dispersion is due in part to the dynamical influence of the MBH and in part to the stellar population. There is much uncertainty in the total mass of this region, although future observations of the S-stars may be able to better constrain this mass (Mouawad et al. 2005). Even if the total mass of the stellar cusp could be determined it is unknown precisely how much mass resides in compact remnants and how much in stars, since the dense environment make all but the most massive stars difficult to resolve.

As has been mentioned star formation can still occur in the central parsec of the galactic centre and since most stars are thought to form in binary systems (Goodwin et al. 2007) it is reasonable to suppose that a large binary population exists in the galactic centre. These binaries will encounter other stars on a frequent basis, with the average effect of these encounters on the binary population possible to characterise using the concept of hard and soft binaries. The boundary between these is referred to as the hard binary limit and is defined by the maximum semi-major axis for a hard binary in a stellar environment. The hard binary limit is given by (Heggie 1975)

$$a_{crit} = \frac{G(m_1 + m_2)}{\sigma^2}, \tag{8.1}$$

which for equal mass $1\mathrm{M}_\odot$ stars with $\sigma = 150$ km/s is 0.08 AU. Binary systems are divided into two groups using this limit; hard binaries with semi-major axis $a < a_{crit}$ and soft binaries with $a > a_{crit}$. Heggie's law states that on average encounters with passing stars cause the population of hard binaries to become harder and soft binaries to become softer (Heggie 1975). Soft binaries that undergo repeated distant encounters with single stars will on average transfer energy to the kinetic energy of the star, resulting in the binary becoming less bound (i.e. softer). Unlike soft binaries, hard binaries that encounter single stars can temporarily form a bound three-body system. This interaction will result in the ejection of one star and the formation of a binary system that may not be composed of the original binary stars. On average the new binary will be more tightly bound than the original binary system. For a good description of interactions involving hard and soft binaries the reader is referred to Binney and Tremaine (1987).

In a stellar environment of density ρ soft binaries will dissociate on a timescale given by (Binney and Tremaine 1987)

$$t_{evap} = \frac{m_1 + m_2}{m_s} \frac{\sigma}{16\sqrt{\pi} G \rho a \ln \Lambda} \tag{8.2}$$

where $\ln \Lambda$ is the Coulomb logarithm, m_s is the average mass of the surrounding field stars and a is the semi-major axis of the binary. The Coulomb logarithm is approximated by (Binney and Tremaine 1987) $\Lambda \approx \frac{m_s \sigma^2}{|E|}$ where E is the binding energy of the binary, given by Equation (1.8). The widest binary considered here has semi-major axis $a = 10$ AU, which for $\rho = 10^6$ $\mathrm{M}_\odot$ pc^{-3} and $\sigma = 150$ km/s has an evaporation timescale of approximately 4 Myr. This value has important ramifications for the production of hypervelocity stars in Chapter 11.

Assuming the formation of binary systems precedes in the same manner as in the galactic field then a combination of hard and soft binaries will be produced. While it is true that soft binaries will be preferentially disrupted in the galactic centre it remains possible that they can interact with the MBH before they are disrupted by passing stars. The timescale associated with a binary interacting with the MBH is unknown but it is assumed here that it is shorter than the 4 Myr timescale associated with the disruption of a binary with semi-major axis of 10 AU. This allows a large range of semi-major axes for the distribution adopted to produced hypervelocity stars in Chapter 11, but makes no difference to the scale independent scattering experiment results presented in Chapter 9.

The number of soft binaries able to interact with the MBH can be increased if stellar clusters can spiral into the galactic centre (e.g. Gerhard 2001; Portegies Zwart et al. 2002; McMillan and Portegies Zwart 2003). An in-falling stellar cluster will lose most of its mass before reaching the vicinity of the MBH, at which point only the dense cluster core survives (Gerhard 2001). This dense core will be composed of a higher proportion of high mass single stars and binary systems, discussed previously in Section 2.2. The core may also contain intermediate mass black holes (Gualandris and Portegies Zwart 2007), depositing them as close as a few hundred AU of the MBH (Portegies Zwart et al. 2006). The disruption the cores of clusters in the galactic centre will then provide the MBH with the opportunity to interact with a population of binaries from an environment with a different hard/soft limit, which can therefore include binaries with $a > 10$ AU. The reader is referred to Sollima (2008) for a population synthesis model of the effect of dense cluster environments on the time evolution of the fraction and parameters of binary systems.

Recall that we are interested in mechanisms that can scatter binaries to within 0.04 pc of the MBH. Various possible mechanisms are reviewed in Section 8.4 along with alternative interactions involving the MBH. Firstly we will outline the astronomical observations that any potential dynamical process involving the MBH must reproduce.

8.3 Astronomical implications

This project is concerned with the interaction between a stellar binary and the MBH in the centre of the Milky Way. This mechanism will produce captured stars and stars ejected from the galactic centre with high velocities. Therefore two observational discoveries made in the last decade are of great interest to us. These are the discovery of young, $\sim 10\mathrm{M}_\odot$ stars orbiting a single point in the galactic centre (Schödel et al. 2003) and $\sim 4\mathrm{M}_\odot$ stars with velocities greater than the escape velocity of the galaxy (Brown et al. 2005). The first of these discoveries are of captured stars within 0.04 pc of the MBH, commonly called the S-stars, the observed orbits and velocities of which constitute the best evidence for a $3.4\times10^6\mathrm{M}_\odot$ black hole in the galactic centre. The second discovery is of the hypervelocity stars (HVS) observed in the galactic halo, which are generally thought to have originated in the galactic centre $\lesssim$ 200 Myr ago (Brown et al. 2007).

The details of these observations are the subject of Section 8.3.1 for the captured S-stars and Section 8.3.2 for the HVS. Constraints derived from these observations are used to discuss possible production mechanisms in Section 8.4.

8.3.1 Closely captured stars around the MBH in the Galactic centre

The discovery of the S-stars orbiting an intermittent X-ray source (Sgr A*) in the galactic centre is currently the best evidence for a $3.4 \times 10^6\mathrm{M}_\odot$ black hole (Schödel et al. 2003). This black hole mass assumes Keplerian orbits for the S-stars, however they can be equally well fit by non-Keplerian orbits with a central MBH and a dark stellar cusp (Mouawad et al. 2005). Such non-Keplerian motion would manifest as apsidal advance, which has been seen previously for particles in a Plummer potential in Figure 3.3. The study by Mouawad et al. (2005) did not argue against the existence of a central MBH, rather they hypothesised an additional stellar cusp centred on the position of the MBH. Alternatives to the black hole paradigm are reviewed in Miller (2006) with the conclusion that the majority of these theories are ruled out by current observations.

The S-stars have periods ranging from 15 to 340 years and pericentre distances between 0.59 and 8 mpc (120 and 1650 AU). The associated eccentricities range from 0.47 to 0.97 with the more well constrained orbits having eccentricities greater than 0.7 (Schödel et al. 2003). These stars are significantly closer to the galactic centre than star formation theories expect (Phinney 1989), although recent work suggests that close stellar clusters, such as IRS 13E (Paumard et al. 2006), can form from dense gas disks (Levin and Beloborodov 2003; Milosavljević and Loeb 2004). The dynamical interaction between two stellar disks is likely to lead to the formation of the S-stars via the interaction of binaries with the MBH (Löckmann et al. 2008).

In addition to proximity to the MBH the S-stars are spectrally identified as $\sim 10\mathrm{M}_\odot$ main sequence stars that have a main sequence lifetime of ~ 20 Myr (Tout et al. 1997). Based on this timescale any origin scenario must be able to replenish this population within $\lesssim$ 20 Myr. A good review of the problems that the S-stars pose for star formation and dynamical scattering theories alike can be found in Alexander (2005) and more recently in Löckmann et al. (2008). Ramifications of the S-stars for dynamical mechanisms are also discussed in Section 8.4.

An object with a sufficiently small pericentre distance will undergo tidal disruption by the MBH leading to the formation of an X-ray emitting accretion disc. Observations consistent with a 1 $\mathrm{M}_\odot$ object forming an accretion disk around a MBH were recently found in the centre of the spiral galaxy RX J1242-1119 (Komossa et al. 2004). To date only the tidal disruption of comet sized objects have been seen in our galaxy (see for example Bananoff et al. 2001) and similar low mass events have also been observed in other galaxies (Li et al. 2002).

The tidal disruption of a captured star occurs when the tidal acceleration overcomes the binding energy of the star, the distance from the MBH for which this occurs is referred to as the tidal radius. The accretion disk formed by this process will be observable if the closest approach of the star (R_p) lies between the Schwarzchild radius (R_s) and the tidal radius (R_t). If the star is disrupted inside the Schwarzchild radius then no light will escape the black hole and the star is said to have been swallowed whole. The condition for an observable disruption event is equivalent to (Sigurdsson and Rees 1997)

$$R_s = \frac{GM_{BH}}{c^2} < R_p < R_t \approx 2\left(\frac{M_{BH}}{m}\right)^{1/3} r_* \tag{8.3}$$

where c is the speed of light, m and M_{BH} are the masses of the star and MBH respectively and r_* is the radius of the star. This condition is satisfied for a sun-like star disrupted by a black hole of mass $M_{BH} = 3.4 \times 10^6 \mathrm{M}_\odot$, as the Schwarzchild radius is 7.2 $\mathrm{R}_\odot$ and the tidal radius is approximately 1.4 AU. This condition is also satisfied for all stars in the mass range of interest to this study, i.e. $m \lesssim 10\mathrm{M}_\odot$.

Gravitational radiation will cause the orbits of captured stars to decay such that $R_p < R_t$ if the timescale for gravitational decay is less than the age of the galaxy. The timescale for orbital decay via gravitational radiation of a binary of eccentricity e and semi-major axis a is

(Sigurdsson and Rees 1997)

$$t_{GR} = \frac{16}{5}\left(\frac{c^5 a^4}{G^3 M_{BH}^2 m}\right)\left(1 + \frac{73}{24}e^2 + \frac{37}{96}e^4\right)(1 - e^2)^{7/2}. \tag{8.4}$$

When this timescale is less than the age of the galaxy, stars on decaying orbits will eventually pass within R_t resulting in the tidal disruption of the star.

8.3.2 Hypervelocity stars

Hypervelocity stars were predicted by Hills (1988) and have recently been discovered in the galactic halo by Brown et al. (2005). All observed HVS have been identified as $3-4$ $M_{\odot}$ main sequence stars travelling at speeds > 275 km/s at typical distances of 50 kpc from the galactic centre, which is greater than the escape velocity of the galaxy at these distances (see Brown et al. 2007 for a recent list of known HVS). The lower mass limit of these stars is due to current observational studies only able to see bright stars and not due to any physical constraint.

The main sequence lifetimes for 3 and $4M_{\odot}$ stars are approximately 130 and 270 Myr respectively (Tout et al. 1997). This means that the original position of the HVS can be estimated based on their current trajectories and the time constraint imposed by their main sequence lifetimes. This procedure leads to the galactic centre as the likely origin for most HVS (Brown et al. 2007 and references therein). The exception being an 8 $M_{\odot}$ main sequence star possibly ejected from the Large Magellanic Cloud (Edelmann et al. 2005), although this star may also be the result of a binary merger requiring a triple stellar interaction with an MBH (Perets 2008). In the scenario put forward by Perets (2008) the observed star is the result of the stellar evolution of binary merger product and is not an 8 $M_{\odot}$ main sequence star. If this star is a true main sequence star then a galactic centre origin is ruled out, since the required flight time is less than the main sequence lifetime of an 8 $M_{\odot}$ star.

The possibility of hypervelocity stars being produced in the star clusters within the LMC has been investigated by Gualandris and Portegies Zwart (2007). They found that interactions between stellar binaries and an intermediate mass black hole (IMBH) of mass $\gtrsim 10^3 M_{\odot}$ could produce sufficient velocities to explain the observed 8 $M_{\odot}$ HVS. Similar interactions between binaries and IMBHs in the galactic centre can also produce the rest of the HVS population (Yu and Tremaine 2003; Baumgardt et al. 2006). Such IMBHs are expected to form in the dense cores of star clusters through the tidal capture and subsequent merging of stars (Baumgardt et al. 2006). These reside in the centres of clusters and can either eject HVS themselves (Gualandris and Portegies Zwart 2007) or fall into the galactic centre embedded in the cluster until the cluster dissolves leaving the IMBH near the MBH (Portegies Zwart et al. 2006). A similar star cluster origin for HVS being the tidal debris from disrupted dwarf galaxies has recently been suggested by Abadi et al. (2008), although this work is preliminary and not without its short-comings.

Currently there are ~ 10 observed HVS with future surveys expected to yield roughly 100 more (Brown et al. 2007). The kinematic distribution of a sample of this size has significant implications for the understanding of the dynamics in the galactic centre and to probe the luminous and dark matter components of the gravitational potential of the galaxy.

Assuming an origin in the galactic centre then the initial velocity of an ejected star will be considerably larger than the presently observed velocity. This is due to the galactic potential reducing the velocity of the star before it is observed at $\sim$ 50 kpc from the galactic centre (Brown et al. 2007). After these stars have reached a distance of 50 kpc they will have had their velocities reduced by between 20 and 50 percent depending on the galactic mass distribution (Kenyon et al. 2008).

Typical velocities for these stars in the galactic centre must therefore be $\sim$ 1000 km/s before decelerating to $\sim$ 600 km/s by the time they reach the galactic halo. To generate velocities of this magnitude requires extremely violent dynamical interactions. A brief review of the possible dynamical mechanisms that can produce such high velocities is presented in the next section.

8.4 Dynamical mechanisms in the galactic centre

A summary of six possible dynamical mechanisms operating in the galactic centre that can possibly explain the closely orbiting S-stars and the hypervelocity stars is given here. In this study we focus on the interaction between stellar binaries and the MBH in the centre of the galaxy, which can produce both of these observations discussed in the previous section. However we wish to investigate the alternative mechanisms in the galactic centre that may each operate in the galactic centre to some extent.

One or more of these alternatives may be responsible for scattering stars and binary systems to within 0.04 parsecs of the MBH, where they can closely interact with the MBH. Due to the large uncertainty of the nature of the scattering mechanism, an event rate of the order of 10^{-6} per year per galaxy for main sequence stars will be adopted. This event rate is consistent with the estimates by Sigurdsson and Rees (1997) and Yu and Tremaine (2003) for stars encountering the MBH in the galactic centre.

The observational constraints outlined in the previous sections suggest that any mechanism that can generate stars orbiting an MBH and/or HVS must be able to do so within $\sim$ 20 Myr. It is difficult to distinguish between a continuous or discrete process at work in the galactic centre based on the small number of HVS observed (Brown et al. 2007). There is recent evidence suggesting that all of the S-stars may have been created in a single event (Lu et al. 2007), but this could not have been the same event that produced the observed population of HVS, since these were ejected from the galactic centre between 60 and 200 Myr ago (Brown et al. 2007). Note that the short replenishment timescale of scattering objects into the galactic centre ($\lesssim$ 20 Myr) is not much more than the soft binary disruption timescale ($\approx$ 4 Myr from Section 8.2). This means that it is possible for some soft binaries to be scattered towards the MBH before the background field stars disrupt them.

Some of the mechanisms that have been considered in the literature to be capable of producing the HVS and stars on close orbits with the MBH are:

1. The tidal disruption of a binary system by the MBH, also called the Hills mechanism (Hills 1988). For suitable impact parameters one star is captured and the other escapes with increased kinetic energy. Hills (1988) originally predicted that the escaping star could be observed as a HVS. Recently the tidal disruption of massive binaries by the Hills mechanism was also found to produce the S-stars (Gould and Quillen 2003).

2. In-spiralling intermediate mass black holes (IMBH) may exist in close proximity to the MBH. These IMBH may bring a population of stars with them which can interact with each other and the MBH (Yu and Tremaine 2003; Hansen and Milosavljević 2003). Such events are likely to produce HVS in bursts of a few Myr since the IMBH quickly mergers with the MBH (Baumgardt et al. 2006). Hansen and Milosavljević (2003) suggested that a 10^{3-4} $M_\odot$ IMBH falling into the galactic centre via dynamical friction can deposit stars within 0.1 pc of the MBH.

3. The scattering of stars by a cluster of stellar mass black holes centred on the MBH (Miralda-Escudé and Gould 2000). Interactions between stars and stellar mass black holes can produce velocities up to 2000 km/s at rates comparable to the Hills mechanism (O'Leary and Loeb 2008). The fraction of black holes in the central regions of the galaxy will be high as a result of dynamical friction[1] having time to decay the orbits of all stellar mass black holes within 5 pc within the age of the galaxy (Miralda-Escudé and Gould 2000). Alexander and Livio (2004) found that this mechanism can account for up to 25% of the S-stars.

4. The gravitational interactions between stars in the galactic field or within a cluster in close proximity to the galactic centre. Such clusters are young, reside within 100 pc of the galactic centre and are expected to quickly dissolve in the galactic centre but will also be continually replenished (Portegies Zwart et al. 2002). Excluding very rare encounters between multiple stars, interactions inside clusters produce stars with velocities $\sim$ 300 km/s (see for example Brown et al. 2007 and references therein), which are too low to explain the HVS.

5. The scattering of stars by a binary MBH. Massive binary black holes were originally suggested in the context of active galactic nuclei by Begelman et al. (1980). For stellar densities and velocity dispersions in the galactic centre both MBHs are expected to have approximately equal masses (Yu 2002). Encounters between stellar binaries and binary MBHs is the only mechanism capable of producing hypervelocity binaries (Lu et al. 2007). However, no observational evidence exists for a binary MBH in the galactic centre, nor have any binary HVS been observed.

6. A star in a binary system ejected when its companion explodes as a supernova. The expected velocity of the main star after its companion receives a velocity kick during

[1]Refer to Equation (2.3) for the dynamical friction timescale discussed for globular clusters moving through the galactic disk in Section 2.3.

supernova was not high enough to result in a HVS (Gualandris et al. 2005).

Numerical simulations conducted by Sesana et al. (2007) for three of these mechanisms ruled out an IMBH (Scenario 2), but could not distinguish between a cluster of black holes (3) and the Hills mechanism (1). Combining this together with the fact that stellar velocities produced by scenarios (4) and (6) are too low leaves scenarios (1), (3) and (5).

Even if IMBHs are not directly responsible for HVS their existence will provide an additional means of bringing stars close to the MBH. The region within 10 pc of the MBH may contain approximately 50 IMBHs of roughly $10^3 M_\odot$ (Portegies Zwart et al. 2006), which are predicted to be continually replenished. Thus it is possible for a binary composed of a star and an IMBH to encounter the MBH, although this is not considered here.

Future surveys using current telescope technology are expected to yield observations of approximately 100 HVS (Brown et al. 2007). Statistical studies of an observed population of this size will allow the individual models to be discerned, e.g. a binary MBH will produce a bias in the spatial distribution of HVS in the orbital plane of the binary MBH (Sesana et al. 2006). At this point a binary MBH in the galactic centre seems unlikely considering the lack of a second population of stars closely orbiting a second dark point in space. Also binary MBH systems are subject to decay via gravitational radiation (Equation 8.4) and depending on the stellar environment this may result in the merger of the binary MBH within 10^8 years (Spurzem et al. 2003), thus such systems are unlikely to still exist.

This study will consider a stellar binary system encountering a single MBH, i.e. Hills mechanism. This mechanism can explain both the tightly bound stars and the HVS. The Hills mechanism is also required by N-body simulations of the interaction between stellar disks to produced stars on close orbits with the MBH with properties consistent with the observed S-stars (Perets et al. 2008; Löckmann et al. 2008).

The Hills mechanism requires a scattering process operating beyond 0.04 parsecs of the MBH to produce in-falling binary systems. Possible mechanisms for scattering binaries towards the MBH are provided by scenarios (2), (3) and (4). The scattering of a bound binary system towards the MBH requires the interaction of three or more bodies. Such interactions are far more frequent in dense stellar environments, such as the cores on stellar clusters. Possible sources of binary systems the stellar disks observed between 0.04 and 0.4 pc from the MBH (Löckmann et al. 2008) and clusters within 100 parsecs of the MBH (Gerhard 2001; Portegies Zwart et al. 2002). It is assumed that some combination of these processes will result in binary systems being scattered towards the MBH on nearly parabolic orbits. The precise details of the interaction, resulting distribution and associated scattering rate are beyond the scope of this work.

In the next chapter we investigate the Hills mechanism using scattering experiments, which are used to predict the velocity distribution of HVS in Chapter 11. Neither Chapter 9 or 11 crucially depend on the details of the scattering process that produces in-falling binaries. Chapter 10 will focus on comparisons between numerical results, stability predictions from the MSC and theoretical estimates from the literature given in the next section.

Chapter 9

Scattering experiments for Hills mechanism

The aim here is to conduct scattering experiments for the tidal disruption of a stellar mass binary system by a massive black hole (MBH). The trajectory of the in-falling binary system relative to the MBH is characterised by its distance at closest approach and its velocity at this distance, or equivalently its eccentricity. Scattering experiments for two eccentricity values are conducted; one where the binary is initially bound to the MBH, and one unbound parabolic orbit.

A binary system will be tidally disrupted by the MBH if it passes within some maximum distance from the MBH. The maximum distances of closest approach determined from the scattering experiments will be compared to theoretical maximums from the literature and determined using the Mardling stability criterion (MSC; introduced in Section 1.3.2). The results from these scattering experiments will also be used to determine the velocity distribution of the hypervelocity stars in Chapter 11.

In the following numerical experiments the mass ratio of the central MBH to one component of the binary is taken as 3×10^6. For an equal mass binary of two $1\mathrm{M}_\odot$ stars, this ratio is consistent with the current mass for the MBH in the galactic centre of the Milky Way of $3.4 \times 10^6\ \mathrm{M}_\odot$ (Schödel et al. 2003).

Two values are chosen for the eccentricity of the binary-MBH orbit, referred to as e_o. Firstly parabolic ($e_o = 1$) orbits are chosen to allow direct comparisons with estimates by Hills (1992) and Heggie et al. (1996), discussed in Section 9.1. The MSC is used to predict the stability of a hierarchical three-body system of point masses (see Chapter 1). To be able to apply it to a binary system encountering an MBH in the galactic centre a second orbital eccentricity of $e = 0.9$ is chosen for the binary-MBH orbit.

As discussed in Section 1.3.2 the MSC does not distinguish between the escape of the outer body (i.e. the binary escapes) or exchange. For both of these cases the MSC will predict the binary-MBH system to be unstable. The mass ratios involved in the binary-MBH system mean that almost all unstable systems will result in the exchange of the MBH for one of the original binary components (exchange) except for a small fraction of orbits very close to $e_o = 1$. This has been illustrated in Figure 1.6 (b) where the unstable region is divided into exchange and the escape of the binary. The critical value which divides these regions in not determined in this study and so the binary eccentricity of $e_o = 0.9$ is chosen to ensure that all unstable systems are equivalent to systems that will eventually eject one of the original binary components. The results for $e_o = 0.9$ are not expected to significantly differ from the results we would get for $e_o = 0.99$ etc. as discussed in Section 1.3.2. The choice of $e_o = 0.9$ is also a numerical convenience since the orbital period is substantially reduced by lowering the eccentricity and therefore saving the total simulation time required to resolve the disruption of the binary (see Section 9.2)

Recall from Section 1.3.2 that this is a random walk process so the stellar mass particle that will eventually escape the system will take a long time to do so, in fact no simulations ran for long enough to see this occur. While this star may not completely escape the system it will be removed from the original on a much shorter timescale. This means that the unstable systems predicted by the MSC can be directly compared to binaries that are disrupted by the MBH, which is the focus of Chapter 10.

In total, over half a million individual scattering experiments were carried out, all of which allow for repeated encounters between the binary and the MBH. The data collected represents many months of CPU time and is the most comprehensive examination of the Hills mechanism as far as the author is aware.

Once again, Jacobian coordinates are used with the inner and outer orbits being denoted by a subscript i or o respectively. The inner orbit refers in this case to the orbit of the original stellar binary system, while the outer orbit refers to the orbit of the binary-MBH (see Figure 1.3 for a schematic diagram). Interaction between the binary and the MBH either leaves the original binary unaltered or creates a new binary composed of a captured star and the MBH. The orbital parameters for the newly created binary are denoted by the subscript n. For parabolic binary-MBH orbits conservation of energy requires that capturing a star into an orbit with the MBH will also produce an escaping star. We are only interested in the magnitude of the velocity of the escaping stars once it has escaped to infinity. In Chapter 11 these velocity magnitudes are used to produce a theoretical velocity distribution for the hypervelocity stars that can be compared to future observational surveys.

The structure of this chapter is as follows: the theoretical estimates for the maximum pericentre distances for which a binary disruption is expected are given in Section 9.1. Section 9.2 sets up the three-body problem and describes the numerical simulation method used to model the encounter between the binary and the MBH. The parameter space that will be examined in this study is given in Section 9.3. The results of these scattering experiments are presented and discussed along side theoretical estimates for the maximum distance at closest approach in Section 9.4. Results from the scattering experiments involving a bound binary-MBH orbit are discussed with detailed stability predictions using the MSC in the next chapter.

9.1 Distance estimates for the Hills mechanism

This section investigates theoretical estimates of the maximum pericentre distance (R_p) for a binary system to the MBH which results in the tidal disruption of binary. Both of the estimates from the literature given below are concerned with parabolic binary-MBH orbits.

Two estimates are given here for the maximum pericentre distance that can result in an exchange event. An exchange involves the capture of a star into an orbit with the MBH, since the MBH is exchanged for one of the original binary components (see the discussion in Section 1.3.2). Hence a new binary composed of a star and the MBH is created.

The first estimate is based on scattering experiments for a circular binary system of equal masses m_1 encountering a star of mass m_3 on a parabolic orbit (Hills 1992). Hills (1992) found that the maximum pericentre distance for which exchange was possible could be fit by

$$R_p \approx 2.1a \left(\frac{m_3 + 2m_1}{2m_1} \right)^{1/3} \tag{9.1}$$

where the binary is composed of equal masses m_1 and m_3 is the mass of the MBH. Hills (1992) considered encounters in the range $0.01 \leq m_3/m_1 \leq 10000$, which does not include the required mass ratio for a binary-MBH encounter of 3×10^6. We therefore have to extrapolate the fitting function given by Equation 9.1 to this mass ratio. This gives $P_{Hills} = R_p/a \approx 240$ for a binary composed of two solar mass stars and a $3 \times 10^6 \mathrm{M}_\odot$ black hole[1].

The second estimate is based on an analysis was conducted by Heggie et al. (1996), the key arguments of which are reiterated here. Consider a binary falling towards the MBH with a very small original relative velocity. This is equivalent to a parabolic binary-MBH orbit with the velocity at the pericentre distance approximately $V_p^2 \sim Gm_{123}/R_p$, where m_{123} is the sum of binary and black hole masses. At the pericentre distance the tidal acceleration acting on the relative position vector joining the two stars is of order Gm_3a/R_p^3 (Murray and Dermott 2000). Tidal acceleration results in a change in the relative speed between the binary components. This is enough to disrupt the binary if the pericentre distance is less than (Heggie et al. 1996)

$$R_p \approx a \left(\frac{m_3^2}{m_{12}m_{123}} \right)^{1/3} \tag{9.2}$$

where $m_{12} = m_1 + m_2$ and $m_{123} = m_1 + m_2 + m_3$. For an equal mass binary of two 1 $\mathrm{M}_\odot$ stars encountering a $3 \times 10^6 \mathrm{M}_\odot$ black hole this gives $P_{Heggie} = R_p/a \approx 114$.

These two distances predict the maximum pericentre distance for which the Hills mechanism will result in the tidal disruption of the binary. The first estimate is based on a previous numerical study (Equation 9.1) and the second on an analytical study (Equation 9.2). These maximum pericentre distances are compared to the maximum distances where the binary is disrupted in numerical simulations in Section 9.4. For binaries initially bound to the MBH, the maximum pericentre distances will be compared to predictions using the MSC in Chapter 10.

[1] The more precise value for the Milky Way MBH of $3.4 \times 10^6 \mathrm{M}_\odot$ is not used to allow direct comparison of P_{Hills} and P_{Heggie} to numerical results in later chapters.

9.2 Methodology

All scattering experiments assume point mass potentials for the stars and the MBH. Thus we are not restricted to any particular length scale, as was the case with the compactness parameter for globular clusters in Section 3.1. This scale independence has the advantage that the scattering results presented in Section 9.4 can be applied to any physical system with the same mass ratios given in Section 9.3. This is particularly useful when discussing the physical distribution of velocities in Chapter 11.

The system is expressed using Jacobian coordinates (Section 1.2) and a schematic diagram of the position vectors and masses has been shown in Figure 1.3. The inner binary refers to the original stellar binary composed of particles of two masses m_1 and m_2 which we take to be equal, and is assigned the position vector $\mathbf{r}$. The outer binary is composed of the centre of mass of the inner binary and the MBH, represented by a particle of mass m_3. The position vector connecting the centre of mass of the inner binary to the MBH is denoted by $\mathbf{R}$. The equation of motion for the inner orbit is given by Equation (1.16), i.e.

$$\ddot{\mathbf{r}} = -\frac{Gm_{12}}{r^3}\mathbf{r} + Gm_3\left[\frac{\left(\mathbf{R}+\frac{m_1}{m_{12}}\mathbf{r}\right)}{\left|\mathbf{R}+\frac{m_1}{m_{12}}\mathbf{r}\right|^3} - \frac{\left(\mathbf{R}-\frac{m_2}{m_{12}}\mathbf{r}\right)}{\left|\mathbf{R}-\frac{m_2}{m_{12}}\mathbf{r}\right|^3}\right] \tag{9.3}$$

and for the outer orbit by Equation (1.17), i.e.

$$\ddot{\mathbf{R}} = -\frac{Gm_{123}}{m_{12}}\left[\frac{m_1\left(\mathbf{R}-\frac{m_2}{m_{12}}\mathbf{r}\right)}{\left|\mathbf{R}-\frac{m_2}{m_{12}}\mathbf{r}\right|^3} + \frac{m_2\left(\mathbf{R}+\frac{m_1}{m_{12}}\mathbf{r}\right)}{\left|\mathbf{R}+\frac{m_1}{m_{12}}\mathbf{r}\right|^3}\right]. \tag{9.4}$$

The scaling for this system uses the procedure outlined in Section 3.1. The masses of the system are scaled by mass of one of the stars. The length is scaled by the semi-major axis of the inner binary orbit, a_i, and the time scaling is taken to be

$$\tau = \sqrt{\frac{a_i^3}{Gm}}. \tag{9.5}$$

The velocity scale is then

$$v_{scale} = \sqrt{\frac{Gm}{a_i}}, \tag{9.6}$$

which for the length and mass scales of interest here becomes

$$v_{scale} = 29.786\left(\frac{m}{\mathrm{M}_\odot}\right)^{1/2}\left(\frac{a_i}{AU}\right)^{-1/2} km/s, \tag{9.7}$$

which will be used in Chapter 11 to determine the physical distribution of hypervelocity stars ejected from the galactic centre. As with Section 3.1 it is more convenient to drop the prime notation for scaled quantities and in the following un-primed quantities will be assumed to be scaled. The pericentre distance of the outer orbit as scaled by the inner semi-major axis will be denoted by $p = R_{p,o}/a_i$.

This problem can involve very close encounters between bodies, which requires a different numerical integrator than that used for Parts I and III. To ensure the trajectories of masses after close encounters are accurate, a regularisation method is required. Regularisation methods involve a suitable coordinate transformation to remove the mathematical singularities due to the $1/r$ terms in Equations (9.3) and (9.4).

As such the numerical simulations were conducted using the generalised three-body code provided by Sverre Aarseth and described by Aarseth and Zare (1974). This numerical integrator is based on Kustannheimo-Stiefei regularisation of a two-body system, which is described in Kustaanheimo and Stiefel (1965). This numerical integrator means that the total energy and angular momentum of the system are conserved to a high degree of accuracy, and that close encounters between bodies do not induce unphysical velocities. Any unphysical velocities would be impossible to distinguish from high velocity escaping stars, so it is essential that velocities are accurate.

All simulations start far enough away for the interaction energy (Equation 1.21) between the binary and the binary-MBH orbit to be small. For parabolic orbits this distance was found to be approximately 120 times the pericentre distance, and for $e_o = 0.9$ it is the apocentre distance. The distances at $t = 0$ are seen in Figure 9.1 which shows the magnitudes of the vectors $\mathbf{r}$ and $\mathbf{R}$ as a function of time for initial conditions of interest in Section 9.4.

The relative inclination of the outer to the inner orbit and the relative phase of the inner binary are varied for each value of p, e_i and e_o (see next section). The phase of the binary is altered by changing the initial value of the inner mean anomaly M_i - this approach allows the stability of orbits to be determined in Chapter 10.

The three-bodies are numerically integrated using Equations (9.3) and (9.4) until: (i) the original binary breaks up with one of the masses becoming bound to the MBH; (ii) the binary remains intact and escapes beyond a preset distance after the encounter; and (iii) the simulation exceeds a preset maximum time. For parabolic binary-MBH orbits the system is referred to as a capture when the binary is broken apart (leaving one star in a tight orbit with the MBH) and as a fly-by encounter otherwise (where the binary-MBH orbital eccentricity is parabolic or hyperbolic). In the case of capture the orbital parameters of the newly created binary and the velocity of the escaping star are stored.

For parabolic binary-MBH orbits the binary is deemed to have broken apart if the distance between one of the stars and the MBH is less than the distance between the two stars. The position and velocity vectors of the capture star and MBH are used to determine the instantaneous Kepler elements. These are then used to check that the new star-MBH orbit has negative binding energy; if this is not the case then the simulation is continued. Ideally each system should be determined to be either a capture or a fly-by, but realistically a maximum time limit has to be set for the simulation. How this maximum time is set is discussed in the next section.

For binary-MBH orbits with an orbital eccentricity of $e_o = 0.9$ it is highly improbable for the binary to escape to infinity, so fly-by encounters as previously described are not expected to occur. Instead we focus on when the stellar binary is disrupted, i.e. when the instantaneous Kepler elements have eccentricity greater than unity. In this scenario both stars are independently bound to the MBH. It is possible for a single star to escape to infinity if a close enough encounter between all three masses occurred, however this was not observed to happen in any of the simulations conducted in this chapter.

To better understand the capture of one of the binary components by the MBH, the magnitudes of the position vectors between the two stars $|\mathbf{r}|$ and for the binary centre of mass to the MBH $|\mathbf{R}|$ are shown respectively as solid and dashed lines Figure 9.1. This figure shows all of the encounter types previously discussed for both bound and parabolic binary-MBH orbits.

For a binary-MBH orbit with $e_o = 0.9$ the disruption of the binary and the formation of a "stable" hierarchical system are shown in Figure 9.1 (a) and (b) respectively. The hierarchical triple system shown in panel (b) can only be said to be stable to escape of one of the bodies for the duration of the simulation, see also the discussion of the nature of stability in Section 1.3. The average time for a binary to be disrupted is discussed in the next section, with a view to choosing the maximum simulation time such that the number of "stable" binaries that would eventually become disrupted is kept to a minium.

For the binary disruption shown in Figure 9.1 (a) the distance between the stars (solid line) is comparable with the distance between the MBH and the centre of mass of the two stars after approximately 150 T_i. This means that the binary has been pulled apart, but one star has not been ejected to infinity. If one star had been ejected then the distance between the stars $|\mathbf{r}|$ would increase indefinitely, as would the distance between the MBH and the centre of mass of the two stars $|\mathbf{R}|$. This is seen to occur for the captured star from a parabolic binary-MBH orbit shown in Figure 9.1 (c). In this case the binary is pulled apart as soon as the MBH is at the distance at closest approach. The fly-by encounter for $e_o = 1.0$ in Figure 9.1 (d) is easily distinguishable from the capture scenario in (c) as the distance between the stars (solid line) continues to oscillate from pericentre to apocentre distances after the closest approach of the MBH (dashed line). For a fly-by encounter from an initially parabolic binary-MBH orbit the transfer of energy has gone from the stellar binary to the binary-MBH binding energy making this orbit hyperbolic.

Overall the instantaneous Kepler elements for the stellar binary are used to determine if and when it is disrupted, while the distances between particles are used to determine which star is closely bound to the MBH. When a new orbit consisting of a star and MBH is formed the instantaneous Kepler elements are calculated from the relative position and velocity vectors.

9.3 Parameter space mapped out

To reduce the parameter space considered in this study the binary components are assumed to have equal masses (m) and the ratio of the MBH mass (M_{BH}) to one binary component $q = M_{BH} \ / \ m$ is fixed at $3{\times}10^6$. The validity of assuming a fixed mass ratio is examined in

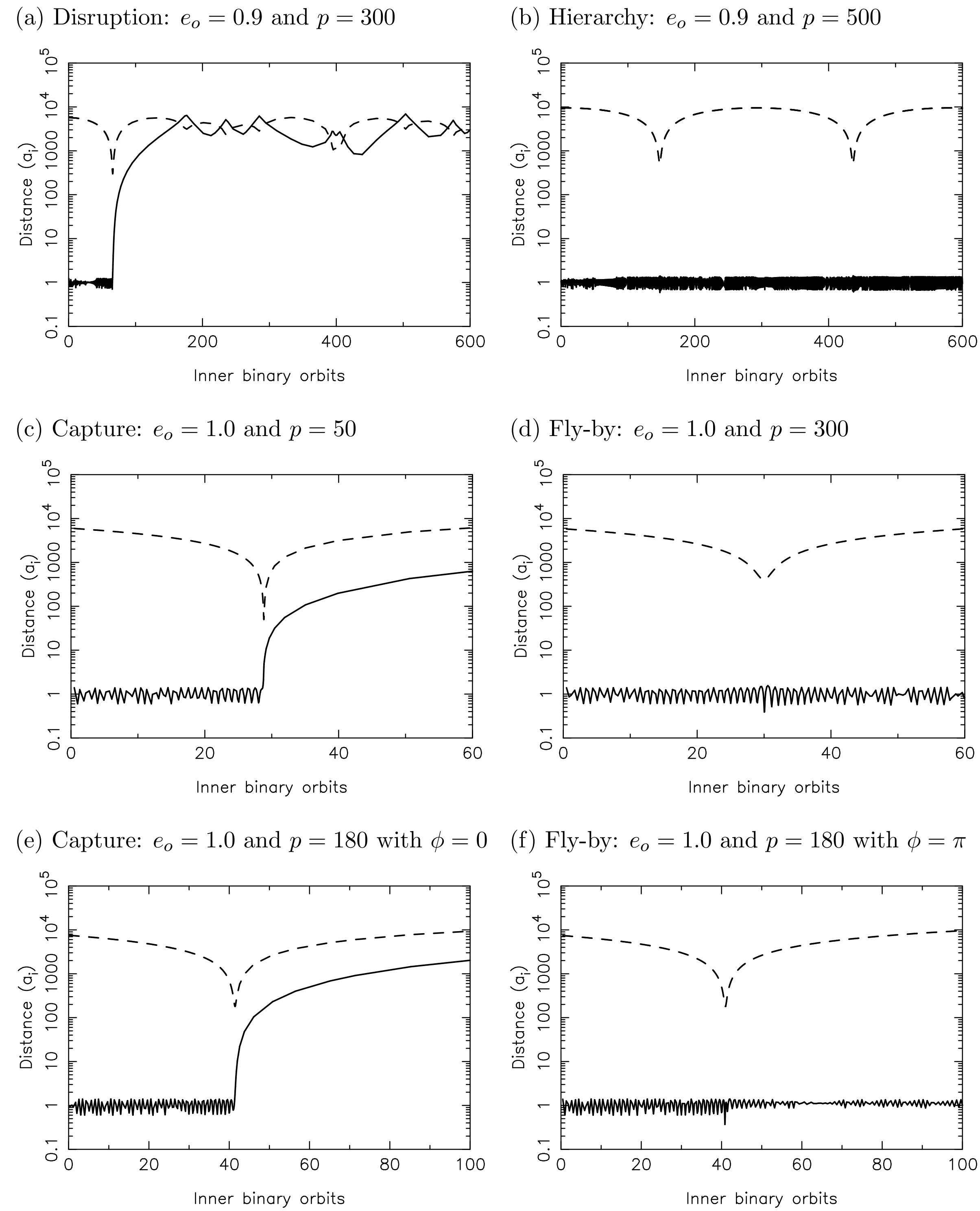

Figure 9.1: Distances between stars (solid lines) and between the centre of mass of the two stars and the MBH (dashed lines) against time. The possible interactions for a binary-MBH orbital eccentricity of $e_o = 0.9$ are shown in panels (a) and (b). The capture of a star into orbit with the MBH (panels c and e) and the fly-by of a binary system (panels d and f) are shown for parabolic binary-MBH orbits. All numerical integrations are conducted with stellar binary eccentricity of $e_i = 0.4$ and for coplanar orbits, using the method given in Section 9.2.

Section 10.5, since it has implications when predicting the velocity distribution of hypervelocity stars in Chapter 11.

The following variables and their stated ranges describe the total parameter space examined using numerical experiments:

- Inner eccentricity (e_i) = 0.0, 0.4 and 0.7
- Outer eccentricity (e_o) = 0.9 and 1.0
- Scaled pericentre (p) = 1, 2 , ..., 400 for $e_o = 1.0$ and is discussed below for $e_o = 0.9$
- Inclination[2] between orbits (I) = 0, ΔI, $2\Delta I$, ..., π where $\Delta I = \pi/18$
- Phase of the binary orbit, $\phi = M_i(t = 0) = 0$, $\Delta\phi$, $2\Delta\phi$, ..., $2\pi - \Delta\phi$ where $\Delta\phi = \pi/5$

The high resolution for the pericentre distance is chosen such that the maximum pericentre distance for which the binary is disrupted can be accurately determined as a function of inclination and eccentricity. The pericentre distance cut-off of $p = 400$ in units of a_i for $e_o = 1.0$ is chosen to limit the number of parameters studied so as to economise on CPU-time.

For an binary-MBH orbital eccentricity of $e_o = 0.9$ the pericentre distances p are chosen in steps of 1 unit of a_i to span the region around the maximum pericentre distance predicted by the MSC in Chapter 10. This is done to minimise the number of computationally expensive simulations for bound $e_o = 0.9$ systems. The algorithm used to ensure that the maximum pericentre distance for which the stellar binary is disrupted is resolved is as follows. Taking the pericentre distance predicted by the MSC as a starting point p is increased in steps of unity until the fraction of disrupted binaries first falls to zero for two consecutive values of p. A similar procedure is used as p decreases where we begin at the predicted value and continue in steps of -1 until the fraction of disrupted binaries increases above 40%. The minimum and maximum pericentre distances for which simulations are conducted are denoted as $p_{sim}(min)$ and $p_{sim}(max)$ respectively.

The relative phase (ϕ) and inclination (I) between the binary and binary-MBH orbits are taken as being uniformly distributed on a sphere. The same procedure is used to calculate the probabilities of disruption associated with ϕ and I as is described in Section 4.1.2 in the context of globular clusters. The uniform spacing in inclination, i.e. $I = 0$, $10°$ etc, is chosen to allow a more detailed comparison to stability results predicted by the MSC in the next chapter.

For parabolic binary-MBH orbits the maximum time that the simulation is run for is set as 10^4 orbits of the original binary system (T_i). This maximum time is based on the original binary orbit since the period of the binary-MBH orbit (T_o) is infinite for parabolic orbits. For bound orbits the maximum time is set as 400 binary-MBH orbital periods. As remarked upon in Section 1.3.1, this should be sufficient time for the system to display evidence of chaotic behaviour.

[2] An inclination of $I = 0$ corresponds to the inner binary starting on a prograde co-planar orbit relative to the motion of the MBH about the binary.

The choice of maximum time is not as much of a problem for binaries on initially parabolic orbits with the MBH, since the binding energy of the binary-MBH orbit must become negative after the first passage for a second passage to occur. The binding energy of the binary-MBH orbit can only become negative by transferring energy into the binding energy of the stellar binary. This may not disrupt the binary instantly, but subsequent pericentre passages of the now bound binary-MBH orbit will typically disrupt the binary. This total process takes significantly less than 10^4 orbits of the initial stellar binary to determine if the binary is disrupted or eventually escapes the influence of the MBH.

The maximum simulation time for bound binary-MBH orbits is chosen so that it does not affect our results. This will be true if the maximum time is well above the average time taken for a stellar binary to be disrupted. Figure 9.2 shows the time taken for the binary to be pulled apart for all simulations with $e_i = 0.4$ and $e_o = 0.9$ against the binary-MBH pericentre distance, p. The mean and the standard deviation of the times taken for the stellar binary to be disrupted against p are shown as data points and error bars respectively in this figure. Note that the average disruption times reflect the fact that the semi-major axis and eccentricity of the stellar binary change over time in a random walk process, as discussed in Section 1.3.

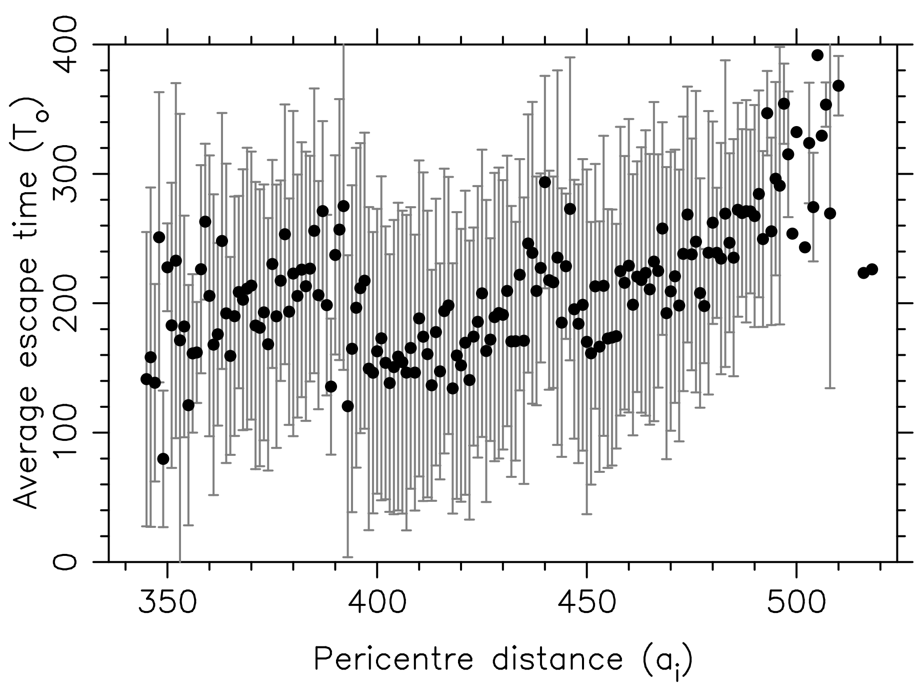

Figure 9.2: The average time taken for the binary to be disrupted against the pericentre distance of the binary-MBH orbit. The stellar binary has an orbital eccentricity of $e_i = 0.4$ and the binary-MBH orbit has an eccentricity of $e_o = 0.9$. All inclination and phase values listed in Section 9.3 are used to calculate the mean and standard deviation (1 σ indicated by the error bars) of the time taken to disrupt the original stellar binary. All times are in units of the orbital period of the binary-MBH orbit, T_o.

The average disruption times for binaries in the binary-MBH system shown in Figure 9.2 make an interesting contrast with previous results for stars escaping from the star-cluster-galaxy system examined in Section 5.3. The typical timescale associated with the escape of a star from the cluster is of the order of a few outer (cluster-galaxy) orbits in Figure 5.12, while here it varies from a few to hundreds of outer (binary-MBH) orbits. This is due to the different mass ratios for the inner binary: these being unity for the star-star orbit, and 10^{-6} for the star to the cluster mass in the previous chapter.

Thus we expect that most systems examined with parameters given above will have had time to disrupt the stellar binary. The binary can only be disrupted when enough energy is transferred from the binary-MBH orbit to the binding energy of the star-star orbit to make it positive. As discussed in Section 1.3, the chaotic transfer of energy between orbits is a signature of an unstable system. As previously discussed in Section 1.3.2, all unstable systems for this mass ratio are expected to result in the disruption of the stellar binary and not of the MBH (i.e. the escape of the binary)

Therefore the fraction of unstable orbits predicted by the MSC is expected to be identical to the fraction of disrupted binaries for the results for $e_o = 0.9$ presented in the next section. We will return to this topic when the MSC is applied to the Hills mechanism in Section 10.2.

The next section presents the results from the scattering experiments conducted for each combination of e_i, e_o, p, I and ϕ using the method described in Section 9.2.

9.4 Results of scattering experiments

The results for the disruption of stellar binaries by the MBH for the parameter space outlined in Section 9.3 and using the method described in Section 9.2 are ordered in the following way. Firstly the fraction of orbits resulting in the disruption of the stellar binaries is examined for both parabolic and bound binary-MBH orbits. Secondly we present the velocities of stars ejected from systems with parabolic binary-MBH orbits. These stars can escape the galactic centre to be observed as hypervelocity stars and are further discussed in Chapter 11.

9.4.1 The dependence of binary disruption on the pericentre and inclination

The focus of this section is how the disruption of the binary depends on the relative inclination and the pericentre distance of the binary-MBH orbit. The disruption of the binary results in one star being captured by the MBH while the other is ejected for parabolic binary-MBH orbits. For systems with $e_o < 1$ initially the disruption of the binary generally creates two independently bound star-MBH orbits, as discussed in Section 9.2.

Figure 9.3 shows the fraction of orbits for which one star is captured by the MBH as a function of pericentre and inclination. These results are for a binary approaching the MBH on a parabolic orbit with the stellar binary orbital eccentricity of $e_i = 0.0$ (top panels), $e_i = 0.4$ (middle panels) and $e_i = 0.7$ (bottom panels). For the left panels, the shading of each cell indicates the number of simulations for which the binary was disrupted divided by the number of values of the orbital phase run for this set of e_o, e_i, I and p. Note that defining the fraction of captures in this way implicitly assumes that there is no bias in the relative orientation between the binary and the binary-MBH orbits. This is equivalent to assuming that the mechanism that causes binaries to be scattered towards the MBH has no preferential orientation. For a review of dynamical mechanisms in the galactic centre the reader is referred back to Section 8.4.

An interesting side note is also revealed by the $e_o = 1.0$ results in panels (d) and (f) of Figure 9.3. A second sharp boundary exists between $f_{capture} \approx 0.9$ and $f_{capture} \approx 0.6$ visible at $p \approx 175$ and $p \approx 160$ for $e_i = 0.4$ and $e_i = 0.7$ respectively when $I = 0$. The cause of this band of seemingly low capture fraction is unknown at present but detailed examination of the orbits revealed that it is a real result and not a numerical artefact. Two test orbits both with $e_o = 1.0$, $e_i = 0.4$, $I = 0$ and $p = 180$ and differing only by the phase of the binary at $t = 0$ were run and the distance between stars $|\mathbf{r}|$ and from the binary to the MBH $|\mathbf{R}|$ are plotted in panels (e) and (f) of Figure 9.1. The magnitudes of the position that is associated with the inner and outer orbits clearly show a capture occurring for the case in panel (e) and a fly-by in panel (f). Therefore the cause of the relative depletion of captures present in the bands in Figure 9.3 is probably due to a strong dependence on the phase.

To summarise the capture results, each plot in the left panels of Figure 9.3 is averaged over the inclination to give the corresponding plots in the right panels of Figure 9.3. This averaging process uses the probability distribution function given by Equation (4.2) in Section 4.1.2. This distribution assumes that there is no preferred direction in the approach of the binaries to the MBH, and so $\sin(I)$ is distributed uniformly. The resulting capture fraction as a function of the distance at closest approach p is given in the right hand panels of Figure 9.3 and represents the probability of any orbit with a given e_i, e_o and p resulting in a capture. Note the bump seen in the capture fraction corresponding to the relative depletion of captures for $e_i > 0$ at $p \approx 170$ remains after averaging over the inclination. Of particular interest is the dependence of the maximum distance at closest approach (p_{max}) on the relative inclination and its increase with binary eccentricity. We return to this below when discussing theoretical estimates from the literature.

The dependence on inclination is not quite as strong for bound $e_o = 0.9$ binary-MBH orbits. This can be seen in the left panels of Figure 9.4 where the fraction of disrupted binaries is shown as a function of the pericentre distance and the inclination. The hatched line regions in the left panels of Figure 9.4 indicate where no simulations were conducted. Each of the orbital integrations used to produce this figure was extremely computationally expensive, so only the pericentre distances close to the expected maximum (see next chapter) were run. The algorithm used to resolve the maximum pericentre distance for which binaries are disrupted has been outline in Section 9.3. As seen in Figure 9.2 many systems with $e_o = 0.9$ required a large number of binary-MBH orbits for the binary to be disrupted. This meant that the maximum simulation time is set very high and each set of values for $e_o = 0.9$ takes a lot longer to run than the save values for $e_o = 1.0$.

The procedure used to average over the inclination in Figure 9.3 is applied to the fraction of disrupted binaries for $e_o = 0.9$ to produce the right hand panels of Figure 9.4. For regions where no simulations were conducted the fraction of disrupted binaries was taken as 100% when

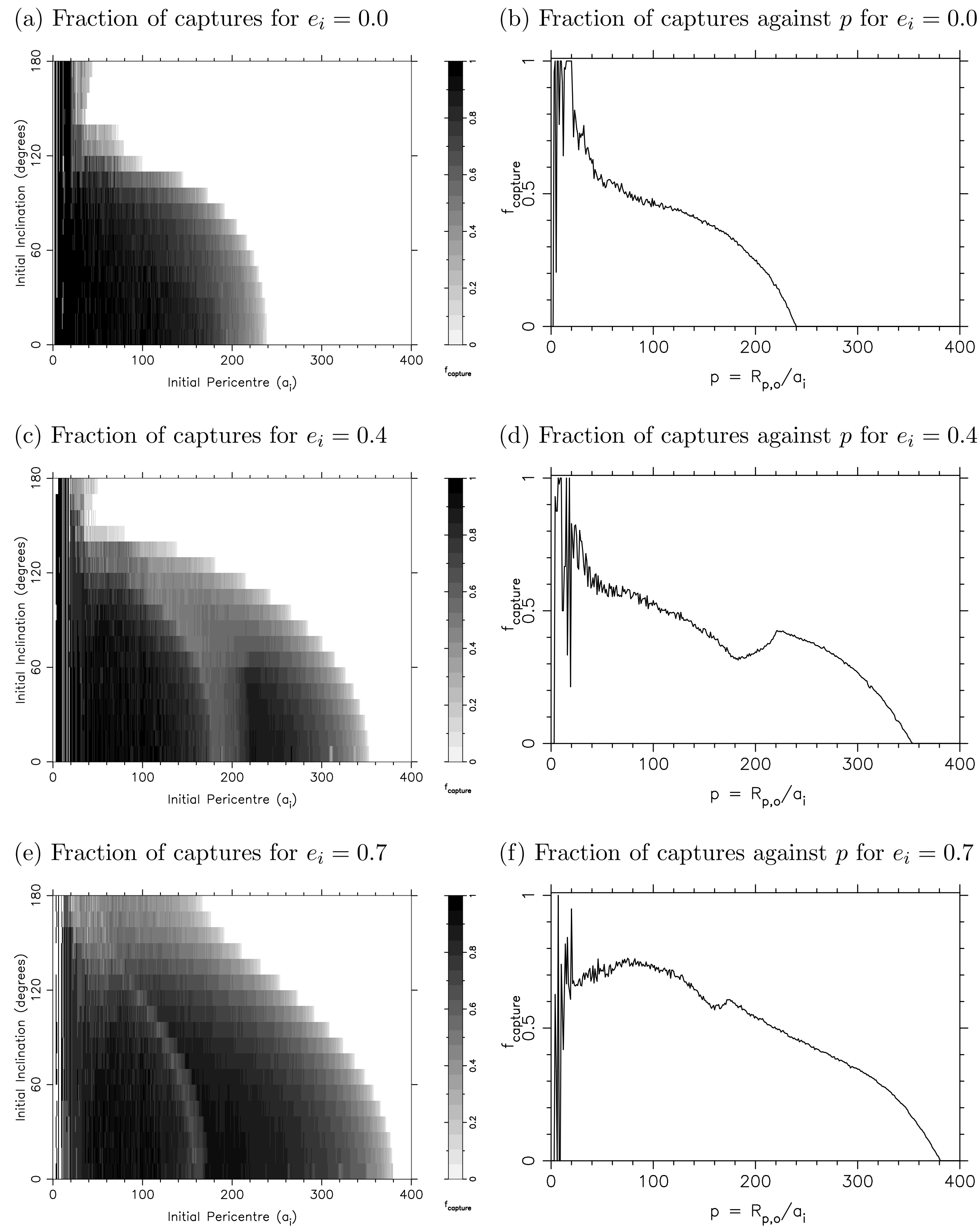

Figure 9.3: The fraction of captured orbits for $e_o = 1.0$ as a function of inclination and initial distance at closest approach of the MBH to the stellar binary (left panels). The results are broken down by the stellar binary orbital eccentricity of $e_i = 0.0$ (top panels), $e_i = 0.4$ (middle panels) and $e_i = 0.7$ (bottom panels). The right panels shown the fraction of captured orbits against the distance at closest approach after averaging over the inclination, assuming it is distributed over a uniform sphere. The origin of the phase effect seen most clearly in (c) is not clear.

$p < p_{sim}(min)$ and 0% when $p > p_{sim}(max)$, where $p_{sim}(min/max)$ are defined in Section 9.3. As before the simulations are performed for three cases of the stellar binary orbital eccentricity, these being $e_i = 0.0$ (top panels), $e_i = 0.4$ (middle panels) and $e_i = 0.7$ (bottom panels).

For bound $e_o = 0.9$ binary-MBH orbits the proportion of disrupted binaries remains near 100% for much higher pericentre distances than the $e_o = 1.0$ case. This is particularly evident for $e_i = 0.0$ and 0.4 where $f_{disrupt}$ stays around 100% for all low p values where simulations were conducted. The fall off from 100% to 0% for a given inclination is also fairly linear and typically occurs over 100 units of p. By comparison the fall off in $f_{capture}$ seen for parabolic orbits in Figure 9.3 was over less than 50 units of p for $I = 0$ and even less for higher inclinations. Once again the maximum pericentre distance for which $f_{disrupt} > 0$ (referred to as p_{max}) increases with e_i, which again shows that near circular binaries are more difficult to disrupt than highly eccentric ones.

For both $e_o = 0.9$ and $e_o = 1.0$ the star captured into orbit with the MBH (denoted by the subscript n) has a very similar orbit to that of the original binary-MBH orbit. For initially parabolic approaches of the binary to the MBH typical values for $|R_{p,n} - R_{p,o}|/R_{p,o} \lesssim 0.01$ and was negative for all cases, except some in retrograde orbits ($I = 180°$). The change in eccentricity was also small with $1 - e_n \lesssim 0.01$. Similar results were found for $e_o = 0.9$ but with no noticeable preference in direction. The further complication with binary-MBH orbits with eccentricity $e_o = 0.9$ is that both stars are in bound orbits with respect to the MBH after the initial stellar binary is disrupted. Both resulting star-MBH orbits were found to have similar orbital parameters to the original binary-MBH, and differ only by the orientation angles. For simplicity the new orbit consisting of a star and the MBH is assumed to have $e_n \simeq e_o$ and $r_n \simeq R_p$. Thus it is concluded that the captured population of stars will reflect the distribution of p and e_o of the initial in-falling binaries. Since precise details of this distribution remain unknown no further comments can be made.

There are three main points to be taken from Figures 9.3 and 9.4. The first is that the maximum pericentre distance for which captures are possible increases as e_i increases, as expected since the binary is becoming easier to disrupt. This is expected to occur since more eccentric orbits will spend more time near apocentre where they have slower speeds, which will more closely match the relative speed of the MBH at the pericentre distance of the binary-MBH orbit. This means that binaries with higher orbital eccentricities will be easier to disrupt than binaries with lower orbital eccentricities. Secondly the capture fraction is significantly less for retrograde orbits in the range $120° < I \leq 180°$, particularly for parabolic approaches of the MBH. Discussion on the cause of this is postponed until Chapter 10. Thirdly the maximum pericentre distance does not correspond with co-planar orbits for $e_o = 0.9$ (see panels a and c). Again the affect of inclination is more naturally explained alongside results presented in Chapter 10.

Two theoretical estimates of the maximum distance at closest approach for a parabolic binary-MBH orbit from the literature were described in Section 9.1. These are compared to the maximum pericentre distances as a function of the inclination in Figure 9.5. The theoret-

(a) Fraction of disruptions for $e_i = 0.0$

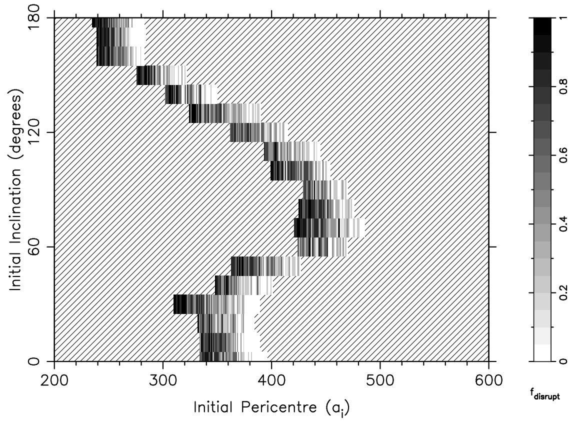

(b) Fraction of disruptions against p: $e_i = 0.0$

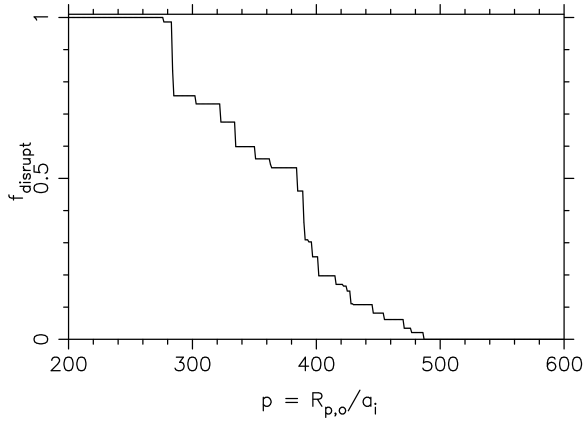

(c) Fraction of disruptions for $e_i = 0.4$

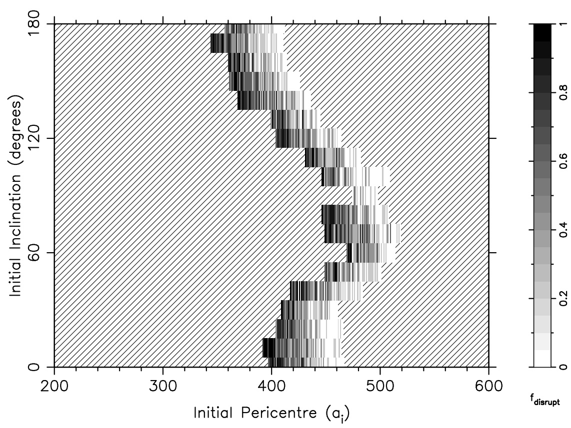

(d) Fraction of disruptions against p: $e_i = 0.4$

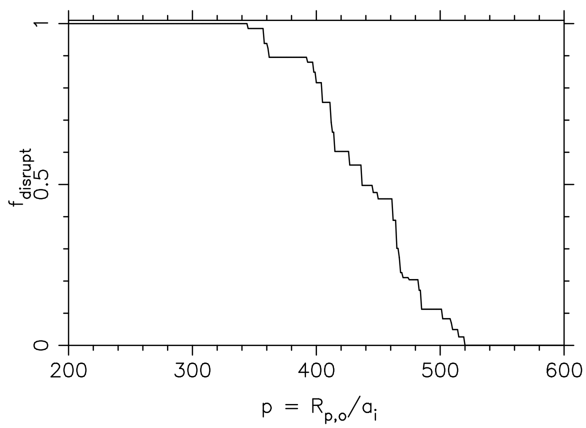

(e) Fraction of disruptions for $e_i = 0.7$

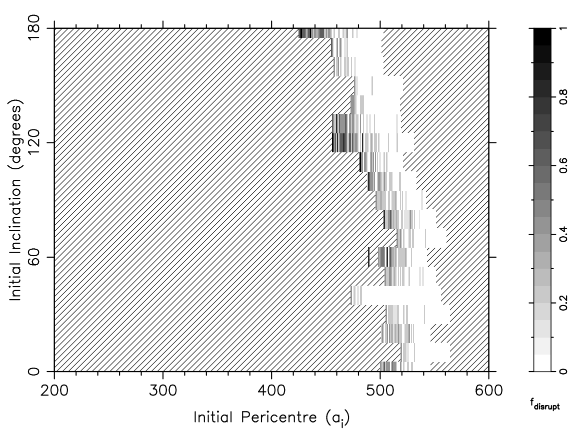

(f) Fraction of disruptions against p: $e_i = 0.7$

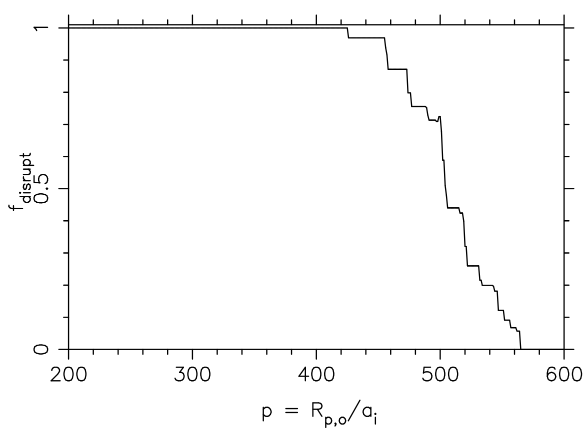

Figure 9.4: The fraction of disrupted binaries for $e_o = 0.9$ as a function of inclination and the initial pericentre distance of the binary-MBH orbit (left panels). The results are broken down by the stellar binary orbital eccentricity of $e_i = 0.0$ (top panels), $e_i = 0.4$ (middle panels) and $e_i = 0.7$ (bottom panels). The right panels shown the fraction of disrupted binaries against the binary-MBH pericentre distance after averaging over the inclination, assuming it is distributed over a uniform sphere. The hatched lines in the left panels indicate p and I combinations for which no orbital integrations were conducted.

ical estimates of $P_{Hills} = 240$ (Hills 1992) and $P_{Heggie} = 114$ (Heggie et al. 1996) are shown respectively as black solid and dotted lines in Figure 9.5. Note that these are for parabolic binary-MBH orbits shown in the top panel, but are included in the $e_o = 0.9$ plot for comparison.

From Figure 9.5 both theoretical estimates are on average less than the maximum pericentre distances found from the simulations. The P_{Hills} estimate is based on numerical experiments of circular binaries (Hills 1992), so it is not surprising that this agrees with our own numerical experiments for $e_i = 0.0$ with $I = 0$ in Figure 9.5 (a). Both estimates fail to include the significant effect that the relative inclination and eccentricity of the stellar binary orbit have on this distance. We will investigate the dependence of the maximum pericentre distance on e_i and I for bound orbits ($e_o = 0.9$) using the maximum distances predicted by the MSC in Chapter 10. For the remainder of this chapter we will limit our discussion to binaries approaching the MBH on parabolic orbits.

The probability of an exchange of the MBH for one of the original binary components is often characterised in the literature by a cross-sectional area (σ, not to be confused with the velocity dispersion or ratio of periods). The capture process is effectively a three-body exchange and the terms capture and exchange are used interchangeably in this context. The cross-section for capture is given by

$$\sigma_{capture}(e_i) = 2\pi\Delta p \sum_{i=1}^{\infty} f(p_i, e_i))p_i \tag{9.8}$$

where $\Delta p = 1$ and $f(p_i, e_i)$ is the fraction of captures recorded for the pericentre distace p_i for eccentricity e_i and is shown in the right hand panels of Figure 9.3. For comparison the cross-sectional areas associated with the theoretical estimates are defined as

$$\sigma_{Heggie} = \pi p_{Heggie}^2 \qquad \sigma_{Hills} = \pi p_{Hills}^2. \tag{9.9}$$

The most recent of these estimates, σ_{Heggie} associated with Heggie et al. (1996), is used as a point of comparison with the other cross-sections. Thus we define the ratio

$$X_c(e_i) = \frac{\sigma_{capture}(e_i)}{\sigma_{Heggie}} \tag{9.10}$$

to quantify how much easier it is to tidally disrupt a binary on a parabolic orbit with a MBH than predicted by p_{Heggie} (see Equation 9.2). The results from the numerical experiments shown in Figure 9.3 are then $X_c(e_i = 0.0) = 1.45$, $X_c(e_i = 0.4) = 3.12$ and $X_c(e_i = 0.7) = 4.48$. The ratio of cross-sectional areas for the theoretical estimate of Hills (1992) (see Equation 9.1) to the estimate of Heggie et al. (1996) is $X_{Hills} = 4.41$. The cross-sectional area using the maximum distance of P_{Hills} overestimates the areas found from the numerical scattering experiments. It also does not explain the depletion of captured stars for retrograde ($I \gtrsim 120°$) orbits as seen in Figure 9.5 (a).

Two main results emerge from this work. The first of these is that estimates of the cross-section for exchange in the literature are roughly consistent with the results from the scattering experiments presented here. The theoretically estimated maximum pericentre distances by

(a) Maximum distance at closest approach resulting in the capture of a star for $e_o = 1.0$

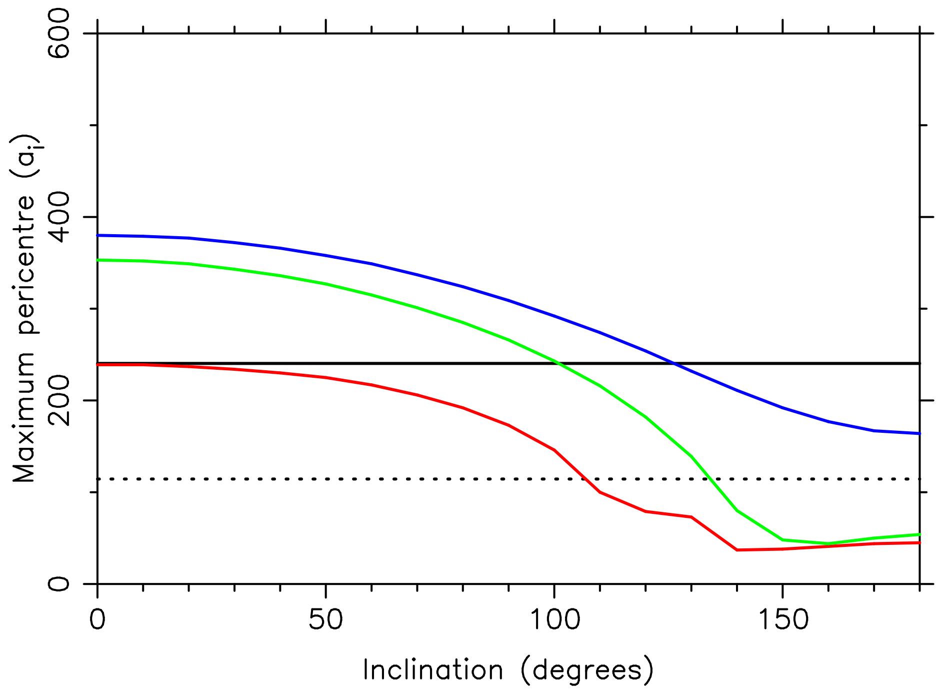

(b) Maximum pericentre distance resulting in binary disruption for $e_o = 0.9$

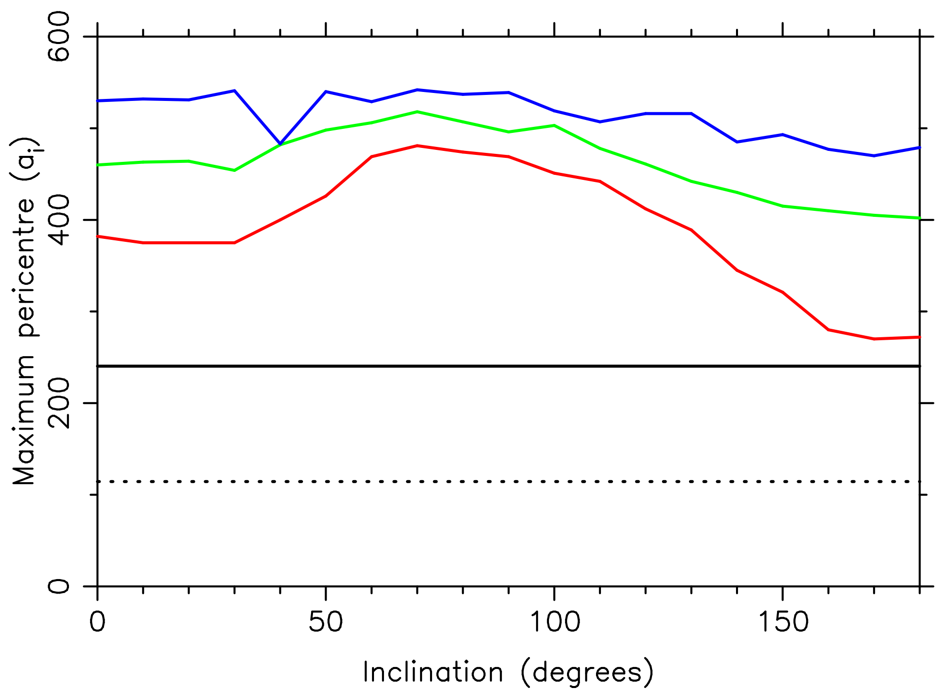

Figure 9.5: Maximum pericentre distance between the stellar binary and the MBH for which the binary was disrupted against the relative inclination between the binary and binary-MBH orbits. The initial orbital eccentricity of the stellar binary is indicated by colour with $e_i = 0.0$ (red), $e_i = 0.4$ (green) and $e_i = 0.7$ (blue).

Heggie et al. (1996), p_{Heggie}, consistently underestimates the maximum pericentre distance for which binary disruption is possible. This estimate still does a reasonable job considering that it is an order of magnitude estimate based on simple analytical arguments (see Section 9.1). The second main result here is that the maximum pericentre distance for which binaries are disrupted by the MBH strongly depends on the relative inclination between the stellar binary and binary-MBH orbits. This result confirms the results found by (Gould and Quillen 2003) for the Hills mechanism with large mass stars. The theoretical estaimtes for the maximum pericentre distance doe not explain the dependence of this distance on the inclination and orbital eccentricity of the stellar binary.

We conclude that future improvements in theoretical estimates for parabolic binary-MBH orbits in the extreme mass ratio region of this problem will need to take eccentricity into account. An analysis of the inclination and eccentricity dependence is presented in the next chapter using the MSC, although this is limited to high eccentricity ($e_o = 0.9$) binary-MBH orbits and is not directly applicable to parabolic binary-MBH orbits.

9.4.2 Velocity of stars that escape the Galactic centre

For binaries approaching the MBH on parabolic orbits the tidal disruption of the binary results in one star being captured and one star escaping the system. Stars ejected from the system can have sufficient velocities to escape the galactic centre. As discussed in Section 8.3.2, this is the favoured scenario for producing the hypervelocity stars, recently observed in the Milky Way galaxy (Brown et al. 2005). The results from this section will be used to predict the velocity distribution of HVS in Chapter 11.

The scattering experiments discussed above are used in this section to determine magnitude of the velocity of the escaping stars. The magnitude of the escaping stars velocity is recorded once the star has escaped the gravitational influence of the MBH, taken as ten times the initial distance of the MBH for $e_o = 1$ (i.e. $|\mathbf{R}| \gtrsim 1000p$). This velocity is practically equivalent to the velocity of the star at infinity and will be used in Chapter 11 as the velocity of the star as it exits the Galactic centre. The magnitude of the velocity as averaged over the orbital phase is shown as a function of p and I in the left panels of Figure 9.6. These velocities are in scaled units, which can be converted into physical velocities using Equation (9.7) for a particular stellar mass and initial binary semi-major axis.

The left panels in Figure 9.6 are averaged over the inclination using the same procedure as for the fraction of captured orbits in Figure 9.3, the resulting velocities are shown in the right hand panels of Figure 9.6. Note that these velocities are only averaged over the inclinations that resulted in the escape for a star. For example if only the coplanar case for a particular pericentre distance escaped with $v = 10$ units then the averaging procedure would give $v = 10$ for that p_o value. Thus these velocities are the average escape velocity given that an escape has occurred and must be used in conjunction with the right hand panels of Figure 9.3 to get the probability of this occurring. From Figure 9.6 the general trend of increasing velocity with decreasing distance at closest approach is evident. Although the poor statistics for low values

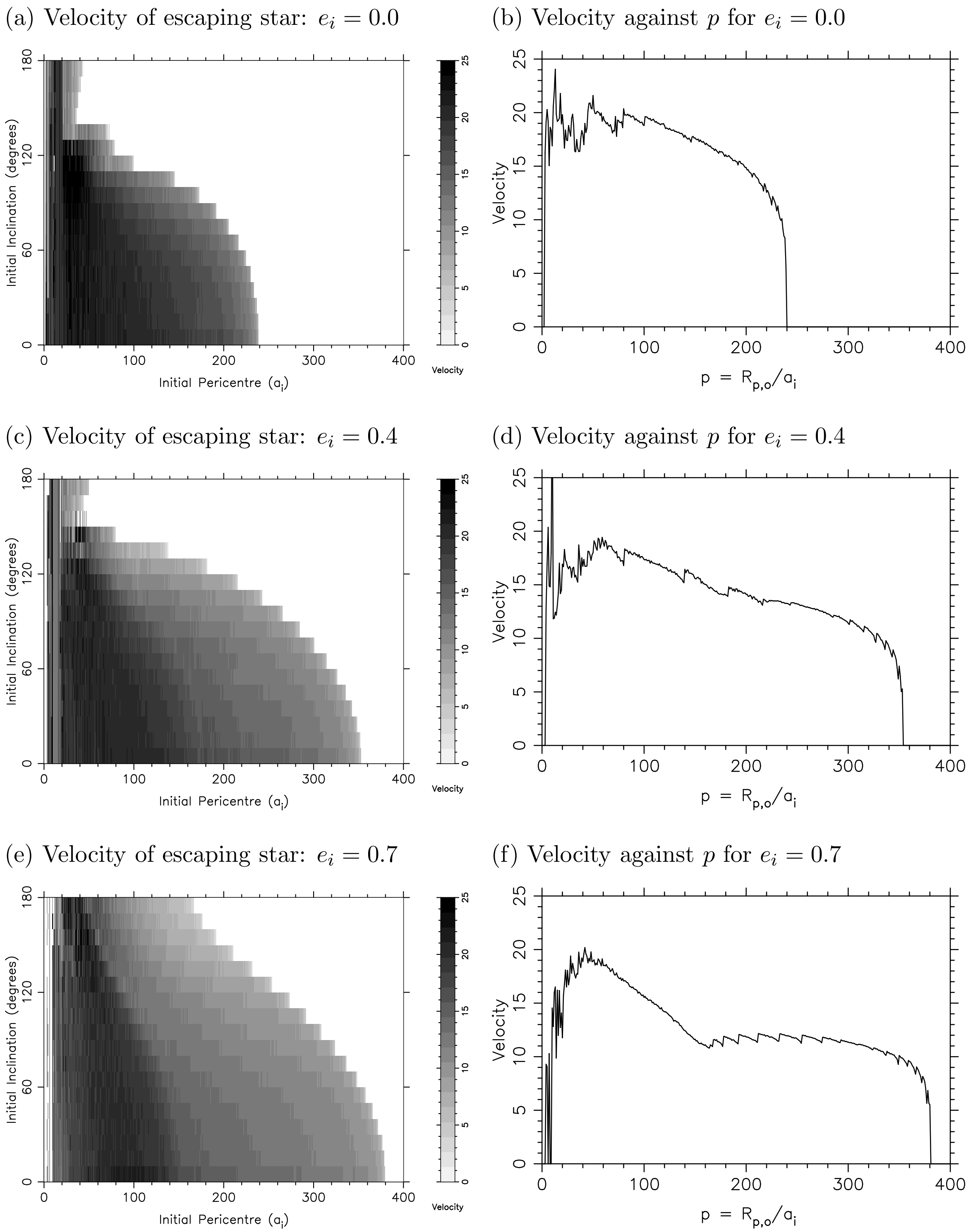

Figure 9.6: The effect of inclination and pericentre distance on the velocity of the escaping star from the tidal disruption of a binary on a parabolic orbit with the MBH. The velocities presented in these figures are in scaled units with physical velocities given by Equation (9.7) for a particular stellar mass and initial binary semi-major axis. For a binary composed of two solar mass stars with semi-major axis $a_i = 1$ AU a velocity of 20 in these units corresponds to approximately 600 km/s.

of p still lead to some noise, most is removed during the averaging process.

Note that the structure of the velocity plots in Figure 9.6 are similar to the capture plots in Figure 9.3 for $e_o = 1$. In general, the closer the binary passed to the MBH the more violent the interaction and the higher the velocity of the ejected star. The exception to this is a band at $p \lesssim 10$ for $e_o = 1$ (particularly $e_i = 0.4$) which is due to poor resolution at these distances.

The results from Figure 9.6 are used to obtain a distribution of velocities of observable hypervelocity stars in Chapter 11. But before applying the results of these scattering experiments to hypervelocity stars, the strong dependence of the fraction of disrupted binaries on inclination is investigated. This will be achieved in the next chapter using the MSC to examine the effect of inclinations (and e_i) on the maximum pericentre distance that can result in the tidal disruption of a binary. This analysis is confined to binary-MBH orbits with $e_o = 0.9$, but a theoretical approach to predicting the disruption of binaries on a parabolic binary-MBH orbit is expected to be similar.

Chapter 10

Application of the Mardling stability criterion to Hills mechanism

The aim of this chapter is to use the Mardling stability criterion (MSC) to understand the variation of the maximum pericentre distance of the binary-MBH orbit as a function of inclination seen in Chapter 9. For the reasons discussed below it is not possible to use the MSC to predict the disruption of binaries during an encounter with the MBH for parabolic binary-MBH orbits. Therefore the predicted stability a stellar binary against disruption will be examined for binary-MBH orbital eccentricities of $e_o = 0.9$ and compared against the results of scattering experiments done in the previous chapter.

Recall from Section 1.3.2 that the MSC predicts the stability against the escape of one of the bodies for a given three-body system. It does not distinguish between which body will eventually escape the system. For the mass ratios of interest here, i.e. $m_1 = m_2$ and $m_3/m_1 = 3 \times 10^6$, almost all unstable triples will result in the escape of one of the stars (m_1 or m_2). The exception to this general rule is for a small range of binary-MBH orbital eccentricities e_o near 1, where it is possible the MBH (m_3) to be ejected from the system. The former case where one of the stars is ejected is referred to as exchange since one of the stars is now bound to the MBH, the other cases is referred to as escape since the binary has been ejected. In the case of escape the binary-MBH orbit becomes unbound by taking energy from the original stellar binary, which responds by becoming more tightly bound. The boundary between these cases will occur at some maximum pericentre distance of the binary-MBH orbit for $e_o \approx 1$. An illustration of this scenario has been shown in Figure 1.6 (b) of Section 1.3.2 where the region of exchange is lightly shaded and the region of escape is darkly shaded.

The resonance widths used by the MSC to predict the stability of three-body systems do not significantly change for high values of e_o (see Figure 1.6 a). Therefore the occurrence of unstable systems is predicted to be very similar between $e_o = 0.9$ and higher values such as $e_o = 0.999$ (Mardling 2008, private communication). It is also expected that the predicted stability for systems with parabolic binary-MBH orbits will be very similar to the stability for $e_o = 0.9$. The only difference between these eccentricity values is that practically all unstable orbits with

$e_o = 0.9$ will result in exchange, but the same is not true for higher e_o. Therefore $e_o = 0.9$ is chosen to ensure that all unstable systems are equivalent to exchange and to allow a shorter orbital period than higher values of e_o (as originally discussed in Section 8.1).

In the previous chapter the maximum pericentre distance (p_{max}) that resulted in the disruption of the original stellar binary was seen to vary as a function of the inclination. Estimates of the maximum pericentre distance found in the literature do not consider the effect of the orbital eccentricity of the original binary or to the relative inclination between the stellar binary and the binary-MBH orbits (I). Similar results were seen for the maximum pericentre distances for parabolic ($e_o = 1.0$) and highly eccentric ($e_o = 0.9$) binary-MBH orbits; specifically the increase in p_{max} as the orbital eccentricity of the stellar binary (e_i) increased and the dependence on I.

The dependence of the maximum pericentre distance on e_i and I is predicted by the MSC. For binaries on initially bound orbits with the MBH the stability of the star-star-MBH system is determined as a function of the ratio of the binary-MBH to stellar binary orbital periods by the MSC. The overall approach adopted here is the same as that taken for stars orbiting within globular clusters in Chapter 4. We begin by applying the MSC to the Hills mechanism in Section 10.1, this allows the fraction of unstable orbits as a function of both I and σ to be examined for a given e_i.

Section 10.2 compares the predicted fraction of unstable orbits to the fraction of disrupted binaries found by numerically integrating the three-body system in the previous chapter. In particular dependence of the maximum pericentre distance on the relative inclination found by numerical integration is well predicted by the MSC. The previous chapter found that the maximum pericentre distance increases as the orbital eccentricity of the stellar binary increases; this result is also reproduced using the MSC.

Since the MSC is found to reproduce the maximum pericentre distance with reasonable accuracy for bound binary-MBH systems it is used in Section 10.2 to examine the effect of changing the mass ratio of the MBH to the binary mass. This mass ratio has been defined previously as $q = M_{BH}/m$ where m is the mass of one of the components of the equal mass stellar binary. For all of the numerical scattering experiments conducted in Chapter 9 this ratio was taken as $q = 3\times10^6$. To examine the effect of changing this ratio with scattering experiments would be very computationally intensive, recall the size of the parameter space studied for one value of q given in Section 9.3. By using the MSC to predict the maximum distance for which unstable orbits occur the dependence of p_{max} on q can be instantly determined.

By assuming that the maximum pericentre for which the binary is disrupted has a similar dependence on q for parabolic binary-MBH orbits as it does for bound orbits then we can use this dependence to see what affect changing the stellar mass has on the velocities of stars escaping in the next chapter. This uses the theoretical prediction by the MSC that the stability of parabolic binary-MBH orbits and bound binary-MBH orbits are fundamentally similar (Mardling 2008, private communication).

The timescale for the disruption of a stellar binary was examined numerically in Figure 9.2 where it was found that an average of approximately 200 periods of the binary-MBH orbit are required to disrupt a binary. Having a bound binary-MBH orbit guarantees subsequent pericentre passages between the binary and the MBH. Repeated pericentre passages will also occur for parabolic orbits if enough energy is transferred from the binary-MBH orbit to the binding energy of the stellar binary. If this occurs then the binary and the MBH will have multiple encounters ending in either the escape of a single star (exchange) or the escape of the binary. Aside from the problem of transferring energy in the first passage of a parabolic orbit the behaviour between bound and parabolic binary-MBH orbits is expected to be similar for the reasons stated above.

The analysis presented in this chapter highlights the need to include binary eccentricity and relative inclination in any theoretical estimate of the maximum distance that the Hills mechanism can disrupt binary systems. We return to the relevance of the results obtained for $e_o = 0.9$ to parabolic binary-MBH orbits in more detail in Section 10.3, along with a summary of the results presented in this chapter.

10.1 Theoretically stable regions

The aim of this section is to use the MSC to predict the occurrence of systems that are unstable to the disruption of the stellar binary. A stable system here refers to the binary remaining in a stable hierarchical triple system with the MBH forming a binary with the stellar binary. An unstable system will eventually result in the tidal disruption of the stellar binary. This means that systems predicted to be unstable by the MSC are directly comparable to the numerical results presented in the previous chapter.

For the problem of a stellar binary and a MBH each of the bodies can be well approximated by point masses. This means that the stability results can be directly compared to numerical results without the extra complexity required for the globular cluster in Part I.

An unstable orbit in the context of globular clusters meant that a particular halo star would eventually be ejected from the cluster. For a binary orbiting the MBH an unstable system is equivalent to the eventual disruption of the original stellar binary. Application of the MSC requires that the binary-MBH eccentricity e_o, the stellar binary eccentricity e_i, the masses m_1, m_2, m_3 and the ratio of periods σ be specified. The relative orientation between the star-star binary orbit and the binary-MBH orbit are described using the longitudes of pericentre $\varpi_{i/o}$ and the inclination I.

Varying the relative orbital phase between the orbits is effectively the same as varying the resonance angle ϕ_n. However varying the resonance angle in the MSC gives inaccurate predictions of the stability of systems due to unstable systems occurring outside regions of overlapping resonances. These unpredicted unstable orbits occur near the separatrix between libration and circulation, the location of which is used to calculate the resonance widths. As discussed in Section 1.3.2 this is more of a problem when the resonance overlap region is zero at $\phi_n \approx \pi$ than when it reaches maximum at $\phi_n = 0$. Throughout this analysis we take the resonance angle as $\phi_n = 0$ and reiterate that this provides a good estimate of the location of unstable systems for all orbital phases.

To directly compare the results for the MSC (Section 4) a mapping from the ratio of periods, σ, to the pericentre distance is required[1]. This is straightforward, unlike in Chapter 4, and involves a rearrangement of Equation (1.4) to give

$$\sigma = \frac{T_o}{T_i} = \left(\frac{p}{1-e_o}\right)^{3/2}\left(\frac{m_{12}}{m_{123}}\right)^{1/2} \tag{10.1}$$

where $p = R_{p,o}/a_i$ and $R_{p,o}$ is the pericentre distance of the binary-MBH orbit.

The regions of overlap between neighbouring resonances for a co-planar system with resonance angle $\phi_n = 0$ and masses $m_1 = m_2 = 1\mathrm{M}_\odot$ and $m_3 = 3 \times 10^6\mathrm{M}_\odot$ is shown in Figure 10.1. The resonance widths are calculated using Equation (1.27) for the $n:1$ resonances with $e_o = 0.9$. As was the case for the scattering experiments in Chapter 9 the longitude of pericentre for the inner and outer orbits are aligned and set to zero, i.e. $\varpi_i = \varpi_o = 0$. The same method used to generate Figure 10.1 was used for Figure 4.2 in the context of globular clusters.

In the next section the primary concern is the dependence of stability on the relative inclination between the binary orbit and the binary-MBH orbit. The MSC includes the effect of inclination via the inclination factors presented in Section 1.3.3. The resonance width ($\Delta\sigma$) for the $n:1$ resonance is then given by Equation (1.42). The dependence of the resonance width on each of the inclination factors for $\sigma = 10$ and $e_i = 0.3$ is shown in Figure 1.8 (f).

10.2 Comparison to scattering experiments

The previous section used the MSC to determine the stability of the star-star-MBH system. This section examines the accuracy of this stability analysis for bound binary-MBH orbits by comparison with scattering experiments conducted in Chapter 9. In particular the fraction of disrupted binaries is compared to the predicted fraction of unstable orbits as a function of inclination and pericentre distance of the binary-MBH orbit. The maximum pericentre distances as a function of the inclination and of the mass ratio are also discussed in this section.

The fraction of disrupted binaries for $e_o = 0.9$ and $e_i = 0.0$, 0.4 and 0.7 for the star-star-MBH system is shown in the left panels of Figure 10.2. These plots are reproduced from the left panels of Figure 9.4 in the previous chapter. The hatched lines indicate regions where no simulations were conducted to reduce the computational time required to see the transition from disrupted binaries (dark shading) to stable hierarchies (while shading). The right panels of Figure 10.2 show the fraction of unstable orbits predicted by the MSC as a function of the pericentre distance p and the relative inclination I.

Once again we assume that the sine of the relative inclination between the binary orbit and the binary-MBH orbit is uniformly distributed. Thus the probability distribution function is given by Equation (4.2) and the same method used in Sections 4.1.2 and 9.4.1 to average

[1] The symbol σ has three uses in this part; as a velocity dispersion, ratio of periods and later as a scattering cross-section. Rather than re-labelling these it has been arranged such that the σ in any given section is not mixed in with any other.

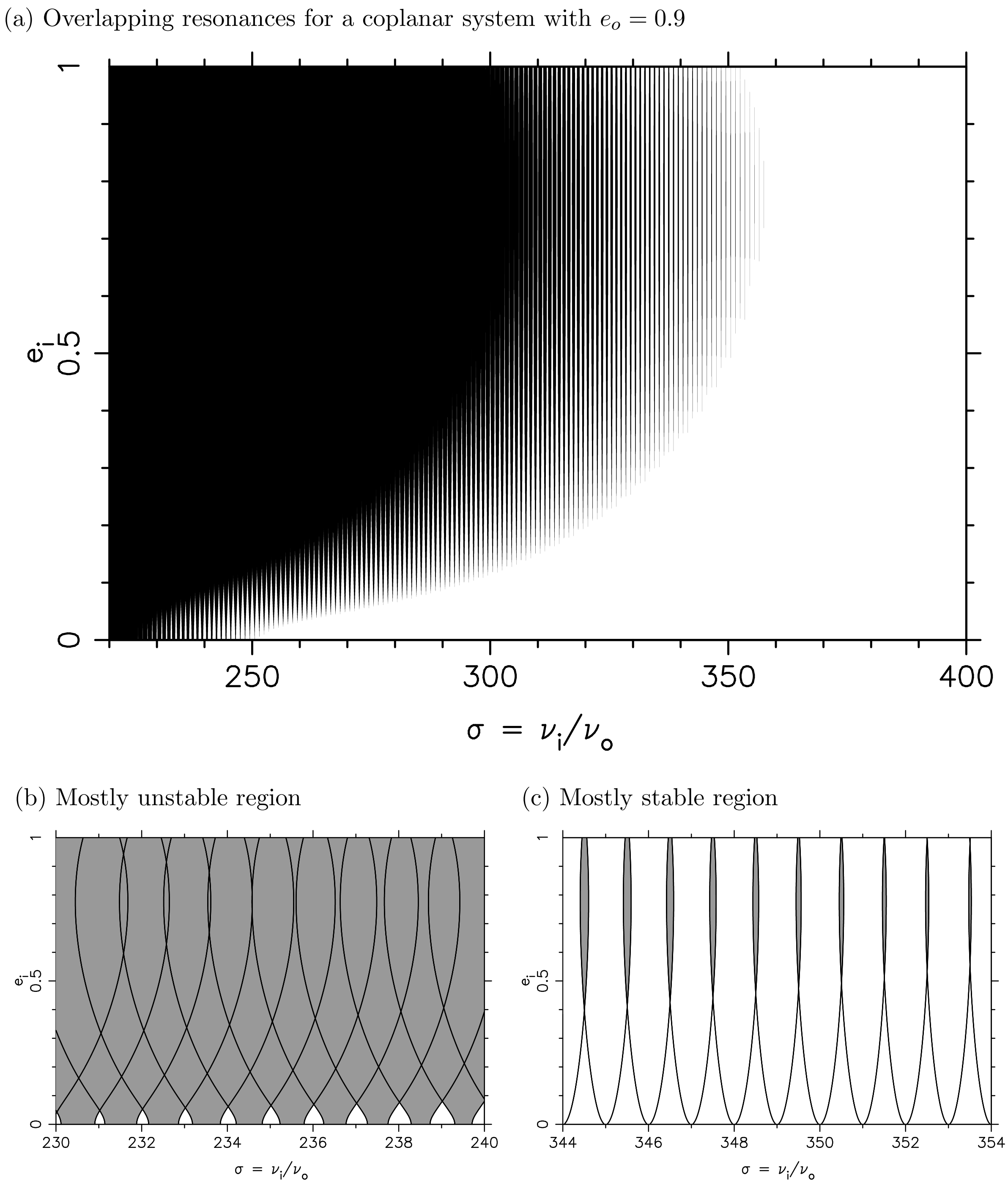

Figure 10.1: Resonance widths for an equal mass binary in an $e_o = 0.9$ orbit with the MBH shown in the top panel. The system is coplanar and the resonance angle is taken as $\phi_n = 0$. Regions of resonance overlap corresponding to orbital parameters that are predicted by the MSC to be unstable to binary disruption are shaded. Panels (b) and (c) show the regions of orbital parameters that are predicted to be mostly unstable and mostly stable respectively.

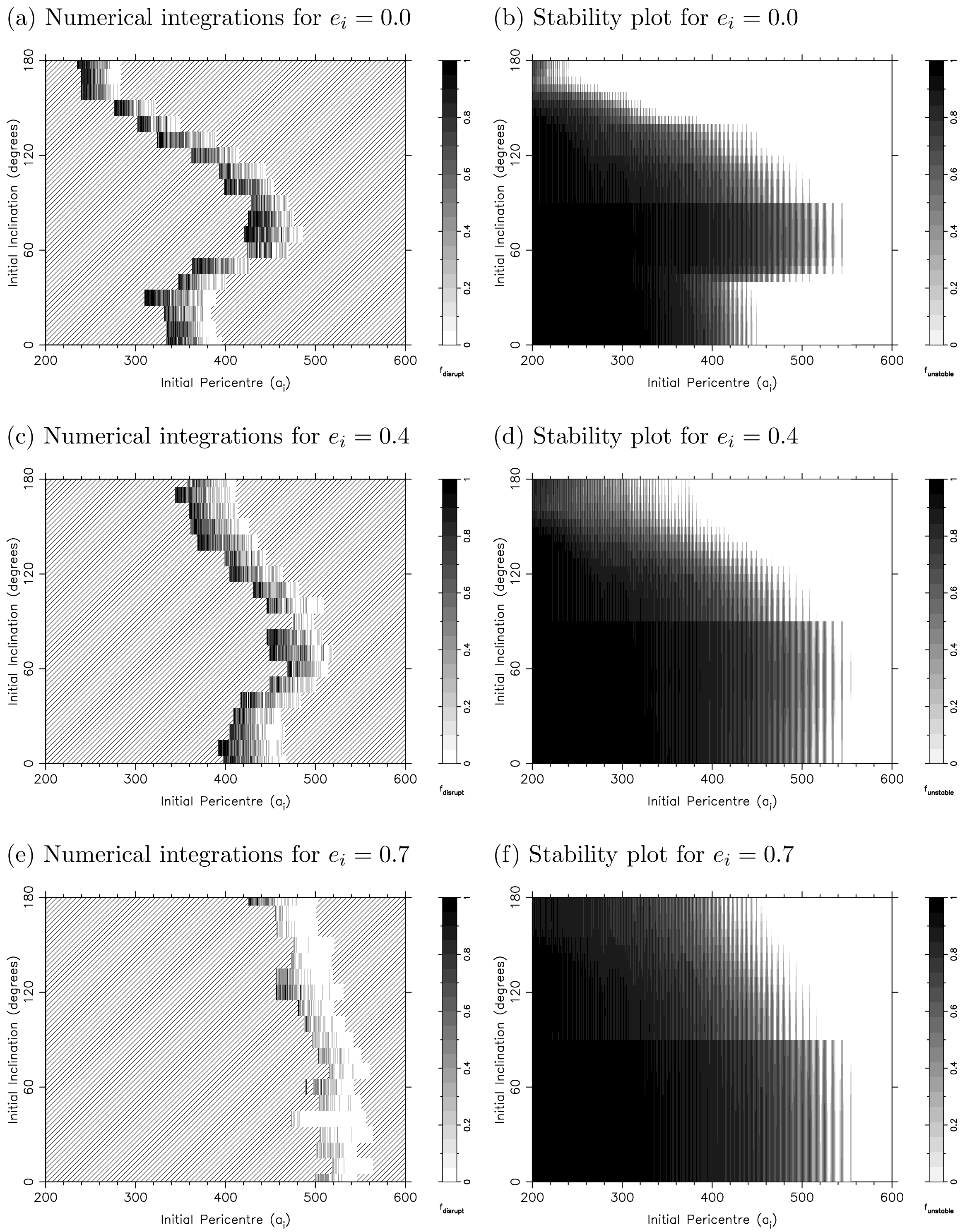

Figure 10.2: The fraction of disrupted binaries found from scattering experiments in Chapter 9 (left panels) and the fraction of unstable orbits predicted by the MSC (right) shown against the pericentre distance and relative inclination. The orbital eccentricity of the binary-MBH orbit is $e_o = 0.9$ for all panels and the orbital eccentricity of the stellar binary is $e_i = 0.0$, 0.4 and 0.7 from top to bottom panels. Note that the stability predictions in the right panels have $\phi_n = 0$ and therefore do not include a phase dependence.

the fraction of unstable orbits over the inclination. The resulting fraction of unstable orbits predicted by the MSC as a function of the initial pericentre distance of the binary-MBH orbit is shown as a solid curve in Figure 10.3. Each panel in this figure corresponds to a different stellar binary orbital eccentricity for which numerical integrations were conducted in Chapter 9. The numerical results for $e_i = 0.0$, 0.4 and 0.7 are shown as dashed red lines in Figure 10.3. These results have also been averaged over the inclination assuming a uniform sphere and are reproduced from the right hand side panels in Figure 9.4.

To provide a comparison to binaries on parabolic in-falling orbits with respect to the MBH the theoretical estimates discussed in Section 9.1 are indicated in Figure 10.3. These estimates are $P_{Heggie} = 114$ (vertical dotted line) defined by Equation (9.2) (Heggie et al. 1996) and $P_{Hills} = 240$ (solid vertical line) defined by Equation (9.1) based on numerical simulations by Hills (1992). Note that these are not expected to predict the maximum pericentre distance for bound binary-MBH orbits since they are based on parabolic approaches of the binary, i.e. a single pericentre passage. Recall that binary-MBH orbits with eccentricity $e_o = 0.9$ typically take 200 orbital periods for the binary to be disrupted (see Figure 9.2).

From Figures 10.2 and 10.3 the MSC is seen to provide a good estimate of the maximum pericentre distance resulting in the disruption of the stellar binary (p_{max}). The shape of the fraction of disrupted binaries as a function of the pericentre distance is also reproduced well for high eccentricities, as seen in Figure 10.3 (c). Even for lower eccentricities the predictions of the MSC are in good agreement with the numerical results, particularly compared to the accuracy of the theoretical estimates.

Recall that P_{Heggie} and P_{Hills} estimate the maximum distance at closest approach for parabolic binary-MBH orbits without considering the effect of the binary eccentricity (e_i) or the relative inclination (I) between orbits. For bound binary-MBH orbits with $e_o = 0.9$ the MSC is used to examine the effect of e_i and I on p_{max}. We take p_{max} to be the last pericentre distance for which the MSC predicts any unstable orbits for a given e_i and I. The resulting predictions of the maximum pericentre distance using the MSC against the relative inclination are shown as solid curves in Figure 10.4. The maximum pericentre distances found by numerical experiments to result in the disruption of the stellar binary are shown as dashed curves in Figure 10.4. These numerical results are reproduced from Figure 9.5 (b) but are shown on a different vertical scale to aid comparison to the predicted values. The curves in Figure 10.4 are shown for different orbital eccentricities of the stellar binary with $e_i = 0.0$ (red curves), 0.4 (green) and 0.7 (blue).

As a side note the maximum pericentre distance predicted by the MSC was used in the previous chapter to specify a range of p values that needed to be simulated. This helped reduce the number of simulations required to resolve the transition from parameters that typically resulted in the disruption of the binary to those that left the binary intact. This save an enormous amount of computer time as is evident from the large hatched line regions in Figure 9.4.

Returning to Figure 10.4, we see that the maximum p_{max} value is reached at $I \approx 70^\circ$, not at $I = 0$ as might be expected. This is predicted to occur by the MSC particularly for low binary

(a) $e_i = 0.0$

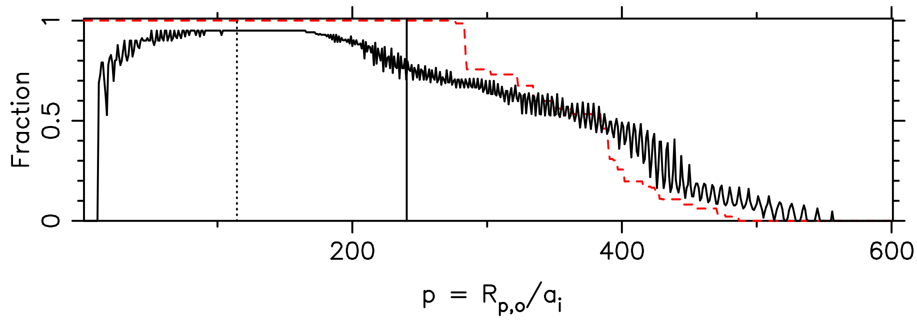

(b) $e_i = 0.4$

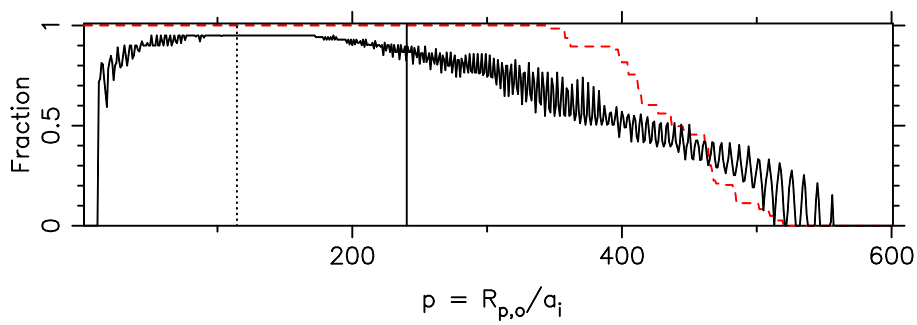

(c) $e_i = 0.7$

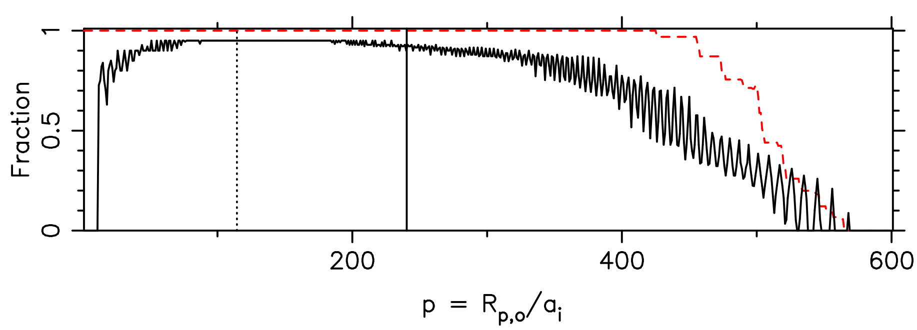

Figure 10.3: The fraction of orbits predicted to be unstable by the MSC (solid line) and the fraction of disrupted binaries (dashed red line) against the pericentre distance of the binary-MBH orbit. The fraction of disrupted binaries is reproduced from the right hand panels in Figure 9.4, which show the results of numerical experiments conducted in Chapter 9. Panels (a) - (c) show the effect of increasing the eccentricity of the original stellar binary. For comparison with the distance at closest approach for binaries in-falling on parabolic orbits with respect to the MBH, the theoretical estimates P_{Heggie} and P_{Hills} are shown as vertical dotted and solid lines respectively.

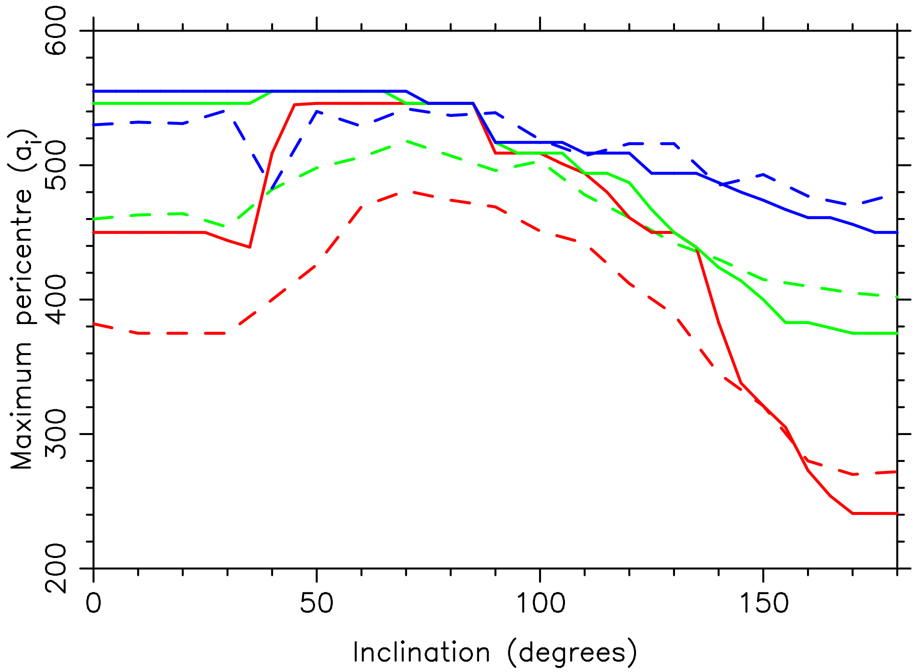

Figure 10.4: The maximum pericentre distances for which the MSC predicts unstable orbits (solid lines) and numerical integrations of the bound binary-MBH system result in the disruption of the stellar binary (dashed lines) shown against the relative inclination between orbits. The dashed curves are a reproduction of the numerical results for $e_o = 0.9$ originally presented in Figure 9.5 (b). The initial orbital eccentricity of the stellar binary is indicated by colour with $e_i = 0.0$ (red), $e_i = 0.4$ (green) and $e_i = 0.7$ (blue).

eccentricities ($e_i = 0.0$) due to the influence of the Kozai effect (see Section 1.3.3), which is also seen in the numerical results. The MSC tends to overestimate the extent of binary disruptions for $I \approx 150°$ and underestimate it for higher inclinations. The apparent overestimates for low inclinations can be understood by considering that the orbital integrations were run for a maximum of 400 orbital periods of the binary-MBH orbit (see Section 9.3). From Figure 9.2 the average time for the binary to be disrupted was close to this limit at pericentre distances of around 500. Therefore the numerically integrated binaries may not have had time to be disrupted resulting in the maximum pericentre distance being lower than it should be. This will particularly effect $e_i = 0.4$ and 0.7 since these have p_{max} values around 500 for inclinations less than 120°. The underestimation of p_{max} by the MSC for $I \gtrsim 150°$ cannot be explained in this way, instead we note that the discrepancy is actually fairly small (at most 30 units for $e_i = 0.0$).

We conclude that the MSC gives a good estimate of the maximum pericentre distance for which the disruption of the stellar binary by the MBH is possible. As the MSC gives good results for a black hole to stellar mass ratio of $q = M_{BH}/m = 3 \times 10^6$ it is reasonable to assume that this would also be the case for similar mass ratios. In the next chapter we are interested in mass ratios in the range $0.5 \times 10^6 \leq q \leq 7.0 \times 10^6$. To investigate this range of mass ratios would require the parameter space covered by simulations in Section 9.3 to be repeated many times over. This would take a prohibitive amount of computational time to complete. However by using the MSC to predict the dependence of unstable systems on the mass ratio q the same study can be completed instantly.

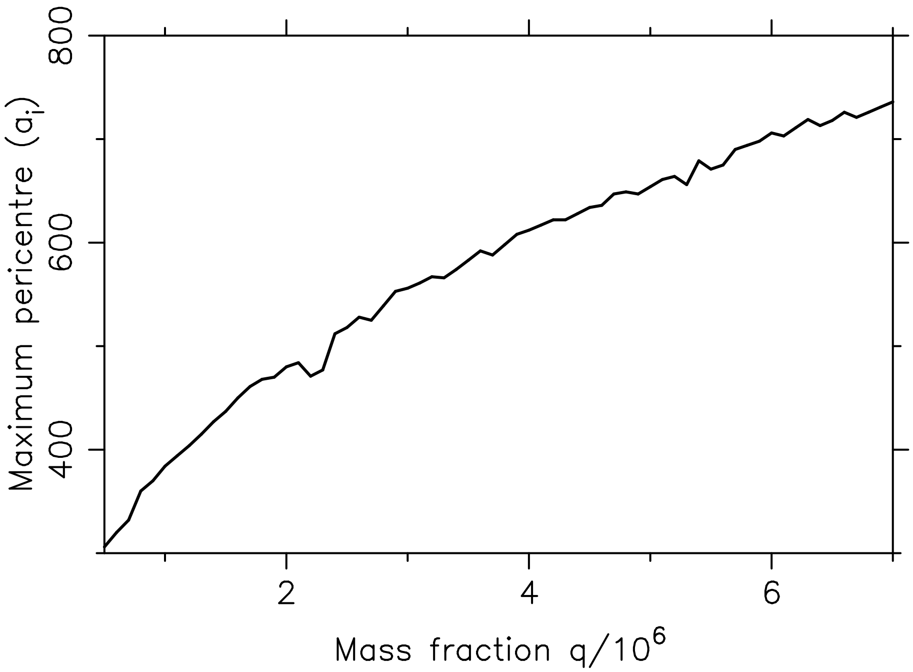

Figure 10.5: The maximum pericentre distance predicted by the MSC for $e_o = 0.9$ against the mass ratio q. For simplicity the stellar binary and MBH are in the same plane and the orbital eccentricity of the stellar binary is given by $e_i = 0.4$.

The dependence of p_{max} on the mass ratio q for coplanar systems with eccentricities $e_o = 0.9$ and $e_i = 0.4$ is shown in Figure 10.5. The mass ratio is altered by varying the mass of the black hole (m_3) while the stellar masses are fixed as $m_1 = m_2 = m = 1$, this changes the resonance widths discussed in the previous section. The main result from this figure is that for a fixed mass of the MBH it is easier to disrupt equal mass binaries composed of low mass stars (i.e. higher q values) than high mass stars.

We will use the dependence of p_{max} on q in the next chapter to estimate the effect of changing the stellar masses on the velocity distribution of the hypervelocity stars. This rests on the assumption that the dependence predicted by the MSC for $e_o = 0.9$ is analogous to the dependence of p_{max} on q for binaries on parabolic approaches to the MBH. The degree to which the results presented in this chapter for bound binary-MBH orbits are applicable to parabolic binary-MBH orbits is discussed in the next section.

10.3 Summary and discussion of results

We have used the Mardling stability criterion introduced in Section 1.3.2 to predict the stability of the three-body system consisting of a stellar binary and a massive black hole. By necessity the binary and the MBH must be in a bound orbit, chosen to have eccentricity of $e_o = 0.9$. The MSC was used to determine the occurrence of unstable systems with particular sets of the orbital eccentricity of the stellar binary e_i, the pericentre distance of the binary-MBH orbit p and the relative inclination between these orbits I. Unstable systems were found to be good predictors of when the influence of the MBH results in the eventual disruption of the stellar binary.

The fraction of disrupted binaries as a function of pericentre distance p and the relative inclination I were determined numerically in Chapter 9 for $e_o = 0.9$ and $e_o = 1.0$ (parabolic approaches of the binary to the MBH). Comparisons between the predicted fraction of unstable systems and the fraction of disrupted binaries against p and I was shown in Figure 10.2 for the stellar binary eccentricities of $e_i = 0.0$, 0.4 and 0.7.

In the previous chapter the maximum pericentre distance for which binaries were disrupted was found to depend on the stellar binary eccentricity and on the relative inclination. Theoretical estimates of the maximum pericentre distance (p_{max}) for parabolic binary-MBH orbits neglected the effect of the relative inclination and eccentricity of the stellar binary orbit.

The MSC was found to naturally reproduce the dependence of the maximum pericentre distance on e_i and I, as seen in Figure 10.4. Discrepancies between p_{max} from the numerical experiments of the previous chapter and the predicted p_{max} values using the MSC were due to the maximum time limit imposed on the numerical experiments. This time limit is of the same order as the timescale required to disrupt the stellar binary (see Figure 9.2) and therefore resulted in lower p_{max} values than predicted.

The key question with the stability analysis conducted for $e_o = 0.9$ is how relevant are these results to binaries encountering the MBH on parabolic orbits? Inclination and eccentricity were seen to affect the maximum pericentre distance in very similar ways from the numerical results in the previous chapter. Namely, higher orbital eccentricities of the stellar binary meant that it was easier to disrupt and subsequently p_{max} was increased. This was successfully predicted by the MSC for $e_o = 0.9$ binary-MBH orbits and it is reasonable to assume that increased instability for higher e_i binaries explains why they are easier to disrupt in parabolic binary-MBH orbits as well.

As mentioned previously the resonance widths used by the MSC to predict the stability of three-body systems do not significantly change for high values of e_o. Therefore the occurrence of unstable systems is predicted to be very similar between $e_o = 0.9$ and higher values such as $e_o = 1.0$ (Mardling 2008, private communication). The only difference between these from a theoretical point of view is that practically all systems with $e_o = 0.9$ are expected to end in the exchange of the MBH for one of the stars, while both exchange and the escape of the binary are possible for $e_o = 1.0$. The similarities in the underling physics of this problem can be demonstrated by considering the relative speed of the binary (v_p) and the MBH at the pericentre distance (R_p), given by

$$v_p = \sqrt{\frac{GM_{BH}}{R_p}}\sqrt{1 + e_o}. \tag{10.2}$$

This demonstrates the weak dependence on the eccentricity of the binary-MBH orbit (e_o) which means that the speed barely changes between $e_o = 0.9$ and parabolic orbits. This means that the behaviour of $e_o = 0.9$ and 1.0 are expected to be fundamentally similar and that the difference between these seen in the dependence on the relative inclination in Figure 9.5 is currently without explanation.

Chapter 11

Predicted velocity distribution of hypervelocity stars

The aim of this chapter is to apply the results of scattering experiments from Chapter 9 to the observable velocity distribution of hypervelocity stars (HVS). As discussed in Chapter 8 these stars were predicted to be an outcome of a stellar binary closely encountering a massive black hole (MBH) (Hills 1988). Currently only 10 HVS with velocities in between 420 to 720 km/s have been discovered in the Milky Way, which are not enough stars to build a statistically significant velocity distribution (Brown et al. 2007).

This chapter uses the velocities of stars escaping from simulated encounters between binaries and a MBH to predict the velocity distribution of the galactic hypervelocity stars. To estimate a velocity distribution requires the velocity results from the scattering experiments for equal mass binaries approaching the MBH on parabolic orbits ($e_o = 1.0$) conducted in Chapter 9 and some knowledge of the mechanism that initially scatters binaries towards the MBH. As discussed in Section 8.4, the details of the types of binaries and how they are scattered to within 0.04 parsecs of the MBH are unresolved problems. For this reason the stellar masses, semi-major axis and orbital eccentricity of the binary, its pericentre distance from the MBH will all be specified by simple and physically plausible distributions. Details of the adopted distributions for the scattering mechanism and for the binaries themselves are presented in Section 11.1.

The relative velocity of the binary centre of mass and the MBH is fixed such that the binary has a parabolic approach to the MBH, i.e. the binary-MBH orbit has eccentricity equal to unity. This allows the results from the scattering experiments conducted in Chapter 9 for equal mass binaries to be used to determine the velocities of the escaping star. Note that the scattering experiments were conducted for a fixed mass ratio of the black hole to one of the equal mass binary constituents given by $q = 3 \times 10^6$. The massive black hole in the Galactic centre is currently thought to have a mass of 3.4×10^6 M$_\odot$ (Schödel et al. 2003), which gives a stellar mass of $m = 1.13$M$_\odot$.

The dependence of the velocity distribution on the mass ratio q is approximated using how the maximum pericentre distance for which binaries were disrupted (p_{max}) was predicted to depend on q for $e_o = 0.9$. The dependence of p_{max} on the mass ratio was predicted by the Mardling stability criterion (MSC) in Chapter 10 for binaries in bound orbits with the MBH. Bound orbits were used rather than parabolic orbits since the MSC can only predict the stability of bound three-body systems. The problems with applying a stability analysis for binary-MBH orbits with eccentricity $e_o = 0.9$ has already been discussed in Section 10.3. It is found here that the mass ratio does not significantly effect the velocity distribution of HVS, so the problems of applying the stability analysis for $e_o = 0.9$ to $e_o = 1.0$ is relatively unimportant.

The adopted distributions for the binary and relative motion of the binary to the MBH are summarised in Section 11.1. Five models are chosen to represent the range of possible distributions. Three of these differ only by the orbital eccentricity of the stellar binary, one is based on the dependence of the mass ratio and the final model has the semi-major axis set at the hard binary limit. The intention is not to present an exhaustive analysis of the distributions of all orbital parameters for the binary and the orbit about the MBH. Instead the results from the scattering experiments will be utilised in such a way as to make it as easy as possible for more accurate distributions when they become available.

Section 11.2 presents the velocity distributions for hypervelocity stars resulting from the adopted distributions in Section 11.1. Comparison is made between the predicted velocity distributions and theoretical estimates using the analytical results from Yu and Tremaine (2003). The differences between the predicted velocity distributions for the five models are used in Section 11.2 to discuss the effect the different in-falling binary parameters.

11.1 Adopted distributions for in-falling binaries

Simple distributions are required to describe the encounter of the binary with the MBH before using the results of Chapter 9 to predict the velocity distribution of HVS. This section will present physically reasonable distributions for the distance at closest approach between the binary and the MBH ($R_{p,o}$), semi-major axis of the stellar binary a_i and for the stellar masses.

For all of the results presented in this chapter the binary is taken to be on a parabolic orbit with respect to the MBH. The relative phase between the binary orbit and the binary-MBH orbit is taken to be uniformly distributed. The relative inclination between orbits is chosen such that the distribution in $\sin I$ is uniform. All scattering experiments in Chapter 9 were conducted for equal mass binaries. As the next section uses these results we consider only equal mass binaries. The mass ratio of the MBH to one of the binary components is taken as $q = 3 \times 10^6$, although the effect of this is examined below. These assumptions are identical to those used to study the dependence of the velocity on the pericentre distance.

No distributions are adopted for the orbital eccentricity of the stellar binary e_i. Instead we will use the three values from which results from scattering experiments are available to examine the effect of the initial binary eccentricity on the velocity distribution of the HVS. These three values of $e_i = 0.0$, 0.4 and 0.7 give us our first three models used in the next section.

It is assumed that star formation in the galactic centre proceeds in the same way as in the local field stars. This assumption allows one to use the mass function and orbital period distribution for binary systems observed in the local stellar neighbourhood. N-body simulations for young star clusters in the galactic centre show that the initial mass function of the cluster is consistent with a Salpeter distribution for masses greater than a solar mass (Portegies Zwart et al. 2007).

A Salpeter distribution with $\alpha = 2.35$ (Salpeter 1955) is adopted for the mass range of 1 $M_\odot$ to 6 $M_\odot$. The minimum mass is chosen to be the lowest mass that can currently be observed in the galactic halo. The maximum mass is chosen such that the main sequence lifetime for a star of this mass is shorter than the travel time required for the observed HVS population (see also the discussion in Section 8.3). A maximum mass of 6 $M_\odot$ with a main sequence lifetime of $\approx$ 60 Myr (Tout et al. 1997) is consistent with the shortest observed travel time for a B star (Brown et al. 2007). The mean stellar mass associated with this distribution is $m = 1.57 M_\odot$.

Recall from Section 8.2 that conditions in the galactic centre can be characterised by a velocity dispersion of $\sigma = 150$ km/s and a stellar density of $\rho = 10^6 M_\odot$ pc^{-3} (Genzel et al. 2003). Using these values the hard binary limit for a $1M_\odot$ star is given by Equation (8.1) to be $a_{crit} =$ 0.08 AU. The timescale for disruption of soft binaries with separation $a_i = 10$ AU is 4 Myr by Equation (8.2). This timescale is of the same order as the timescale for scattering binaries towards the MBH, therefore some soft binaries are expected to be included in the distribution. The number of soft binaries able to encounter the MBH will be increased if binaries can be provided by stellar clusters spiralling into the galactic centre (e.g. Portegies Zwart et al. 2002). Binaries originating in open clusters near the galactic centre will have higher hard binary limits than 0.08 AU, because other environments will have different densities and velocity dispersions and therefore higher hard binary limits compared to binaries closer to the galactic centre.

Assuming a mix of soft and hard binaries the distribution of the binary semi-major axis is taken to be a log normal distribution with minimum $a_i = 0.05$ AU and maximum $a_i = 10$ AU (Gould and Quillen 2003). This distribution is consistent with the distribution of orbital periods in the local neighbourhood (Duquennoy and Mayor 1991) and favours widely separated binaries over tight binaries. The minimum value is chosen to remove binaries that can undergo a common envelope evolution and corresponds to $\sim 10\ R_{star}$ for a $6M_\odot$ star. As discussed in Section 8.2 the disruption timescale for a 10 AU binary is approximately 4 Myr, so it represents the maximum binary separation that can be scattered towards the MBH before it is disrupted.

The distribution of semi-major axes described above is used for four of the five models. The remaining model has the semi-major axis fixed at the hard binary limit, i.e. $a_i = a_{crit} = 0.08$ AU. This allows us to examine what difference is made to the velocity distribution of HVS if all soft binaries are disrupted before they can encounter the MBH. For simplicity this model takes a single stellar binary orbital eccentricity value of $e_i = 0.4$ and is referred to as Model B.

The pericentre distance, $R_{p,o}$, is taken as a uniform distribution from 1 to 700 AU. Chapter 9 presented the velocities of the escaping star from the Hills mechanism in terms of the scaled distance at closest approach $p = R_{p,o}/a_i$, thus the semi-major axis a_i is also required before using these results.

All of the distributions discussed so far are directly applicable to the velocity results from scattering experiments conducted in Chapter 9 since the mass ratio is fixed as $q = 3 \times 10^6$. The final model aims to test how much of an effect changing the mass ratio of the black hole to one of the binary components will have on the velocity distribution of HVS. To investigate the effect of changing the mass ratio on the distribution of velocities would require the parameter space described in Section 9.3 be repeated for each value of q. This is far too computationally expensive to be undertaken for the sake of a small effect (as seen later).

In Chapter 10 the Mardling stability criterion (MSC) was used to predict the maximum pericentre distance for which a stellar binary was disrupted by the addition of a MBH on a bound orbit with the stellar binary. The predictions were found to compare well with the numerical scattering experiments conducted in Chapter 9 for a binary-MBH orbital eccentricity of $e_o = 0.9$. Predictions using the MSC for the maximum pericentre distance resulting in the tidal disruption of the binary can be calculated almost instantly. This allows the dependence of the maximum pericentre distance on the mass ratio to be determined, which is shown in Figure 10.5 for a stellar binary eccentricity of $e_i = 0.4$. The range of mass ratios was chosen as $0.5 \times 10^6 \leq q \leq 7 \times 10^6$, which reflects a stellar mass range of $0.5 \leq m/\mathrm{M}_\odot \leq 6$ for a black hole mass of 3.4×10^6 $\mathrm{M}_\odot$ (Schödel et al. 2003).

For the final model, Model A, the mass of the MBH is held constant at $M_{BH} = 3.4 \times 10^6$ $\mathrm{M}_\odot$ and the mass ratio $q = M_{BH}/m$ is varied. For each choice of the stellar mass, from the distribution above, a new mass ratio q is calculated and a correction factor is applied to the scaled pericentre distance $p = R_{p,o}/a_i$. This correction is given by $p_{max}(q = 3 \times 10^6)/p_{max}(q)$ and results in the scaled pericentre distance used to determine the velocity of the escaping star being given by

$$p = \left(\frac{p_{max}(q = 3 \times 10^6)}{p_{max}(q)} \right) \left(\frac{R_{p,o}}{a_i} \right) \tag{11.1}$$

where the value of $p_{max}(q)$ is taken from Figure 10.5.

The largest errors in the velocity distribution due to the distributions adopted here are expected to come from the $R_{p,o}$ and a_i distributions. The effect of a bias to low (high) values of $R_{p,o}$ and/or a_i would be an increase (decrease) in the escaping star velocities. Both of these distributions depend on the mechanism for initially scattering binaries towards the MBH. The distributions adopted for these quantities are chosen to be as simple as possible and will be replaced when observational constraints on the scattering mechanism become available.

11.2 Velocity distribution for the HVS

Using the distributions from the previous section and scattering experiments for binaries approaching the MBH on parabolic orbits from Chapter 9 the distribution of velocities for the HVS can be estimated. Due to the limited parameter space covered by these simulations we consider only a fixed mass ratio of $q = M_{BH}/m = 3 \times 10^6$ where M_{BH} and m are the black hole and star masses respectively. The assumption of a fixed mass ratio is tested using Model A described in the Section 11.1.

The velocity scale used to convert the results from the left panels of Figure 9.6 into physical units has been previously stated in Equation (9.7) and was

$$v_{scale} = 29.786 \left(\frac{m}{\mathrm{M}_\odot}\right)^{1/2} \left(\frac{a_i}{AU}\right)^{-1/2} km/s \tag{11.2}$$

for an equal mass binary of component masses m and semi-major axis a_i. For example a binary with separation given by the hard binary limit in the previous section was $a_i = 0.08$ AU for solar mass stars so $v_{scale} = 105.3$ km/s. For an in-falling binary on a parabolic orbit with closest approach given by $R_{p,o} = 200a_i$ the expected velocity magnitude of an escaping star is ~ 1500 km/s, where the scattering experiment results shown in the right hand panels of Figure 9.6 have been used. Note from this figure that for $e_i > 0$ the magnitude of the velocity of the escaping star is roughly constant for $p \gtrsim 200$ until no binaries are disrupted. This means that even fairly wide encounters between the binary and the MBH can produce a HVS with velocities greater than 1000 km/s.

Larger velocities are possible but require much closer impact parameters, which are unlikely, or closer binary separations. As mentioned in the previous section a_i cannot be smaller than the respective Roche lobes for each star to avoid coalescence. Smaller velocities of ~ 1000 km/s are more likely when moderate values of a_i and R_p are considered.

A distribution of velocities is produced by randomly allocating sets of $R_{p,o}$, a_i and m using the distributions for these parameters given in the previous section. The orbital eccentricity of the stellar binary e_i is kept distinct and used along with $p = R_{p,o}/a_i$ to get an expected velocity in scaled units from Figure 9.6. Note that velocities from this figure already take into account the relative phase and inclination of the orbits. To convert the scaled velocity into a physical velocity the allocated values of a_i and m are used in Equation (11.2). The resulting velocity distribution function and cumulative distribution functions are shown in panels (a) and (b) of Figure 11.1 respectively.

The theoretical velocity distribution shown in Figure 11.1 as a dashed black curve is determined from analytical estimates of the velocity given in (Yu and Tremaine 2003) combined with the distributions presented in Section 11.1. Theoretical velocities are determined for each set of m, a_i and $R_{p,o}$ with $M_{BH} = 3.4 \times 10^6 \mathrm{M}_\odot$ by Yu and Tremaine (2003)

$$v_{theory} = 614 \left(\frac{M_{BH}}{10^6 \mathrm{M}_\odot}\right)^{1/4} \left(\frac{m}{\mathrm{M}_\odot}\right)^{1/4} \left(\frac{1mpc}{R_{p,o}}\right)^{1/4} \left(\frac{0.1AU}{a_i}\right)^{1/4} km/s \tag{11.3}$$

assuming an equal mass binary. Since not every combination of a_i and $R_{p,o}$ produce a hypervelocity star we take the fraction of captures for $e_i = 0.4$ (Figure 9.3 d) as the probability of a star escaping the galactic centre for the theoretical distribution.

Figure 11.1 shows the distribution of velocities for the escaping star as it leaves the galactic centre for five models and one theoretical comparison. Three of the five models are for different stellar binary eccentricities for the same mass and semi-major axis distributions, these are coloured by and $e_i = 0.0$ (red), 0.4 (green) and 0.7 (blue). Model A (solid black curve) shows

(a) Probability distribution for models with the same semi-major axis distribution

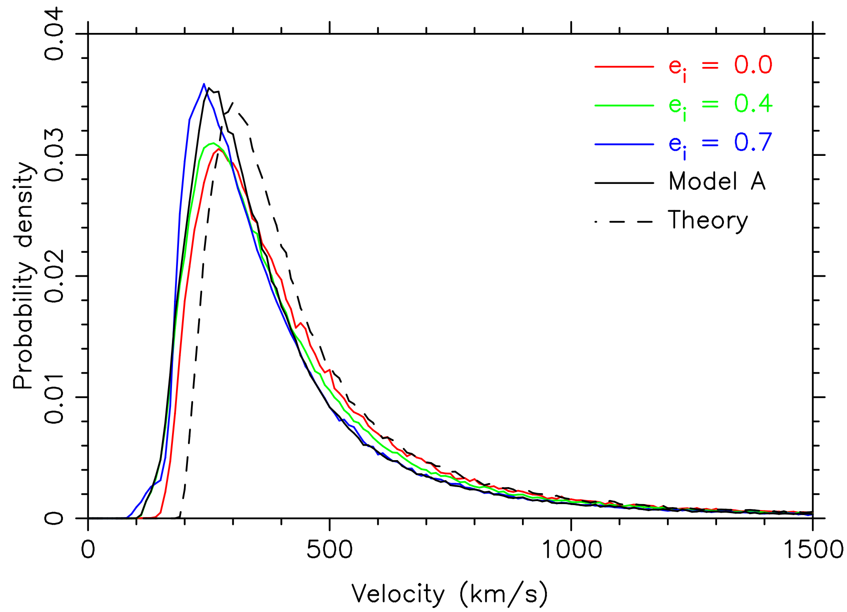

(b) Cumulative velocity distribution for all five models and a theoretical estimate

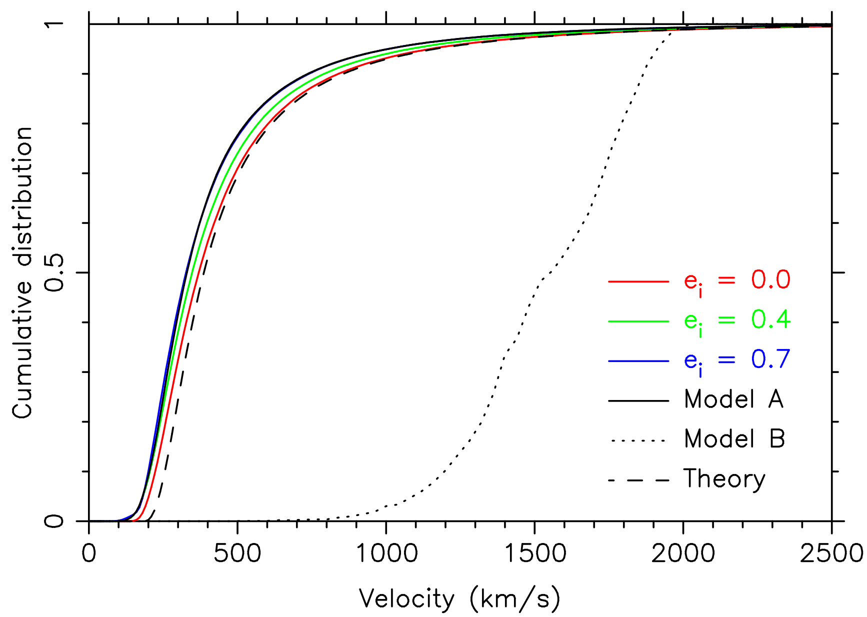

Figure 11.1: Predicted ejection velocity distribution for hypervelocity stars once they exit the galactic centre after an interaction of a binary and a MBH using results from scattering experiments conducted in Chapter 9 and parameter distributions from Section 11.1. Three of the five models differ only by their stellar binary eccentricities ($e_i = 0.0$, 0.4 and 0.7) and use the same mass and semi-major axis distributions. Model A includes the effect of a varying mass ratio for different stellar masses, while keeping the black hole mass fixed. Model B has the semi-major axis fixed at the hard binary limit, i.e. $a_i = 0.08$ AU. This model is only shown in the bottom panel as it draws attention from our main results. Theoretical velocity estimates are determined using Equation (11.3), which is based on the analytical results of Yu and Tremaine (2003). Models A, B and the theoretical velocity estimates make use of the scattering results for a binary eccentricity of $e_i = 0.4$.

Model	v_{median}	v>300 km/s	v>1000 km/s	v>1500 km/s	v>2500 km/s
$e_i = 0.0$	360	0.705	0.070	0.026	0.005
$e_i = 0.4$	340	0.648	0.061	0.022	0.004
$e_i = 0.7$	320	0.599	0.052	0.018	0.003
Model A	320	0.616	0.052	0.018	0.003
Model B	1520	0.981	0.568	0.017	0.000
Theoretical	380	0.790	0.072	0.027	0.004

Table 11.1: Summary of the velocity distributions shown in Figure 11.1 for the five models introduced in Section 11.1 and the theoretical estimate based on analytical formulae from Yu and Tremaine (2003). All five models are based on the results of scattering experiments conducted in Chapter 9 for a binary approaching a MBH on a parabolic orbit. Models A, B and the theoretical estimate are based on scattering results for $e_i = 0.4$. Model A includes the effect of a changing mass ratio q for a fixed black hole mass of $3.4 \times 10^6 M_\odot$. The distribution of binary semi-major axis is taken to be a log normal distribution, except for Model B where the semi-major axis is the hard binary limit ($a_i = a_{crit} = 0.08$ AU).

the effect of changing the mass ratio of $q = 3 \times 10^6$ for different stellar masses while keeping the black hole mass fixed. This model uses velocity results from scattering experiments conducted with $e_i = 0.4$ in Chapter 9. These four models are shown in Figure 11.1 (a) to demonstrate the near independence of the velocity distribution on the stellar binary eccentricity and the mass ratio q. The theoretical velocity distribution is also shown in the top panel of Figure 11.1 and has only slightly higher velocities than the equivalent model for $e_i = 0.4$ (green curve). The theoretical estimates by Yu and Tremaine (2003) are vindicated by these simulations.

Model B has the semi-major axis fixed at the hard binary limit, i.e. $a_i = 0.08$ AU, and is shown as a dotted black curve in Figure 11.1 (b). The cumulative distribution for Model B is shown in the bottom panel. Model B also uses the velocity data from $e_i = 0.4$, which allows direct comparisons to be made between models A, B, $e_i = 0.4$ and the theoretical estimates.

To summarise the cumulative velocity distributions shown in Figure 11.1 the probability of velocities being greater particular values is shown in Table 11.1. Each of the three eccentricity models, Models A and B and the theoretical velocity distribution are shown in this table. The medium velocity for each distribution is given in column 2, while columns 4 - 8 show the probability associated with the escaping star having a velocity greater than 300, 1000, 1500 and 2500 km/s.

Table 11.1 shows that increasing the orbital eccentricity of the stellar binary (e_i) slightly decreases the median velocity. Including the effects of the mass ratio q (Model A) was found to decrease the median velocity compared to the $e_i = 0.4$ distribution. Overall the eccentricity and mass ratio have negligible effect on the predicted velocity distribution of hypervelocity stars at the point where they are ejected from the galactic centre.

The distribution of semi-major axis of the original binary has the largest effect on the velocity distribution of stars ejected from a binary during an encounter with a MBH. This is demonstrated by Model B which uses the same distributions described in the previous section with $e_i = 0.4$, but takes a single value of the semi-major axis. The semi-major axis is taken as the hard binary limit, i.e. $a_i = a_{crit} = 0.08$ AU for a solar mass star. This model is found to produce far higher average velocities than the wide separation bias distribution used for the other models.

The single a_i value used by Model B allows it to be compared to other velocity distributions in the literature. The first of two comparisons is with the results of Gualandris et al. (2005) who also examine the interaction between an equal mass binary system and a MBH. For scattering experiments conducted with two 3 $M_\odot$ stars and a $3.5 \times 10^6 M_\odot$ they found the average escape velocity to be approximately 2000 km/s for $a_i = 0.08$ AU. For the Salpeter distribution with a mean stellar mass of $m = 1.57M_\odot$ Model B has an average escape velocity of 1520 km/s (Table 11.1). Using the velocity dependence on mass of $m^{1/2}$ (Equation 11.2) this value becomes an equivalent velocity of 1716 km/s for a binary composed of $3M_\odot$ stars. This is a little lower than the average velocity given by Gualandris et al. (2005), but well within the error bars.

The second comparison is with results for an equal mass binary of $7M_\odot$ stars with orbital eccentricity $e_i = 0.0$ and semi-major axis $a_i = 0.05$ (Bromley et al. 2006). Since we have shown that the eccentricity does not significantly affect the velocity distributions we again use Model B ($e_i = 0.4$) as a comparison. To determine the escape velocities of stars as they leave the galactic centre Bromley et al. (2006) used an analytical formula determined by Hills (1988). For the set of parameters described above this gave an average velocity of 4800 km/s, using Equation (11.2) to adjust for mass and semi-major axis the median velocity of Model B becomes 4060 km/s. Again the median velocities the scattering results are a little lower than expected. This is expected in this case since Bromley et al. (2006) use an analytical approach similar to the theoretical estimate given by Equation (11.3).

Before applying the velocity distribution to the observed hypervelocity stars the motion through the galaxy must be taken into account. The velocity distributions shown in Figure 11.1 are for stars ejected during an encounter between a binary and a MBH just after they leave the galactic centre. Work by Kenyon et al. (2008) indicates that the galactic potential acts as a filter removing all low velocity stars and reducing the velocities of the rest by 20 to 50 percent depending on galaxy model at a distance of 50 kpc, where most are observed (Brown et al. 2007). The difference between the observed velocity distribution of HVS and the predicted distribution as they left the galactic centre can be used to model the gravitational potential of the galaxy (e.g. Bromley et al. 2006). An examination of the gravitational potential will require a larger population of HVS (Brown et al. 2007) and will provide constraints on the distributions discussed in Section 11.1.

Overall we find good agreement between our models and with theoretical estimates by Yu and Tremaine (2003) as well as with other predicted velocity distributions from the literature (Gualandris et al. 2005; Bromley et al. 2006). We find that the orbital eccentricity of the binary and the mass ratio of the black hole to the stellar mass are relatively unimportant for the distribution of HVS. By analytical estimates the mass ratio of the binary components is also expected not to significantly alter these results (Hills 1988; Yu and Tremaine 2003; Bromley et al. 2006). The main effects on the velocity distribution are from the distribution of semi-major axis and the pericentre distance of the binary-MBH orbit.

Chapter 12

Summary and discussion

Scattering experiments have been conducted for the tidal disruption of a stellar mass binary system by a massive black hole (MBH), referred to as the Hills mechanism (Hills 1988). Dynamical interactions of this type can result in the destruction of the binary system, leaving one star bound to the MBH, while the other star is ejected from the system with high velocity. The probability of disrupting a binary for both parabolic and bound binary-MBH orbits has been investigated. Theoretical estimates of the maximum pericentre distance for which the binary was disrupted are compared to the scattering experiment results using two estimates from the literature (Hills 1992; Heggie et al. 1996) for parabolic orbits and the Mardling stability criterion (MSC) introduced in Section 1.3.2 for bound orbits. The escape velocities for stars ejected from encounters between a binary on a parabolic approach to the MBH have also been used to predict the velocity distribution of hypervelocity stars (HVS) as they leave the Galactic centre. Comparing this distribution to the observed velocity distribution of HVS allows one to constrain the gravitational potential of the galaxy and the dynamical interaction that ejected them.

Scattering experiments were conducted in Chapter 9 for a binary system on parabolic orbits ($e_o = 1.0$) and highly eccentric bound orbits ($e_o = 0.9$) with three binary eccentricities ($e_i =$ 0.0, 0.4 and 0.7). All orbital integrations were done for an equal mass binary with the mass ratio of the black hole mass (M_{BH}) to one of the binary component masses (m), given by $q = M_{BH}/m = 3 \times 10^6$. For an equal mass binary of two $1\mathrm{M}_\odot$ stars, this ratio is consistent with the current mass for the MBH in the galactic centre of the Milky Way of 3.4×10^6 $\mathrm{M}_\odot$ (Schödel et al. 2003). Details of the special purpose numerical integrator and the scaling used were given in Section 9.2 and the parameter space covered by scattering experiments was described in Section 9.3.

The fraction of orbital phases of the stellar binary with respect to the binary-MBH orbit for which the binary was disrupted was examined as a function of the initial pericentre distance (p_o) and the relative inclination between orbits (I). The fraction of disrupted binaries was determined from scattering experiments for each e_i value and is shown in the left panels of Figures 9.3 and 9.4 for parabolic and bound binary-MBH orbits respectively. The right hand panels of these figures shows the fraction of disrupted binaries after averaging over the relative inclination, assumed to be distributed over a uniform sphere.

A useful diagnostic for the fraction of disrupted binaries was the pericentre distance of the binary-MBH orbit for which $f_{disrupt} > 0$ (referred to as p_{max}). This was found from the scattering experiments to vary as a function of the relative inclination and to increase with increasing binary eccentricity. For binaries on parabolic approaches to the MBH in the same plane, the maximum pericentre distance was $p_{max} \approx 240$, 350 and 380 for $e_i = 0.0$, 0.4 and 0.7 respectively. Neither the dependence on eccentricity or on inclination was included in the theoretical estimates for the maximum distance, as shown in Figure 9.5. The studies examined here estimated this distance as $p_{Hills} \approx 240$ (Hills 1992) and $p_{Heggie} \approx 114$ (Heggie et al. 1996). The latter is linked to analytical estimates of the cross-sectional area associated with exchange. This leads to a systematic underestimation of the cross-section associated with the capture of a star by the MBH of between 1.4 and 4.5 depending on the orbital eccentricity of the stellar binary.

In Chapter 10 the MSC was used to investigate the dependence of the maximum pericentre distance on the binary eccentricity and the relative inclination of the stellar binary to the binary-MBH orbit. Since the MSC can only be applied to bound triple systems the parabolic approach of a binary to the MBH could not be investigated directly. Instead the fraction of disrupted binaries from numerical results for a high eccentricity binary-MBH orbit ($e_o = 0.9$) was compared to the fraction of unstable systems predicted by the MSC. An unstable system in this context is equivalent to a system that results in the break up of the original stellar binary.

Figure 10.2 shows the numerical binary disruption results for $e_o = 0.9$ alongside the fraction binary disruptions predicted by the MSC as a function of pericentre distance and inclination. Once again the maximum pericentre distance for which the fraction of disrupted binaries was greater than zero was used to characterise the results. These are shown against the inclination for $e_i = 0.0$, 0.4 and 0.7 in Figure 10.4. Good agreement is seen for all values with the small differences for high p_{max} values due to the maximum simulation time (400 binary-MBH orbits) being too short for all binaries to be disrupted. The average time taken for binaries to be disrupted is typically 200 binary-MBH orbits but can exceed this when the pericentre distance is greater than 500 a_i, as shown in Figure 9.2 for $e_i = 0.4$.

As the MSC was good at reproducing the maximum pericentre distance from numerical results, it was used to predict the dependence of p_{max} on the mass ratio $q = M_{BH}/m$. To investigate the effect of changing the mass ratio would require the parameter space covered by simulations in Section 9.3 to be repeated many times over. This would take a prohibitive amount of computational time to complete. However by using the MSC to predict the dependence of unstable systems on the mass ratio q the same study can be completed instantly. The dependence of p_{max} on the mass ratio was shown in Figure 10.5 for the range $0.5 \times 10^6 \leq q \leq 7.0 \times 10^6$. The MSC predicted that the maximum pericentre distance can vary by up to 45% from p_{max} at $q = 3 \times 10^6$ over this range. It was found that it is easier to disrupt equal mass binaries composed of low mass stars (i.e. higher q values) than high mass stars for a fixed mass of the MBH. The predicted dependence of p_{max} on q was used by one of the HVS models in Chapter 11, discussed below.

By using the dependence of p_{max} on q from $e_o = 0.9$ with velocity results from $e_o = 1.0$ we are assuming that the dependence of p_{max} is analogous for both values of e_o. The main difference between bound and parabolic binary-MBH orbits is that parabolic orbits only have a single pericentre passage unless sufficient energy is transferred to the stellar binary to make the binary-MBH orbit bound. Aside from this complication, the MSC is expected to be equally good at predicting the stability of systems with bound or parabolic binary-MBH orbits. It was not used to predict the stability of parabolic orbits because it does not distinguish between which of the bodies ultimately escapes the system. Exchange occurs if one of the stars escapes and the other is captured by the MBH. The other option is for the binary to escape the system, i.e. energy is transferred from the stellar binary to make the binary-MBH orbit hyperbolic. As discussed in Section 1.3.2 the boundary between these outcomes can be determined in principal.

For binaries approaching the MBH on parabolic orbits, the disruption of the binary results in the capture of one star and the ejection of the other. This dynamical interaction has long been expected to produce hypervelocity stars originating in the galactic centre (Hills 1988) but it is only recently that such stars have been observed (Brown et al. 2005). The velocities of escaping stars from the scattering experiments conducted in Chapter 9 are used in Chapter 11 to predict the velocity distribution of the HVS. To produce the distribution of velocities required simple distributions to describe the encounter between the binary and the MBH.

Simple distributions describing the encounter between the binary and the MBH are used to produce the velocity distribution of the HVS. Firstly all binaries were assumed to encounter the MBH on parabolic orbits, i.e. $e_o = 1.0$. Secondly the orbital eccentricity of the stellar binaries were not assigned a distribution, rather they were separated into the values of $e_i = 0.0$, 0.4 and 0.7, thus allowing the results of Chapter 9 to be used. Using these results also includes adopting the same assumption of no bias in the orientation between the binary orbit and the binary-MBH orbit, i.e. the inclination is distributed over a uniform sphere. Finally physically reasonable distributions were adopted for the distance at closest approach between the binary and the MBH ($R_{p,o}$), the stellar masses (equal binary masses of m) and for the semi-major axis of the stellar binary a_i. These distributions are unconstrained as they strongly depend on the mechanism for producing in-falling binaries before they encounter the MBH (Section 8.3).

The adopted distributions were

- Pericentre distance $R_{p,o}$: Drawn from a uniform distribution from 1 to 700 AU.
- Mass of one binary component m: Drawn from a Salpeter distribution with $\alpha = 2.35$ (Salpeter 1955) over the mass range of 1 $M_\odot$ to 6 $M_\odot$.
- Semi-major of binary a_i: Assumed a mix of hard and soft binaries and was taken from a log normal distribution with minimum $a_i = 0.05$ AU and maximum $a_i = 10$ AU (Gould and Quillen 2003).

All of these were discussed in detail in Section 11.1, with the most problematic being the a_i distribution as discussed below.

Five models describing different variations of these distributions were used. Three of these were identical except for their orbital eccentricity of the binary ($e_i = 0.0$, 0.4 and 0.7) and were labelled by the eccentricity value. Model A examined the effect of changing the mass ratio of $q = 3 \times 10^6$ for different stellar masses keeping the black hole mass fixed. This model scaled the pericentre distances for the mass ratio q in the same way that the MSC found p_{max} to vary with q. Model B examined the effect of including only binaries with semi-major axis fixed at the hard binary limit for a $1M_\odot$ star, i.e. $a_i = 0.08$ AU from Equation (8.1). Both models A and B were based on the velocity results from scattering experiments for $e_i = 0.4$.

The velocity from scattering experiments for each set of $R_{p,o}/a_i$ and e_i was determined from the right hand panels of Figure 9.6, after taking account of the probability of a star escaping (right panels of Figure 9.3). This velocity in scaled units is transformed into a physical velocity for the values of m and a_i using Equation (11.2). The resulting distributions are shown in Figure 11.1 and the probabilities of velocities greater than indicative velocities are given in Table 11.1. Overall the velocity distributions for models that included a mix of hard and soft binaries compared well with theoretical distributions (Yu and Tremaine 2003) and previous studies (Gualandris et al. 2005; Bromley et al. 2006).

It was found that the eccentricity and mass ratio have negligible effect on the predicted velocity distribution of hypervelocity stars at the point where they are ejected from the galactic centre. The largest effect on this distribution was found to be the choice of semi-major axis distribution. Model B was a good illustration of this effect as it took the semi-major axis to be the hard binary limit and had much larger average velocities. All other models had a mix of hard and soft binaries with a distributional bias towards long period binaries. As discussed in Section 8.2, soft binaries will be preferentially disrupted in stellar clusters (Hills 1975). The inclusion of soft binaries in the semi-major axis distribution given in Section 11.1 must then be justified.

The upper limit for the semi-major axis distribution of $a_i = 10$ AU corresponds to the semi-major axis for which the timescale for soft binary disruption (Equation 8.2) is of the same order as the timescale associated with binaries being scattered towards the MBH (about 4 Myr). Thus some of these binaries will be scattered towards the MBH before they can be disrupted by other encounters with stellar mass objects. Binaries with wide separations can also be produced elsewhere, in regions where the hard binary limit is greater than 0.08 AU, and scattered into the galactic centre. Some examples of how this can occur are in-falling clusters (Portegies Zwart et al. 2002) and interacting stellar disks known to exist at ~ 0.1 pc from the MBH (Paumard et al. 2006). The stellar disks near the galactic centre are currently thought to be able to produce the S-stars via the Hills mechanism (Löckmann et al. 2008).

The velocity distributions produced in Chapter 11 are for stars ejected from an interaction between a binary and a MBH that have just escaped the galactic centre. The observable velocity distribution of HVS will be determined by the velocity distribution in the galactic centre and by the gravitational potential of the galaxy experienced by the star as it escapes to the galactic field. Currently, not enough HVS have been observed to accurately determine the velocity distribution of HVS in the galactic field. However, present telescope technology has the potential to observe approximately 100 more HVS (Brown et al. 2007), which will allow for the determination of the velocity distribution within the next decade.

Future comparison between the observed velocity distribution of HVS and the predicted distribution as they left the galactic centre can be used as a probe of the gravitational potential of the galaxy (e.g. Bromley et al. 2006; Kenyon et al. 2008). It will allow the individual models for producing hypervelocity stars to be discerned (Section 8.4) and may constrain the distributions associated with the scattering mechanism that produces in-falling binaries and the nature of these binaries, which had to be approximated in Section 11.1.

There remains significant scope for future work relating to the scattering experiments and the stability analysis of a related bound orbit presented here. The MSC can be extended to distinguish between escape and exchange for parabolic orbits, which can then be compared to results from the scattering experiments conducted in Chapter 9. From the numerical point of view, the effect of unequal mass binaries and a larger range of orbital eccentricities on the tidal disruption of binaries by the MBH as a function of inclination and pericentre distance is an obvious next step. The inclusion of unequal mass binaries is expected to affect the distribution of velocities predicted for the HVS by lowering the average velocities by a few hundred km/s compared to equal mass binaries (Bromley et al. 2006). Simulations of unequal masses will allow one to see if the inclination dependence seen for binaries on parabolic approaches to the MBH is specific to equal masses or not.

The dependence of the maximum pericentre distance for which binaries are disrupted on the relative inclination between the binary and the binary-MBH orbits was found to differ between $e_o = 0.9$ and $e_o = 1.0$ in the scattering experiments. This difference was clearly seen in Figure 9.5 where the peak in p_{max} was higher in inclination for $e_o = 0.9$ than for $e_o = 1.0$. The peak for higher inclination for $e_o = 0.9$ was due to the Kozai effect on the orbital eccentricity of the stellar binary. This is at odds with the expectation that for high eccentricities the stability should only weakly depend on e_o since the same resonances are exited (Mardling 2008, private communication). An extension of the scattering experiments conducted in this study which covers the binary-MBH orbital eccentricity range of $0.9 < e_o < 1.0$ would greatly complement our results and clarify the inclination effects seen here. Further work is required on distinguishing between escape and exchange for systems with a parabolic outer orbit. This would also have ramifications for the capture of dwarf spheroidal galaxies by the galaxy discussed in Chapter 7.

Part III

Signatures of resonant terrestrial planets in long-period systems

Chapter 13

Signatures of resonant terrestrial planets in long-period systems

Authored by: Gareth F. Kennedy and Rosemary A. Mardling

This chapter reproduces a paper submitted to MNRAS.

13.1 Abstract

The majority of extrasolar planets discovered to date have significantly eccentric orbits, some if not all of which may have been produced through planetary migration. During this process, any planets interior to such an orbit would therefore have been susceptible to resonance capture (as well as ejection and collision). While no energy is exchanged between planets in non-resonant systems so that their orbital periods remain constant, significant energy can be exchanged in resonant systems resulting in substantial long-term period modulation of the observed planet, even when the mass of the companion planet is small. Here we examine the possibility of detecting low-mass planets which have suffered resonance capture, particularly into the strong 2:1 resonance. Using simulated data we show that it is possible to identify the existence of a low-mass companion in the internal 2:1 resonance by calculating the orbital period using piecewise sections of radial velocity data. This works as long as the amplitude of modulation of the orbital period is greater than its uncertainty, which in practice means that the system should not be too close to exact resonance. Using a new formulation by Mardling for studying stability in the general three body problem, simple expressions for the libration period and the change in the observed orbital period are provided, these being valid for arbitrary eccentricities and planet masses. They in turn allow one to constrain the mass and eccentricity of a companion planet

if the orbital period is sufficiently modulated. Stability maps for a selection of currently known (apparently) single-planet systems are also provided.

13.2 Introduction

One of the holy grails of astronomy is to discover an Earth-mass planet orbiting a solar-type star at around 1 AU. While several low-mass planets have been discovered to date, only Gl 581c comes close to fitting the description of a terrestrial mass planet residing in the habitable zone of its parent star (Udry et al 2007; minimum planet mass $4.7M_\oplus$, distance from star 0.07 AU, habitable zone 0.05-0.1 AU). Like most extrasolar planets discovered to date, Gl 581c was discovered using the radial velocity technique, however, this discovery was possible currently because of the low stellar mass and short orbital period.

Transits of low-mass planets are a viable option even for planets at appreciable distances from their stars because the probability of observing a transit for any given system is proportional to R_*/d and not $(R_*/d)^2$ as one might naively expect (Borucki and Summers 1984). Here d is the distance of the planet from the star and R_* is the stellar radius. However, such discoveries will have to wait for the launch of missions such as Kepler, so that a technique which offers the possibility of deducing *now* the presence of low mass planets orbiting solar-type stars at appreciable distances is highly desirable.

One of the most startling differences between the majority of the extrasolar planets discovered to date and the planets in the Solar System is their eccentricities. Moreover, if our current understanding of how planets form is anywhere near correct their current positions are not where they formed. The two main mechanisms suggested to explain such movement are 1. migration via planet-disk tidal interaction (the disk being composed of either gas and dust (Lin et al. 1996) or planetesimals (Murray et al. 1998) or both), and 2. planet scattering (Rasio and Ford 1996). Both these mechanisms acting together are likely to account for at least some of the systems observed so far (Moorhead and Adams 2005). Of particular interest for this paper is the situation where migration results in resonance capture. Such a capture may in turn result in a stable or an unstable system, the former being associated with capture into a single resonance, and the latter with two or more resonances. This scenario has been studied numerically by Moorhead and Adams (2005).

Whether or not a system is captured permanently into a resonance, eventually escapes, or passes straight through, depends on whether the fixed point at exact resonance remains stable (elliptical) as the orbital elements evolve (Peale 1976). Analytical studies to date have concentrated exclusively on the circular restricted three-body problem (eg. Henrard 1982; Borderies and Goldreich 1984), and in particular have assumed small eccentricities and inclinations for the massless body. They are therefore not applicable to potential resonance capture in most of the known extrasolar planets so that at this stage, we cannot say much about the likelihood of low-mass planets being captured into low-order resonances. Moreover, one of the biggest uncertainties in the theory of planet-disk interaction is the way a planet's eccentricity evolves, this depending sensitively on the delicate torques produced by resonances (and hence density enhancements) in the disk (eg. Murray et al. 2002). Since resonance capture depends sensitively on the eccentricities *as well as* the rate of change of the semimajor axes, this adds another level of complexity to the problem. It is also likely that the orbital elements evolve stochastically (Murray-Clay and Chiang 2006); how this affects resonance capture for systems with arbitrary eccentricities and inclinations is unknown at this stage.

The role of Jupiter in the formation of the terrestrial planets is uncertain, but recent studies suggest that it may have been pivotal in forcing smaller bodies to merge to form Earth-size planets via secular-mean motion resonances (Nagasawa et al. 2005). Gas giant migration has also been shown to produce low-mass planets through the subsequent coagulation of scattered planetesimals, both interior and exterior to the giant's orbit (Raymond et al. 2006; Fogg and Nelson 2007). It is not unreasonable, therefore, to assume that systems exhibiting evidence of migration (high eccentricities, presence inside the snow-line) were capable of forming terrestrial planets interior to the orbits of the observed planets, and that some of these may have been captured into resonance.

So far we know of six resonant systems for which the planet masses are similar (and Jupiter-like), the parent stars being GJ 876, HD 160691, HD 73526, HD 82943, HD 128311 and 55 Cnc (see `http://exoplanet.eu/catalog-all.php` for discovery papers and data). All of these involve 2:1 resonances except for 55 Cnc which involves the 3:1 resonance, and all have significant eccentricities. None appear to be at exact resonance, and apart from GJ 876 and perhaps HD 28943, it is difficult to say whether or not these systems are apsidally locked. The 2:1 systems range from 0.3% to 5% away from exact resonance (not withstanding uncertainties in the orbital periods). Thus it seems that Nature produces resonant systems which are left with finite libration amplitudes once the protoplanetary disk responsible for resonance capture disappears, although whether this is true for systems with significantly different planetary masses is not known. Our proposal for discovering low-mass resonant companions to known gas giants relies on the system being a finite distance from exact resonance, with minimum viability depending on the parameters of the system and confidence intervals for the orbital period.

The plan of this paper is as follows. We begin with a discussion of some theoretical aspects of resonance, providing expressions for the resonance width, libration period and amplitude of orbital period modulation, each valid for arbitrary inner and outer eccentricities and planet mass ratios. In Section 3 we present stability maps for a selection of known apparently single systems in order to determine which systems have the potential to harbour a low-mass companion. In Section 4 we describe and illustrate our technique using some synthetic data for the system HD 216770. Section 5 presents a summary.

We will draw on theoretical work developed by one of us (Mardling) and refer to two papers in preparation: the first deals with stability and resonance in the general three-body problem, while the second deals with resonant structure in eccentric planetary systems. These will be referred to as M1 and M2 respectively.

13.3 Theoretical considerations

13.3.1 Resonance widths

A resonant system is characterized by the libration of one or more *resonance angles*[1]. Using a spherical harmonic expansion of the disturbing function for systems with arbitrary masses, orientations, and eccentricities (M1), a resonance angle may be identified by the integers n and n', where $n/n' \simeq \nu_i/\nu_o \equiv \sigma$, with ν_i and ν_o the inner and outer orbital frequencies (mean motions) respectively, and the spherical harmonic orders m, m' and m''. For a coplanar system, $m' = m'' = m$ and the $[n : n'](m)$ resonance angle is[2]

$$\phi_{mnn'} = n'\lambda_i - n\lambda_o + (m - n')\varpi_i - (m - n)\varpi_o, \tag{13.1}$$

where λ_i and λ_o are the inner and outer mean longitudes, and ϖ_i and ϖ_o are the corresponding longitudes of periastron (see also Equation (1.24)). For example, according to Lee and Peale (2002) (although they do not use our notation), the two outer planets orbiting GJ876 reside in the quadrupole $[2 : 1](2)$ mean motion resonance

$$\phi_{221} = \lambda_i - 2\lambda_o + \varpi_i, \tag{13.2}$$

the octopole $[2 : 1](1)$ mean motion resonance

$$\phi_{121} = \lambda_i - 2\lambda_o + \varpi_o, \tag{13.3}$$

and the $[0 : 0](1)$ secular "resonance"

$$\phi_{100} = \varpi_i - \varpi_o. \tag{13.4}$$

For pairs of planets the width of the 2:1 resonance is given approximately by the width of the [2:1](2) resonance,[3] which is given in terms of the variation of the ratio of orbital frequencies by (M1)

$$\Delta\sigma = 2\sqrt{\mathcal{A}_{221}}, \tag{13.5}$$

where

$$\mathcal{A}_{221} = -\tfrac{9}{4} s_1^{(22)}(e_i) F_2^{(22)}(e_o) \left[(m_o/m_*) + 2^{2/3}(m_i/m_*)\right]. \tag{13.6}$$

Here m_* is the mass of the star, m_i and m_o are the masses of the inner and outer planet respectively (we assume in this paper that $m_i \ll m_*$ and $m_o \ll m_*$), and the dependence on the inner and outer eccentricities, e_i and e_o respectively, is via the Fourier integrals $s_1^{(22)}(e_i)$ and $F_2^{(22)}(e_o)$, also known as Hansen coefficients (Hughes 1981; see M1 for their definitions). These

[1] The reader is referred to Section 1.3.2 of this thesis for further discussion.

[2] The value of m also indicates the leading harmonic degree ($l = 2$ quadrupole, $l = 3$ octopole etc.) except for $m = 0$ and $m = 1$ which are quadrupole and octopole respectively).

[3] See M2 for discussion and analysis of how the 2:1 resonance is a superposition of many resonances.

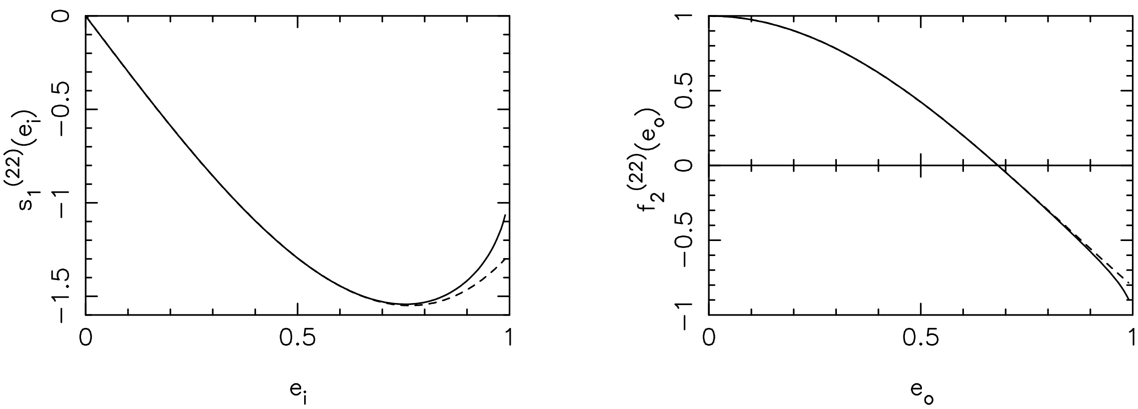

Figure 13.1: Eccentricity functions $s_1^{(22)}(e_i)$ and $F_2^{(22)}(e_o)$ (solid curves) together with seventh-order correct approximations given by equations (13.8) and (13.7) (dashed curves).

are given to seventh order in the eccentricities by

$$s_1^{(22)}(e_i) \simeq -3e_i + \tfrac{13}{8}e_i^3 + \tfrac{5}{192}e_i^5 - \tfrac{227}{3072}e_i^7, \tag{13.7}$$

and

$$F_2^{(22)}(e_o) \simeq 1 - \tfrac{5}{2}e_o^2 + \tfrac{13}{16}e_o^4 - \tfrac{35}{288}e_o^6 \tag{13.8}$$

and are plotted in Figure 13.1. If ϵ_i and ϵ_o are the differences between the exact and approximate values of $s_1^{(22)}(e_i)$ and $F_2^{(22)}(e_o)$ respectively, then $|\epsilon_i| < 0.001$ for $e_i < 0.63$, $|\epsilon_i| < 0.01$ for $e_i < 0.79$ and $|\epsilon_i| < 0.1$ for $e_i < 1$, while $|\epsilon_o| < 0.001$ for $e_o < 0.7$, $|\epsilon_o| < 0.01$ for $e_o < 0.86$ and $|\epsilon_o| < 0.28$ for $e_o < 1$. Note that (13.6) ignores contributions from $\ddot{\varpi}_i$ and $\ddot{\varpi}_o$ (M1), which in general is valid as long as the associated eccentricities are not too small.

Note also that the resonance width given by (13.5) is essentially independent of the mass of the hypothetical companion for $m_i \ll m_o$, and to first order in the ratio of semimajor axes (the zeroth-order term dominates), reduces to equation (8.57) in Murray and Dermott (2000) when $m_i = 0$ and $s_1^{(22)}(e_i)$ and $F_2^{(22)}(e_o)$ are given to first order in the eccentricities. In contrast to this, the variation in the outer orbital period is proportional to m_i/m_o as we now discuss.

13.3.2 Libration periods and orbital period variations

The libration period[4], that is, the period of variation of the orbital periods of two planets residing in the 2:1 resonance, is given approximately by (M1)

$$P_{lib} = P_o/\sqrt{\mathcal{A}_{221}} = \alpha \left[-s_1^{(22)}(e_i)\right]^{-1/2} P_o, \tag{13.9}$$

where α depends on known parameters when $m_i \ll m_o$. Thus for systems with a measurable modulation amplitude (see following paragraph), the libration period in principle allows one

[4]See also the discussion of libration and circulation for the three-body problem in Section 1.3.2 and illustrated in Figure 1.5.

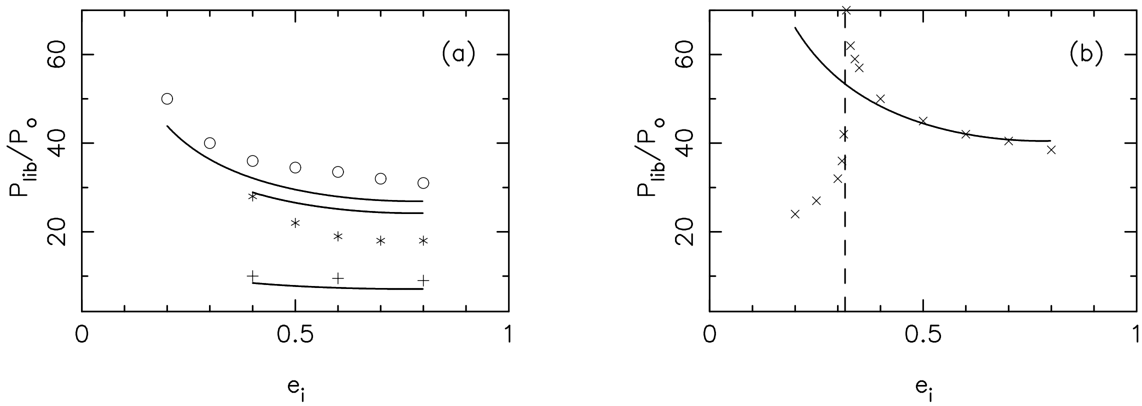

Figure 13.2: Comparison of data from direct numerical integrations to the theoretical estimate for P_{lib}, equation (13.9) (only stable systems were considered) for selected systems from Table 13.1. Symbols and corresponding system numbers are: ($\circ$: #6), ($*$: #11), ($+$: #7), ($\times$: #1). System #1 in panel (b) shows asymptotic behaviour around $e_i = 0.31$ which corresponds to the system crossing the separatrix at $\sigma = 1.95$ as e_i is increased. See text for discussion.

to estimate the eccentricity of an otherwise undetectable companion because it is effectively independent of its mass and the distance from exact resonance. The libration period is typically tens of orbital periods for systems studied here. Figure 13.2 compares (13.9) with data calculated from direct three-body integrations for four systems from Table 13.1 (6, 11, 7 and 1). The actual libration period is somewhat underestimated for systems 6 and 11 because (13.5) overestimates the true resonance width in those cases (see Figures 13.4 and 13.5). A more accurate estimate is obtained when one includes terms in addition to [2:1](2) (M2). Figure 13.2(b) (system 1) suggests asymptotic behaviour around $e_i = 0.31$. This in fact corresponds to the system crossing the separatrix at $\sigma = 1.95$ as e_i is increased, at which point the libration period is formally infinite. From Figure 13.4 it is clear that stable systems exist either side of the separatrix. Note that the expression for P_{lib} assumes small angle librations. We can conclude from these results that in practice one should use direct three-body integrations and a least squares fit to estimate the eccentricity of a low-mass companion when the libration period has been estimated from observational data (see Section 13.5). Note that reducing the mass of the companion has very little effect on the results shown in Figure 13.2, consistent with the weak dependence of (13.9) on m_i.

The total variations in the inner and outer orbital periods are given very accurately by (M1)

$$\delta P_i/P_i = 2\left[1 + (m_i/m_o)\sigma^{2/3}\right]^{-1} \delta\sigma/\sigma \simeq \delta\sigma \tag{13.10}$$

and

$$\delta P_o/P_o = -2\left[1 + (m_o/m_i)\sigma^{-2/3}\right]^{-1} \delta\sigma/\sigma \simeq -2^{2/3}\,(m_i/m_o)\,\delta\sigma, \tag{13.11}$$

where the equalities hold for $m_i, m_o \ll m_*$ and the approximations for $m_i \ll m_o$. Here $\delta\sigma = \sigma - 2$ and we have put $\sigma = 2$ where it appears on its own. Thus the total period variation depends

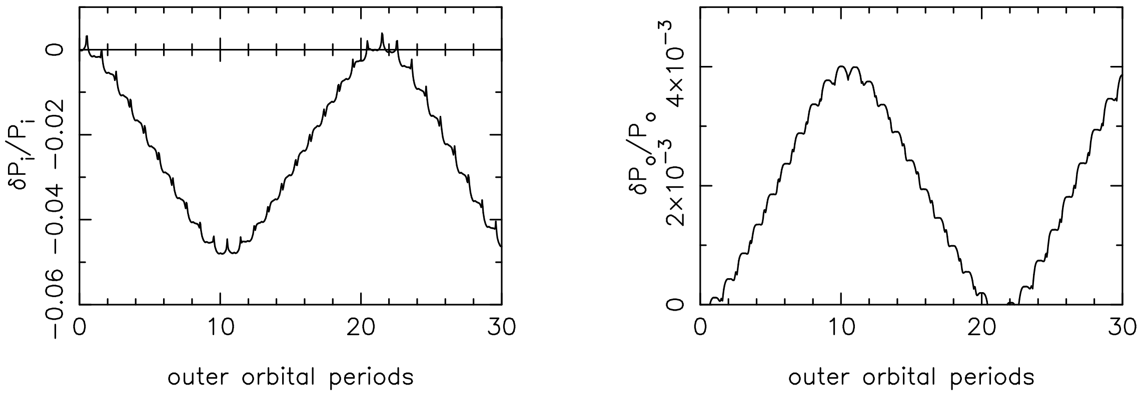

Figure 13.3: Period variations of HD 216770b (right-hand panel) and a hypothetical companion with mass $10M_\oplus$, eccentricity 0.5 and $\delta\sigma = -0.05$. Theoretical estimates give $\delta P_i/P_i \simeq \delta\sigma = -0.05$, $\delta P_o/P_o = 0.0038$ and $P_{lib} = 25.6P_o$.

only on the mass of the otherwise undetectable companion as well as its distance from exact resonance (assuming that the mutual inclination is small).

To illustrate the effect a hypothetical low-mass companion would have on the orbital period of a known system, we select a stable set of initial conditions from Figure 13.5 for HD 216770 (system 11; see next section) and Table 13.1 and integrate the equations for three-body motion directly. Figure 13.3 plots the evolution of the inner and outer orbital periods for the case where $e_i(0) = 0.5$ and $\sigma = 1.95$. Equations (13.10) and (13.11) predict quite accurately $\delta P_i/P_i \simeq \delta\sigma = -0.05$ and $\delta P_o/P_o = 0.0038$ respectively, while (13.9) gives $P_{lib} = 25.6P_o$ compared to the true value of $22P_o$.

13.4 Candidate systems

While this paper focuses on theoretical issues associated with the discovery of long-period terrestrial planets, in this section we present stability maps for a selection of candidates from the inventory of known systems in order to illustrate the viability of our proposal. In a subsequent paper, we will investigate the adequacy of existing data and apply our technique to those systems which can be analysed immediately (or recommend that more data be collected for promising systems).

13.4.1 Selection criteria

Criteria for selection from the inventory of known systems include:

1. Only one planet is known;

2. Orbital periods (and eccentricities) should indicate some migration during formation (for example, periods significantly less than Jupiter's period for a solar-mass star);

3. Orbital periods should be long enough to harbour a low-mass planet in the internal 2:1 resonance, but not so short that the orbital decay timescale of such a planet due to tidal interaction with the host star is less than the age of the system;

4. Stable configurations should exist;

5. The resonance width is such that a whole libration period can be measured in a reasonable time.

Table 13.1 lists systems from `http://exoplanet.eu/catalog-all.php` which satisfy these criteria. As well as orbital period in units of days, stellar mass m_* in units of solar masses, minimum planetary mass m_o in units of Jupiter masses and eccentricity e_o, we have listed the number of orbital periods in a libration period for a system with a $m_i = 10M_\oplus$ planet a distance $\delta\sigma = -0.05$ from exact resonance with $e_i = 0.5$, giving both the theoretical estimate $[P_{lib}/P_o]_{est}$ (equation (13.9)) and the actual number $[P_{lib}/P_o]_{act}$ calculated from a direct numerical integration. The average value of $|P_{lib,est}/P_{lib,act} - 1|$ is 0.24, a result attributable to using only the $[2:1](2)$ contribution to the 2:1 resonance (M2; see also Figure 13.2). The total change in the orbital period over a complete libration cycle, δP_o (equation (13.11)), and the maximum possible change in the orbital period, ΔP_o, as estimated using the resonance width $\Delta\sigma$ (equation (13.5)) in place of $\delta\sigma$ in equation (13.11) are given, both measured in hours. Note that $\delta P_o > \Delta P_o$ (ie. $\Delta\sigma < 0.05$) for system 4; this is indicated by square brackets and in fact corresponds to an unstable system. Values for ΔP_o corresponding to systems which are not stable for the entire resonance width (for example, system 7) are given in brackets. Finally, the circular reflex velocity of the star due to the hypothetical companion is given in the last column. Note that systems with small values of m_o/m_i tend to have relatively large values of $\delta P_o/P_o$.

Figures 13.4, 13.5 and 13.6 show stability maps for systems listed in Table 13.1. Each red dot corresponds to a numerically integrated unstable system whose initial values for the eccentricity of a hypothetical companion, e_i, as well as $\sigma = \nu_i/\nu_o$ are indicated by its position in the plot. The mass of the companion is taken to be $10M_\oplus$. The initial semimajor axis of the hypothetical companion is varied such that the ratio of mean motion frequencies is between 1.5 and 2.5 for a given observed semimajor axis. The sign of $\mathcal{A}_{221}$ indicates that libration is around $\phi_{221} = 0(\mathrm{mod})2\pi$ (M1) so we take $\varpi_i = \varpi_o = \lambda_i = 0$ initially. The outer orbit is started at apastron so that the orbit interaction is a minimum initially. Rather than integrate a system until one body escapes, we take advantage of the sensitivity to initial conditions of chaotic systems and simply compare two almost identical systems for 1000 outer orbits (the initial values for e_i differ by 10^{-7}). If the semimajor axis of the inner orbit varies between the two systems by more than what would be expected for two linearly diverging systems, it is deemed unstable (note that the comparison is made at outer apastron). See M1 for a more detailed discussion of this test. Also plotted in Figures 13.4 and 13.5 are boundaries for the [2:1](2) resonance as well as those for the [5:3](5) and [7:3](7) resonances, calculated using (13.5) (with $\mathcal{A}_{221}$ replaced by $\mathcal{A}_{553}$ and $\mathcal{A}_{773}$: see M1 for the general definition of $\mathcal{A}_{mnn'}$). These maps give an indication of how "clean" the 2:1 resonance is. In general, systems with relatively

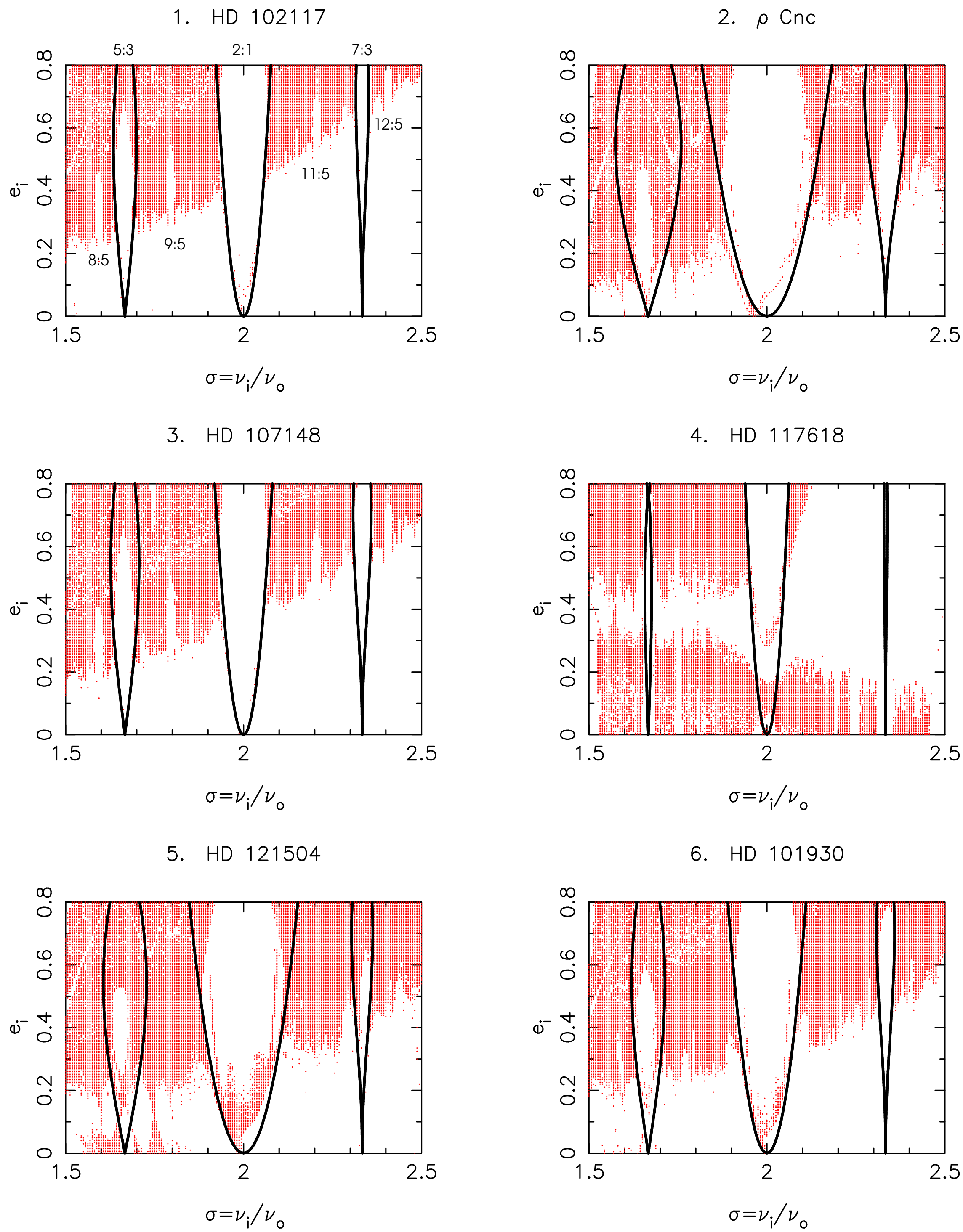

Figure 13.4: Stability maps for systems listed in Table 13.1 together with boundaries for the [2:1](2), [5:3](5) and [7:3](7) resonances. The [2:1](2) resonance boundary is given by $\sigma(e_i) = 2 \pm \Delta\sigma$, with $\Delta\sigma$ defined in (13.5), while the other two resonances are defined in M1. Some significant resonances are indicated for system 1. *Note that these maps are independent of the mass of the hypothetical companion as long as $m_i/m_o \ll 1$.* Note also that they assume the minimum mass is the actual mass; increasing the planetary masses (holding other parameters constant) increases the width of the resonances by a factor $\sim \sqrt{m_o/m_*}$. To gauge the extent of this effect, compare systems 1 and 6 for which $e_o = 0.11$ but m_o/m_* differs by a factor of 2.3.

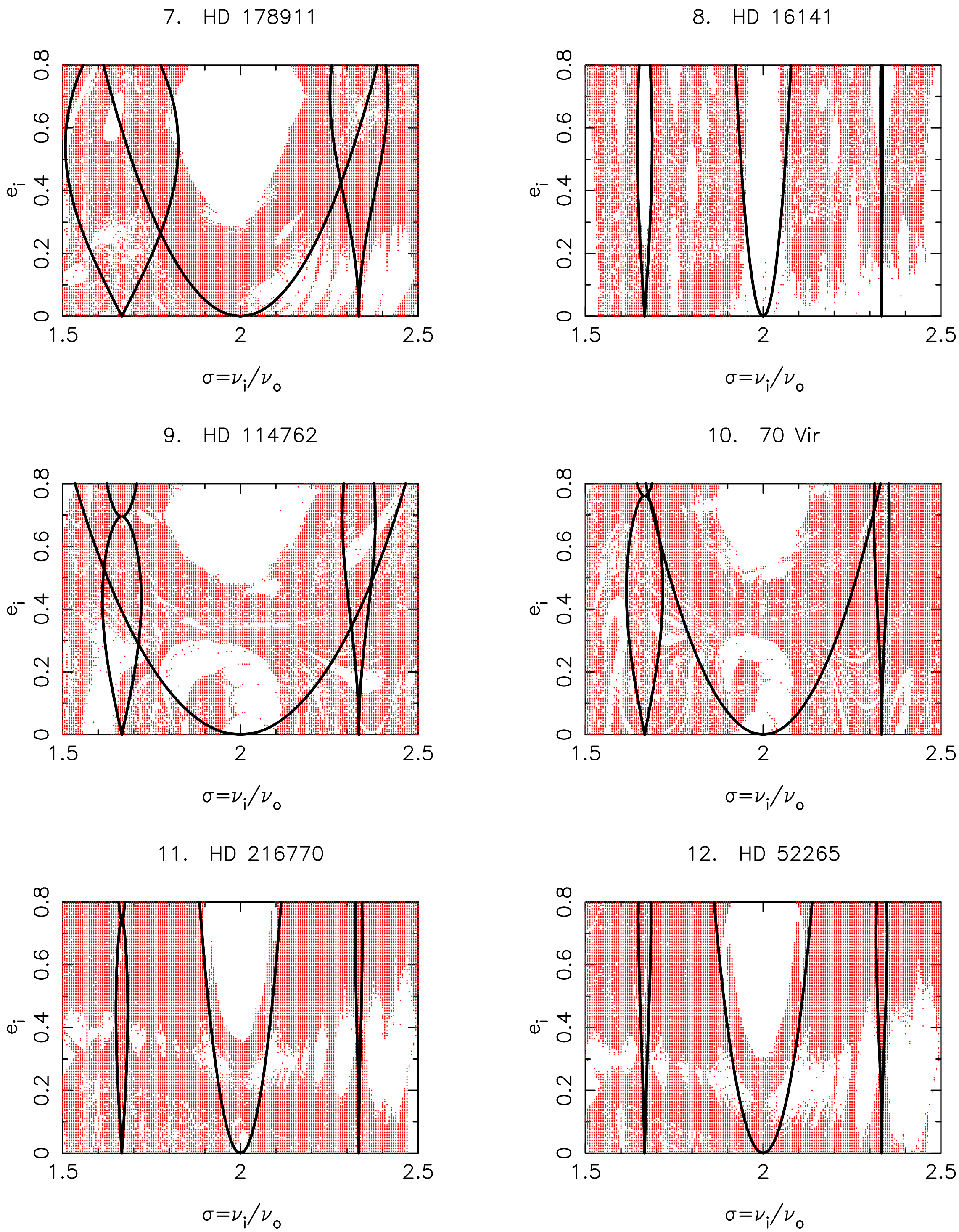

Figure 13.5: Stability maps for systems listed in Table 13.1 together with boundaries for the [2:1](2), [5:3](5) and [7:3](7) resonances.

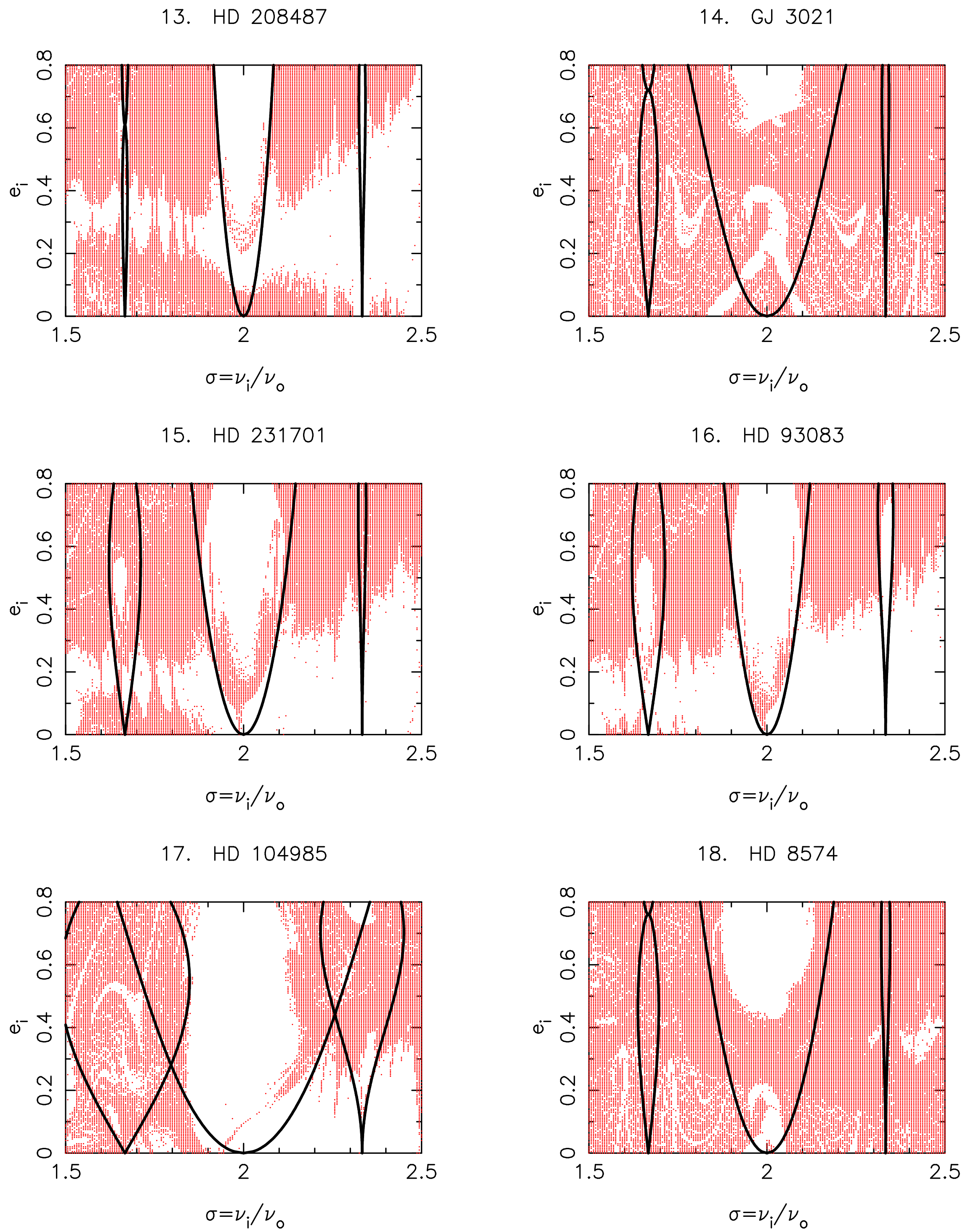

Figure 13.6: Stability maps for systems listed in Table 13.1 together with boundaries for the [2:1](2), [5:3](5) and [7:3](7) resonances.

low values of m_o/m_* are stable for most configurations inside the 2:1 resonance. In contrast, systems such as HD 178911 and HD 114762 (systems 7 and 9) have relatively large values of this parameter so that the width of the [2:1](2) resonance is large (see equations (13.5) and (13.6)) and there is much more opportunity for resonance overlap with significant nearby resonances such as 5:3, 9:5, 11:5 and 7:3. For many systems (for example, system 11) the 2:1 resonance is bounded below at a finite value of e_i. This can be accurately predicted when more terms are included in the analysis (for example, not just $m = 2$; see M2).

Note that the effect of increasing e_o is to decrease the width of the [2:1](2) resonance as Figure 13.1 demonstrates, at least until $e_o \simeq 0.68$ at which point the contribution from this term vanishes. Note also that these stability maps are not sensitive to the mass of the companion as long as $m_i \ll m_o$; systems with more significant companion masses have wider resonance widths and hence more opportunity for resonance overlap as the dependence on m_i in (13.6) shows.

13.5 Data analysis

Radial velocity data for extrasolar planetary systems tend to be patchy in time, with observing rates from one or two measurements per year to many over several days depending on the orbital period (and when the presence of a planet is confirmed). The whole time series is fitted with a single Keplerian solution, and unusually large scatter prompts further analysis for the presence of companion planets. Since the orbital periods are unaffected secularly by such companions (as long as they are not in resonance), the residuals of systems with large scatter are also fitted with Kepler solutions. If the periods are commensurate, a self-consistent three-body solution can be sought (Laughlin and Chambers 2001).

Stellar reflex velocities due to a hypothetical $10M_\oplus$ companion in the internal 2:1 resonance are listed in the last column of Table 13.1. These are around 1-2 $\mathrm{m\,s^{-1}}$ and hence are below the stellar jitter limit for mature solar-type stars so that a straight-forward Kepler fit to the residuals would not reveal the presence of such a companion. Similarly, a periodogram analysis is not capable of identifying the libration frequency because the contribution to the total power is of the order of $\delta P_o/P_o$ per libration period. In other words, one needs to collect data for $P_{lib}/\delta P_o \sim$ several thousand orbital periods to see a measurable effect.

However, if enough data exists over at least a libration period (recall that this quantity is almost independent of the parameters of a low-mass companion for most stable systems so it is easy to estimate), it can be divided into several adjacent time periods, each with its own orbital solution. If a system does harbour a low-mass companion in the inner 2:1 resonance, the orbital period thus calculated will vary with an amplitude δP_o given by (13.11), and with a modulation period given by (13.9), depending on the values of e_i, m_i and $\delta\sigma$. As long as δP_o is significantly more than the uncertainty in P_o, this procedure has the potential to reveal the presence of a resonant companion.

#	System	P_o (d)	$m_*/M_\odot$	m_o/M_J	e_o	$[P_{lib}/P_o]_{est}$	$[P_{lib}/P_o]_{act}$	δP_o (hr)	ΔP_o (hr)	v_* ($\mathrm{m\,s^{-1}}$)
1	HD 102117	20.67	0.95	0.17	0.11	39.3	45	5.42	5.52	3.1
2	ρ Cnc B	39.845	0.95	1.04	0.04	17.3	26	2.0	4.6	2.5
3	HD 107148	48.056	1.12	0.21	0.05	38.7	45	10.7	11.0	2.1
4	HD 117618	52.2	1.05	0.19	0.39	48.7	43	[12.5]	10.3	2.1
5	HD 121504	64.6	1.0	0.89	0.13	19.5	30	3.9	8.1	2.0
6	HD 101930	70.46	0.74	0.3	0.11	27.4	36	11.6	(16.9)	2.4
7	HD 178911	71.487	1.07	6.29	0.12	7.7	9.5	0.6	(3.3)	1.9
8	HD 16141	75.56	1.0	0.23	0.21	37.2	48	15.5	16.7	1.9
9	HD 114762	83.89	0.9	11.02	0.34	6.2	5	0.4	(2.8)	2.0
10	70 Vir	116.689	1.1	7.44	0.4	9.0	25	0.9	(4.0)	1.6
11	HD 216770	118.45	0.9	0.65	0.37	25.6	22	9.7	15.1	1.8
12	HD 52265	118.96	1.2	1.13	0.29	21.0	20	5.8	(11.0)	1.5
13	HD 208487	123	1.3	0.45	0.32	34.5	30	14.1	16.4	1.5
14	GJ 3021	133.82	0.9	3.32	0.51	15.0	chaotic			
15	HD 231701	143.5	1.14	1.03	0.19	20.0	22	7.6	(15.2)	1.4
16	HD 93083	143.58	0.7	0.37	0.14	24.6	32	19.6	32.0	2.0
17	HD 104985	198.2	1.5	6.3	0.03	9.0	15	1.8	(7.9)	1.1
18	HD 8574	228.8	1.04	2.23	0.4	15.9	12	5.7	(14.4)	1.3

Table 13.1: Orbital and resonance parameters for systems in Figures 13.4-13.6. m_o is the minimum mass of the observed planet and v_* is the stellar reflex velocity due to the hypothetical companion.

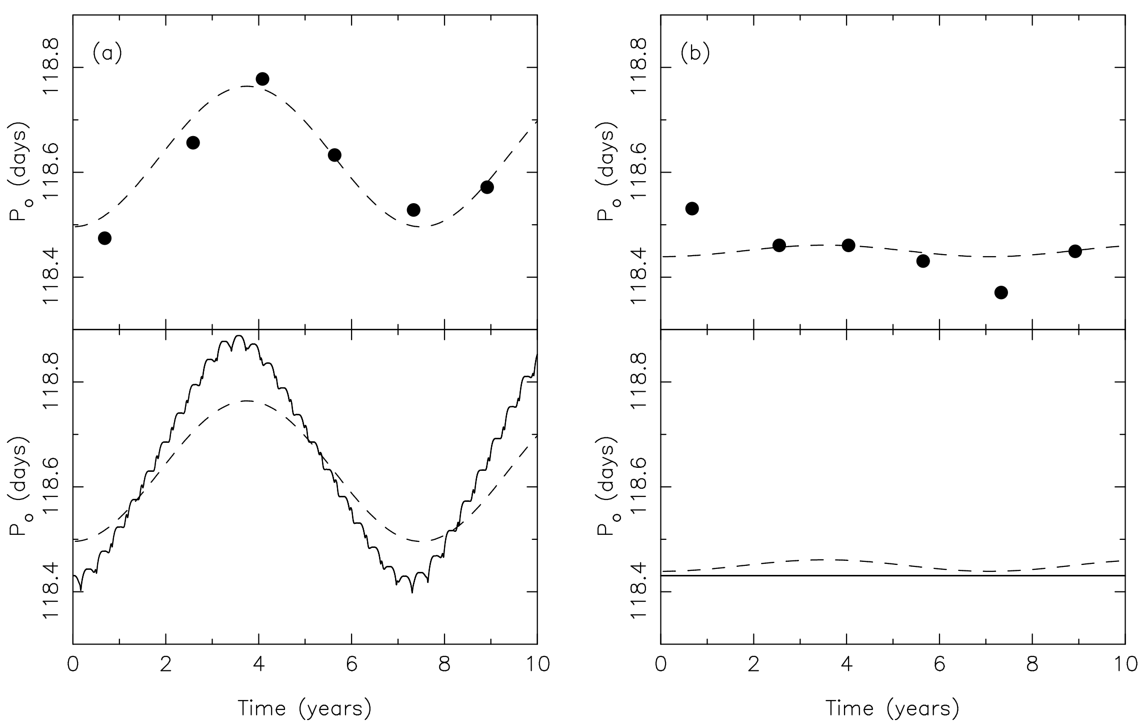

Figure 13.7: Piecewise estimates (filled circles) of the orbital period for a simulated HD 216770-type system (a) with and (b) without a $10M_\oplus$ companion in the interior 2:1 resonance. The solid curves are exact solutions from three-body integrations while the dashed curves are sine curve fits to the points, constrained by knowledge of possible values for the libration period. Simulated radial velocity data includes instrument and stellar jitter noise. Reduced chi-squared values for piece-wise orbital fits range from 0.48 to 0.81.

Figure 13.7(a) illustrates this for a hypothetical $10M_\oplus$ companion to HD 216770 (system 11) with $e_i = 0.5$ and $\delta\sigma = -0.05$. Synthetic radial velocity data was generated using a direct three-body integrator, and noise representing both instrumental and stellar jitter was added, this being drawn at random from zero-centred normal distributions with standard deviations of 2 and 3 $\mathrm{m\,s^{-1}}$ respectively (Butler et al. 1996). Each point in Figure 13.7(a) was calculated from five successive orbital periods sampled at the rate of around 16 radial velocity measurements per orbit using a Levenberg-Marquardt algorithm to calculate (single-planet) orbital solutions (Press et al. 1986).[5] While this is an unrealistic sampling rate for the entire libration period for most systems ($22P_o \sim 7.1\,\mathrm{yr}$ for HD 216770), in practice it is only necessary to have reasonable coverage of enough segments of the libration cycle to produce an estimate of the modulation amplitude. If the estimated (say, 2σ) error in the orbital period for each subset of data, $\delta P_{2\sigma}$, is less than the apparent maximum variation in the period, one can fit a sine curve with period in the range $P_{lib}(e_i^{max})$ to $P_{lib}(e_i^{min})$, where e_i^{min} corresponds to the minimum value of e_i for which systems are stable, and $e_i^{max} \simeq 0.8$ corresponds the minimum in $s_1^{(22)}(e_i)$. A least squares fit is

[5] To simplify the procedure and in particular, to improve the likelihood of convergence, we performed an initial fit to the whole data set. Keeping all parameters fixed except the orbital period and the periastron time, we then found fits to each subset of data.

indicated by the dashed curves in Figure 13.7(a), and this is overlayed in the bottom panel by the "exact" three-body solution (with no noise). An initial guess for the period is selected from within the range $P_{lib}(e_i^{max})$ to $P_{lib}(e_i^{min})$ (20-30P_o for HD 216770), and subsequent iterations are constrained to stay in this range. Similarly, the initial guess for the amplitude is bounded above by the resonance width, ΔP_o, or the value of δP_o corresponding to the maximum width of the stable region, whichever is smaller. The initial guess for the phase can be taken as zero. For the example shown here, this procedure produces an estimated period variation of 6 hr or 55% of the true value, with a much smaller error in the libration period (around 4%). The reduced chi-squared values for the period estimate points (calculated from the fitted radial velocity solutions) ranged from 0.48 to 0.81.

Using the libration period obtained from the least squares fit (dashed curve in Figure 13.7(a): $P_{lib}/P_o|_{est} \simeq 23.11$), an estimate for the eccentricity of the companion planet can be obtained using a least squares cubic fit to the numerical data shown in Figure 13.2 for HD 216770. This gives $e_i^{est} = 0.476$ which differs from the true value by 0.024. Similarly, using $\delta P_o/P_o|_{est} = 0.55\,\delta P_o/P_o|_{true}$ together with (13.11) we find $(m_i/M_\oplus)\,\delta\sigma = -0.233$. This allows us to put a lower bound on m_i (or rather, $m_i \sin i$, where i is the inclination to the line of sight) of $3.33 M_\oplus$ given the upper bound for $|\delta\sigma|$ of $\Delta\sigma = 0.077$ for HD 206770. An upper bound on m_i is provided by the sensitivity of the radial velocity measurements.

The exercise described above was repeated, this time with *no* companion planet to modulate the orbital period. Figure 13.7(b) shows the results for this, with the best fit solution having an amplitude of a little more than half an hour, and with similar reduced chi-squared values as before. Thus in this case the technique is capable of distinguishing between systems which do and do not harbour a low-mass companion in the interior 2:1 resonance.

Confidence intervals for orbital periods naturally depend on the quantity and quality of radial velocity data, with typical uncertainties varying from half an hour to half a day. This range should be compared with entries in Table 13.1 under the heading δP_o; clearly a system such as #7 is unlikely ever to reveal the presence of a low-mass companion even if one exists, while system 6, for example, shows a lot more promise. Note that while we did not calculate confidence intervals for P_o for each data point in Figure 13.7, these are calculated as a matter or course for real systems (although they are not always quoted!). The number of segments used also depends on the quantity and quality of data; the fewer segments used the lower the uncertainties for each period estimate, while the more segments used the more constrained the fit is to the time dependence of the period. This presents an optimisation problem which will be peculiar to each data set.

In practice one can use an existing orbit-fitting package to estimate the individual periods and their uncertainties. It is not clear whether any advantage is gained by using the simplified approach taken here since we did not calculate uncertainties. Either way, the guiding principle for a real system should be that the error in each measurement should be significantly less than the predicted measurement.

13.6 Summary

We have presented simple expressions for the resonance width, the libration period and the change in the observed orbital period of a planet with a companion in the internal 2:1 resonance, *these being valid for arbitrary eccentricities and planet masses*. Unlike the standard formulae derived using the restricted three-body problem, this formulation allows one to determine the effect of a low-mass body on a massive body. Stability maps for a selection of currently known single-planet systems have been provided for the purpose of determining which systems are capable of harbouring a companion planet, and moreover, to constrain possible orbital parameters of such a companion. Finally we have suggested how these expressions and stability maps can be used together with existing and future radial velocity data to determine whether or not an apparently single-planet system harbours a low-mass companion in the interior 2:1 resonance, at least one which is not at exact resonance.

Systems for which radial velocity data covering at least one libration cycle has been collected can be analysed as follows. The data is divided into a number of segments and estimates for the orbital period are made for each segment. If a companion exists away from exact resonance, the orbital periods associated with each solution will vary by an amount δP_o (equation (13.11)) on a timescale P_{lib} (equation (13.9)). As long as the error estimates for each orbital period are sufficiently less than δP_o, this technique has the potential to identify such companions. Moreover, a lower bound can be placed on the (minimum) mass of the companion, with an upper bound naturally provided by the sensitivity of the radial velocity measurements. In addition, the orbital eccentricity can be estimated reasonably accurately since we know the dependence of the libration period on e_i (via three-body integrations rather than (13.9)).

Finally, if orbital period modulation is suggested by existing data using the procedure described here, a series of more intensive observing campaigns can be planned to refine period estimates and their variation. A preliminary result for the detection of orbital period modulation in HD 121504 using existing data is presented in the next chapter.

Chapter 14

Evidence for a low mass companion to the planet HD 121504 b

In this chapter preliminary results are presented that provide evidence for the existence of a low mass companion to the Jupiter mass planet HD 121504 b. The existing data for this system are analysed using the theoretical approach introduced in Chapter 13 and a similar data analysis method to Section 13.5. The analysis presented in this chapter can be used to constrain the mass of a potential low mass companion residing near the inner 2:1 mean motion resonance.

At the time of publication the best available fit to the radial velocity (RV) data for HD 121504 is a single planet with a minimum mass of $m_o \sin i = 0.89$ $\mathrm{M_J}$ (refer to footnote [1]), orbital period of $P = 64.6$ days, eccentricity of $e = 0.13$, argument of pericentre $\omega = 199°$ and time at pericentre of $t_0 = 1563$ (JD-2450000).

This study provides a significantly better fit to the data that the single planet Keplerian fit and in so doing provides strong evidence of a low mass companion in the inner 2:1 mean motion resonance. The available parameters for the single Jupiter mass planet are taken as a starting point for the fitting procedure.

With the exception of t_0, the available best fit orbital parameters are given in Table 13.1. Note that the parameters that best fit the data using a single planet quoted in this table are from a more recent source (late 2005) than the original discovery paper (Mayor et al. 2004). The RV data is taken from Mayor et al. (2004) and consists of 100 data triplets of radial velocity (v_k), time (t_k) and associated uncertainty (δv_k), taken over 4.1 years. The observed radial velocities are shown as black data points in Figure 14.1, along with the best fit obtained for a single planet shown as a red curve. The radial velocity data in Mayor et al. (2004) has been corrected for the stellar velocity and rotation.

The perturbation to a stars radial velocity due to a single planet in a Keplerian orbit is given

[1] Note that $\sin i$ refers to the inclination to the line of sight not to the relative inclination between orbits, the latter denoted throughout this thesis by I.

(a) Fits to radial velcity data for HD 121504

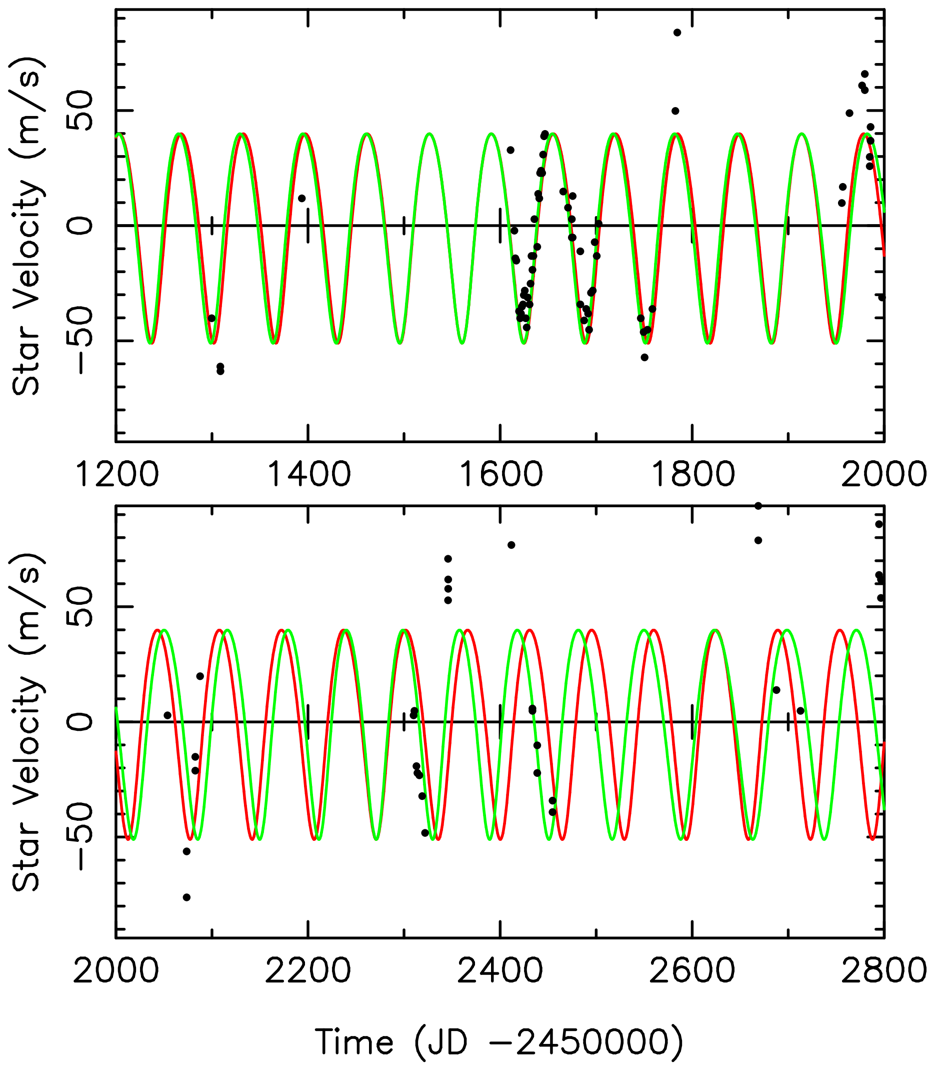

(b) Period as a function of time

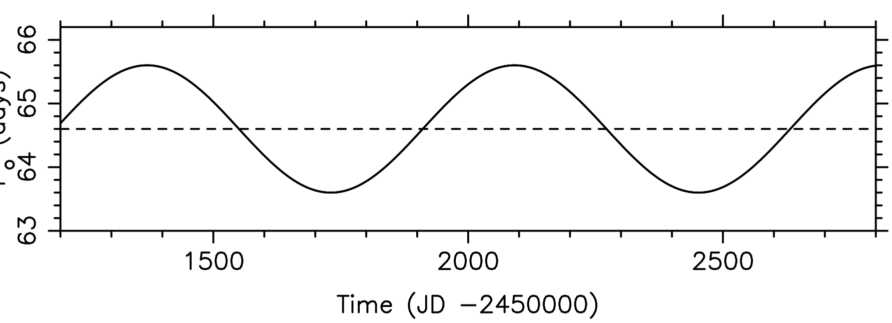

Figure 14.1: Radial velocity data for HD 121504 (black points) and best fit for a single planet in a Keplerian orbit (red curve) is shown in the top panel. The green curve is an example fit obtained using the method described in the text with $\delta P_o = 1$ day, $e_i = 0.4$ and $\phi = 2.20$. Values for the reduced χ^2 statistic defined by Equation (14.6) are 45.30 and 38.97 for the red and green curves respectively. The bottom panel shows the corresponding period for the observed Jupiter mass planet for the two planet fit, given by Equation (14.4).

by (based on the form given in Ford 2005)

$$f(t_k) = K\left[\cos\omega\left(e + \frac{\cos E - e}{1 - e\cos E}\right) - \sin\omega\left(\frac{\sin E\sqrt{1-e^2}}{1 - e\cos E}\right)\right] \tag{14.1}$$

with

$$K = \frac{m_o \sin i\sqrt{G}}{\sqrt{(m_o + m_*)a(1-e^2)}} \tag{14.2}$$

where m_o is the mass of the observed Jovian planet, m_* is the mass of the star and a and e are the semi-major axis and eccentricity of the orbit respectively. The eccentric anomaly (E) is found iteratively from the time (t_k) of each observed velocity (v_k) using the mean anomaly (Equation 1.6), i.e.

$$E - e\sin E = \frac{2\pi}{P(t_k)}\,(t_k - t_0) \tag{14.3}$$

where t_0 is the time at pericentre and is given above. For a non-resonant system the orbital period is constant, i.e. $P(t_k) = P_o$, and P_o is determined using the five Keplerian parameter fit (K, P_o, e, ω and t_o). This fit to the RV data for HD 121504 is shown as the red curve in Figure 14.1 and uses the orbital parameters given previously.

For a two planet fit the orbital period of the observed Jupiter mass planet is time dependent. For a system with an unseen low mass companion in the inner 2:1 mean motion resonance the variation in the orbital period of the observable planet is given by

$$P(t_k) = P_o + \delta P_o \sin\left(\frac{2\pi t_k}{P_{lib}} + \phi\right) \tag{14.4}$$

where the libration period (P_{lib}) is given by (Equation 13.9)

$$P_{lib} = \alpha\left[-s_1^{(22)}(e_i)\right]^{-1/2} P_o, \tag{14.5}$$

$s_1^{(22)}(e_i)$ is defined by Equation (13.7) and $\alpha = 11.68$ for the orbital parameters given in Table 13.1 for HD 121504. The value of ϕ in Equation (14.4) must be fitted to the RV data from the range 0 to 2π. The other free parameters are the orbital eccentricity of the low mass companion (e_i) and the magnitude of the period variation it can induce in the detectable planetary orbit (ΔP_o). This introduces three additional parameters to fit the orbit with, which are now K, e, ω, t_o, P_o, δP_o, e_i and ϕ.

We can place constraints on the free parameters e_i and δP_o using the stability maps presented in the previous chapter. From the stability map for HD 121504 (#5 in Figure 13.4) the system is stable near the 2:1 mean motion resonance for a 10 $M_\oplus$ planet if $e_i > 0.2$ and $\delta\sigma \lesssim 0.1$, where $\delta\sigma = |2 - T_o/T_i|$ is the distance from exact resonance. To provide an upper limit on δP_o consider that the maximum mass of an undetected planet (m_i) is constrained by the stellar jitter and measurement uncertainties of the RV data. The data taken from Mayor et al. (2004) has uncertainties of $\sim$ 10 m/s, so the maximum planetary mass is given by $m_i \sin i \approx 30 M_\oplus$. Using

Equation (13.11) with this mass and the maximum distance from resonance that gives a stable system yields $\delta P_o \approx 1.1$ days. The magnitude of the change in the orbital period may be twice this theoretically predicted amount, as was seen in the discrepancy between numerical results and theoretical predictions for HD 121504 in Table 13.1. The lower limit for the period change is $\delta P_o = 0$, which corresponds to the system being in exact resonance or to there being no low mass companion in the system.

To compare the fits to the RV data for a single planet with and without a low mass companion we require a quality of fit that includes the extra three parameters introduced for a low mass companion. To this end the reduced χ^2 statistic with the same form as Brown (2004) is used, i.e.

$$\chi_r^2 = \frac{1}{N - N_p} \sum_{k=1}^{N} \left(\frac{f(t_k) - v_k}{\delta v_k} \right)^2 \tag{14.6}$$

where N is the number of observations and N_p is the number of free parameters used to fit the data. For an unperturbed single planet system $N_p = 5$ and when $\delta P \neq 0$ this becomes $N_p = 8$. Both fits to the RV data use Equation (14.1) with the period constant for the single planet fit and given by Equation (14.4) for the two planet fit. Using Equation (14.6) without a low mass companion and with $N_p = 6$ gives $\chi_r^2(\delta P_o = 0) = 45.30$ for the fit shown as a red curve in Figure 14.1.

For systems with a low mass companion fits to the RV data were performed for 132000 candidate three-body systems with e_i and δP_o in the ranges [0.2, 0.8] and [0.0, 1.1] respectively. The steps in e_i and δP_o were both chosen to be 0.01 and 20 values of ϕ were tested for each set of e_i and δP_o. For each pair of e_i and δP_o, the phase of the period variation (ϕ) was varied on $[0, 2\pi]$ and the best fit recorded. The reduced χ^2 statistic values were scaled by the value corresponding to no third body (i.e. the single planet fit) using the ratio

$$X = \frac{\chi_r^2}{\chi_r^2(\delta P_o = 0)}, \tag{14.7}$$

where χ_r^2 is determined by Equation (14.6) for each fit with 9 parameters. The resulting values of X are shown in Figure 14.2 and are shaded when $X < 1.0$. The previously available fit to the data used a single Jupiter mass planet without a low mass companion. The shaded ($X < 1$) sets of δP_o and e_i obtained in this study represent a better fit to the RV data than the fit to the single planet system.

Currently too few RV data points are available for HD 121504 to constrain the parameters e_i and δP_o, as seen in Figure 14.2. An example of a fit to the RV data of HD 121504 obtained by including a low mass companion near the inner 2:1 mean motion resonance is shown as the green curve in Figure 14.1. This fit has the parameters $e_i = 0.4$, $\delta P_o = 1.0$ days and $\phi = 2.20$, which resulted in $\chi_r^2 = 34.24$.

We use this sample two planet fit to the RV data to demonstrate how the e_i and δP_o values can be used to constrain the mass of a potential low mass companion. Firstly the fitted eccentricity of the low mass companion (e_i) can be used with the stability map for the system to

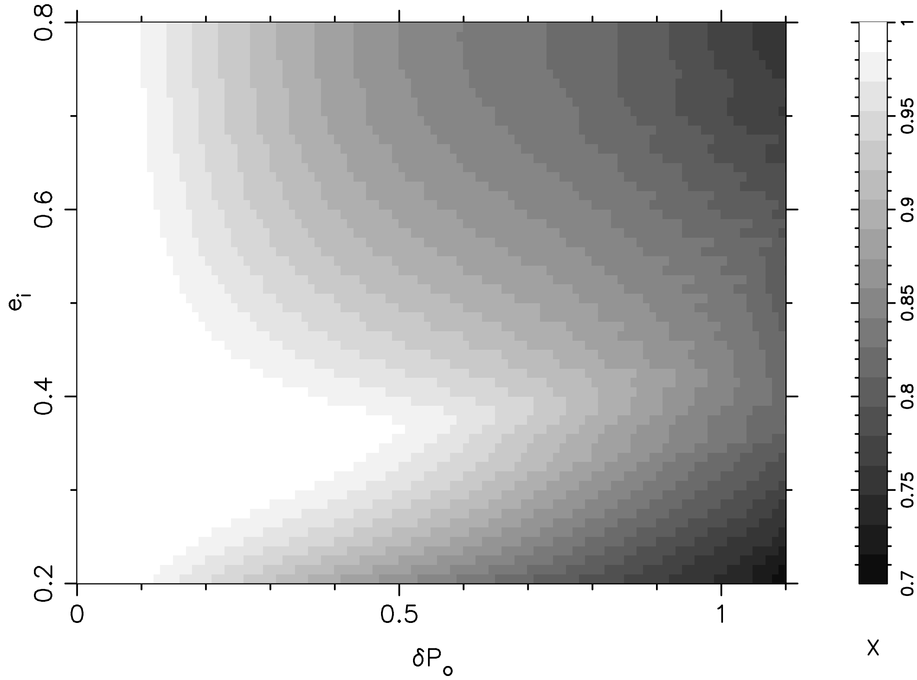

Figure 14.2: Improved fits to RV data of HD 121504 obtained by including a low mass companion near the inner 2:1 mean motion resonance. The ratio between the reduced χ^2 statistic values for the 8 parameter fit with a companion planet and the 5 parameter fit without a companion is denoted by X (see Equation 14.7), which is shown as a function of δP_o (in days) and e_i. See text for details.

give a maximum distance from exact 2:1 resonance σ_{max} which results in a stable system. It is possible to treat e_i and δP_o separately since the libration period (Equation 13.9) only depends on e_i. For this example $\delta\sigma_{max} = 0.1$ for $e_i = 0.4$ as shown in stability map #5 in Figure 13.4. For HD 121504 the value of σ_{max} is approximately constant for $e_i > 0.3$, while most systems with $e_i < 0.3$ are unstable. For a fitted δP_o, Equation (13.11) can be rearranged to get the mass as a function of the distance from exact 2:1 resonance, i.e.

$$m_i \geq \frac{m_o}{2^{2/3}} \frac{\delta P_o}{P_o} \frac{1}{\delta\sigma_{max}} \tag{14.8}$$

where σ_{max} can be estimated using the stability maps presented in the previous chapter for various candidate systems (not just HD 121504), as listed in Table 13.1. For the two planet fit to the RV data shown in Figure 14.1 we find that that $m_i \gtrsim 24\mathrm{M}_\oplus$. Note this lower bound is based on the analytical estimate of the change of the outer planets orbital period and not on numerical integrations of the planetary system.

We can use the results presented in Figure 14.2 to put a minimum mass constraint on the mass as a whole. Better fits to the RV data are found two planet fits with $\delta P_o \gtrsim 0.5$ days for all eccentricity values $0.2 \leq e_i \leq 0.8$ compared to the single planet fit with parameters quoted above. Taking the maximum distance from resonance to be $\sigma_{max} = 0.1$ then the minimum mass of a companion in the 2:1 resonance is $m_i \sin i = 12.3\mathrm{M}_\oplus$. Also recall that a low mass companion must satisfy $m_i \sin i < 30\mathrm{M}_\oplus$ or it would already have been detected using the RV method.

Results presented here are consistent with the existence of a low mass companion with mass range $12\mathrm{M}_\oplus \lesssim m_i \sin i \lesssim 30\mathrm{M}_\oplus$ residing in the interior 2:1 resonance with HD 121504 b. Further higher resolution observations are therefore highly desirable.

Bibliography

Aarseth, S. (2007). *NBODY6 User Manual*. Institute of Astronomy, University of Cambridge.

Aarseth, S. J., Henon, M., and Wielen, R. (1974). *A&A 37*, 183–187.

Aarseth, S. J. and Zare, K. (1974). *Celes. Mech. 10*, 185.

Abadi, M. G., Navarro, J. F., and Steinmetz, M. (2008). *ArXiv: 0810.1429*.

Aguilar, L., Hut, P., and Ostriker, J. P. (1988). *ApJ 335*, 720–747.

Alexander, T. (2005). *Physics Reports 419*, 65–142.

Alexander, T. and Livio, M. (2004). *ApJ 606*, L21–L24.

Allen, C., Moreno, E., and Pichardo, B. (2006). *ApJ 652*, 1150–1169.

Allen, C., Moreno, E., and Pichardo, B. (2008). *ApJ 674*, 237–246.

Athanassoula, E., Vozikis, C. L., and Lambert, J. C. (2001). *A&A 376*, 1135–1146.

Bananoff, F. K., Bautz, M. W., Brandt, W. N., Chartas, G., Feigelson, E. D., Garmire, G. P., Maeda, Y., Morris, M., Ricker, G. R., Townsley, L. K., and Walter, F. (2001). *Nature 413*, 45.

Batygin, K. and Laughlin, G. (2008). *ArXiv: 0804.1946 804*.

Baumgardt, H. (2001). *MNRAS 325*, 1323–1331.

Baumgardt, H., Gualandris, A., and Portegies Zwart, S. (2006). *MNRA 372*, 174–182.

Baumgardt, H., Hopman, C., Portegies Zwart, S., and Makino, J. (2006). *MNRAS 372*, 467–478.

Begelman, M. C., Blandford, R. D., and Rees, M. J. (1980). *Nature 287*, 307–309.

Bellazzini, M. (2004). *MNRAS 347*, 119.

Bica, E., Bonatto, C., Ortolani, S., and Barbuy, B. (2007). *A&A 472*, 483–488.

Binney, J. and Tremaine, S. (1987). *Galactic dynamics*. Princeton, NJ, Princeton University Press, 1987.

Bonnell, I. A. and Rice, W. K. M. (2008). *Science 321*, 1060.

Borderies, N. and Goldreich, P. (1984). *Celestial Mechanics 32*, 127–136.

Borucki, W. J. and Summers, A. L. (1984). *Icarus 58*, 121–134.

Bromley, B. C., Kenyon, S. J., Geller, M. J., Barcikowski, E., Brown, W. R., and Kurtz, M. J. (2006). *ApJ 653*, 1194–1202.

Brown, R. A. (2004). *ApJ 610*, 1079–1092.

Brown, W. R., Geller, M. J., Kenyon, S. J., and Kurtz, M. J. (2005). *ApJL 622*, L33–L36.

Brown, W. R., Geller, M. J., Kenyon, S. J., Kurtz, M. J., and Bromley, B. C. (2007). *ApJ 671*, 1708–1716.

Burstein, D., Li, Y., Freeman, K. C., Norris, J. E., Bessell, M. S., Bland-Hawthorn, J., Gibson, B. K., Beasley, M. A., Lee, H.-c., Barbuy, B., Huchra, J. P., Brodie, J. P., and Forbes, D. A. (2004). *ApJ 614*, 158–166.

Butler, R. P., Marcy, G. W., Williams, E., McCarthy, C., Dosanjh, P., and Vogt, S. S. (1996). *PASP 108*, 500.

Capuzzo-Dolcetta, R. (1993). *ApJ 415*, 616.

Capuzzo-Dolcetta, R. (2004). *Ap&SS 294*, 95–100.

Capuzzo-Dolcetta, R. and Vicari, A. (2005). *MNRAS 356*, 899–912.

Casetti-Dinescu, D. I., Girard, T. M., Herrera, D., van Altena, W. F., López, C. E., and Castillo, D. J. (2007). *AJ 134*, 195–204.

Chandrasekhar, S. (1943). *ApJ 97*, 255.

Chandrasekhar, S. (1949). *Reviews of Modern Physics 21*, 383–388.

Cowling, T. G. (1941). *MNRAS 101*, 367.

Dinescu, D. I., Girard, T. M., and van Altena, W. F. (1999). *ApJ 117*, 1792–1815.

Dinescu, D. I., Girard, T. M., van Altena, W. F., and López, C. E. (2003). *AJ 125*, 1373–1382.

Dinescu, D. I., Girard, T. M., van Altena, W. F., Mendez, R. A., and Lopez, C. E. (1997). *AJ 114*, 1014–1029.

Dinescu, D. I., Majewski, S. R., Girard, T. M., and Cudworth, K. M. (2001). *AJ 122*, 1916–1927.

Duquennoy, A. and Mayor, M. (1991). *A&A 248*, 485–524.

Edelmann, H., Napiwotzki, R., Heber, U., Christlieb, N., and Reimers, D. (2005). *ApJL 634*, L181–L184.

Eisenhauer, F., Schödel, R., Genzel, R., Ott, T., Tecza, M., Abuter, R., Eckart, A., and Alexander, T. (2003). *ApJ 597*, L121–L124.

Ernst, A., Just, A., Spurzem, R., and Porth, O. (2008). *MNRAS 383*, 897–906.

Fall, S. M. and Rees, M. J. (1985). *ApJ 298*, 18–26.

Fellhauer, M., Evans, N. W., Belokurov, V., Wilkinson, M. I., and Gilmore, G. (2007). *MNRAS 380*, 749–756.

Fellhauer, M. and Kroupa, P. (2003). *Ap&SS 284*, 643–646.

Fogg, M. J. and Nelson, R. P. (2007). *A&A 461*, 1195–1208.

Forbes, D. A. and Spitler, L. (2008). In *IAU Symposium*, Volume 245 of *IAU Symposium*, pp. 281–284.

Ford, E. B. (2005). *AJ 129*, 1706–1717.

Fregeau, J. M., Joshi, K. J., Portegies Zwart, S. F., and Rasio, F. A. (2002). *ApJ 570*, 171–183.

Froebrich, D., Meusinger, H., and Scholz, A. (2007). *MNRAS 377*, L54–L58.

Fukushige, T. and Heggie, D. C. (2000). *MNRAS 318*, 753–761.

Genzel, R., Schödel, R., Ott, T., Eisenhauer, F., Hofmann, R., Lehnert, M., Eckart, A., Alexander, T., Sternberg, A., Lenzen, R., Clénet, Y., Lacombe, F., Rouan, D., Renzini, A., and Tacconi-Garman, L. E. (2003). *ApJ 594*, 812–832.

Gerhard, O. (2001). *ApJ 546*, L39–L42.

Ghez, A. M., Morris, M., Becklin, E. E., Tanner, A., and Kremenek, T. (2000). *Nature 407*, 349.

Giersz, M. and Heggie, D. C. (1994). *MNRAS 268*, 257.

Gnedin, O. Y., Lee, H. M., and Ostriker, J. P. (1999). *ApJ 522*, 935–949.

Gnedin, O. Y. and Ostriker, J. P. (1997). *ApJ 474*, 223–255.

Goldstein, H. (1959). *Classical Mechanics*. Addison-Wesley Publishing Company, Inc.

Goodwin, S. P., Kroupa, P., Goodman, A., and Burkert, A. (2007). In B. Reipurth, D. Jewitt, and K. Keil (Eds.), *Protostars and Planets V*, pp. 133–147.

Gould, A. and Quillen, A. C. (2003). *ApJ 592*, 935–940.

Gualandris, A. and Portegies Zwart, S. (2007). *MNRAS 376*, L29–L33.

Gualandris, A., Portegies Zwart, S., and Sipior, M. S. (2005). *MNRAS 363*, 223–228.

Hansen, B. M. S. and Milosavljević, M. (2003). *ApJL 593*, L77–L80.

Harris, W. E. (1996). *AJ 112*, 1487.

Heggie, D. and Hut, P. (2003). *The Gravitational Million-Body Problem: A Multidisciplinary Approach to Star Cluster Dynamics*. Cambridge University Press.

Heggie, D. C. (1975). *MNRAS 173*, 729–787.

Heggie, D. C., Hut, P., and McMillan, S. L. W. (1996). *ApJ 467*, 359.

Henrard, J. (1982). *Celestial Mechanics 27*, 3–22.

Hills, J. G. (1975). *Nature 254*, 295–298.

Hills, J. G. (1988). *Nature 331*, 687–689.

Hills, J. G. (1992). *AJ 103*, 1955–1969.

Hughes, S. (1981). *Celestial Mechanics 25*, 235–266.

Hut, P. and Bahcall, J. N. (1983). *ApJ 268*, 319–341.

Hut, P., McMillan, S., Goodman, J., Mateo, M., Phinney, E. S., Pryor, C., Richer, H. B., Verbunt, F., and Weinberg, M. (1992). *PASP 104*, 981–1034.

Ideta, M. and Makino, J. (2004). *ApJL 616*, L107–L110.

Innanen, K. A., Zheng, J. Q., Mikkola, S., and Valtonen, M. J. (1997). *AJ 113*, 1915.

Keenan, D. W. (1981). *A&A 95*, 340–348.

Kennedy, G. (2001). Honours thesis, Monash University.

Kenyon, S. J., Bromley, B. C., Geller, M. J., and Brown, W. R. (2008). *ApJ 680*, 312–327.

Kim, E., Yoon, I., Lee, H. M., and Spurzem, R. (2008). *MNRAS 383*, 2–10.

King, I. (1962). *AJ 67*, 471.

Komossa, S., Halpern, J., Schartel, N., Günther, H., Santos-Lleo, M., and Predehl, P. (2004). *ApJ 603*, L17.

Kravtsov, A. V., Gnedin, O. Y., and Klypin, A. A. (2004). *ApJ 609*, 482–497.

Kubala, A., Black, D., and Szebehely, V. (1993). *Celestial Mechanics and Dynamical Astronomy 56*, 51–68.

Kundic, T. and Ostriker, J. P. (1995). *ApJ 438*, 702–707.

Kustaanheimo, P. and Stiefel, E. (1965). *J. Reine Angew. Math. 218*, 204.

Laughlin, G. and Chambers, J. E. (2001). *ApJL 551*, L109–L113.

Lee, M. H. and Peale, S. J. (2002). *ApJ 567*, 596–609.

Levin, Y. and Beloborodov, A. M. (2003). *ApJ 590*, L33–L36.

Li, L., Narayan, R., and Menou, K. (2002). *ApJ 576*, 753–761.

Lin, D. N. C., Bodenheimer, P., and Richardson, D. C. (1996). *Nature 380*, 606–607.

Löckmann, U., Baumgardt, H., and Kroupa, P. (2008). *ApJL 683*, L151–L154.

Lu, J. R., Ghez, A. M., Hornstein, S. D., Morris, M. R., Becklin, E. E., and Matthews, K. (2007). In *American Astronomical Society Meeting Abstracts*, Volume 211 of *American Astronomical Society Meeting Abstracts*, pp. 33.

Lu, Y., Yu, Q., and Lin, D. N. C. (2007). *ApJL 666*, L89–L92.

Mardling, R. A. (1991). *Chaos in Binary Star Systems*. Ph. D. thesis, Department of Mathematics, Monash University.

Mardling, R. A. (1995a). *ApJ 450*, 722.

Mardling, R. A. (1995b). *ApJ 450*, 732.

Mardling, R. A. (2008a). in preparation.

Mardling, R. A. (2008b). In S. J. Aarseth, C. A. Tout, and R. A. Mardling (Eds.), *Lecture Notes in Physics, Vol. 760: The Cambridge N-body Lectures*.

Mayor, M., Udry, S., Naef, D., Pepe, F., Queloz, D., Santos, N. C., and Burnet, M. (2004). *A&A 415*, 391–402.

McMillan, S. L. W. and Portegies Zwart, S. F. (2003). *ApJ 596*, 314–322.

Meylan, G. and Heggie, D. (1997). *Astron. Astrophys. Rev. 8*, 1–143.

Meziane, K. and Colin, J. (1996). *A&A 306*, 747.

Miller, M. C. (2006). *MNRAS 367*, L32–L36.

Milosavljević, M. and Loeb, A. (2004). *ApJL 604*, L45–L48.

Miralda-Escudé, J. and Gould, A. (2000). *ApJ 545*, 847–853.

Miyamoto, M. and Nagai, R. (1975). *PASJ 27*, 533–543.

Montuori, M., Capuzzo-Dolcetta, R., Di Matteo, P., Lepinette, A., and Miocchi, P. (2007). *ApJ 659*, 1212–1221.

Moorhead, A. V. and Adams, F. C. (2005). *Icarus 178*, 517–539.

Mouawad, N., Eckart, A., Pfalzner, S., Schödel, R., Moultaka, J., and Spurzem, R. (2005). *Astronomische Nachrichten 326*, 83–95.

Murray, C. D. and Dermott, S. F. (2000). *Solar System Dynamics*. Cambridge University Press.

Murray, N., Hansen, B., Holman, M., and Tremaine, S. (1998). *Science 279*, 69.

Murray, N., Paskowitz, M., and Holman, M. (2002). *ApJ 565*, 608–620.

Murray-Clay, R. A. and Chiang, E. I. (2006). *ApJ 651*, 1194–1208.

Nagasawa, M., Lin, D. N. C., and Thommes, E. (2005). *ApJ 635*, 578–598.

O'Leary, R. M. and Loeb, A. (2008). *MNRAS 383*, 86–92.

Ostriker, J. P., Binney, J., and Saha, P. (1989). *MNRAS 241*, 849–871.

Paumard, T., Genzel, R., Martins, F., Nayakshin, S., Beloborodov, A. M., Levin, Y., Trippe, S., Eisenhauer, F., Ott, T., Gillessen, S., Abuter, R., Cuadra, J., Alexander, T., and Sternberg, A. (2006). *ApJ 643*, 1011–1035.

Peale, S. J. (1976). *ARAA 14*, 215–246.

Perets, H. B. (2008). *ArXiv: 0802.1004 802*.

Perets, H. B., Gualandris, A., Merritt, D., and Alexander, T. (2008). *ArXiv: 0807.2340 807*.

Phinney, E. S. (1989). In *IAU Symp. 136: The Center of the Galaxy*, pp. 543.

Portegies Zwart, S., Gaburov, E., Chen, H.-C., and Gürkan, M. A. (2007). *MNRAS 378*, L29–L33.

Portegies Zwart, S. F., Baumgardt, H., McMillan, S. L. W., Makino, J., Hut, P., and Ebisuzaki, T. (2006). *ApJ 641*, 319–326.

Portegies Zwart, S. F., Makino, J., McMillan, S. L. W., and Hut, P. (2002). *ApJ 565*, 265–279.

Power, C., Navarro, J. F., Jenkins, A., Frenk, C. S., White, S. D. M., Springel, V., Stadel, J., and Quinn, T. (2003). *MNRAS 338*, 14–34.

Press, W. B., Flannery, B. P., Teukolsky, S. A., and Vettering, W. T. (1986). *Numerical Recipes: The Art of Scientific Computing*. Cambridge Univ. Press, Cambridge.

Rasio, F. A. and Ford, E. B. (1996). *Science 274*, 954–956.

Raymond, S. N., Mandell, A. M., and Sigurdsson, S. (2006). *Science 313*, 1413–1416.

Read, J. I., Wilkinson, M. I., Evans, N. W., Gilmore, G., and Kleyna, J. T. (2006). *MNRAS 366*, 429–437.

Salpeter, E. E. (1955). *ApJ 121*, 161.

Schödel, R., Ott, T., Genzel, R., Eckart, A., Mouawad, N., and Alexander, T. (2003). *ApJ 596*, 1015–1034.

Sesana, A., Haardt, F., and Madau, P. (2006). *ApJ 651*, 392–400.

Sesana, A., Haardt, F., and Madau, P. (2007). *MNRAS 379*, L45–L49.

Sigurdsson, S. and Rees, M. J. (1997). *MNRAS 284*, 318.

Sollima, A. (2008). *MNRAS 388*, 307–322.

Sollima, A., Beccari, G., Ferraro, F. R., Fusi Pecci, F., and Sarajedini, A. (2007). *MNRAS 380*, 781–791.

Sosin, C. (1997). *AJ 114*, 1517.

Spitzer, L. (1987). *Dynamical evolution of globular clusters*. Princeton, NJ, Princeton University Press, 1987.

Spurzem, R. and Baumgardt, H. (2003). submitted to MNRAS. Preprint available via ftp://ftp.ari.uni-heidelberg.de/pub/staff/spurzem/edinpaper.ps.gz.

Spurzem, R., Giersz, M., Heggie, D. C., and Lin, D. N. C. (2006). *ArXiv: 0612757v2*.

Spurzem, R., Hemsendorf, M., Sigurdsson, S., Benacquista, M., and Makino, J. (2003). In J. M. Centrella (Ed.), *The Astrophysics of Gravitational Wave Sources*, Volume 686 of *American Institute of Physics Conference Series*, pp. 235–238.

Takahashi, K., Lee, H. M., and Inagaki, S. (1997). *MNRAS 292*, 331.

Tout, C. A., Aarseth, S. J., and Pols, O. R. (1997). *MNRAS 291*, 732–748.

Tremaine, S. D., Ostriker, J. P., and Spitzer, L. (1975). *ApJ 196*, 407–411.

Tsuchiya, T., Korchagin, V. I., and Dinescu, D. I. (2004). *MNRAS 350*, 1141–1151.

Yu, Q. (2002). *MNRAS 331*, 935–958.

Yu, Q. and Tremaine, S. (2003). *ApJ 599*, 1129–1138.